Energy

FOSSIL

X-RAY COMPUTED TOMOGRAPHY OF COAL

Final Report

By
D. H. Maylotte
C. L. Spiro
P. G. Kosky
E. J. Lamby

December 1986

DISCLAIMER

DISCLAIMER

Portions of this document may be illegible in electronic image products. Images are produced from the best available original document.

X-Ray Computed Tomography of Coal

Final Report

D.H. Maylotte
C.L. Spiro
P.G. Kosky
E.J. Lamby

December 1986

Prepared for the

U.S. Department of Energy
Morgantown Energy Technology Center
P.O. Box 880
Morgantown, WV 26505

Work Performed Under

Contract DE-AC21-82MC19210

General Electric Corporate Research & Development
P.O. Box 8
Schenectady, NY 12301

X-Ray Computed Tomography of Coal

Final Report

D.H. Maylotte
C.L. Spiro
P.G. Kosky
E.J. Lamby

December 1986

Prepared for the

U.S. Department of Energy
Morgantown Energy Technology Center
P.O. Box 880
Morgantown, WV 26505

Work Performed Under

Contract DE-AC21-82MC19210

General Electric Corporate Research & Development
P.O. Box 8
Schenectady, NY 12301

MASTER

TABLE OF CONTENTS

LIST OF ILLUSTRATIONS

LIST OF ILLUSTRATIONS (Cont'd)

LIST OF ILLUSTRATIONS (Cont'd)

LIST OF ILLUSTRATIONS (Cont'd)

LIST OF ILLUSTRATIONS (Cont'd)

LIST OF ILLUSTRATIONS (Cont'd)

x

LIST OF ILLUSTRATIONS (Cont'd)

LIST OF TABLES

Section 1

ABSTRACT

X-ray Computed Tomography (CT) is a method of mapping with x-rays the the internal structures of coal. The technique normally produces 2-D images of the internal structures of an object. These images can be recast to create pseudo 3-D representations.

CT of coal has beeen explored for a variety of different applications to coal and coal processing technology. In a comparison of CT data with conventional coal analyses and petrography, CT was found to offer a good indication of the total ash content of the coal. The spatial distribution of the coal mineral matter as seen with CT has been suggested as an indicator of coal washability. Studies of gas flow through coal using xenon gas as a tracer have shown the extremely complicated nature of the modes of penetration of gas through coal, with significant differences in the rates at which the gas can pass along and across the bedding planes of coal.

In a special furnace designed to allow CT images to be taken while the coal was being heated, the pyrolysis and gasification of coal have been studied. Gasification rates with steam and CO_2 for a range of coal ranks have been obtained, and the location of the gasification reactions within the piece of coal can be seen. Coal drying and the progress of the pyrolysis wave into coal have been examined when the coal was subjected to the kind of sudden temperature jump that it might experience in fixed bed gasifier applications.

CT has also been used to examine stable flow structures within model fluidized beds and the accessibility of lump coal to microbial desulfurisation.

Section 2

INTRODUCTION

By itself coal is a difficult material to characterize, and many of the processes through which coal is put (e.g., gasification and combustion) are also difficult to study because of their hostile environments. Numerous and well known techniques have been developed for studying various attributes of coal and its processes, but, it is safe to say, none of them by itself, or even the available group of techniques, gives a satisfyingly complete picture of coal or the changes it undergoes during processing. New techniques, as they appear, are usually impressed to determine what new aspects of coal technology they might help clarify.

Recent advances in x-ray imaging have been driven primarily by the requirements of medical applications, but the machines developed for these purposes can be applied to some aspects of coal science and technology because coal has a similar elemental composition to the human body. X-ray Computerized Tomography (CT) provides clearer images of the internal structures of an object than can be obtained by conventional x-ray radiography. While the latter technique passes x-rays through an object and superimposes the density data from all planes onto one 2-D plane, the CT technique provides an image of a 2-D slice through the object not complicated by out-of-plane data.

The present experimental program has shown that it is possible to image the internal structures of coal and to provide a correlation between the CT images and some of the standard characterizations of coal. More importantly it has been shown that the internal structures of coal can be imaged while the coal is undergoing processing. Most of the experimental effort has been directed at the gasification and combustion of single pieces of coal; however, auxiliary applications of CT to coal slurry stability, microbial desulfurization of lump coal, and fluidized bed flows have been demonstrated.

Section 3

X-RAY COMPUTED TOMOGRAPHY

3.1 OVERVIEW

The CT machine used in this work was a General Electric 8800. A simplified schematic diagram of the important physical elements of the system are shown in Figure 3-1. The x-ray source is a "rotating anode" x-ray tube mounted on a rotatable gantry. The x-rays, as a flat fan beam with a half angle of 30°, pass through the object under test and are detected by an array of 523 pressurized xenon filled detectors mounted on the gantry opposite to the x-ray tube. These detectors measure the intensity of the x-rays which have penetrated the object along the chord connecting the x-ray tube focal spot to the aperture of the detector. The 523 intensity readings taken at one position of the gantry are referred to as a "view." The gantry rotates 360° around the object during the acquisition of the data for one image. During the rotation, 576 views of the object are taken, making a total of 294,366 intensity measurements used to generate the image. In this work the data acquisition time for one image was 9 s. Some newer CT machines have acquisition times of 2 s, and experimental devices using numerous x-ray tubes simultaneously can have acquisition times in the milliseconds. In the 8800, images can be acquired with a delay time of down to about 1 s. Because the x-ray tube will overheat with extended continuous operation, the number of images that can be acquired at this minimum delay time is restricted. The safe number depends upon the operating conditions of the tube and, for our work, 10 images at this fast acquisition rate was a typical limit.

The image that is reconstructed is a map of the x-ray attenuation in a slice through the object under test. The thickness of the slice in all of the images used for this work is 1.5 mm. The images are digital images on a 320 × 320 grid. Each picture element (pixel) in the grid represents an area of 0.2537 × 0.2537 mm square. Each number in the digital image is related to the averaged x-ray attenuation of a volume 0.2537 × 0.2537 × 1.5

mm^3. The spatial resolution of the 8800 is at least 2 pixels, although the presence of a smaller feature with a large density difference to the bulk can be detected. General reviews of the computed tomography technique are given in References 1 and 2.

3.2 DATA ACQUISITION

All of the experiments discussed in this report were carried out using a General Electric 8800 CT/T machine at a General Electric plant in Milwaukee. Upon taking a CT picture, the data were reconstructed into an image and stored on disk. At the end of a series of experiments, the data were transferred to tape and taken to the General Electric Research and Development Center where the data were displayed on a Digital Equipment Company VAX 11/782 with a Lexidata 3400 frame buffer, an Ayadin High Resolution Color Monitor, and a Matrix film copier (Figure 3-2). The necessary software for display and analysis of the images was written in Fortran 77. The analysis features of the software will become apparent during the discussion of the results.

FIELD OF VIEW

X-RAY TUBE

DETECTOR
ARRAY

FAN BEAM
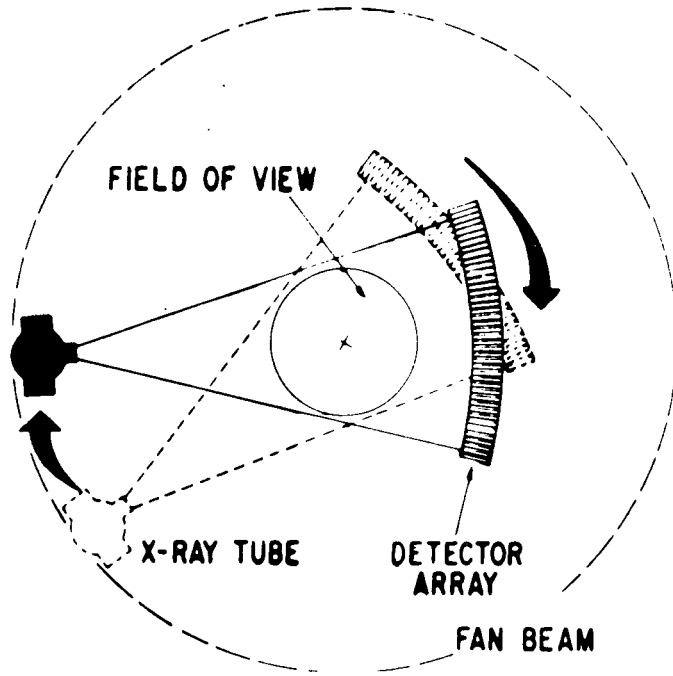
Figure 3-1. Schematic of CT machine

FIELD OF
VIEW

X-RAY
TUBE

DETECTOR
ARRAY

FAN BEAM

CT X-RAY
APPARTUS

CT
COMPUTER
DATA
GENERAL
S200

TAPE

MEDICAL SYSTEMS DIVISION
MILWAUKEE, WISCONSIN

TAPE

DIGITAL
VAX
COMPUTER
II/780

LEXI DATA
3400
GRAPHIC
DISPLAY

MATRIX
2000
SERIES
COLOR
GRAPHICS
MONITOR

BOLEX
H16
CAMERA

AYDIN
C6911
COLOR
DISPLAY
MONITOR

CRD
SCHENECTADY, NEW YORK
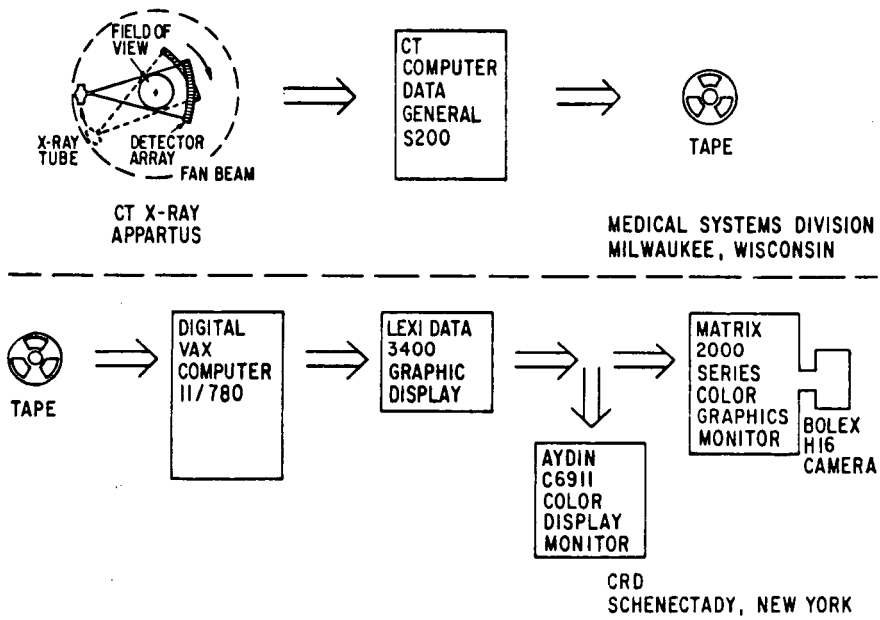
Figure 3-2. Schematic of CT image data acquisition

Section 4

CALIBRATION OF THE X-RAY COMPUTED TOMOGRAPHY MACHINE

4.1 ORGANIC STANDARDS

Medical CT machines are set up for imaging the soft tissues of the body and the bone structures. They are therefore optimized for a mixture of low-density (about 1 g/cm^3) materials with an elemental composition of mainly oxygen, hydrogen, and carbon, and high-density (2 to 3 g/cm^3) materials with high atomic number elements such as calcium. Coal consists of a somewhat similar suite of elements, although in different proportions, and the basic calibration sequence of the CT machine could be left intact for coal experiments. Figure 4-1 shows the 8800 CT machine being calibrated against a water phantom. The CT images are initially maps of the linear x-ray absorption coefficients of the different volume elements within the reconstruction field. The relationship between the attenuation coefficient and the normally reported "CT number" is

$$CT \text{ number} = 1024 \times \left[1 + \frac{\mu(\text{material}) - \mu(\text{water})}{\mu(\text{water})_{E_o}} \right] \qquad (4\text{-}1)$$

where μ(material) is the x-ray linear attenuation coefficient under the experimental conditions, μ(water) is the coefficient for water under the same conditions, and $\mu(\text{water})_{E_o}$ is the coefficient for water under standard conditions.

The x-ray attenuation coefficients for a material vary with the x-ray wavelength and, because the x-rays used in these experiments are not monochromatic but cover a range of wavelengths, there is no fundamentally defined linear absorption coefficient, but rather an instrument-dependent observed coefficient. The observed linear absorption coefficient is given by:

$$\mu(\text{material}) = \frac{1}{L} \ln \left[\frac{I_T}{I_o} \right] \qquad (4\text{-}2)$$

where L is the length (in mm) of the x-ray path through the material; I_o is the detected signal with no material in the beam, and I_t is the detected signal with material in the beam.

In order to make the CT number dimensionless, the observed attenuation coefficients are referenced to that of water under standard conditions. The standard condition for our experiments is the linear absorption of water using monochromatic radiation at 73 keV. The value is 0.01905 mm^{-1}.

From the form of Equation 4-1, it is clear that if the unknown material is itself water, then the CT number is 1024; if the "material" is a vacuum, then the CT number is zero. Air is effectively a vacuum for the conditions of our experiments. The signal from the x-ray detectors is originally analog and passed through a 12 bit A/D converter. The CT number range is therefore 1 to 4096, meaning that materials with up to four times the density of water can be covered.

A number of organic materials consisting primarily of carbon, hydrogen, and oxygen were imaged on the CT machine to determine the machine's sensitivity to elemental composition and bulk density. Water was also imaged for comparison. Figure 4-2 shows the CT image of distilled deionized water in a plastic bottle. An arbitrary square has been chosen covering the water part of the image, and a histogram has been displayed along with a number of statistical parameters. These are:

a. Average

$$\overline{CT} = \sum_{i}^{N} CT(i)/N \tag{4-3}$$

b. Standard Deviation

$$\sigma = \left[\frac{\sum_{i}^{N} \left[CT(i) - \overline{CT} \right]^2}{N} \right]^{\frac{1}{2}} \tag{4-4}$$

c. Skewness from the Average

$$\text{skew(av)} = \left[\frac{\sum\limits_{i}^{N} \left[CT(i) - \overline{CT} \right]^3}{N} \right]^{1/3} \tag{4-5}$$

d. Skewness from the Peak

$$\text{skew(pk)} = \left[\frac{\sum\limits_{i}^{N} \left[CT(i) - CT(\text{peak}) \right]^3}{N} \right]^{1/3} \tag{4-6}$$

The skewness factors are a measure of the asymmetry of the histogram distribution. If the distribution is perfectly symmetrical, then the skewness factor is zero. If more numbers occur below the average than above it, then the skew(av) number will be negative, etc. We have defined our own skew(pk) parameter because we will need a measure of the skewness around the most commonly occurring CT value, which need not be the same as the average value. The usefulness of this skew(pk) parameter will be seen later when the histograms from coal are discussed.

Statistical data from other standard materials are summarized in Table 4-1. The standard deviations and skewness parameters of some of these standards were not as good as the corresponding values for water, and the results suggest that the "standards" were not uniform. Better standards with a narrower density range were made by using hydrocarbon liquids of known density. The CT pictures were taken with the liquids in a thermostatted bath at 27 °C. The results are plotted in Figure 4-3.

The best fit line with the origin included has the form

$$CT\# = 58.0 \times (\text{density})^2 + 894.4 \times (\text{density}) + 9.0 \tag{4-7}$$

A best fit excluding the origin has the form

$$CT\# = 508.9 \times (\text{density})^2 + 5.76 \times (\text{density}) + 429.0 \tag{4-8}$$

The elemental difference between water and the hydrocarbons was enough to bring the CT value of water off the curve in Figure 4-3, therefore, water was not included. The second relationship above is the one we will use for hydrocarbon materials with a density between 1 and 2 g/cm^3.

CT pictures of a number of minerals commonly found in coal were also taken. The conditions under which the pictures were taken were the same as for the liquid standards and these conditions were also the ones most commonly used for the coals. The minerals tested are listed in Table 4-2, along with their composition and nominal densities. In the case of illite, the sample was an "illite containing shale" from Fithian, Illinois, and was found from the CT pictures to be clearly heterogeneous. For kaolin, the sample was a weakly bound lump from Macon County, Georgia, and was highly porous. The bulk density of the kaolin sample was considerably less than the nominal density of the material, as reported in Table 4-2.

In order to reduce the edge artifacts in the CT images of the minerals, each sample was potted in epoxy resin before the CT pictures were taken. The edge artifacts therefore occurred at the outside edge of the epoxy and not at the much smaller density jump at the epoxy-mineral interface. In the kaolin case, the epoxy potting compound soaked into the outer layers of the kaolin sample before it cured. This caused a high-density ring around the outside of the CT image of the kaolin (Figure 4-4). For the unimpregnated kaolin, the CT number is 1882, while for the pure cured epoxy compound the CT number is 1127. The composite material where the epoxy has penetrated into the kaolin has a CT number of 2320. Assuming that the epoxy displaces air and leaves the kaolin structure unaffected, the void fraction (V) in the mineral can be found, along with the CT number for kaolin (K):

$$V \times 0 + (1-V) \times K = 1882 \tag{4-9}$$

$$V \times 1127 + (1-V) \times K = 2320 \tag{4-10}$$

$$V = 0.38 \tag{4-11}$$

$$K = 3078 \tag{4-12}$$

In Table 4-2 the observed CT numbers are listed for these minerals along with their electron density, the ratio of their electron density compared to that of water, and their expected CT numbers, based upon the assumption that all of the x-ray beam attenuation has been by Compton scattering (i.e., that the CT numbers scale with electron density). As can be seen, the agreement between experiment and theory is poor. This lack of agreement

is due to not taking into account the contribution of photoelectric absorption to the attenuation of the x-ray beam.

4.2 MINERAL STANDARDS

The x-ray tubes used in this work have a characteristic emission spectrum or color, as shown in Figure 4-5. Photoelectric absorption causes a complication in the analysis because the xenon detectors used in the CT machines are color sensitive; i.e., they give a different electrical response to photons of different wavelength. Photoelectric absorption in the material being studied affects the color of the x-ray beam incident on the detector and that, in turn, affects the detector response, the observed attenuation coefficient, and hence the CT number. The detectors used in these CT machines are filled with high-pressure xenon. The x-ray K absorption edge of xenon occurs close to the peak of the filtered x-ray tube emission curve. Incoming photons are absorbed by the xenon gas primarily by photoelectric absorption. This causes emission of energetic electrons whose energy is thermalized by ionizing collisions with neutral xenon atoms. The effective energy lost per ionizing collision is 22 eV. The detector electronics records the current in the gas caused by this ionization. If I is the current and $d(E)$ is the spectrum of the deposited x-ray energy, then the detector signal is given by

$$I \propto \int \frac{d(E)E}{E_d} \, dE \qquad (4\text{-}13)$$

where E is the energy of the photon and E_d is the electron energy lost per ionizing collision.

If the emitted x-ray tube intensity (after the inherent aluminum filtration of the tube) is $i(E)$, then $d(E)$ is some function of $i(E)$, depending upon the absorption characteristics of the xenon detector. In the case with no absorber in the beam,

$$d(E) = A(E) \times i(E) \qquad (4\text{-}14)$$

and

$$I_o \propto \int A(E) \times i(E) \times E \, dE \qquad (4\text{-}15)$$

where I_o is the detector current with nothing in the beam.

4-5

If an absorber is in the beam, it modifies the x-ray beam by a function $T(E)$

$$I_T = \frac{1}{E_d} \int T(E) \times A(E) \times i(E) \times EdE \qquad (4\text{-}16)$$

If $T(E)$ is a constant (i.e., does not affect the x-ray color), then

$$I_T = \text{const} \times I_o \qquad (4\text{-}17)$$

and the attenuation coefficient can be calculated by the expression

$$\alpha = -\frac{1}{L} \ln \left[\frac{I_T}{I_o} \right] \qquad (4\text{-}18)$$

where L is the length of the absorber.

If $T(E)$ is, instead, a function of the x-ray wavelength, then

$$\frac{I_T}{I_o} = \frac{\int T(E) \times A(E) \times i(E) \times EdE}{\int A(E) \times i(E) \times EdE} \qquad (4\text{-}19)$$

and the value of the ratio

$$\frac{I_T}{I_o} \qquad (4\text{-}20)$$

clearly depends upon the function $T(E)$, i.e., the color change in the x-ray spectrum caused by the absorber.

The x-ray absorption and detection processes in the CT experiment have been modeled to specifically take into account the varying attenuation mechanisms of the elements commonly found in the minerals of coal. Figure 4-6 shows a schematic of the absorption process. The emission spectrum of a medical x-ray tube operated at 150 kV is shown in Figure 4-5. The spectrum is essentially the bremsstrahlung emission continuum modified by the inherent aluminum absorption of the tube window at the low energy end and by the tungsten emission lines in the region around 67 keV.

The absorption spectra of carbon and calcium are shown in Figures 4-7 and 4-8. These elements cover the atomic number range of primary interest in this work. Within the

emission of the x-ray tube, the absorption at the low energy end is primarily caused by the photoelectric effect while Comptom scattering causes the attenuation at the higher energies. The ratio of the photoelectric cross section to the Compton cross section varies considerably between carbon and calcium (Table 4-3), and this causes absorbers containing the different elements to not only attenuate the x-ray beam but also change its color. Knowing the elemental composition of the absorber, the spectrum of the transmitted x-ray beam can be calculated. Figures 4-9 and 4-10 show the transmitted spectrum for 1 cm of coal and 1 cm of calcite. The preferential absorption of the low energy photons by calcium is clear. Knowing the absorption spectrum of the xenon detectors, the spectrum of the deposited energy can be calculated and, finally, from a knowledge of the ionization potential of the xenon gas, the detector current can be calculated.

By carrying out these calculations with and without an absorber in the beam, the expected values of the current with and without the absorber can be estimated, and theoretical estimates of the attenuation coefficient can be made. The results of such a calculation for a number of materials is shown in Table 4-4. The CT numbers have been calculated from the linear attenuation coefficients using Equation 4-1. The theoretical numbers are based only on the emission spectrum of the x-ray tube, the x-ray attenuation cross-sections of the elements involved, the absorption characteristics of the detectors, the density of the absorber, and its path length in the beam. The calculations give a good explanation of the CT numbers of the minerals and also an a priori explanation for the CT number of coal. The theory predicts a CT number of 1205 and, as will be seen, many of our coals show a peak in their CT number distribution in the range 1200 to 1250. The results for the minerals suggest that, for the purposes of the CT experiments, they can be grouped into two classes. The first class consists of minerals containing low atomic number (Z) elements (e.g., kaolin, illite, silica, and feldspar) and a second class of minerals with high Z elements (e.g., calcite, rutile, and pyrite). For the light class, we can assign an expected CT number of 3100, while the heavy minerals are off scale at 4095.

4.3 EXPECTED DENSITY RANGES FOR COAL MACERALS

It is well known that the organic fractions of coal are not homogeneous. Historically they have been classified into maceral groupings, based upon the different optical proper-

ties of the materials, and it has been found that the entities isolated by the light microscope have distinguishing features other than optical. For the purposes of a CT examination, the difference in physical densities of the maceral groups in coal is the most promising property by which to distinguish them.

The densities of the organic fractions of coal can be expected to fall in the range 1.0 to 1.5 g/cm^3. Dyrkasz (Reference 3) has developed techniques for the separation of coal components by continuous centrifugation using a density-graded fluid. An adaption of one of their figures is given in Figure 4-11. Without demineralization the three major maceral groups were not well separated and the (predominantly vitrinite) coal fractions ranged from 1.28 to 1.5 g/cm^3 with a peak at 1.32 g/cm^3. This coal had 23% mineral matter, mainly clays, and it appears that the mineral matter occurred as particles below the grinding size of the micronizer, intimately mixed with the coal. In programs parallel to this CT program, we have found that continuous centrifugation of micronized coals can give reasonably sharp peaks without chemical demineralization. For example, Figure 4-12 shows a plot of the density distribution from a Winifrede seam coal (ca. 14% ash). Without demineralization, the plot peaks out at ca. 1.25 g/cm^3, and the peak represents the vitrinite fraction of coal.

Vitrinite is the most commonly occurring maceral in coals and has been the most studied. For non-U.S. coals, Franklin (Reference 4) and van Krevelen (Reference 5) found that the density of vitrinite varied with the coal rank as expressed by the dmmf carbon value (Figure 4-13). The density values obtained by the centrifuge technique are isopycnic, i.e., based upon the density difference between the coal particle and the supporting fluid, while the densities in Figure 4-13 are helium densities. However, both Franklin and Walker (Reference 6) have shown that, to within the accuracy of our CT experiments, the difference between the two methods is negligible.

Where currently available the analysis of our coal seams, as given by the mine operator, is listed in Table 4-5, and a summary of the percent carbon values is listed in Table 4-6. According to the results in Figure 4-13 this should give the vitrinites in these coals a density range of 1.3 to 1.4 g/cm^3.

Density data on macerals other than vitrinite is not very common. On German brown coals, Stach quotes the density of the exinite group (resinite, sporinite and alginite) to be 1.0 to 1.2 g/cm^3 (Reference 7).

In discussing the members of the inertinite group, Stach, where values are quotes at all, gives their densities to be in a range higher than vitrinite, e.g., the density of fusinite is "ca. 1.5," and the density of semi-fusinite in bituminous coals "varies from about 1.35 to 1.45" (Reference 7).

The maceral density results from the centrifuge experiments of Dyrkasz et al. are summarized in Table 4-7. If typical values of 1.2 g/cm^3 for sporinite, 1.3 g/cm^3 for vitrinite, and 1.4 g/cm^3 for inertinite are taken, then the range of CT values covering the range of organic densities is ca. 1150 to 1300. Considering that the accuracy of the CT machine is ±2 CT numbers, this is a wide variation and readily distinguishable by CT.
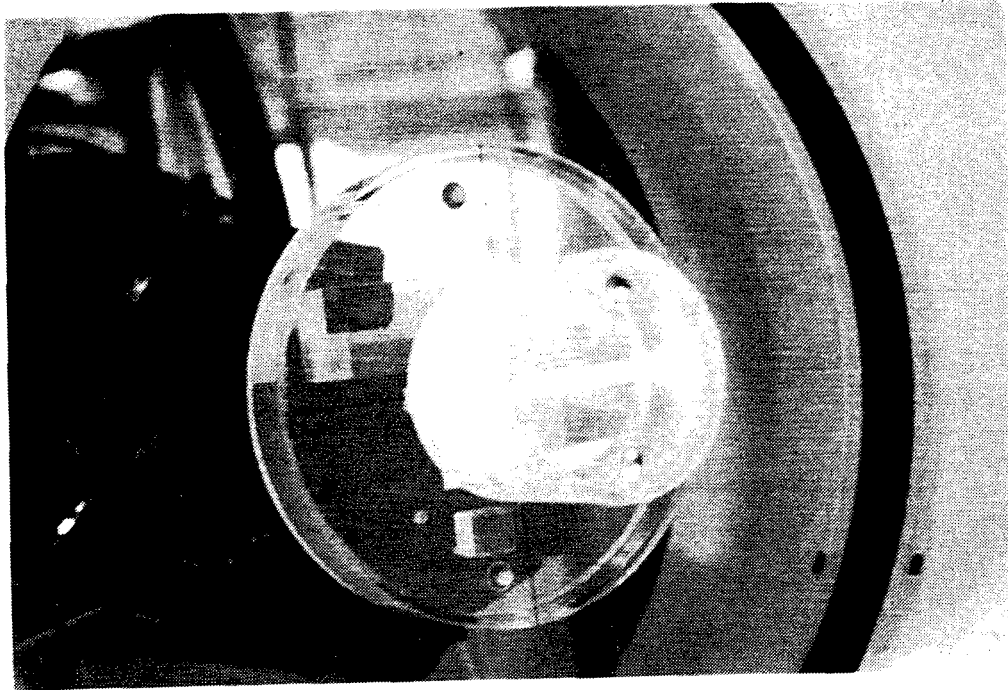
Figure 4-1. CT machine with water calibration phantom in place
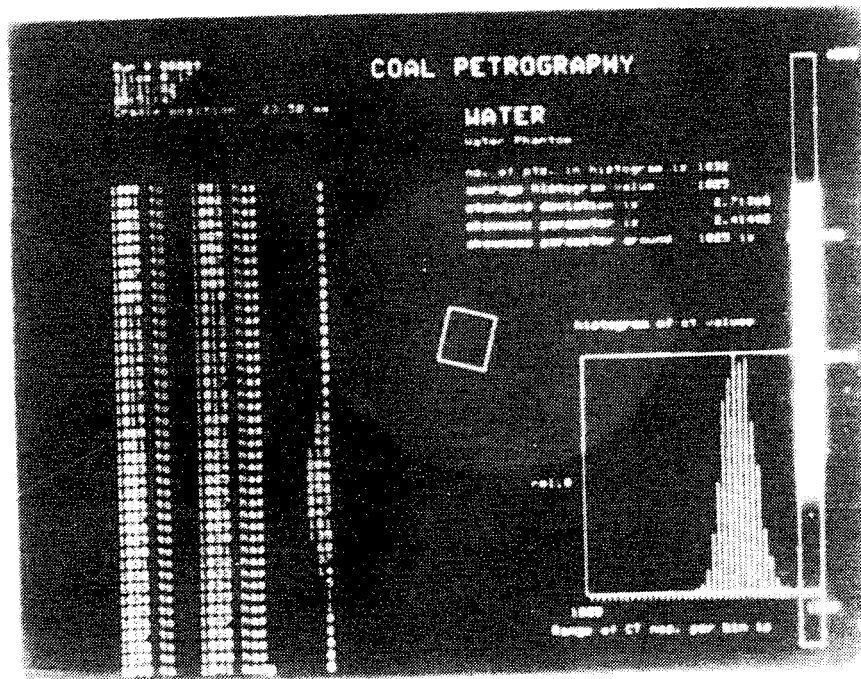
Figure 4-2. CT image of water with statistics
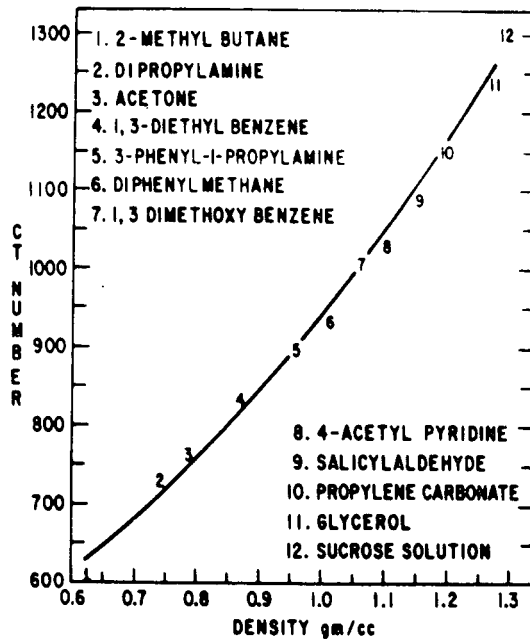
Figure 4-3. Variation of density of hydrocarbon standards with CT number
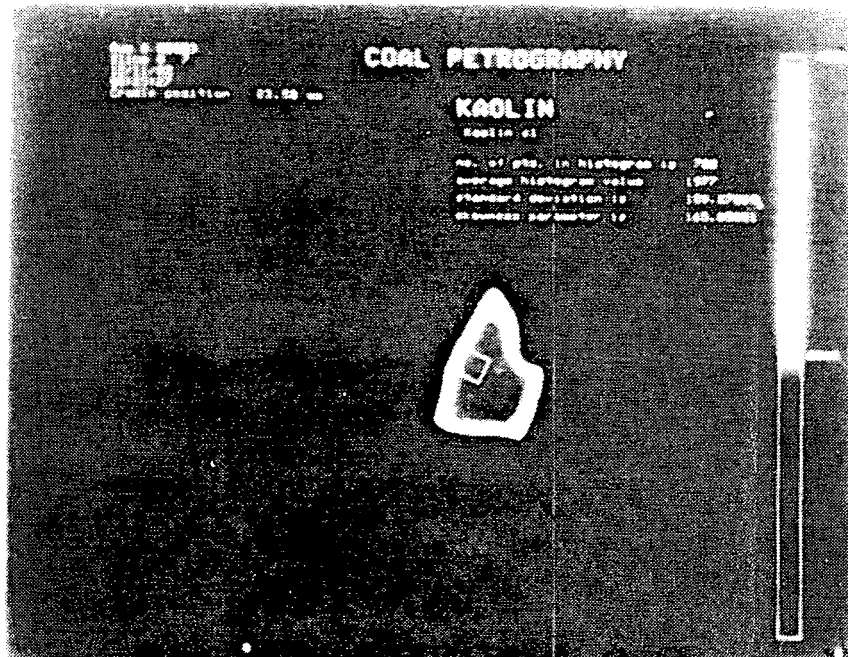
Figure 4-4. CT image of kaolin impregnated with epoxy in the outer edge

4-11

150Kev TUBE 3mm Al

```
650000320
600000320
550000320
500000552
450000584
R
E 400000584
L
A
T
I 350000416
V
E
I 300000416
N
T
E
N 250000416
S
I
T
Y 200000452
150000448
100000464
50000484
0
```

PHOTON ENERGY (Kev)
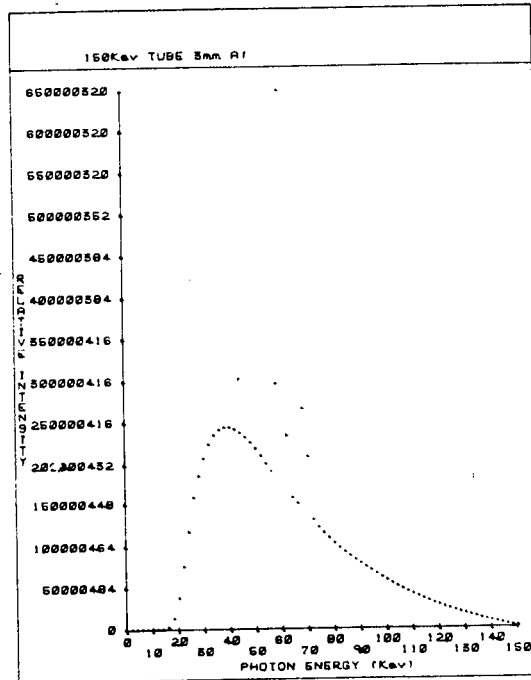
Figure 4-5. X-ray tube emission spectrum, 150 KV, 2 mm Al filtration
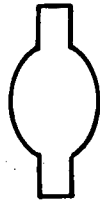
X-RAY TUBE MATERIAL XENON DETECTOR
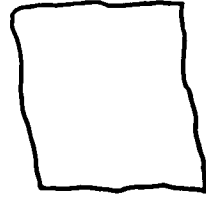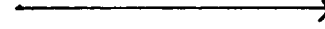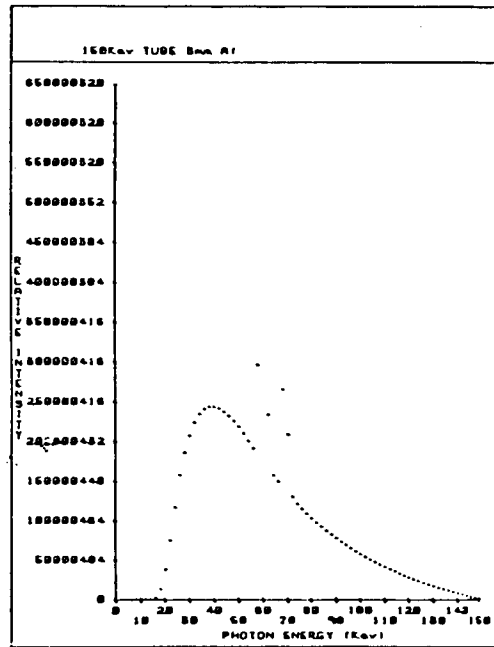
EMISSION
SPECTRUM
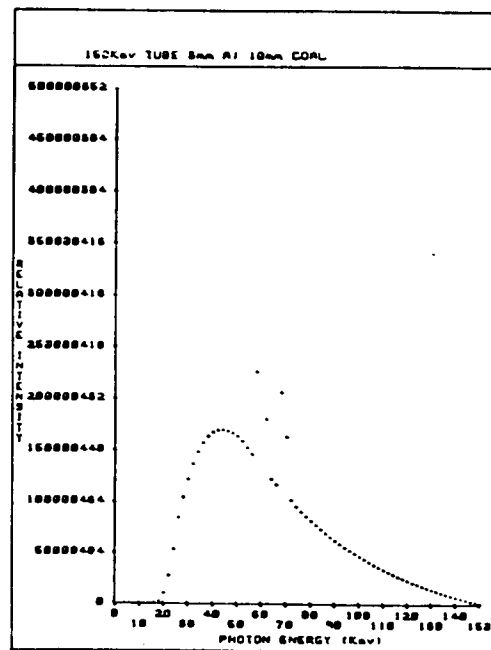
TRANSMITTED
SPECTRUM
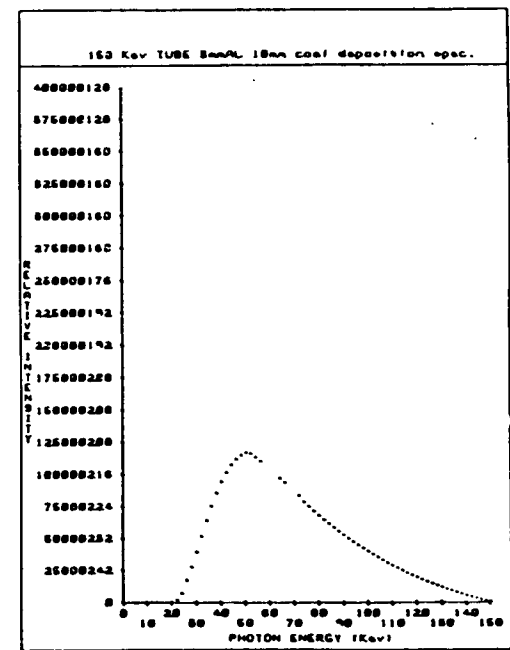
DEPOSITED
SPECTRUM

Figure 4-6. Schematic of x-ray absorption process
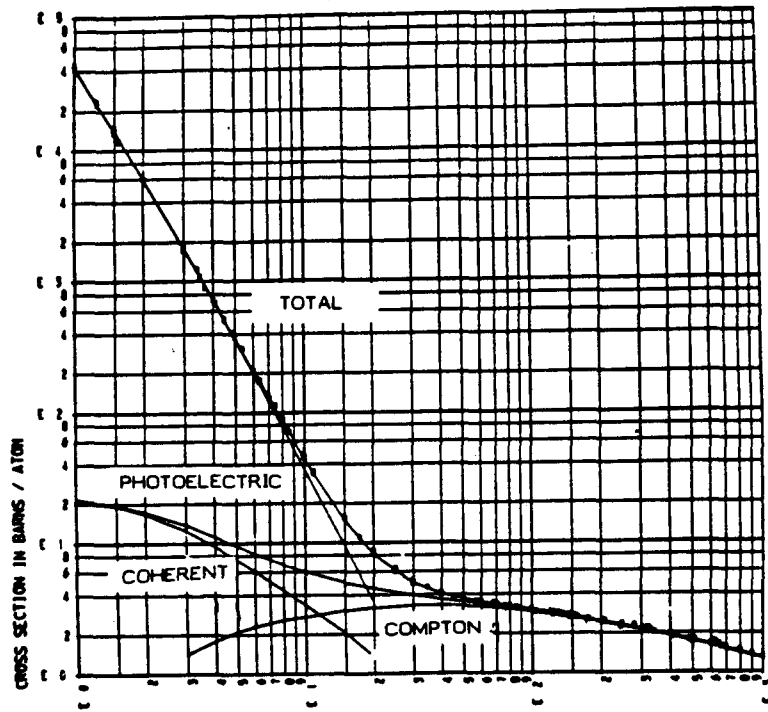
Figure 4-7. X-ray absorption spectrum of carbon
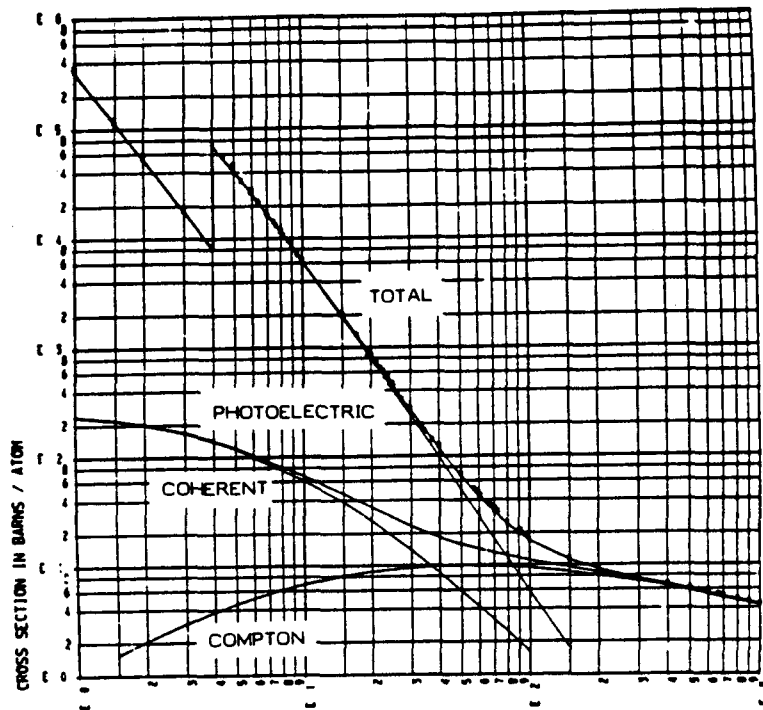
Figure 4-8. X-ray absorption spectrum of calcium

4-14
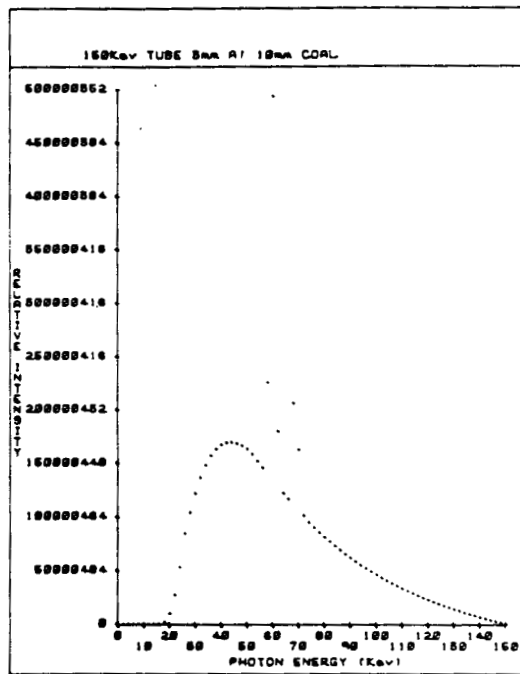
Figure 4-9. Calculated x-ray spectrum following attenuation by 1 cm of coal $(C_{49}H_{43}O_7S_1N_1)$
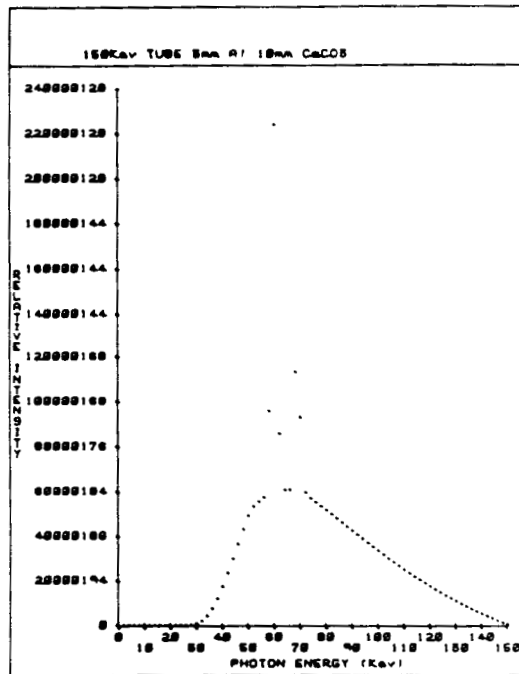
Figure 4-10. Calculated x-ray spectrum following attenuation by 1 cm of calcite $(CaCo_3)$

4-15
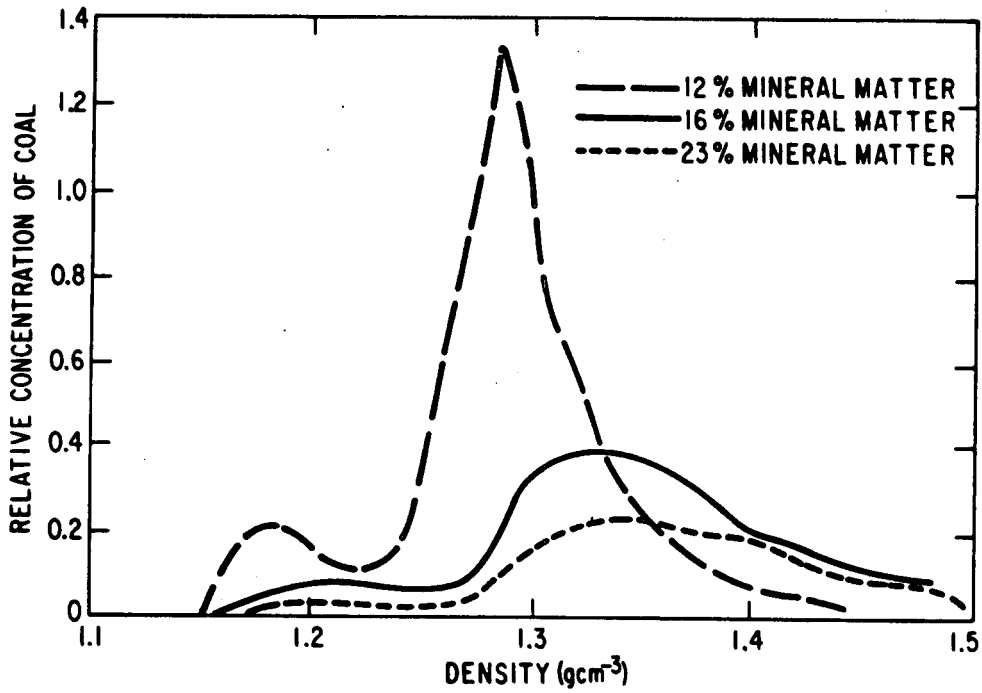
Figure 4-11. Effect of mineral matter on density separation of coal
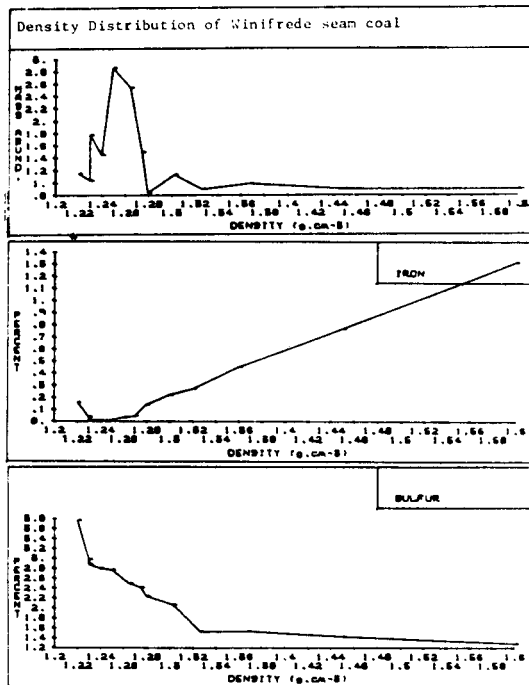
Figure 4-12. Density separation of Winifrede seam coal
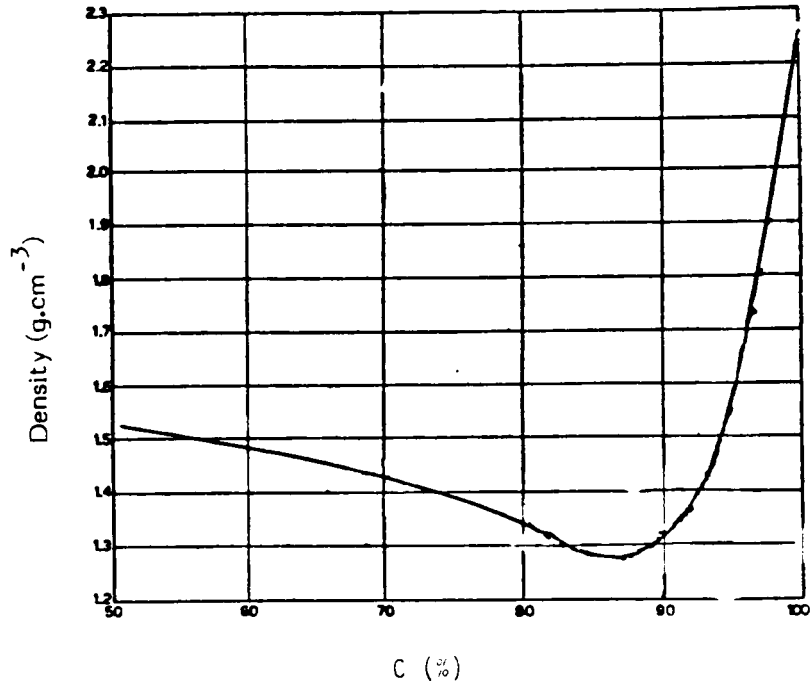
Figure 4-13. Density of vitrinite as a function of coal rank

Table 4-1

CT SOLID ORGANIC STANDARDS

	Density (g.cm^{-3})	$\overline{CT}$	σ	skew (av)	skew (pk)
Air	0	1	0	0	0
Water	1.0	1025	2.7	1.4	2.4
Epoxy	1.19	1128	3.07	1.678	-2.85
Polyester	1.19	1126	3.20	3.05	3.05
Plexiglas	1.21	1130	2.87	1.76	-3.61
Graphite	1.80	1566	4.96	-3.59	-3.59
Teflon	2.25	2050	4.44	2.41	4.2

Table 4-2

CT OF MINERALS USED FOR CALIBRATION

		CT of Minerals				
Mineral	Composition	Density g cm^{-3}	Ne (electrons cm$^{-3)}$ x 10^{23}	Ne/Ne(water)	Cal. CT No.[++]	Actual CT No.
Pyrite	FeS_2	5.0	13.5	4.09	4188	4096
Calcite	$CaCO_3$	2.7	8.7	2.64	2703	4096
Siderite	$FeCO_3$	3.96	11.5	3.48	3563	4096
Illite	$K_{1-1.5}Al_4 Si_{7-6.5}Al_{1-1.5}O_{20} (OH)_4$	2.5[*]	7.48	2.26	2321	3300-4096
Kaolin	$Al_4 Si_4 O_{10} (OH)_8$	2.6[*]	7.8	2.38	2437	3078[**]
Dolomite	$CaMg(CO_3)_2$	2.86	8.5	2.57		3900-4096
Water	H_2O	1.0	3.3	1	1024[+]	1024

[*] Depending upon states of hydration the density
of these mineral classes can vary. Typical
values were taken from Ref. 7.

[**] By subtraction of text

[+] Assumed

[++] No beam hardening.

Table 4-3

RATIO OF PHOTOELECTRIC CROSS SECTION TO COMPTON SCATTERING CROSS SECTION AT 50Kev

Element	Ratio (PE/C)
H	3×10^{-5}
C	0.053
N	0.1
O	0.172
F	0.275
Na	0.568
Mg	0.78
Al	1.1
Si	1.39
S	2.28
K	4.14
Ca	5.11
Fe	12.17

Table 4-4

CALCULATED AND ACTUAL CT NUMBERS FOR COAL AND MINERALS

Material	μ (mm^{-1})	CT (Calc.)	CT (Obs.)
Coal $(C_{49}H_{43}O_7S_1N_1)$*	0.0256	1254	1210
Kaolin $(Al_4Si_4O_{10}(OH)_8)$	0.0632	3096	3078
Teflon C_2F_4	0.043	2106	2050
Calcite $CaCO_3$	0.09228	4521	4096
Dolomite $CaMg(CO_3)_2$	0.080	3924	3900-4096
Water H_2O	0.0209	1024	1024

* Reference 53

Table 4-5

PROXIMATE ANALYSIS OF COALS USED IN THE CT EXPERIMENTS

Summary of Coal Analyses (as received)

Coal Seam	Coal Class	Moisture %	Vol Matter %	Fixed Carbon %	Ash %	S %	C %	H %	N %	O %	Btu lb	MAF Btu lb	Comments
Winifrede	Bituminous lvA	4.09	32.06	49.62	14.23	.76	67.65	4.71	1.30	7.26	12058	14763	seam typical (C234)
Wyodak	Subbituminous C	30.00	32.00	32.10	5.90	.50	47.70	3.35	0.70	11.84	7950		analysis from mine prop.
Rosebud (P)	Subbituminous B	25.94	29.22	36.44	8.39	.63	(68.28	4.62	0.92	13.99)*	8756	11823	analysis from mine prop.
Ohio #6	Bituminous hvC	7.20	32.97	48.80	11.02	2.5					11612	13251	analysis from mine prop.
Dietz	Subbituminous B	23.80	32.00	40.00	4.2	.41	55.13	3.87	0.81	11.74	9620		analysis from mine prop.
Illinois #6	Bituminous hvB	5.92	38.57	40.22	15.29	0.99	63.77	4.66	1.09	7.93	11284		C117
Pittsburgh #8	Bituminous hvA	2.36	39.08	52.47	6.09	3.81	76.59	5.45	1.33	4.30	13941	15228	C093
San Juan #8	Bituminous hvC	13.0	36.0	40.0	22.0	0.70					9000	14048	analysis from mine prop.

* dry basis

Table 4-6

DRY MINERAL MATTER FREE CARBON VALUES FOR COALS USED IN THE CT EXPERIMENTS

Coal Seam	C_{dmmf}
Pittsburgh #8	58.30
Illinois #6	52.02
San Juan #8	63.10
Beulah Lignite	25.90
Winifrede	61.70
Wyodak	50.50
Ohio #6	60.37
Dietz	55.30

Table 4-7

MACERAL DENSITIES FROM CENTRIFUGE EXPERIMENTS

		Exinite			
	Coal	Alginite	Sporinite	Vitrinite	Inertinite
Ohio #5	PSOC-297	1.06	1.19	1.29	1.35
West Virginia #5 (Lower Kittanning)	PSOC-124		1.15	1.25	1.30
	PSOC-106	1.20		1.31	1.40

Section 5

SELECTION OF COAL SAMPLES

A set of coals was assembled for the purposes of this contract ranging in rank from anthracite to lignite. The choice has been governed by the petrographic and economic interest of the seam. Because many of the CT experiments require large pieces (>2 cm), many of the samples had to be collected specifically for this work. The coal seams used for samples are listed in Table 5-1. The samples were collected at freshly opened faces and were taken from a vertical channel cut. Photographs were taken of the seam at the site where the samples were taken.

During the contract the samples have been stored in sealed glass jars under nitrogen.

The sample of Beulah Zap lignite was obtained from Pennsylvania State University. It has been maintained in a plastic bag sealed in argon. Other samples (e.g., Illinois #6, Pittsburgh #8, Reading anthracite) had already been obtained and were being stored, either under nitrogen in glass jars or in deionized water in plastic containers.

Table 5-1

COAL SEAMS USED FOR THE CT EXPERIMENTS

I.D.	Rank	Comments
C268	Bituminous	Lower Kittanning (nonmarine). The sample is ca. 40 lbs and was mined at the Dean Mine, Cambria County of the Bender Coal Company, Carroltown, PA. The sample was mined on November 3, 1982.
C267	Bituminous	Lower Kittanning (marine). The sample is ca. 20 lbs and was mined at Mine No. 9-50,54 of the Stahlman Coal Company, Jefferson, PA. This sample was mined on November 4, 1982.
C269-C271	Bituminous	Ohio #6 (Middle Kittanning). This sample is ca. 20 lbs and was mined at the Coonville Mine, Mason Company, of the Valley Coal Company. The sample was collected on November 5, 1982.
L-C289 U-C290	Bituminous	Small samples (ca. 5 lbs each) were also collected at the Upper Mercer A and Lower Mercer A seams during the visit to the Bender Coal Company.
C240-C248 C291	Subbituminous	Upper Wyokak. The sample was ca. 40 lbs and was mined on November 2, 1982, at the Wyodak Mine of the Wyodak Resources Development Corporation, Gillette, WY.
C249-C254 C272-C273	Subbituminous	Lower Wyodak. This sample is about the same size as the above sample and was collected during the same visit.
C255-C261 (WE) C262-C266 (PEA)	Subbituminous	Rosebud. Two sample of this seam were collected on November 3, 1982. The first was from the Rosebud Mine of the Western Energy Company and the second from the Big Sky Mine of the Peabody Coal Company. Both mines are situated near Colstrip, MT. Each sample was ca. 40 lbs.
C274-C278	Subbituminous	Dietz #1 Upper. This sample is ca. 35 lbs and was collected from the East Mine of the Decker Coal Company, Decker, MT, on November 4, 1982.
C279-C282	Subbituminous	Dietz #1 Lower. The sample is about the same size as the above sample and was collected during the same visit.
C283-C288	Subbituminous	Dietz #2. The sample is ca. 35 lbs and was collected during the same visit as the above sample.

Section 6

COAL CHARACTERIZATION BY COMPUTED TOMOGRAPHY

6.1 SURVEY OF CT IMAGES OF COALS

Large pieces of coal (ca. 5 × 5 × 15 cm) were selected from the coal bank and potted in polyester resin. The potting was necessary for three reasons: (a) it preserved the coal, (b) the potting compound supported the coal in any subsequent slicing operation to examine the coal, and (c) the presence of the plastic prevented a large density discontinuity at the edge of the coal and the consequent edge artifacts on the CT image.

CT pictures and associated histograms for a number of coals are given in Figures 6-1 through 6-26. The statistical parameters defined in Section 4.1 are also given.

The grey scale used to portray the coal images is the same for all the coals in this sequence. The grey look-up-table (LUT) is shown in Figure 6-27. A grey level of 255 is white, while a level of zero is black. The variation in grey is really over a narrow band: 1075 to 1466 CT numbers. The coals were deliberately aligned in the x-ray beam so that the pictures would cut across the bedding planes (if the coal had any). In many of the pictures, the bedding plane organization can be clearly seen. The zone of reconstruction of the computer-generated image is a circle 8.5 cm across for these coal pictures. All of the pictures were taken at the same magnification but not all the coal pieces filled the image zone. The image size can be most easily be seen in the Mercer (upper) image (Figure 6-5). The ability of the CT machine to detect the presence of objects of different density within a matrix depends upon its spatial resolution, the size of the object, and the difference in density between the object and the background material. The spatial resolution is ca. 0.5 mm but, in a different set of CT experiments, individual 250 μm aluminum wires embedded in epoxy quite clearly showed in the CT images.

The grey scale used in the CT pictures covers a range expected for the organic fractions of coal. The white regions in the images are heavily laden with mineral matter.

The bedding plane organization is quite clear in the bituminous coals but is less evident in the subbituminous and lignite coals. Vertical cracks in the coal can be seen in some cases (e.g., Illinois #6). In the case of the nonmarine Lower Kittanning, our samples seem all to have come from an extremely shale-rich lithotype, and it is doubtful if a maceral analysis of this coal would be useful. It is interesting to note the apparently isolated nature of the mineral inclusions in the Dietz coals, compared to the banded organization in the bituminous coals. This difference could have significance for the fracture properties, methane flow paths, and the washability of the coals.

The CT histograms for the coals are usually highly asymmetric. There is a sharp rise in the frequency of occurrence of a CT number with a peak often being reached in the range 1200 to 1250, followed by a gradual tailing off towards the high CT number end. Sometimes there is a secondary peak at higher CT numbers. From the theoretical calculation of CT numbers and from observation, it is clear that the CT numbers in the peak region represent the organic fractions of the coal. Some spread of the CT distribution to higher CT numbers could be explained if high-density macerals were present (e.g., the inertinites). They could account for CT numbers up to 1300. Most of the spread to high CT numbers must be explained by mixtures of mineral matter and organic coal within the same voxel.

A list of the most commonly occurring CT (CTMC) values in the various coals is given in Table 6-1. The value for the nonmarine Lower Kittanning is missing because there was no distinct maximum for this coal. The fact that very few CT numbers fall much below 1200 shows that the coals are not macroporous. The porosity of coals using a xenon probe molecule is described in Section 6.2.

The skewness parameter, skew(pk), is a measure of the asymmetry of the density distribution in the coal, and a large value for this parameter should indicate that the mineral and organic fractions of the coal are well separated. The skew(pk) values for the coals are also given in Table 6-1.

A value of CTMC in the 1250 range together with a large skew(pk) should mean that the coal is relatively easy to clean by grinding and density separation because the organic and mineral fractions are geographically separate in the coal. A value of the CTMC in the

1250 range with a small skew(pk) value suggests a clean coal. A large value of the CTMC (i.e., >1300) suggests that the organic fractions of the coal are intimately mixed with mineral matter. This, taken with a small skewness factor, suggests that the coal would not be easy to clean by conventional heavy media separation. An example of this case is the San Juan #8 where the CTMC is 1389 and the skew(pk) is small. The following diagram outlines the possibilities:

good candidate for cleaning   heavily mineralized; little coal to
                                     be gained by cleaning

clean coal; little gained by physical   finely dispersed minerals difficult
cleaning   to clean

CTMC
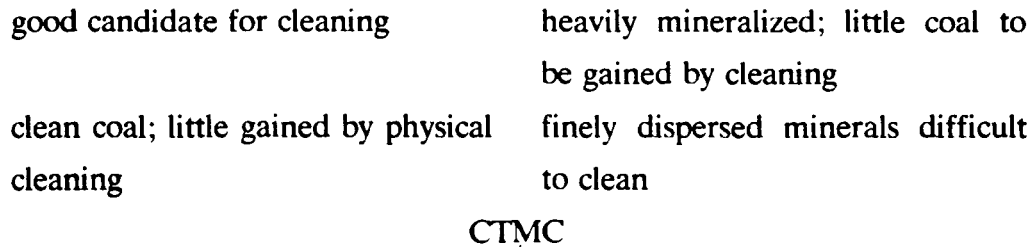
While tentative conclusions have been drawn from the particular pieces of coal examined by CT, it should be remembered that, as yet, no attempt has been made to take enough samples from any one seam to allow the conclusions to be extrapolated to a characterization of the seam.

6.1.1 Coal Samples for Comparison with Petrography

Lump pieces of the coals listed in Table 5-1 were potted in polyester resin, and CT pictures were taken at 2 cm intervals down the length of the polyester block. Where possible, the coals were oriented with the bedding planes orthogonal to the plane of the CT x-ray fan beam. A CT picture at a 1X magnification is shown in Figure 6-28a, and another CT picture at the same place, but at 3X, is shown in Figure 6-28b. The lower magnification picture gives an overall picture of the potted coal, while the 3X picture shows more detail of the coal itself.

One of the elements of this task is the comparison of the CT image with more conventional analysis of the same region of the coal, e.g., by petrography. In order to do this the 1.5 mm thick plane which the CT x-ray beam traversed through the coal must be located and then the coal must be accurately cut to expose this plane.

During the potting operation, location markers were placed in the plastic with which the pieces of coal used in the petrography experiments were encapsulated. The markers were formed by stretching three strings of nylon line (0.5 mm dia.) in the shape of a fan both along the top and bottom of the coal (Figure 6-29). The potting compound, e.g., polyester resin filled with LEXAN® polycarbonate beads, was then added to fill up the mold. After curing, the nylon lines were withdrawn, leaving two sets of diverging holes along the top and bottom of the plastic block. The central hole in each fan is not symmetrically placed between the other two, and consequently the values of x and y (Figure 6-30) uniquely determine the position of a plane passing through the fan. Knowing the line along which a plane cuts the upper fan and also the line at which it cuts the lower fan uniquely determines the x-ray CT plane.

The holes formed in the plastic block by the technique described above can be seen in the 1X magnification CT image of the coal, and the x,y coordinates on the image determined. Through a series of calibrations, these coordinates can be converted to actual distances. The holes in the plastic block are also visible from the outside of the block. Therefore, by fitting the distances taken from the CT image to the distances observed on the block, the location of the CT plane through the plastic block can be obtained.

Professor Alan Davis of the Pennsylvania State University has been subcontracted by General Electric to carry out petrographic examinations of the coals used in this work. Several hundred CT images of coal have been taken, and not all of them can be given a detailed petrographic description. After an examination of the CT images, a certain number have been chosen as being of potential petrographic interest and for further work. A list of these CT images is given in Table 6-2.

The coal pieces used in these experiments have typically a 10 cm × 10 cm cross section, and the plastic block in which they have been embedded has a cross section of 14 cm × 14 cm. This large a block is difficult to section accurately in one operation. The procedure, therefore, has been to rough-cut the coal approximately 5 mm on either side of the desired CT plane and then grind down to the actual CT plane. At the stage when the coal has been rough-cut, the slices have been given a preliminary examination to confirm their petrographic interest. The slices for which this was done are indicated in Table 6-3.

A grinding jig has been developed to attach to a Beuhler Economet III polisher and grinder. This jig allows the coal to be ground down to any arbitrary angle and enables correction of the inevitable errors in rough-cutting.

Once the slice of coal has been rough-cut, then the true position of the registration holes is revealed on the cut faces. A much better measurement of the position of the true CT plane can then be made. The coal is attached to Plate A (Figures 6-31 and 6-32) with double-sided tape, and the two micrometer screws are adjusted so that the CT plane (not the exposed coal face) is parallel to the face of B. The entire holder B is mounted so that it can slide up and down in aluminum sleeve C, always maintaining the face of B parallel to the face of the grinding wheel D. This procedure corrects any misalignment in the original rough-cutting of the coal block. An example of a cut (and partly polished) block compared to the original CT picture is shown in Figures 6-33 and 6-34.

Figure 6-35a shows an annotated photograph of a piece of Pittsburgh #8 bituminous coal, while Figure 6-35b shows the CT image contained within the coal slice. The CT plane is approximately 5 mm below the surface photographed in Figure 6-35a. Similar pairs of pictures are given for Illinois #6 coal (Figure 6-36a and 6-36b) and Lower Kittanning (marine) (Figure 6-37a and 6-37b).

As was shown in Section 4, the CT number for a material can be calculated from first principles, knowing the emission characteristics of the x-ray source, the elemental composition of the material, its density, and the x-ray detector characteristics.

The densities of the different maceral groups are quite different (Table 4-7), and so areas of different maceral inclusions in the coal should be directly observable by CT, provided that the inclusions are larger than the spatial resolution of the instrument.

Several areas in the petrographic photographs have been identified as being pyrite, heavily laden with pyrite, or heavily laden with clay minerals. Typical CT number ranges for pyritic areas, clay areas, and vitrain are given in Table 6-4.

Regular petrographic analysis of the coals under study have been carried out by Professor Allan Davis of the Pennsylvania State University. The coal samples were ground up, potted, and polished according to standard petrographic techniques. The samples were ex-

amined under reflected light to establish the maceral composition of the coals. A sample of the reflectance results is given in Table 6-5, and a summary of the results for the other coals is given in Table 6-6.

Petrograhic Reflectance Mapping

The instrumentation is based on a Leitz Orthoplan microscope equipped with an MPV 2 photometer and a stepping stage which moves in 2.5 μm increments at a rate of 1250 μm/s. The usual magnification of the microscope is 650X and readings are taken on areas 2 μm x 2 μm. Reflectance values flow directly into a Digital Equipment Corporation MINC-11 laboratory computer which controls the scanning pattern and rate, as well as data acquisition. This computer features 32K of memory and a 12-bit analog-to-digital converter. The equipment becomes the latest version of the automated reflectance micro-photometer systems developed at Pennsylvania State University expressly for the petrographic characterization of coals. However, earlier versions were able to generate only a frequency array of reflectance values rather than a two-dimensional matrix.

Control of the system through computer software permits considerable flexibility in establishing operation parameters. The programs are interactive and require the operator to enter these parameters as input variables. Parameters include:

a. Shape and Size of Scan Pattern – operator must specify the length of a traverse in the x direction, the total number of traverses desired, and the distance between traverses in the y direction.

b. Data Acquisition – the distance between sample points along a traverse must be specified as well as the number of actual readings to be taken at each point. The sampling rate of the computer is on the order of microseconds, and even at the maximum speed of the microscope stepping stage, enough overhead time exists to take and average 25 readings at each point.

c. System Calibration and Reflectance Range – the computerized reflectance microscope is calibrated according to the technique used for conventional microscope photometry—with optical glasses of known reflectance value. These reflectance values are entered at the video terminal, and the screen displays a value which is ad-

justed to that of the standard reflectance by adjustment of a potentiometer on an amplifier low-pass filter unit. The program allows data acquisition to be interrupted in order to recalibrate the system. The amount of time between calibrations must be specified; the usual duration is 30 min. The final parameter concerns the range of reflectance values. Ordinarily, only eight bits of computer memory on the analog-to-digital converter are used in order to maximize storage capacity on the computer disk while creating 255 reflectance levels for a 0 to 5% reflectance range. The only component of bituminous coals with a higher reflectance level is pyrite, so all readings taken on pyrite are assigned to the maximum value.

Once the operation parameters have been entered and the sample is properly aligned and leveled, the analysis can begin. Scanning is interrupted by the computer in only two situations. One is for the calibration to be checked periodically, as predetermined by the operator, and the other is for manual translation of the sample to a new "frame." The scanning range of the digital stepping stage is 20 mm × 20 mm. When it is desirable to analyze a greater area than that, such as the surface of a block of coal, the computer divides this area into a number of smaller frames. When a frame has been completed, the microscope stage returns to the origin, and the sample must be moved manually the exact distance specified by the computer by means of spindles equipped with Vernier scales. This manual translation is accurate to within ±50 μm and is necessary only when large areas are scanned. In such cases the usual sample point-to-sample point distance is 100 μm, and a polished block of coal, approximately 4 cm on a side, requires about 3 h for completion. Therefore, practical considerations limit the maximum sample size suitable for analysis by this technique, but great potential exists for mapping smaller features. These can be scanned to a resolution of one step, or 2.5 μm.

Each frame is stored on a computer disk in the proper spatial sequence that would have been created had the entire sample surface been scanned without interruption. When complete, this matrix may be put into an image processor and displayed on a video screen either on a gray scale or color scale.

Figure 6-38a is a photograph of an exposed polished coal surface corresponding to the reflectance map shown in Figure 6-38b. It was displayed on the same equipment used to

display the CT images. Figure 6-39 shows a reflectance map for the Navajo coal. In addition to the Navajo coal, images of Beulah Zap lignite, Wyodak Sub C, Illinois #6, Pittsburgh #8, Lower Kittanning marine and nonmarine, and Decker Dietz have been obtained.

Comparison of the Two Images

In order that the two types of image can be quantitatively compared, they should be put on the same grid size and aligned on the same coordinate system. Normally, in the petrographic analysis, the focal spot of the light beam is a few microns in diameter. This means that a 2-D grid of reflectivity values would only sample a small fraction of the coal specimen even if the grid spacing were the same as that for the CT image. The CT image, on the other hand, averages the properties of the entire volume element in order to arrive at a number representative of that volume. In order to make the reflectivity maps as representative of the surface as possible, the reflectivity light beam was enlarged as much as possible and readings were taken on a finer grid than used for the CT with the intent of averaging the reflectivity readings to get a number comparable to the CT. In particular the reflectivity data were taken on a 125 μm grid, while the CT grid is over 265 μm. As a further check on the scaling, the distance (in CT image pixels) between markers which appeared in CT images were compared with actually measured distances on sectioned coal specimens and distances (in reflectivity image pixels) between copper pins on the reflectivity image were compared with those measured on the actual coal. These sets of measurements were made on a number of CT and reflectivity image pairs and led to an average scaling factor between the two imaging modalities of 2.15. This represents the factor by which the reflectivity image must be shrunk to get the best correspondence with the CT image. The actual range of scaling factors was 2.11 to 2.18, a consequence of errors in sectioning the coal along exactly the CT x-ray plane.

Quantitatively shrinking the reflectivity image was accomplished by neighborhood interpolation. For an arbitrary scaling factor F, (e.g., 2.15) pixel values over an area $F \times F$ on the original image were weight-averaged to yield a single new pixel value. The problem becomes more complicated because it is not generally possible to add the values of 4 whole pixels and 0.62 of a fifth pixel and simply divide by 4.62 to obtain a weighted average.

This is because the particular location in space may include small portions of all the adjacent pixels as illustrated in Figure 6-40. Here the example of a REMAP scaling of 2.15 is illustrated. Only the equation for the left-uppermost transformation is explicitly expanded. The resultant pixel $R'(1,1)$ is composed of a weighted sum of nine separate pixels in R space. It is possible that as many as 16 pixels may be required to generate a single transformed pixel, dependent on the phasing in R space. This variablility had been a source of particular complexity in generating the REMAP code.

The reflectance images were shrunk by the requisite factor in order to establish a one-to-one correspondence between CT images. Occasionally the resultant images were inverted, rotated, or reflected to match the CT orientation before storing in the final form.

As mentioned earlier, several nylon lines were plotted along with the coal in order to establish the precise plane for slicing and polishing, within the 1.5 mm CT x-ray plane width. Each fishline hole is about 3 pixels wide, with centers on the 1X image accurately measurable within 1 pixel in each dimension. Copper pins were placed in the coal after the coal had been rough cut but before the final polish and the reflectivity measurements. These pins showed up in the reflectivity map and were assigned CT coordinates separately by triangulation and by arcing. This measurement introduced another error of 0.2 mm or 1 pixel in each direction. Thus the pin locations in the 1X image were known within 2 pixels, so that for the 3X image, which was used for comparison with the Penn State images, pin locations were known within ± 6 pixels. The reflectivity maps were taken on the samples using the pins to orient the coal block on the microscope stage with respect to vertical and horizontal. Examination of the pin locations on the reflectance images showed an average slope of 3%, relative to the CT image. This means that if the CT image is aligned within ± 6 pixels at a given pin, then 100 pixels away, the alignment is off by an average of 3 pixels in either dimension. Certainly this is reasonable since, in actual terms, the block of coal was oriented on the microscope state within 0.6 mm of normal over the length of the block.

The lengthy discussion in the previous paragraph becomes significant when a pixel-by-pixel comparison of CT and reflectance maps in undertaken. In order to accomplish this, several subroutines were encoded which aid in this analysis. Explicitly, most useful are rou-

6-9

tines which plot pixel values along lines in the images; histograms can be displayed of pixel values in arbitrary shapes drawn in the image; pixel-by-pixel correspondences are determined, sorted, plotted, and fitted to polynomial expressions in corresponding rectangles or arbitrary shapes.

Figure 6-41 shows the simplest case of an image compared with itself. Here two identical CT images of a Lower Kittanning bituminous coal were simultaneously displayed, offset by 320 pixels along the horizontal axis. Two squares, 20 × 20 pixels in dimension, were drawn on either image, centered at (150,150) and (470,150) respectively. As expected, a plot of corresponding pixel values yielded a straight line. Plots of any arbitrary shapes on the images offset by 320 pixels also show straight lines since the images are identical. Slopes in these cases are unity. In Figure 6-42, identical images are compared and offset by 320 pixels, but the regions to be compared are shifted by an additional 3 pixels along the diagonal. The plot appears practically random, though the regions comprising the comparison are nearly identical by visual examination since the 3-pixel shift is quite small. This is even more significant when one considers that the features in the comparative region are not very rapidly changing nor are they sharply dilineated as in Figure 6-39. In general, an offset of 1 pixel showed a high degree of correlation between identical images; an offset of 2 pixels still showed a significant correspondence, while a 3 pixel orientation error yielded near random data in even the more uniform samples.

Consider once again the degree of accuracy in orienting CT images with reflectivity images in light of Figure 6-42. The previous discussion indicated that the alignment of corresponding pin locators was, at best, within 6 pixels in either dimension. An additional average tilt deviation of 3% is expected, so that a location 100 pixels from the pin (25 mm) would show another 3 pixel error. Thus even if there were a perfect correlation between the CT and reflectivity images, there is a very good chance that the bulk of the image correspondences would be outside the two pixel window of accuracy, and an apparent lack of correlation (as in Figure 6-42) would result.

An inherent problem associated with comparison of CT images with reflectivity images is that certain minerals have high density and high reflectance, while other high density minerals (clays) show low reflectances. To accommodate systematic problems of this na-

ture, a subprogram entitled FILTER has been implemented to enable the user to substitute certain values for another. For example, suppose a good correlation was found between reflectance and CT, excepting the clay minerals which showed high CT values of 2000 to 2100, but low reflectance values of 120 to 150. A more reasonable reflectance might be 280 to 320 based on the other matter in the coal. FILTER would enable the user to convert all the reflectance values from 120 to 150 to a value between 280 and 320, for example.

In spite of the alignment issue and the inherent problem associated with mineral inclusions, in most cases, regions of good correlations at or around the pins has been found. Generally, as regions of comparison deviate from the pin locations, errors associated with sloping appear to become significant, though in some cases mapping correlations over wide regions have been found.

Figure 6-43 shows properly aligned Lower Kittanning nonmarine coal images; the top is a reduced reflectance map and the bottom is a corresponding CT map. Note that the lower left corner of the CT image was outside of the reconstruction zone encompassed by the reflectance section. Visual inspection reveals a high degree of correlation in the banding. Two horizontal black bands are rich in pyrite and have both high reflectance and CT values. Figure 6-44 illustrates one form of analysis: a test for correspondence between pixels contained in square regions on the respective images. The data were fitted to the best line as illustrated in the graph on the photo. Figure 6-45 also reveals a good correlation between reflectance and CT using corresponding arbitrary shapes whose geometry is controlled by a cursor. Figures 6-46 and 6-47 also reveal pattern similarities when pixel values are plotted along corresponding lines in reflectance and CT images, respectively.

Good linear correlations have been found on a pixel-by-pixel basis on several regions contained within the aforementioned lower Kittanning nonmarine coal, the Navajo coal, and the Decker coal. The illustrated lower Kittanning coal showed generally good correlations throughout the coal, not just about the pyrites.

The physical properties of coal that determine its petrographic response are those that affect its optical reflectivity, while the property that determines its CT response is its x-ray attenuation. The two techniques operate in quite different regions of the electromagnetic

spectrum. The optical properties used in petrography relate primarily to the behavior of the valence state electrons in the coal constituents, whereas in the CT case the attenuation coefficient of the x-ray beam is mainly dependent on the total electron density of the sample.

The CT, in common with all other commercially available tomography equipment, has the density resolution to distinguish between the different maceral groups of coal and between the coal and minerals; however, the spatial resolution is about an order of magnitude too gross to pick up the coal features normally used in a petrographic analysis. The CT machine can pick up the major microlithotype layers in coal and can perhaps do a better job in separating the minerals from the organics than can optical petrography.

6.1.2 Comparison of CT with Mineral Matter in Coal

One of the subtasks is to compare the distribution of mineral matter in the coal with the CT numbers of the CT image. A series of experiments has been completed in which tests were made for correlations between CT number and mineral matter distribution. For example, a piece of Illinois #6 coal was taken that was also used for a xenon penetration experiment. The CT image for the coal is shown in Figure 6-48. The coal had been cut into a 2.5 cm × 2.5 cm × 10 cm block, potted in an epoxy cylinder, and mounted in an acrylic plastic tube. The square cross section of the coal, the cylindrical epoxy potting material, and the circular ring of the acrylic tube are all features visible in the image. After the xenon experiment, the coal was sectioned through the same plane that was imaged in Figure 6-48. One of the exposed faces was polished, coated with a conductive film of carbon, and further cut to allow sections to be introduced into a Cameca SEM quantitative microprobe. The holder for the coal is shown in Figure 6-50. The microprobe was set up with a square beam profile 50 μm on the side and in the automatic stepping mode with 100 μm between steps. At each location, the weight percent was measured for Na, K, Al, Si, Ca, Fe, and S. Most of the signal at a position was usually obtained from aluminum and silicon (Figures 6-51 and 6-52). (Note that the scan direction has been reversed.)

The relative weight percent for the inorganic species present in a particular location was obtained by combining the weight percents of the seven inorganic species measured. This total was then plotted against distance along the coal for four scans across the coal, each

scan being between 2.5 and 3 cm long (i.e., some 300 points per scan and seven elements at each point). These total mineral plots are shown in Figures 6-53, 6-54, 6-55, and 6-56.

A line has been drawn on the CT image in Figure 6-48, and the CT numbers along that line have been plotted out in Figure 6-49. This line is approximately the position of scan 3 (Figure 6-52). The x-ray microprobe results are on a grid of $50\mu m \times 50\mu m \times$ ca. $1\mu m$ while the CT data is on a grid $300\mu m \times 300\mu m \times 1500\mu m$, i.e., the microprobe data has much higher spatial resolution. If this is taken into account and it is realized that the intense sharp peaks of the microprobe data would become smaller broader peaks upon data smoothing, then it can be seen that a first order correlation appears to exist between the mineral scan and the CT number scan. Other scans were taken using Lower Kittanning (Marine) (C267-L2-S16), Lower Kittanning (nonmarine)(C268-L1-S6), Wyodak(C245), and Decker D2(C285-L1), with similar results.

A series of experiments were run to test the correlation of CT to parameters measured during ultimate and proximate analysis of coal. The coals in Table 6-7 were used. CT pictures were taken along the coal at intervals of 10.5 mm. The actual location of the x-ray image plane in the coal was determined by examining the position of fiducial marks in the plastic potting compound surrounding the coal. These marks could be seen both by the x-ray and by visual inspection. The coals were sectioned 5 mm on either side of a CT image plane, thereby giving a physical slice of coal 10 mm thick with a CT image plane through the center. The coal was knocked out of the plastic support, ground, and used for proximate and ultimate analyses. Because the properties of the coals vary slowly along the bedding plane, as opposed to across them, the CT plane gives an adequate representation of the 10 mm thick slice of coal.

A "computer mouse" was used to outline the coal in the CT image of slice, and the average value of the pixels inside the outline was compared with a number of coal parameters including those of the ultimate and proximate analysis. The best correlation was between the ash content of the coal and the CT value (Figure 6-57).

CT gives a more accurate value of the mineral burden of a coal if only because it is not sample-size dependent. For example a conveyor belt with lump or irregular coal on it presents a varying coal path to a single beam analyzer, making it difficult to determine a

mass absorption coefficient for the coal and its mineral content. The CT suffers from the disadvantage that for the higher atomic number mineral impurities (e.g., pyrite or calcite) the measured attenuation is not linear with coal density. Here the isotopic source devices would be better. Some isotopic source CT machines have been built, but none are commercial and none have a data acquisition time less than several minutes.

6.2 COAL POROSITY

Coal porosity and coal char porosity are important technological parameters because of the effect they have on such diverse properties as gas seepage in coal mines, coal liquefaction, coal pyrolysis, and gasification.

The CT number for a material, regardless of its phase, depends upon the x-ray attenuation coefficients of the elements comprising the material and also their number density (for further discussion, see Section 4).

Coal and the gases normally associated with gasification and combustion (e.g., O_2, CO_2, N_2 consist of elements from the first and second rows of the Periodic Table and have similar x-ray attenuation coefficients (Figure 6-58) over the range of x-ray wavelengths emitted by the CT machine. The difference between the CT number for coal and for the combustion gases will be due to the density difference. While coal has a density of 1.3 g/cm^3 and a CT number of about 1300, air has a density of 1.3×10^{-3} g/cm^3 at STP and therefore would be expected to have a CT number close to 1. Given that the error in the CT measurements is ± 2 CT numbers then an atmosphere of air would be undetectable by the machine. A similar argument applies to all the gases made of elements from the first and second rows of the Periodic Table. Other elements, however, have significantly greater absorption than nitrogen or oxygen. The mass absorption coefficient for xenon is shown in Figure 6-58. Xenon, along with its neighboring elements has an x-ray K-absorption edge close to the maximum of the emission curve of the x-ray tube. At the peak of the K-edge the cross section for xenon is 7.009×10^3 barns/atom; while for nitrogen the cross section is 6.1 barns/atom. Integrated over the emmission range of the x-ray tube this high cross section makes xenon gas visible to the CT machine. An experimental curve of xenon pressure against CT number is given in Figure 6-59. In the linear region of the curve, the sensitivity of the CT measurement is 3.6 torr/CT number at 23 °C. In other

terms, if the CT voxel acquired 1.3×10^{17} atoms of xenon, then there would be a change of one in the CT value for that voxel.

In order to characterize the behavior of xenon as a probe molecule, a series of BET measurements were carried out to compare xenon with nitrogen and CO_2. The xenon experiments were performed at $-111\,°C$ using a slush bath of chlorotrifluoromethane to maintain a constant temperature. The results are listed in Table 6-8.

The substrates used were:

a. Solid glass spheres (3 to 10 μm). The size distribution for these spheres was determined by measuring bead diameters on a photomicrograph. On the assumption of no porosity in these spheres the surface area was calculated to be 0.4 m^2/g. There is good agreement between this theoretical value and the experimental result.

b. Hypersil. This is highly porous silica. All three probe molecules show a much higher surface area than with the solid glass beads.

c. Illinois #6 coal (C134) was micronized to ca. 20 μm particle size. The BET results show the classic variation between N_2 and CO_2. They also show xenon behaving much more like N_2 than CO_2.

d. Lignite (C109) was ground to pass through a 210 μm screen. The results show again that the behavior of xenon is closer to that of N_2 than to CO_2.

The assumed coverage areas for the different probes are:

Gas	$(Å)^2$
N	16.2
CO_2	21.8
Xe	23.2

The results (Table 6-8) show that xenon will not behave in an abnormal fashion in the CT diffusion experiments and should, in fact, behave in a similar fashion to nitrogen.

All of the flow experiments have been carried out on Illinois #6 coal (C118-1-1) This coal had been stored under deionized water since the time it was mined. Three rectangular parallelepipeds were cut from the same lump of coal. The dimensions of the parallelepipeds were 3 cm × 3 cm × 10 cm. In two cases, the long axis of the coal block was cut parallel to the bedding planes, while in the third case the long axis was cut perpendicular to the bedding planes. In all cases the outer surfaces of the coal blocks were sealed by "painting" them with an epoxy resin (Dexter Hysol RE2039 with 15% 3469 hardener). The resin was cured at 50 to 60°C over a period of about 12 h. Several coats of epoxy were applied to make sure that the surface of the coal was sealed and that gas could not leak along the interface between the coal and the potting compound. The sealed block was then put in a mold and a 2-in. OD cylinder of the same epoxy resin was cast around it. Before curing, three diverging 8 mil Al wires were put on the epoxy for use as location markers in the CT image, and also a color-coded plastic thread was put in for sample identification.

After the cure was complete, the square ends of the coal at either end of the parallelepiped were exposed by machining the face in a lathe.

The potted samples were placed in acrylic plastic tubes (2-in. OD by 16-in. long) in such a way that a pressure difference could be applied across the coal. A schematic of the apparatus to handle the coal is shown in Figure 6-60.

Three of these plastic tube sample holders were mounted on a dummy CT cradle and equipped with a gas supply and pressure monitoring system as indicated in Figure 6-61. The pressure monitors on each of the three tubes were Validyne diaphragm gauges. The gauge for the inlet gas manifold was a Wallace-Tiernan absolute pressure meter for the experiments of December 1982, but this was replaced with an MKS capacitance manometer (PDR-C-1B) and a flow controller (244A). The voltages from the pressure transducers were recorded on a data logging system consisting of a Hewlett-Packard 3497A Data Logger, with 3456A Voltmeter, a 9135A Winchester disc/floppy disc combination, and an 85F desk top computer to act as controller. This data logging combination also recorded the temperatures from the Type-K thermocouples placed inside each of the three experiments.

The HP-85 computer was programmed so that data scans over the transducers and thermocouples could be taken on arbitrary time interval. There is a lower limit to the time interval which depends on how many readings are to be taken per scan. The normal number of readings is eight, and under these circumstances the minimum time interval is about 2 s. Normally, the data scans are separated by 15 s.

During the experiment the data is stored on the Winchester disc, and selected portions of the data can be displayed on the screen of the HP-85, either in graphical or numerical form to monitor the progress of the experiment. After the experiment has been finished, the data is transferred to a VAX11/782 and plotted on a Zetaplotter (1453). An example of one of the pressure history plots is given in Figure 6-62. In this experiment the high-pressure side of the coal was held at 754 torr and the pressure was being monitored on the closed low-pressure side as the gas came through the coal. The low-pressure side was periodically evacuated in order to maintain an approximately constant pressure drop across the coal. In addition to the transducer and thermocouple readings, the time of each data scan has been recorded. The clock on the HP-85 has been set to be the same as the clock on the computer that controls the CT machine, and because the time of each CT picture is also recorded, it is possible to correlate the CT pictures with events in the temperature or pressure history of the experiment.

In the first experiments, the coals were deliberately maintained in a moist atmosphere. Free water was present in the acrylic tube apparatus on both sides of all three coals. The coals were designated 1,2, and 3 (Figure 6-61). Samples 1 and 2 were the ones that had been cut parallel to the bedding planes and sample 3 had been cut perpendicular to the bedding planes.

CT pictures were taken down the entire length of all three coal samples. The distance interval between CT slices was 1.5 mm, which was also the thickness of the slice. This means that the entire volume of each sample has been imaged by the CT machine and, in principle, a 3-D map of the coal structure could be produced.

In the case of sample 1, both sides of the coal were pressurized with xenon to a pressure of 754 torr, and the was gas allowed to penetrate into the coal for 19.3 h. At that time the chamber on one side of the coal was evacuated and CT pictures were taken while

the xenon was coming out of the coal. This experiment was designed to mimic the behavior of methane flowing out of a coal seam upon release of pressure.

In the case of samples 2 and 3, the manifold side of the coal was pressurized with 754 torr of xenon, and the downstream side of the apparatus was evacuated, then closed off, and the pressure rise in that section was followed as a function of time. Whenever the pressure reached ca. 100 torr, the section was reevacuated. This maintained a relatively constant pressure difference across the coal. To follow xenon penetration in the coals, CT pictures were taken at 1.5 mm intervals down the length of the coal samples. The flow of xenon through the coals was followed for 10 h in the case of sample 1, for 24 h in the case of sample 2, and for 14 h in the case of sample 3.

To prepare for a second series of experiments, the same three samples of coal were heated at 80 °C for two weeks under vacuum (<1 torr). This treatment removed as much of the water and small molecular weight components as possible from the pore structure of the coal without affecting the pore structure itself.

In the second set of experiments, coal sample 1 was pressurized to 1140 torr of xenon for 12 h, then evacuated on the downstream side, and CT pictures were taken while the gas came out of the coal. In the other two cases, the manifold side of the coal was pressurized to 1140 torr of xenon and the downstream side was evacuated, then allowed to fill back up to equilibrium with the gas penetrating through the coal.

The pattern of xenon penetration is obtained by subtracting the image of the xenon-impregnated coal from the original coal. It has been found that although the CT cradle will accurately return to the same position along the piece of coal, there is a variable sag in the CT cradle causing the image to move around in the zone of reconstruction of the computer. This change in position is illustrated in Figure 6-63. The red ring is the zone of computer reconstruction and remains constant in position. The blue circle is the outline of the plastic tube containing the coal, and it is clear that the position of the tube has changed within the red ring. The effect of this change in position is that when two images are subtracted, the corresponding positions in the coal are not subtracted from one another and this error causes large artifacts in the resulting difference image. For example, in Figure 6-64, the simple difference between the two images is shown. The dominant feature is

the pair of crescents which have been caused by the misalignment of the outer edges of the plastic tube. This effect is illustrated in Figure 6-65.

The approach taken to align the images before subtraction is illustrated in Figures 6-66a and 6-66b. In Figure 6-66a, an image has been displayed and, by manipulating the white band in the color look-up-table (LUT) of the digital display processor, a range of CT values has been found that only occurs on the circumference of the circular outline of the image of the plastic vessel. The positions of the CT numbers in this band are then fitted to a central general conic, and the central point is calculated (Figure 6-66b) and stored. When two images are to be subtracted, the position of their centers is recovered from a data file and used to calculate the offset of one image relative to the other. This method of accounting for the shifting of the images within the computer zone of reconstruction takes into account orthogonal displacements of the two images but not rotation of the images with respect to one another. In our experience, rotation of the two images has not occurred and is very unlikely, given the geometry of the apparatus. The offsets between the two images can be calculated to within one pixel: even then edge artifacts can still occur. Altering the pixel offsets by one pixel in the direction to remove these artifacts produces artifacts in the opposite direction, i.e., subpixel resampling, and registration of the images would be necessary to remove the artifact completely. However, the artifact is now much smaller than the major features of the xenon pattern we are trying to follow (Figure 6-67), and we consider this method of aligning the images sufficient for our present work.

Using another computer routine it is possible to examine the CT numbers with any arbitrary polygon and to transfer that polygon to a sequence of images so that the variation of the CT numbers within that chosen area can be followed throughout the sequence of images. One particular way in which this routine has been used for the gas diffusion work has been to choose an arbitrary polygon which outlines a particular region of interest in the coal and to apply the same polygon to the difference images that follow the flow of xenon into the coal, thus the flow of xenon into the chosen region of the coal could be followed as a function of time. Figure 6-68 shows a CT image of the Illinois #6 coal used in vessel #2, and, along side this image, a black-and-white image of the xenon pattern found in the coal after about 35 min from the time the xenon pressure was applied. Figure 6-69 shows

a white area that has been drawn on the image of the coal using a computer-controlled cursor. The shape of this polygon has been transferred to the xenon image and the amount of xenon appearing within the polygon can then be calculated.

The porous structure within coals has been the subject of numerous investigations using a variety of techniques, e.g., mercury penetration, gas penetration, small-angle x-ray scattering, and small-angle neutron scattering. These investigations have concluded that there is a wide variation of pore size in coals. For convenience in describing this distribution, the pores below 2 nm are called micropores, the pores between 2 and 20 nm are called transitional pores, and the pores greater than 20 nm are called macropores. For example, in an Illinois #6 coal, 30.2% of the internal volume was calculated to be as micropores, 52.6% as transitional pores, and 17.2% as macropores (Reference 9). Quite different results have been obtained for coals of other rank. These experiments have been carried out on either coal that has been pulverized or on coal that showed no obvious cracks or fissures.

Pulverizing the sample clearly eliminates any opportunity for distinguishing between the porosities and flow characteristics within different volumes of the coal, and selection of coal pieces with no obvious cracks or fissures may weight the choice in favor of relatively clean pieces of vitrain and against the other lithotypes present in the coal that may play an important role in gas permeation through the coal.

Flow in a microporous solid such as coal can occur by a variety of mechanisms. The mean free path concept is a key parameter in determining which group of mechanisms is operating. From kinetic theory of ideal gases the mean free path, λ, of a gas of density n/cm^3, molecular diameter σ cm, is given by

$$\lambda = \frac{1}{\sqrt{2}\pi n \sigma^2} \tag{6-1}$$

The number density of an ideal gas (pressure p, temperature T) is given by

$$n = p/kT \tag{6-2}$$

Thus for a gas at 1 atm and 25°C

$$n = 2.46 \times 10^{19}/\text{cm}^3 \qquad (6\text{-}3)$$

$$\lambda = 54.4 \text{ nm} \qquad (6\text{-}4)$$

using $\sigma = 0.41$ nm (Reference 10)

For pores with less than 54.4 nm as a characteristic dimension, collisions are expected with confining walls more often than with other xenon atoms. Such pores do, however, contribute significantly to the internal surface areas of coals (Reference 9). Secondly, as indicated in Equation 6-1, the mean free path is inversely proportional to pressure so that at high pressure the cut-off pore size for continuum flow is correspondingly reduced.

The various types of flow which can be considered are:

a. Flow as a result of pressure gradient

— Laminar flow

— Knudsen flow (or molecular streaming)

— Molecular effusion

b. Diffusion as a result of concentration gradient

— Bulk diffusion

— Hindered (or activated) diffusion

— Surface diffusion

While the difference between sets (a) and (b) seem obvious, there is considerable interchange in the literature between these terms, in part due to difficulties in interpretation of data under a given set of circumstances. Indeed "diffusion" experiments in coal may be conducted in an isobaric chamber (e.g., Reference 12) or across a thin septum of coal driven by pressure (e.g., Reference 11).

Barrer, in a classic book (Reference 13), considers those aspects of flow under group (a).

6.2.1 Laminar Flow

Laminar flow, i.e., flow in the absence of turbulence, conforms to the equation

$$-\vec{\nabla} p + \mu \nabla^2 \vec{v} = 0 \tag{6-5}$$

where p, μ, and $\vec{v}$ are, respectively, the local pressure, dynamic viscosity and vector velocity field of the flow. In particular the flow is continuum in nature and contains a characteristic flow scale d such that:

$$\lambda \ll d \tag{6-6}$$

From the above discussion, it is clear that laminar flow in coal pores is limited to large macropores, cracks, or high-pressure flows. Notwithstanding these difficulties, the laminar flow concept has been exploited (Reference 11) to determine whether a piece of coal was cracked or whether the flow was, in fact, in the Knudsen regime.

6.2.2 Knudsen Flow

Knudsen flow is an intermediate flow which occurs when the characteristic scale is comparable to the mean free path of the fluid species, i.e.

$$\lambda \sim d \tag{6-7}$$

The molar flux, N, of material flowing under these conditions is

$$N = \frac{4}{3} \frac{d}{\sqrt{2\pi MRT}} \frac{\Delta p}{L} \left(\frac{2-f}{f} \right) \tag{6-8}$$

where M is the molecular weight of the flowing species, $\Delta p / L$ is the pressure gradient and f is the fraction of molecules that are diffusely reflected after collision with the walls. The expression can be more complicated for noncircular geometries. For extremely contaminated surfaces, such as coal, the factor f is probably unity.

6.2.3 Molecular Effusion

While not strictly flow under a pressure gradient, molecular effusion is a mean-free-path dominated phenomenon conveniently discussed at this point. At low-pressure the

mean free path of the gaseous molecules is very large compared to the characteristic scale, i.e.,

$$\lambda \gg d \qquad (6\text{-}9)$$

In this flow the simple kinetic theory expressions will suffice, i.e.,

$$N = p / \sqrt{2\pi MRT} \qquad (6\text{-}10)$$

This is a good model for flow through a thin orifice (i.e., thin compared to λ) but flow through a macrosized coal lump will undoubtedly cause collisions with the wall of a pore during flow. In practice one could distinguish between Knudsen flow and effusion, Equations 6-8 and 6-10 respectively, via the pressure dependence thereby implied.

6.2.3 Bulk Diffusion

Diffusive flows are the result not of a pressure gradient but of a concentration gradient; thus they are described by Fick's Law

$$\vec{N} = -\underset{\approx}{D} \cdot \vec{\nabla} C \qquad (6\text{-}11)$$

where the diffusive flux vector N is caused by the concentration gradient C.

In this approach the microscopic view of coal as a 3-D network of pores is replaced by the picture of coal behaving as a material with a bulk parameter D. Whereas, in dilute binary gases, D can be estimated from kinetic theory, no such simple explanation exists for coal. In an anisotropic material such as a banded coal with well defined bedding planes, the diffusion coefficient D is a second-order tensor with elements describing flows parallel to and perpendicular to the bedding planes so that N is not parallel to C. Such anisotropy has been observed with a flow approximately three times greater along the bedding planes than perpendicular to them (Reference 14).

Equations of type (1) can be solved in conjunction with a continuity equation of the form

6-23

$$\frac{\partial C}{\partial t} = -\vec{\nabla} \cdot \vec{N} \tag{6-12}$$

In general, these problems are solved for bulk phase diffusion with D degenerated to a scale quantity, the binary diffusion coefficient. Equations 6-11 and 6-12 combine to give

$$\frac{\partial C}{\partial t} = \vec{\nabla} \cdot (\underset{\approx}{D} : \vec{\nabla} \vec{C}) \tag{6-13}$$

which for constant and isotropic D yields

$$\frac{\partial C}{\partial t} = D \, \nabla^2 C \tag{6-14}$$

This has been exploited by Walker et al. (Reference 12) in a pressurized system that is alternately pumped full of gas and then exhausted. The rate of rise of volume of diffusion gas into a sample of powdered coal is then followed isobarically, and Equation 6-14 is solved for this circumstance. A characteristic flow proportional to $t^{0.5}$ is observed under these conditions. Equation 6-14 has also been used in experiments in which a pressure gradient has been imposed across a thin slice of coal (Reference 11); in this case, there is a time lag as the gas transits the slice before it is detected downstream. Barrer and Grove (Reference 15) have shown that Equation 6-14 leads to a "time lag" t such that

$$t = l^2/6D \tag{6-15}$$

and

$$D = \frac{2d}{3} \sqrt{\frac{2RT}{\pi M}} \tag{6-16}$$

for a uniformly porous capillary system of diameter d and length l when Knudsen flow occurs. Binary bulk diffusion applied in the classic sense gives rise to a rather different diffusion coefficient such that

$$D \propto T^{3/2} / \Omega \tag{6-17}$$

where Ω is a binary Chapman-Enskog temperature correction term (Reference 16). Except for large temperature changes it is a weak function of temperature so that 3/2 power law often surfaces.

6.2.4 Hindered Diffusion

Walker (Reference 12) has stressed that hindered (or activated) diffusion is likely to occur when the dimensions of the diffusing species are comparable to those of the porous interval. This is often the case with coal so that it is postulated (Reference 17) that there should be an activation energy E associated with hindered diffusion. Indeed, in the basis of a narrow temperature range, diffusion data have been better fitted by

$$D = D_o \exp\{-E/RT\} \tag{6-18}$$

than by a $T^{1/2}$ law (Equation 6-16) or a $T^{3/2}$ (Equation 6-17). Plausible values of E are obtained (e.g., 18 kJ/mol for Illinois #6 coal) for a diffusional barrier.

6.2.5 Surface Diffusion

Surface diffusion is a phenomenon in which an adsorbed layer acts as a facilitating plane for the migration of additional molecules that are adsorbed at the edge of the plane. In some circumstances surface diffusion may be a significant contributor to the total flow through a porous solid. As a necessary but not sufficient condition, the gas must be absorbed on the surface. Gan et al. (Reference 9) have shown that many gases do absorb on coal surfaces; on Illinois #6 at 298 K, the surface area was 96 m^2/g for CO_2 absorbate. Xenon is absorbed on coals; e.g., Kini (Reference 18) reports vitrain surface areas of 140 to 270 m^2/g at 0°C.

Using the 96 m^2/g for CO_2, the volumetric number density of adsorbed species within the coal can be estimated. The assumed coverage per molecule of CO_2 is 0.22 nm^2 and for Xe is 0.23 nm^2 (Reference 19) so that, neglecting this difference, the number density of xenon atoms is approximately 5.5×10^{20} cm^{-3}, a density about 20 times that in the gas phase at NTP! The mechanism of the adsorption may be due to absorption from the gas phase or due to film mobility referred to above. Barrer and Grove (Reference 15) considered both of these cases in some detail and for the purely axial flow case they write

$$\frac{\partial C_g}{\partial t} + \frac{\partial C_s}{\partial t} = D \frac{\partial^2 C_g}{\partial x^2} + D_s \frac{\partial^2 C_s}{\partial x^2} \tag{6-19}$$

where C_g and C_s are the number of molecules of diffusing species in the gas phase and the

surface phase per unit length of capillary respectively. In this expression, D is the bulk effusion coefficient, e.g., Equation 6-16 in Knudsen flow and D_s is a surface diffusion coefficient obeying an Arrhenius dependence such as Equation 6-18.

Equation 6-19 can be generalized to the current circumstance for anisotropic materials such that

$$\frac{\partial C_g}{\partial t} + \frac{\partial C_s}{\partial t} = \vec{\nabla} \cdot (\underline{D} : \vec{\nabla} C_g) + \vec{\nabla} \cdot (\underline{D}_s : C_g) \tag{6-20}$$

For sufficiently dilute systems the surface concentration is related to the bulk phase gas concentration by Henry's Law (a degenerate form of the Langmuir Isotherm, in this case), then

$$\frac{C_s}{C_g} = \frac{4K_s}{d} \tag{6-21}$$

where d is the capillary diameter and K_s is Henry's constant for the absorption. Barrer and Grove (Reference 15) proceed to show that

$$\frac{\partial C_g}{\partial t} = \vec{\nabla} \cdot (D_{\text{eff}} : \vec{\nabla} C_g) \tag{6-22}$$

where

$$D_{\text{eff}} = (\underline{D} + \frac{4K_s}{d} \underline{D}_s)/(1 + 4\frac{K_s}{d}) \tag{6-23}$$

The form of Equation 6-22 is identical to Equation 6-13, so that a delay time can be experimentally obtained analogous to Equation 6-15, i.e.

$$\tau = l^2 / 6 D_{\text{eff}} \tag{6-24}$$

where D_{eff} is the axial term derived from $\underline{D}_{\text{eff}}$.

The bulk gaseous concentration per unit length of capillary, C_g, is not measurable directly in a CT experiment; the experiment measures the total electron density of all xenon present, whether in the gaseous or the adsorbed state. However the sum of the two contributions should be proportional to C_g under Henry's Law assumptions.

Then the total concentration of xenon, C_t, gaseous and adsorbed, per unit volume of coal is

$$C_T = C \, [1 + K_s \, \rho_{CL} \, \Sigma] \tag{6-25}$$

where C, ρ_{CL}, and Σ are the bulk gas concentration within the pores, the coal density, and specific surface area, respectively. Knowing that

$$C = 4C_g / \pi \, d^2 \tag{6-26}$$

then substitution of Equations 6-25 and 6-26 into 6-22 yields the following:

$$\frac{\partial C_T}{\partial t} = \vec{\nabla} \cdot (D_{eff} \vec{\nabla} \, C_T) \tag{6-27}$$

In principle, this equation represents the flow of a diffusing species in coal given that Knudsen flow is occurring in the pores and that this is supplemented by surface diffusion terms. It should be inferred from this discussion that several of the phenomena discussed may be at work simultaneously and a combination of all of the basic flows may be involved in different parts of the coal under some circumstances.

The time history of the appearance of xenon in the high-density region outlined in Figure 6-69 is shown in Figure 6-70. This CT picture was taken about 5 cm down the 10 cm length of the piece of Illinois #6 coal used in vessel #2, after the coal had been dried. The time history was followed over 16 hours, and in that time the average increase in the CT number for a pixel within the chosen area was 760. From the calibration chart in Figure 6-59, it can be seen that, at the manifold pressure of 1120 torr, the maximum increase in the CT number for any pixel should be approximately 250. This strongly suggests that significant amounts of xenon are absorbing on the walls of the coal. The CT number increase for any pixel is caused not only by the xenon present in the gas phase within the

pore, but also by the gas adsorbed upon the walls of the pore. Henry's Law will be used to partition the total number of atoms within a voxel between the adsorbed layer and the gas phase.

If the theory outlined in the previous section is applied to diffusion of gas into a pulverized coal sample, then the theory predicts that for small values of the elapsed time the quantity absorbed should be proportional to $t^{0.5}$. Plotting the CT data against $t^{0.5}$ does not give a good fit. A log-log plot of the CT data against time was made (Figure 6-71) to examine if there was a power dependence of CT number increase with time. Only at very long times did there appear to be anything approaching a linear relationship. This relationship suggested that the CT increase was proportional to $t^{0.33}$.

Not all the areas within even the one CT slice showed the same ability to pick up xenon. Figure 6-72 shows another polygon chosen on the same CT slice. Whereas, in the previous polygon, the average CT number of the raw coal within the polygon was 1629, in this second polygon the CT number average was 1451. In neither case would our experience suggest that the material being examined was pure vitrain. It was very probable that both areas have contamination from clays, with significantly more contamination in the first area. Indeed, if the average CT number was to be partitioned between clay (~3100) and organic coal (~1300), then some 20% by weight of the material in the first outline was clay.

The time history of the xenon increase in the low-density region is shown in Figure 6-73, plotted against time, and in Figure 6-74, plotted against the square root of time. The general shapes of the curves for the low-density region are similar to those for the higher-density region. The rate of increase is not so fast in this lower density region, and the level of xenon reached in the pixels is not so high. However, the intercept on the zero-time axis is the same, and the approximate rate of increase at the time the experiment was terminated was also the same (0.2 CT numbers/min).

A third outline was chosen, this time to cover the region of the coal that gained xenon the fastest. The average CT number of the raw coal in this region was 1700. As can be seen from Figure 6-75, the gain of xenon was much greater than either of the two previous outlines, but the rate of gain had slowed to 0.15 CT/min by the end of the experiment.

This region of the coal had apparently adsorbed seven times its volume of xenon at the external ambient pressure.

The diffusion parameters within a chosen geometry have been evaluated . A series of difference images is shown in Figures 6-76 to 6-80. The series was taken during passage of xenon gas into Illinois #6 coal at a driving pressure of 1100 torr. After mining, this particular coal had been stored under water and had been kept as moist as possible during the potting procedure.

Figure 6-81 shows the CT image of the raw coal at a position about 10mm in from the end at which the xenon will be introduced. The images in Figures 6-76 to 6-80 were taken at the same location. The raw coal image shows the bedding plane structure running at about 45° from the horizontal across the image. The bedding planes are also coming out normal from the plane of the figure. The color scheme in the raw coal image has been set to show dense regions as white or red and regions of relatively low density as blue and blue-green. Scanning electron microscopy experiments have been performed on this Illinois #6 coal (Figure 6-82) and and were discussed earlier. For the purpose of understanding the diffusion experiment, we will summarize the results of the SEM investigation and simply say that the high-density regions in the CT image correspond to heavily mineralized bands and that the low density regions are relatively clean organic bedding layers.

The first image in the sequence of difference images (Figures 6-76 to 6-80) is blank. This is because the plane of the coal being imaged is about 10 mm from the end of the coal where the xenon gas has been applied and the gas has not yet penetrated into that plane. A difference image at that time and place would therefore be blank. The pattern of penetration into this plane over the next several hours is shown in the succeeding images. In this series the color scheme has been set up so that the more xenon that has appeared in a region, the more the color has gone in the direction from blue to red. As can be seen from these images, there is a definite banded structure to the pattern of xenon penetration, and this "bandedness" is approximately parallel to the original bedding plane structure of the coal. It is clear that the penetration of xenon into the coal can certainly not be described as a smooth front passing down the length of the block.

Figures 6-83 to 6-87 show the results of an experiment run under the same conditions as the one described above except that in this case the block of coal, while being taken from the same piece of Illinois #6 as the previous block, has been oriented, cut and potted with its bedding planes orthogonal to the long axis of the block. In the first experiment the xenon gas had to pass along the bedding planes of the coal. In this experiment the gas had to pass across the bedding planes.

Figure 6-88 shows a CT image of the raw coal, before any gas addition, at the same plane in the coal where the difference images were taken. The bedding plane structures so apparent in Figure 6-81 are quite absent. The CT image is being taken through quite low density, relatively pure organic material except for two mineral-laden cleats entering the image from the top left corner. Figures 6-83 to 6-87 show the time history of xenon penetration into this plane of the coal. The sequence shows a much slower rate of penetration than was observed for the parallel case and the appearance of the xenon is more random with no obvious structure to it. In this case there does not appear to be any passage of the gas into this plane through the mineral matter regions.

Figure 6-89 shows the same images as Figures 6-77 to 6-80, but a grey scale look-up-table has been used to display them. Furthermore, a graphics software line has been drawn at the bottom edge of the coal image and perpendicular to the bedding plane direction. The CT values along this line have been plotted out in the accompanying graph. The same line has been drawn on all the images in this sequence and the line graphs assembled in Figure 6-90. This figure clearly shows the growth of the xenon signal along this line with time. Figure 6-91 shows the same data, except that all the graphs have been normalized to the same peak value and a curve for a much longer period of time has been included. This presentation shows the apparent spread of the gas from a central source towards the edge of the coal.

In order to quantify the diffusion of gases through coal and to obtain diffusion constants, it is necessary to take some account of the blurring of the image by the limited spatial resolution of the CT machine.

When a uniform solid object is imaged in the CT machine, the edges of the CT image of the object are not infinitely sharp. The spatial resolution of the machine is determined

by fixed geometrical factors such as detector spacing, x-ray spot size, and detector-tube distance. A compromise is set in the reconstruction algorithm to include frequencies in the Fourier integrals sufficiently high to accommodate the maximum allowable resolution, but not too high because the higher frequencies contribute increasingly to noise.

Figure 6-92 shows a CT image of a plastic phantom used for the xenon gas calibration. A line is displayed on this image, and the CT values on the line are displayed in Figure 6-93.

In this case, there was xenon in the phantom, and so the CT number did not drop to zero within the phantom but remained at the number corresponding to the xenon density. All of the rounded edges in Figure 6-93 are, in fact, sharp. The plot in Figure 6-94 shows a possible assumed true distribution, and Figure 6-95 shows the blurring function. These two functions are convolved according to the relationship,

$$C_j = \sum_i^1 b_i \; x \sum_{i=1;k=j-N+1}^{i=2N;k=j+N} B_i O_k \qquad (6\text{-}28)$$

where $2N$ is the number of points in the blurring function. C is the convolved function. O is the original function, and B is the blurring function. This relationship essentially slides the blurring function over the original distribution.

Figure 6-96 shows a comparison of the assumed true distribution, the actual distribution, and the distribution calculated from the assumed distribution and the blurring function. The fit is acceptable on both sides of the actual distribution showing that the blurring function is not sensitive to the step height.

The same function was applied to a line drawn across the diameter of the CT image of the xenon coal (Figure 6-97). The CT numbers along this line are shown in Figure 6-98, along with the assumed initial distribution and the calculated distribution. The assumed distribution only attempted to fit the edges of the plot, not the structures within the plot. An expanded view of the fit of the RH edge is given in Figure 6-99. The initial distribution gives the diameter of the outside acrylic tube to be 63.6 mm and actual measurement gives 63.7 mm. The same blurring function is transferable between images and applies to lines which are normals to density discontinuities. For example, Figure 6-100 shows a

difference image taken during xenon diffusion into Illinois #6 coal. The line drawn on the image is normal to both the edge of the coal and the prominent xenon feature which parallels the bedding planes and the edge of the coal. The CT numbers along this line are also given in Figure 6-100. In Figure 6-101, we show a "true" distribution and the convolved function. The fit is good and it suggests that in this instance the xenon is diffusing into the coal on a simpler pattern that the observed CT line would suggest.

Calculation of a simple 1-D diffusion constant based on the equation

$$\frac{\partial C}{\partial t} = K \frac{\partial^2 C}{\partial x^2} \tag{6-29}$$

gives a value of 1.15×10^{-6} cm^2 s^{-1}, which is in reasonably good agreement with other determinations for coal. This, of course, is the slow rate, across the bedding planes. Our results show that the passage of gas in the direction parallel to the bedding planes is much faster. The other coals examined by xenon infusion at ca. 1150 torr were anthracite (C102), Beulah Zap lignite (C114), Rosebud subbituminous (C260), and Ohio #6 bituminous. Illinois #6 was the coal most extensively examined. In addition to the two orientations of the bedding planes, the coals were imaged with two driving pressures (554 and 1143 torr) and at two temperatures (25 and 60 °C).

An attempt was made to correlate the ultimate porosity of a set of coals with BET measurements on the coal. In this series of tests, coals were cut and potted in epoxy, thoroughly evacuated, and CT images were taken down their length. The coals were then put in a pressurized container under xenon for several months. The intent was to allow the xenon to penetrate everywhere it could inside the coal, then take CT pictures of the xenon-filled coal, and by the usual subtraction technique, determine the distribution of the gas inside the pieces of coal. We found in practice that the coals crumbled too much during the months of pressurization, and no meaningful difference images were obtained. The techniques for 3-D display expected to be used here were instead used in the studies of cokes.

These xenon penetration studies show that the CT technique is extremely useful in examining the nature of flow, gas or liquid, within a porous solid such as coal. The studies show the extremely complex nature of the penetration of fluid into the coal, usually with a

preference along the highly mineralized layers of the coal. The mathematical tools for handling the 3-D data of transport into the coal could not be developed during this work, but the availability of CT data, showing such detailed movements should stimulate new work in the analysis areas.

6.3 COAL CAKING PROPERTIES

Two sets of coals were used here: an 80/20 mixture of Pittsburgh #8 and Phocohantas seam coal. These two are known to be compatible coals during coking. The second pair was Pittsburgh #8 and Illinois #6 which are known to be incompatible 50/50. All the coals were 80% finer than 8 mesh and 20% between 4 and 8 mesh. The two sets were put in the furnace and the temperature was raised to 700°C in a period of one and a half hours in a furnace atmosphere of nitrogen. Both coals showed considerable movement and gas evolution. A moveable probe had been installed in the furnace for this experiment. The probe led to a gas sampling system. Since the probe could be seen in the CT picture it was possible to know where within the coking sample the majority of the gases were coming from (Figure 6-102). The CT experiment did not pick up any difference in the coking pattern of the two sets of coal that could be ascribed to their different compatibilities.
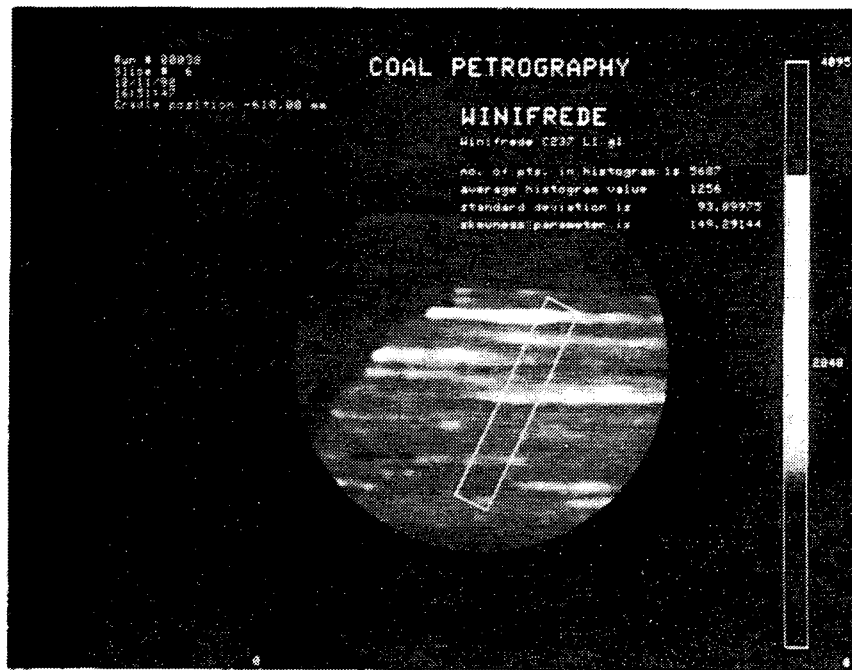
Figure 6-1. CT image of Winifrede seam coal (C237 L1)

Figure 6-2. CT image of Illinois #6 coal (C123 L1)
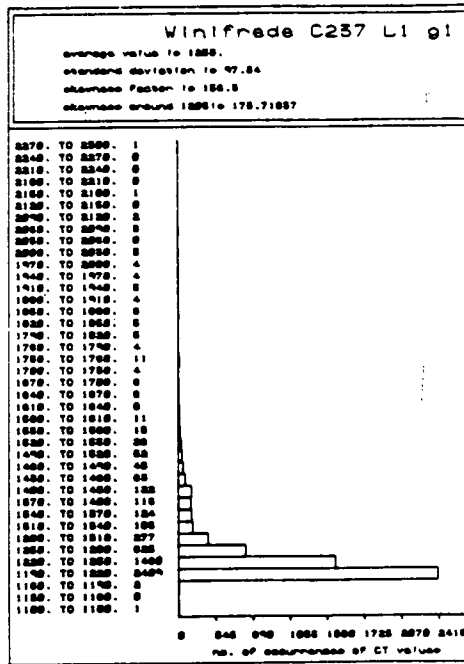
Figure 6-3. Histogram from Winifrede seam coal
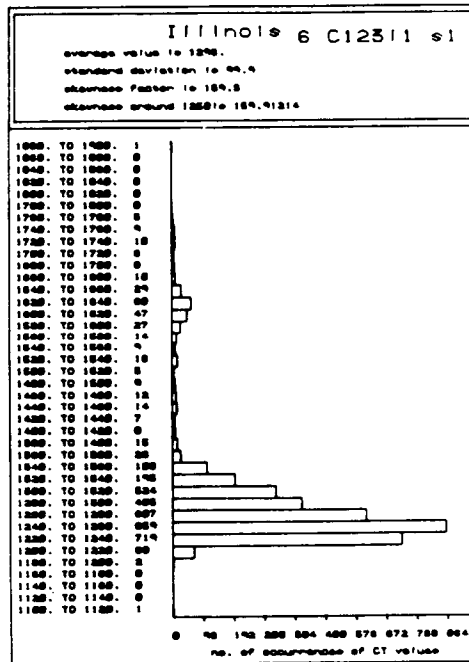
Figure 6-4. Histogram from Illinois #6 seam coal
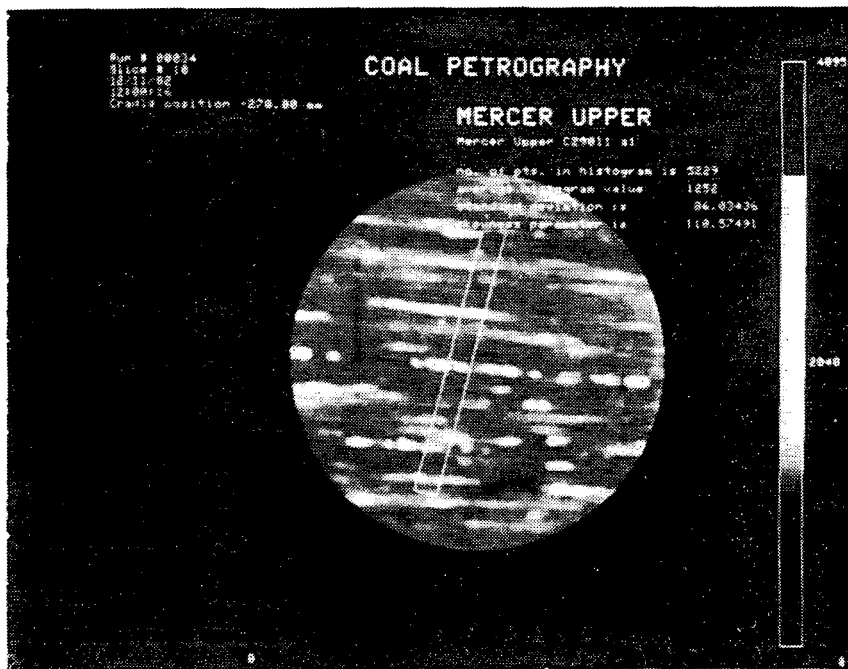
Figure 6-5. CT image of Upper Mercer coal (C290 L1)
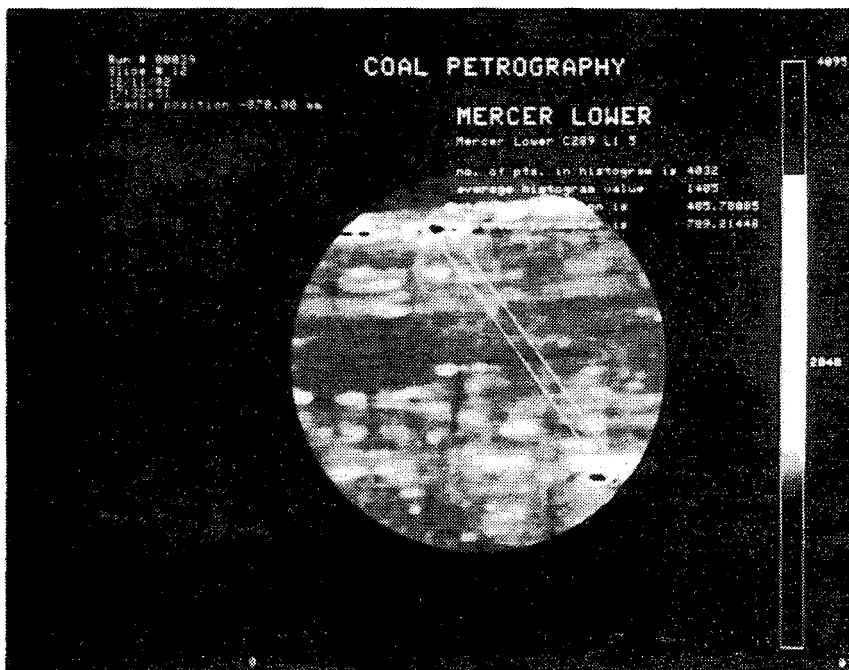
Figure 6-6. CT image of Lower Mercer coal (C289 L1)
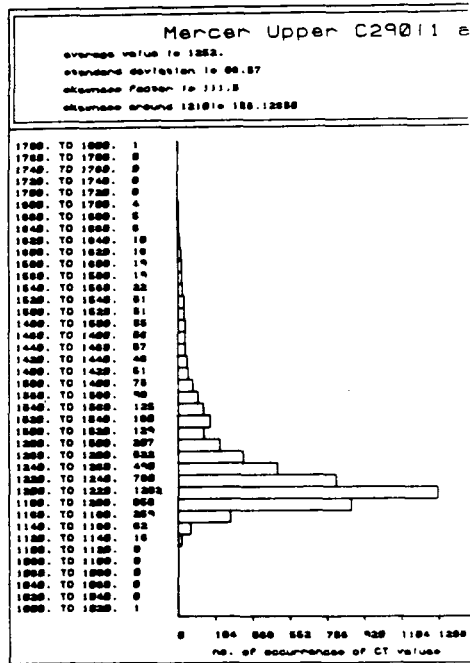
Figure 6-7. Histogram of Upper Mercer coal
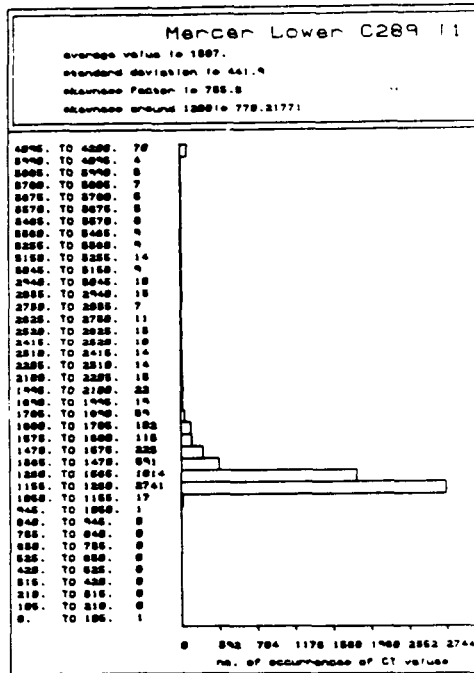
Figure 6-8. Histogram of Lower Mercer coal
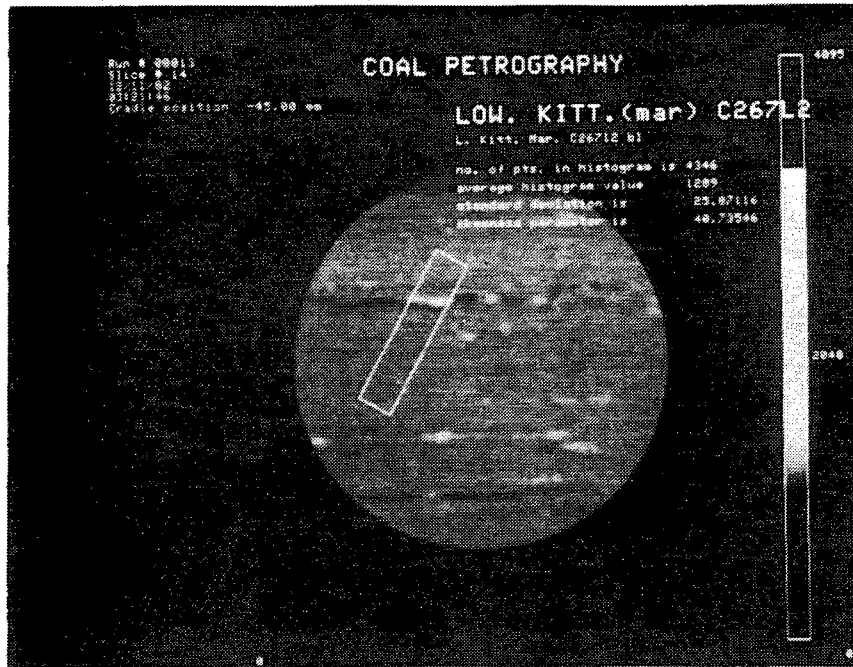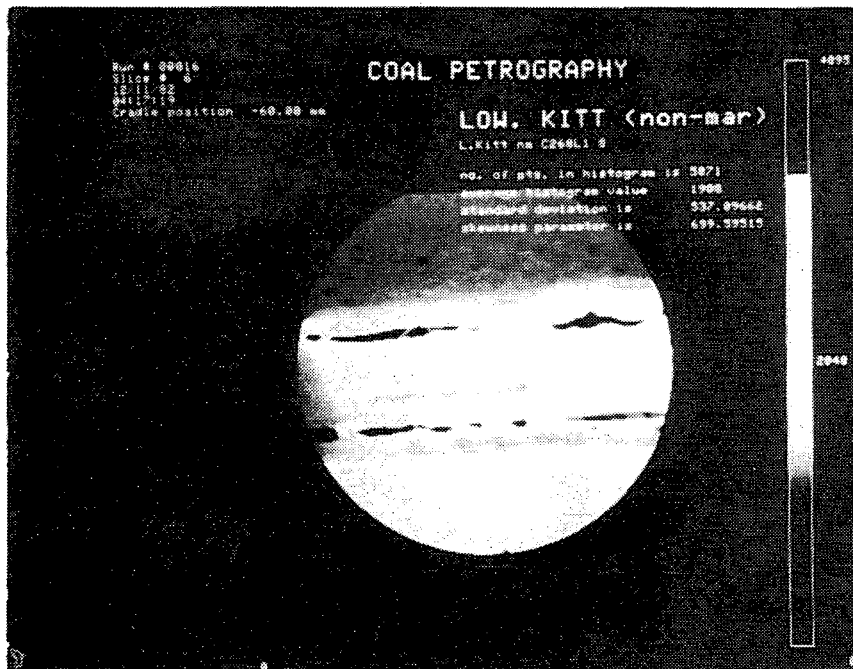
Figure 6-9. CT image of Lower Kittanning (Marine) coal (C267 L2)

Figure 6-10. CT image of Lower Kittanning (Non-Marine) coal (C268 L1)
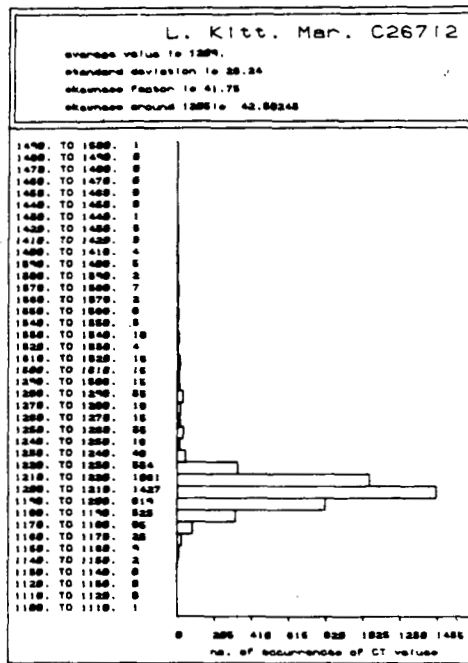
Figure 6-11. Histogram from Lower Kittanning (Marine) coal
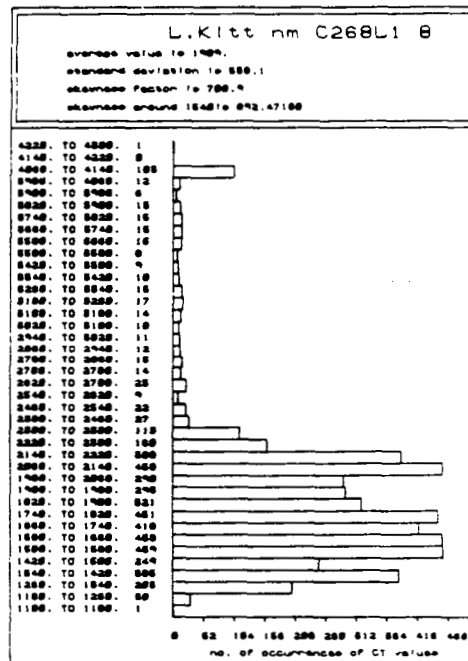
Figure 6-12. Histogram from Lower Kittanning (Non-Marine) coal

6-39
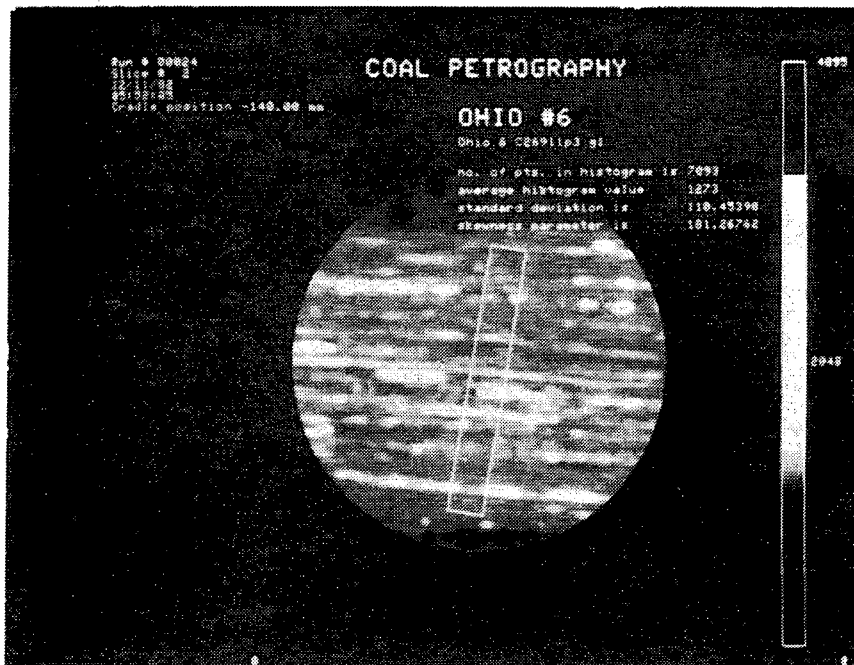
Figure 6-13. CT image of Ohio #6 coal (C269 L1 P3)
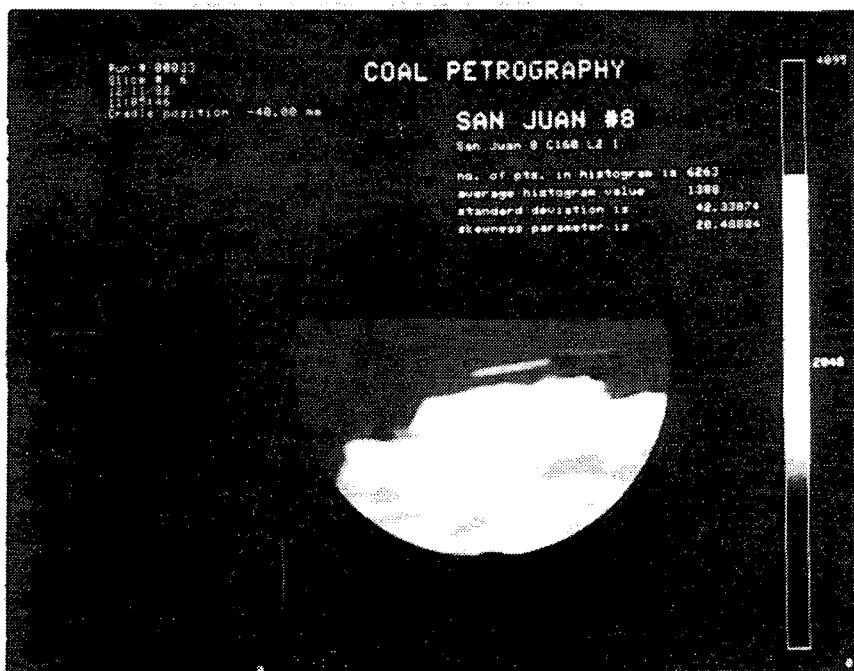
Figure 6-14. CT image of San Juan #8 coal (C160 L1)
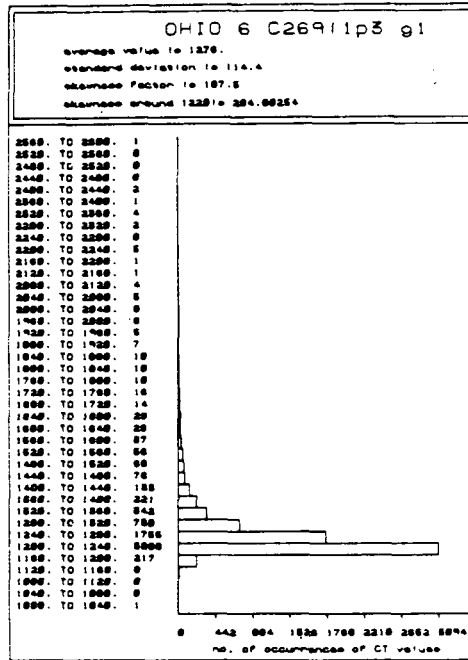
Figure 6-15. Histogram from Ohio #6 coal
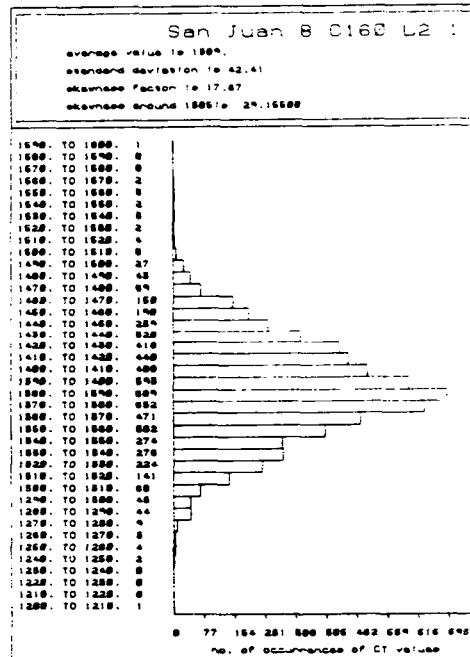
Figure 6-16. Histogram from San Juan #8 coal

6-41
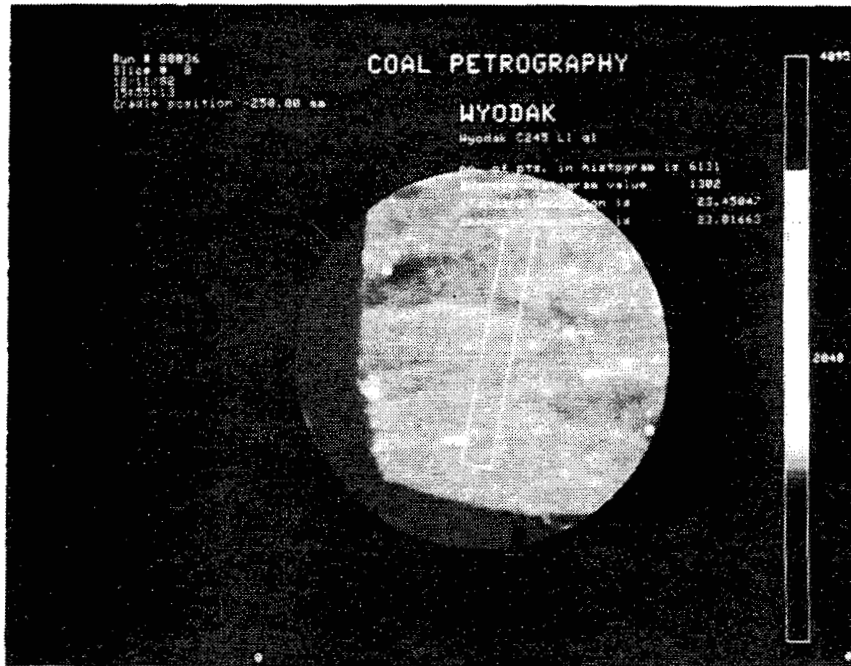
Figure 6-17. CT image of Wyodak coal (C245 L1)
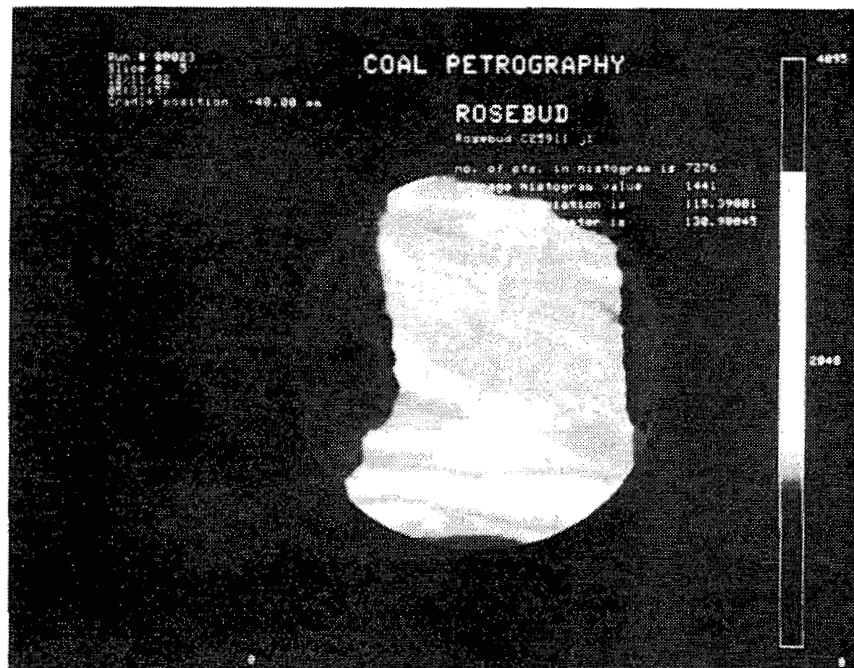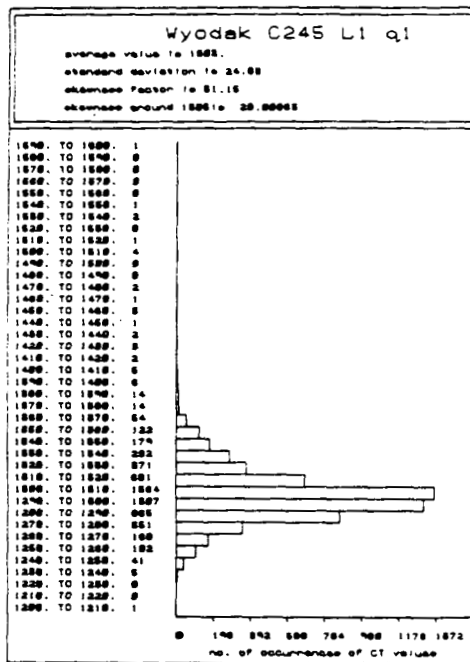

Figure 6-18. CT image of Rosebud coal (C259 L1)
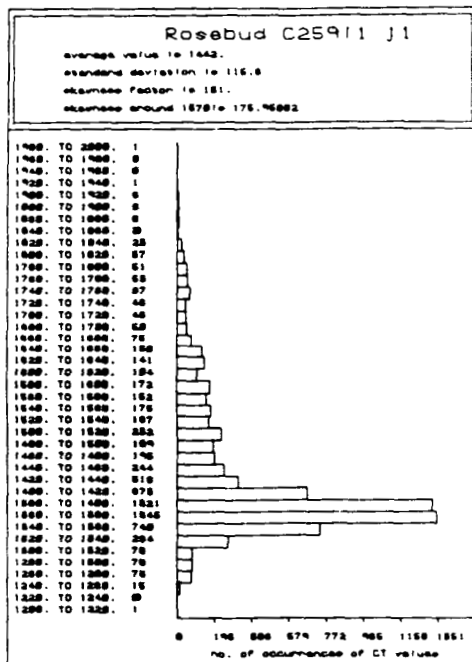
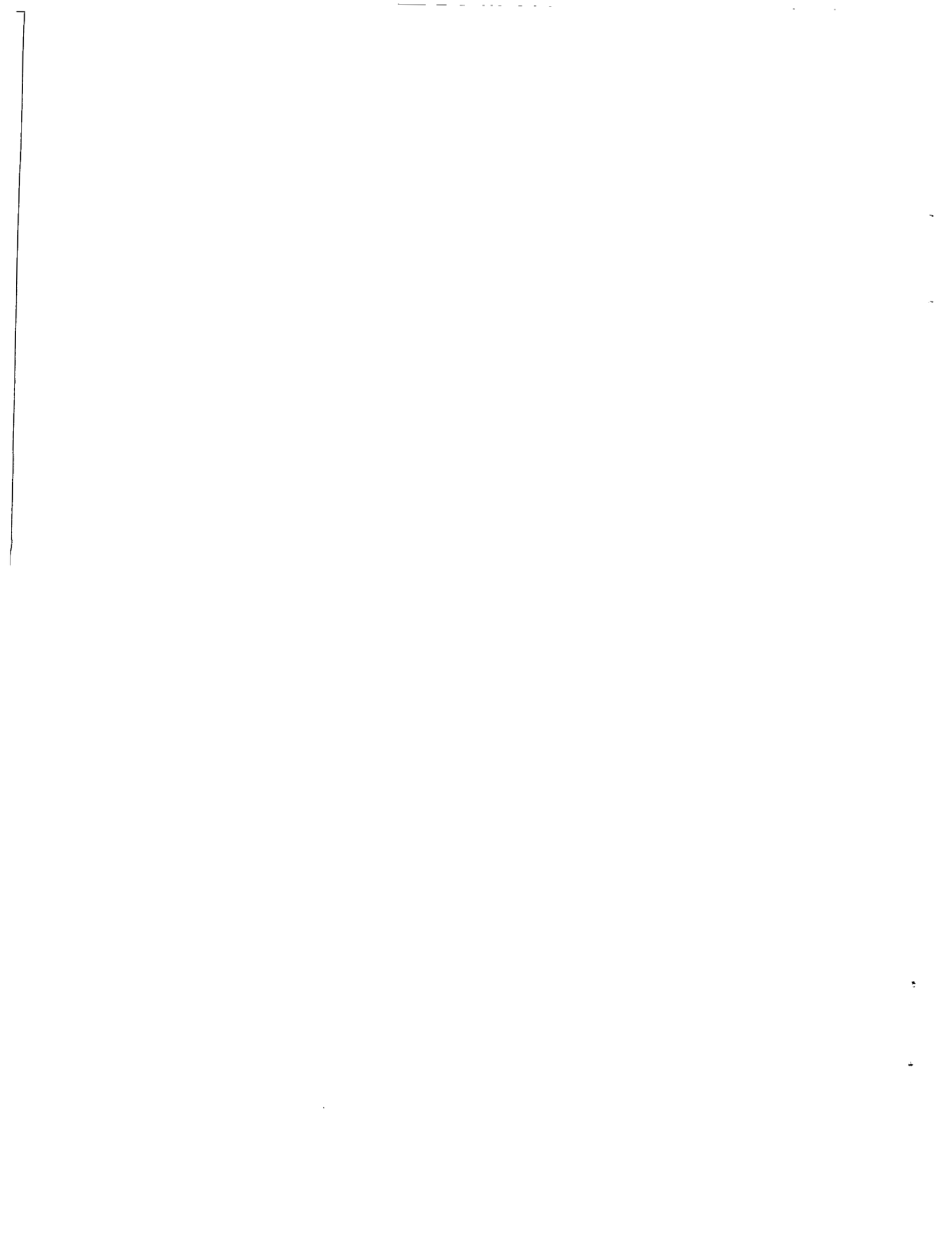**Figure 6-19. Histogram from Wyodak coal**

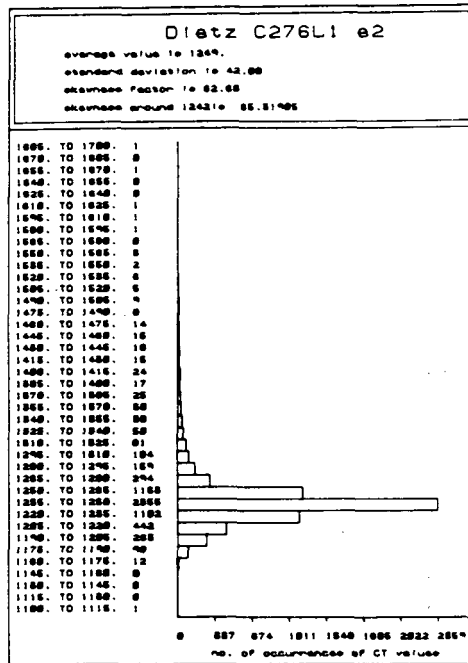**Figure 6-20. Histogram from Rosebud coal**

6-43

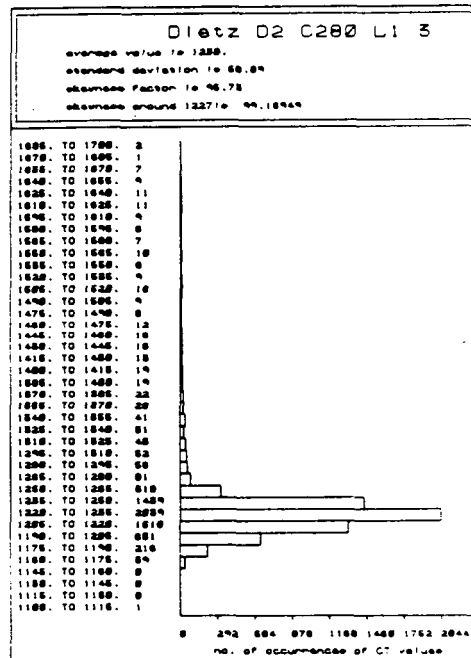Figure 6-23. Histogram from Dietz (Upper) coal

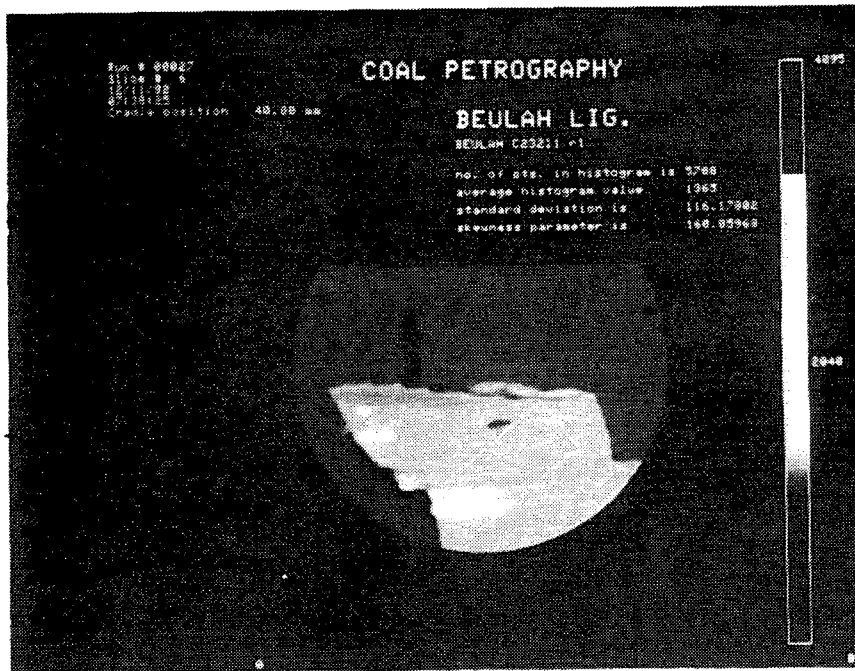Figure 6-24. Histogram from Dietz (Lower) coal
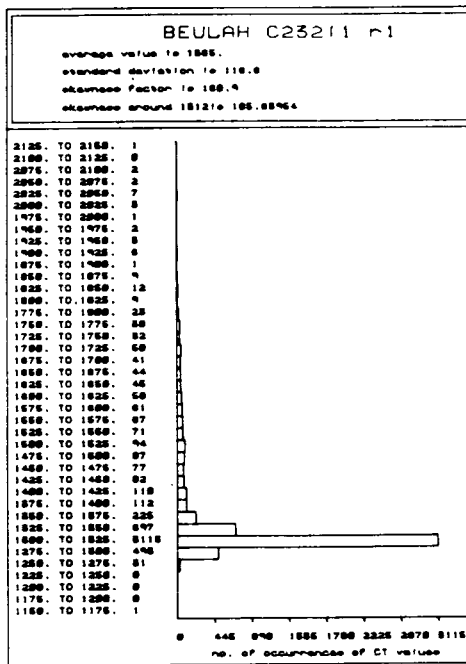
Figure 6-25. CT image of Beulah Zap coal (C232 L1)

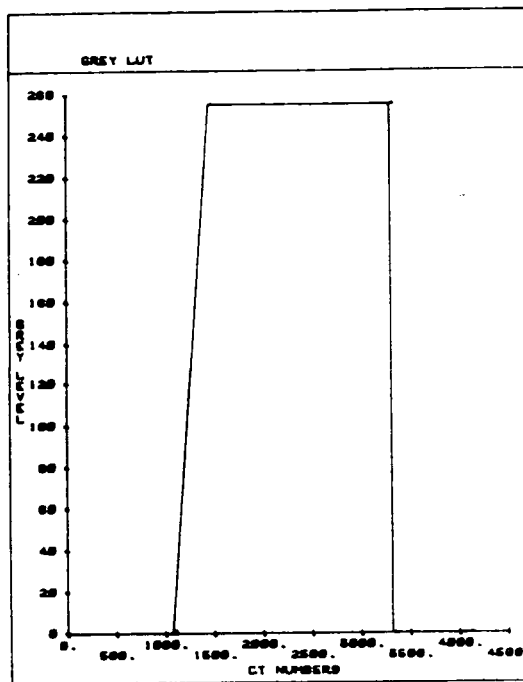**Figure 6-26. Histogram from Beulah Zap**

Figure 6-27. Grey scale Look-Up-Table used for the CT images
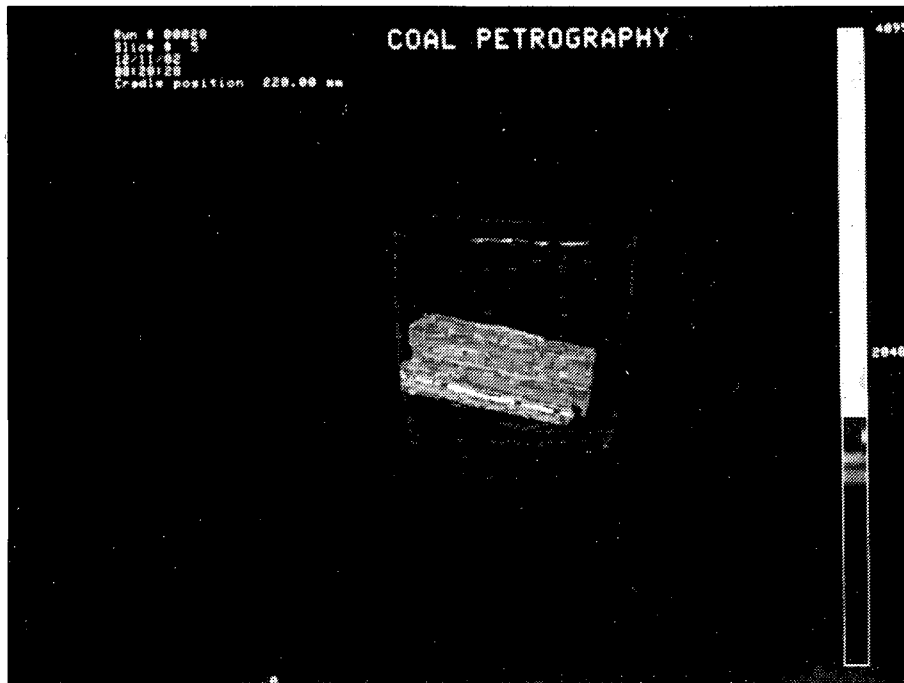
Figure 6-28a. CT image of Illinois #6 Coal at X1 magnification
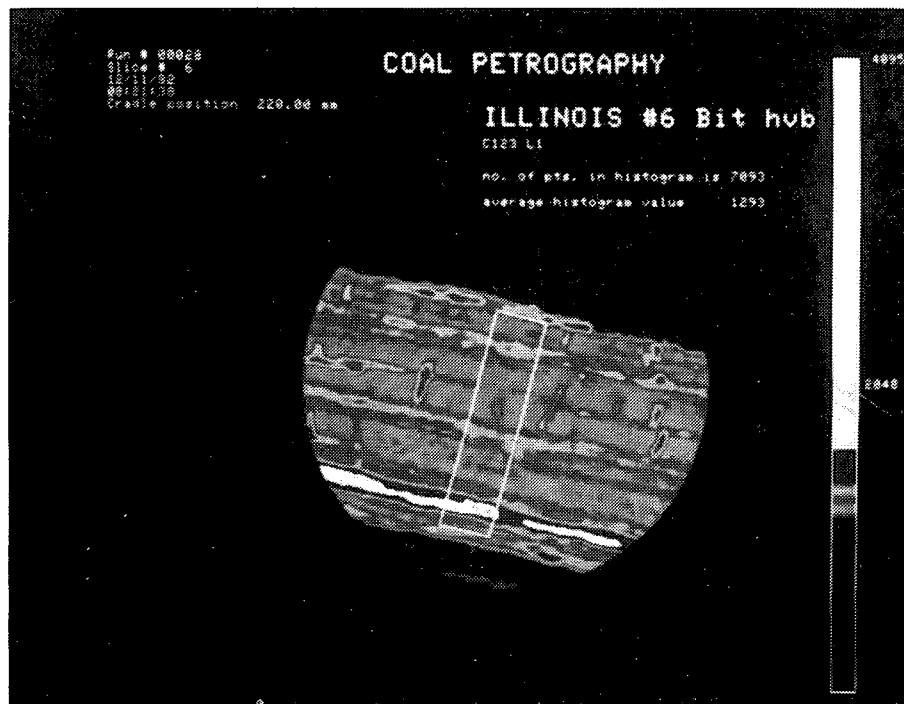
Figure 6-28b. CT image of Illinois #6 Coal at X3 magnification
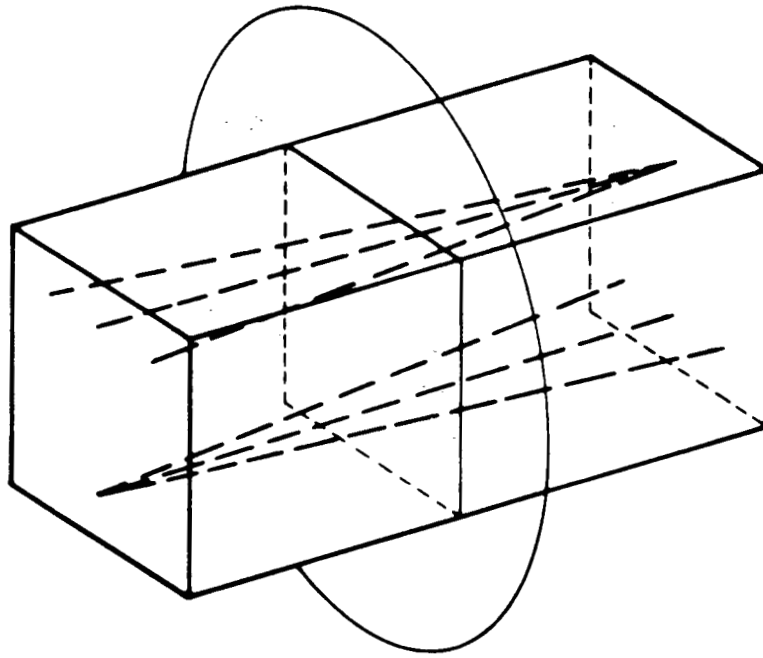
Figure 6-29. Schematic of block showing position of registration holes

OUTLINE OF
PLASTIC
BLOCK

CT PLANE

Figure 6-30. Nonsymmetric arrangement of registration holes
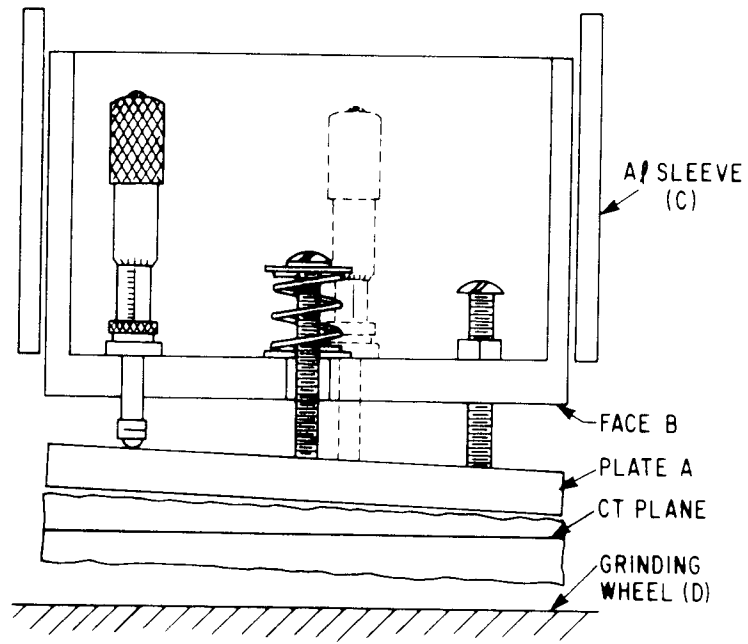
Figure 6-31. Schematic of grinding/polishing jig
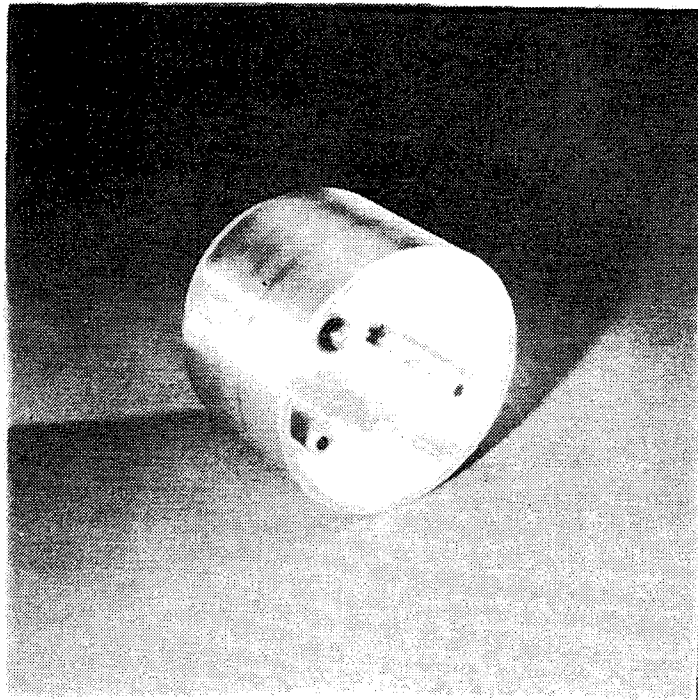
Figure 6-32. Coal slice in place on grinding/polishing jig

Figure 6-33. Exposed CT plane, Illinois #6 coal, Run 00016, Slice 9
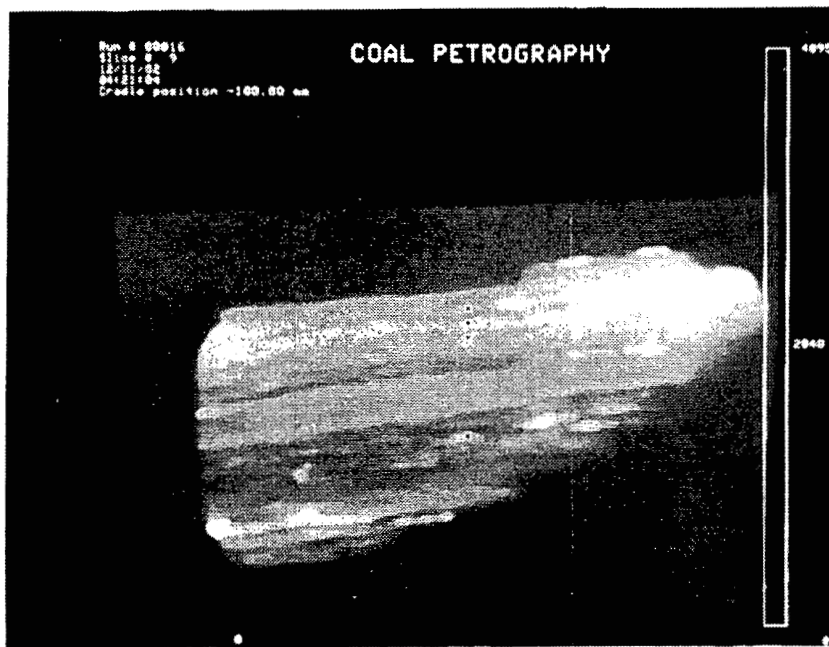
Figure 6-34. CT image, Run 00016, Slice 9

1. Thick vitrain (telocollinite)

2. Predominantly clay, quartz, inertinite (mainly semifusinite, inertro vitrinite) lesser vitrinite, exinite.
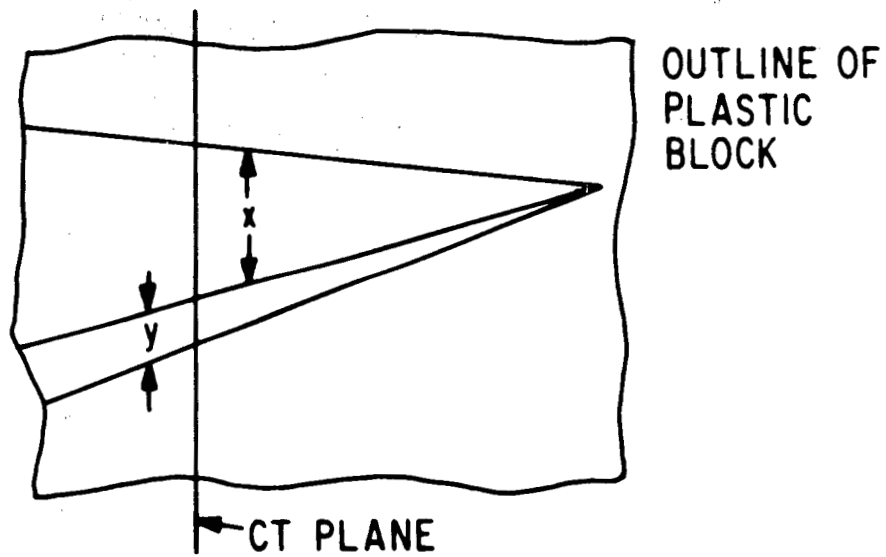
3. Inertinite, moderately high clay in quartz, desmo-collinite and sporinite.

4. Pyrite infilling of fusinite.

5. Pyrite

6. Vitrinite (telocollinite, desmo-collinite), inertinite, lesser amounts of clay, quartz and sporinite.

7. Large proportion of telocollinite.

8. Fusinite lenses with sone pyrite and carbonate infillings of lumens.

9. The dots are pyrite in telocollinite.

Figure 6-35a. Exposed CT plane, Pittsburgh #8 coal, Run 00028, Slice 12
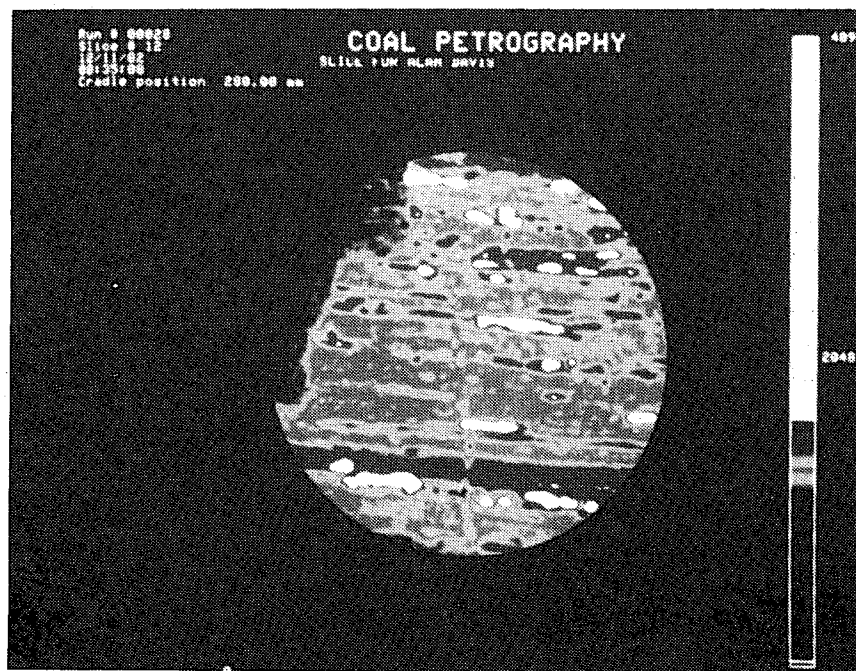
Figure 6-35b. CT image, Run 00028, Slice 12
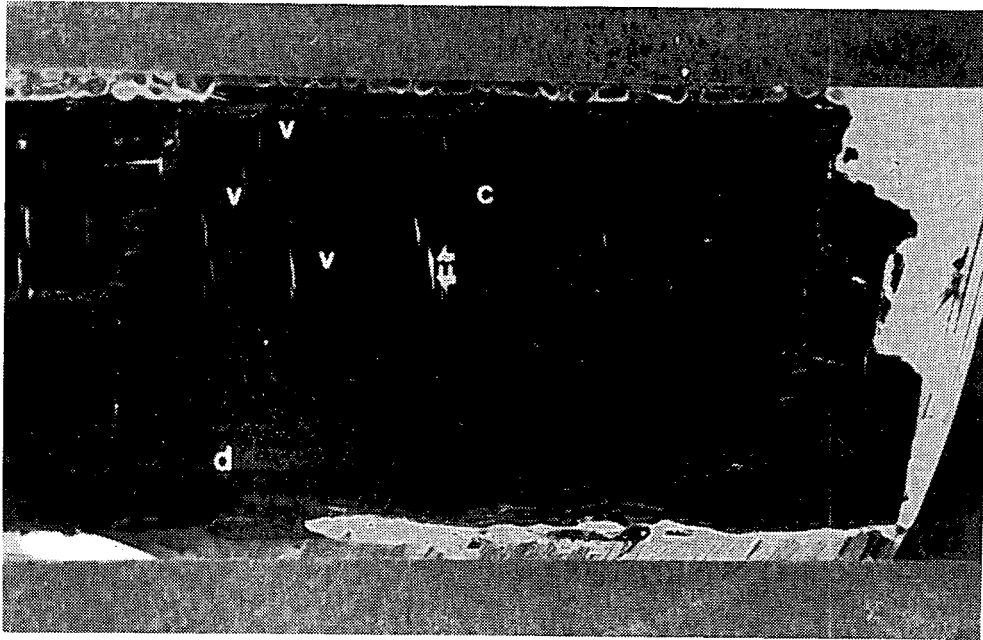
v Vitrain bands

p Pyrite bands

m Consists of clays, vitrinite quartz (lesser amounts of inertinite and pyrite)

d Consists mainly of clay minerals and vitrinite (lesser amounts of inertinite)

Figure 6-36a. Exposed CT plane, Illinois #6 coal, Run 00028, Slice 6

Figure 6-36b. CT image, Run 00028, Slice 6
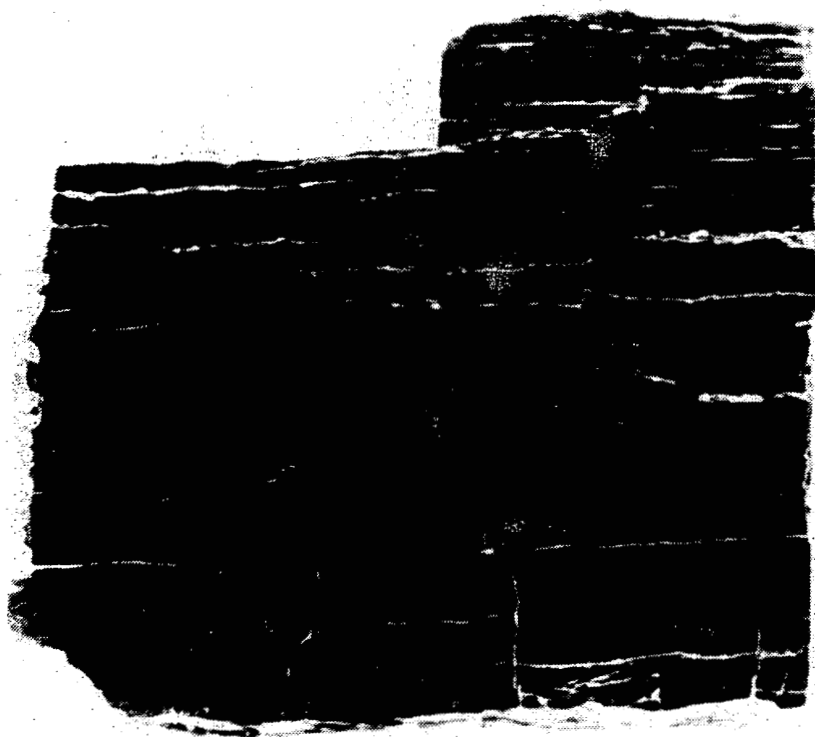
A Mainly telocollinite (a few with sporinite and cutinite)

B Vitrain band (telocollinite)

C Relatively much higher desmocollinite than in A, and far higher sporinite, fusinite and semifusinite (in lenses). More micrinite. Moderate telocollinite

Figure 6-37a. Exposed CT plane, Lower Kittanning (nonmarine), Run 00013, Slice 18
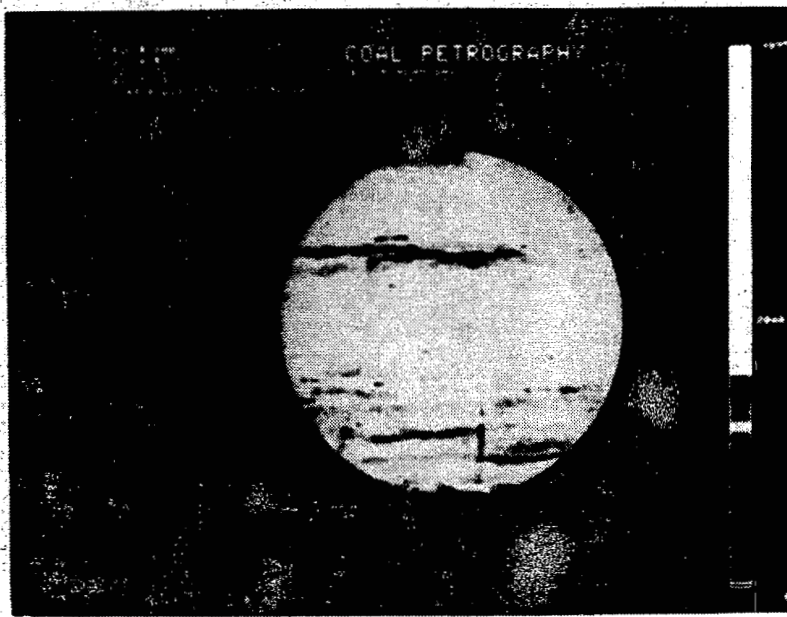
Figure 6-37b. CT image, Run 00013, Slice 18

Figure 6-38a. Polished coal surface
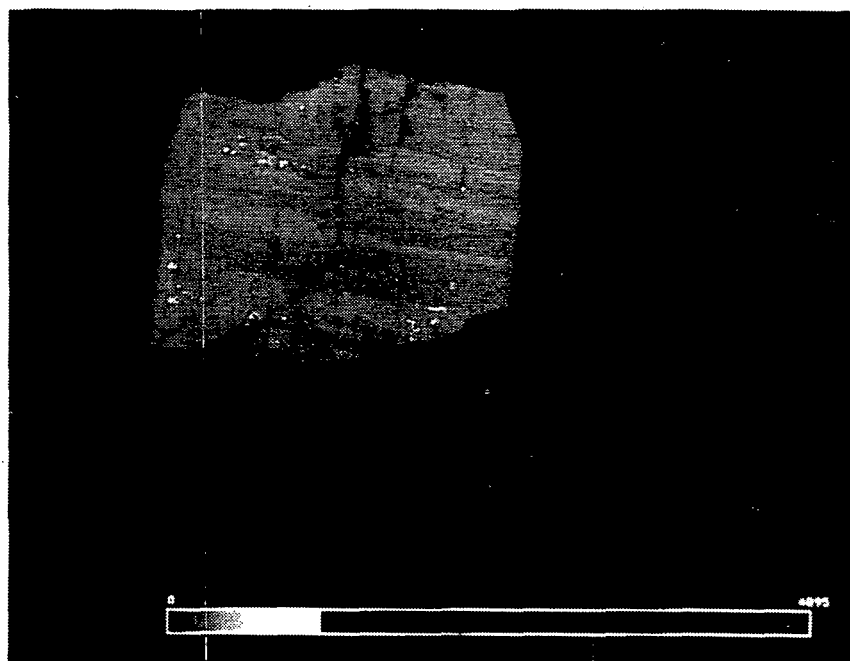
Figure 6-38b. Reflectance map of coal surface shown above
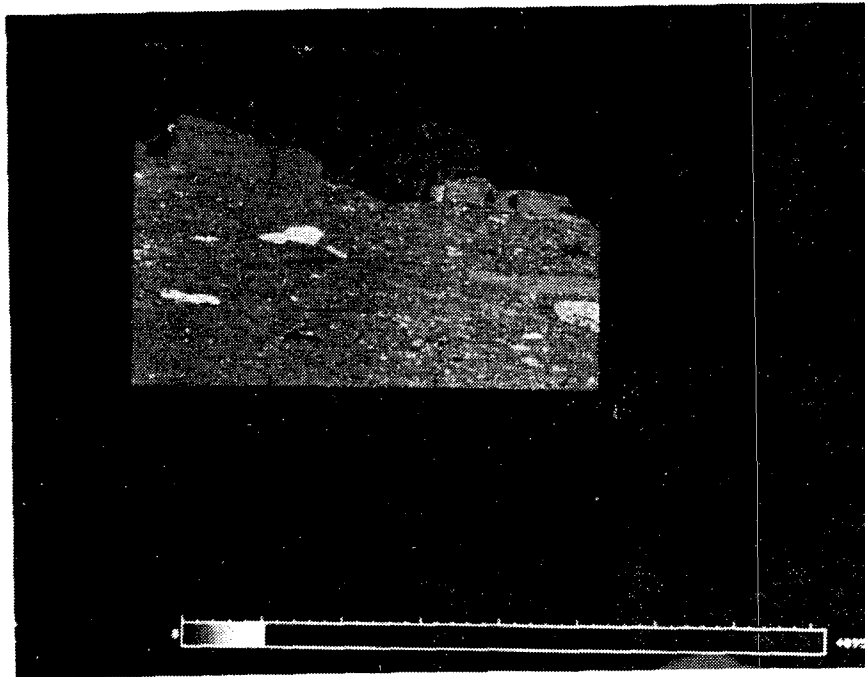
Figure 6-39. Reflectance map of Navajo coal
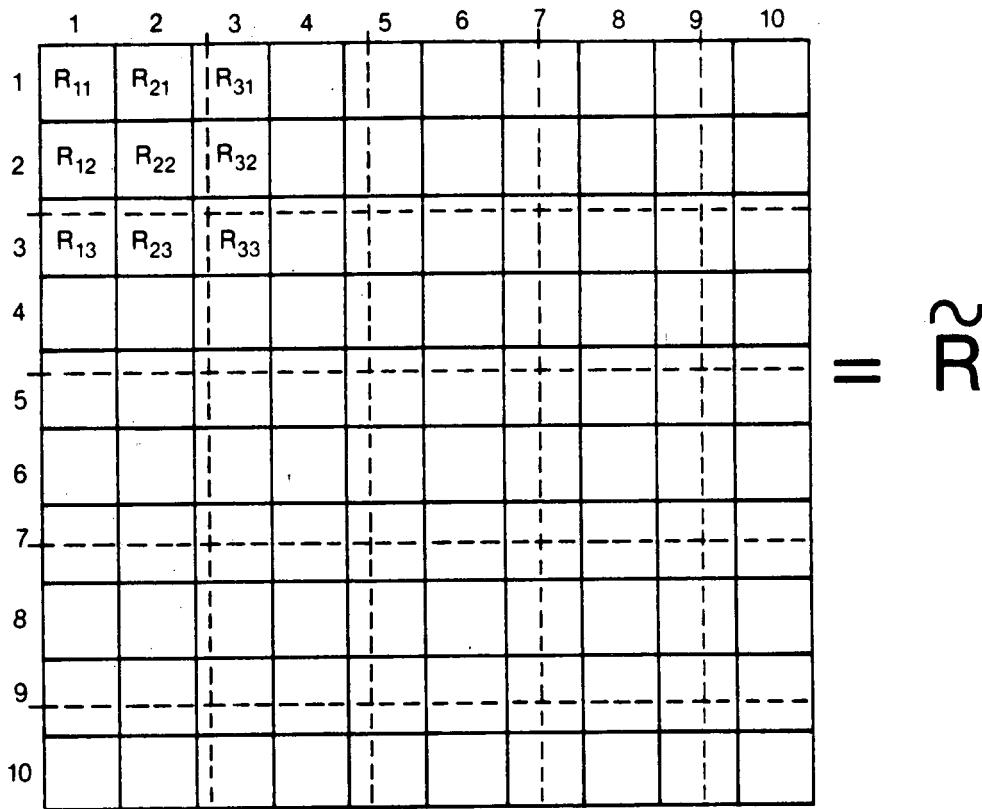
Remap, scale = 2.15
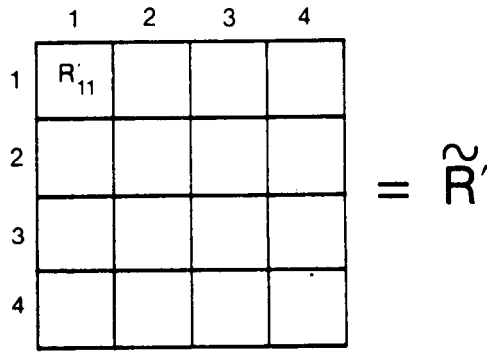
$$R'_{11} = [R_{11} + R_{21} + 0.15\,R_{31}$$
$$+ R_{12} + R_{22} + 0.15\,R_{32}$$
$$+ 0.15\,R_{13} + 0.15\,R_{23} + (0.15)^2\,R_{33}] \div (2.15)^2$$

Figure 6-40. Pixel Mapping for Rescaling Image
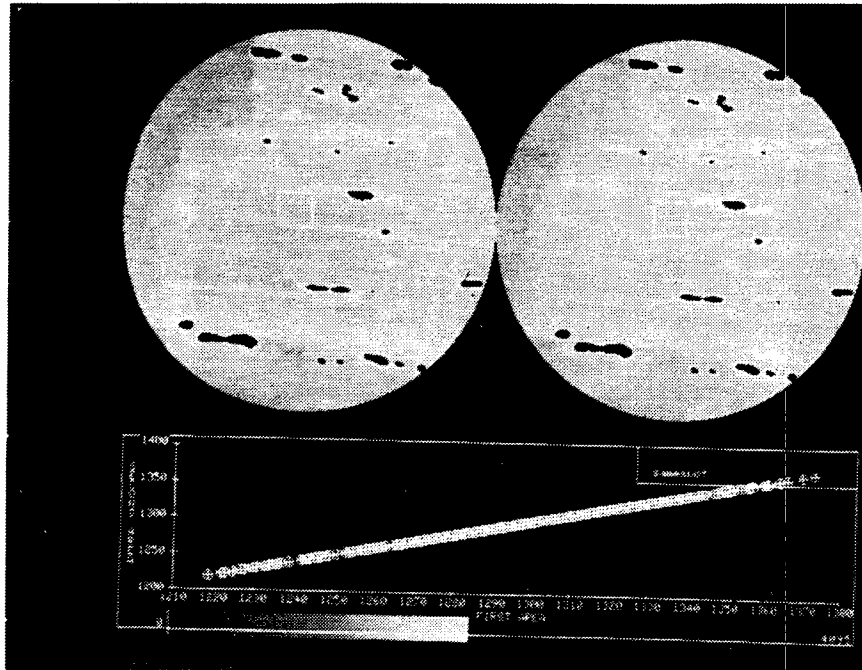
Figure 6-41. Comparison of CT values within identical squares
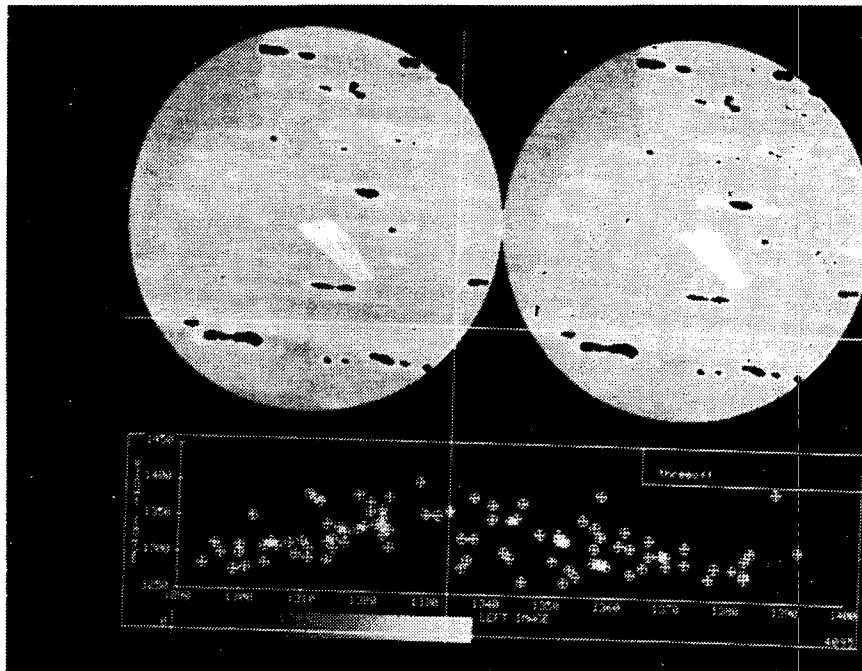
Figure 6-42. Comparison of CT values within identical squares but with an offset of six pixels
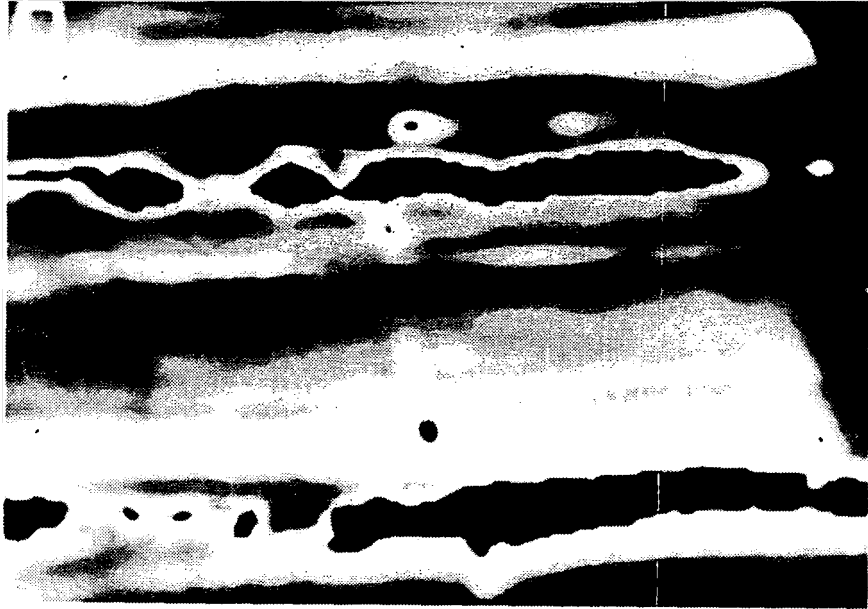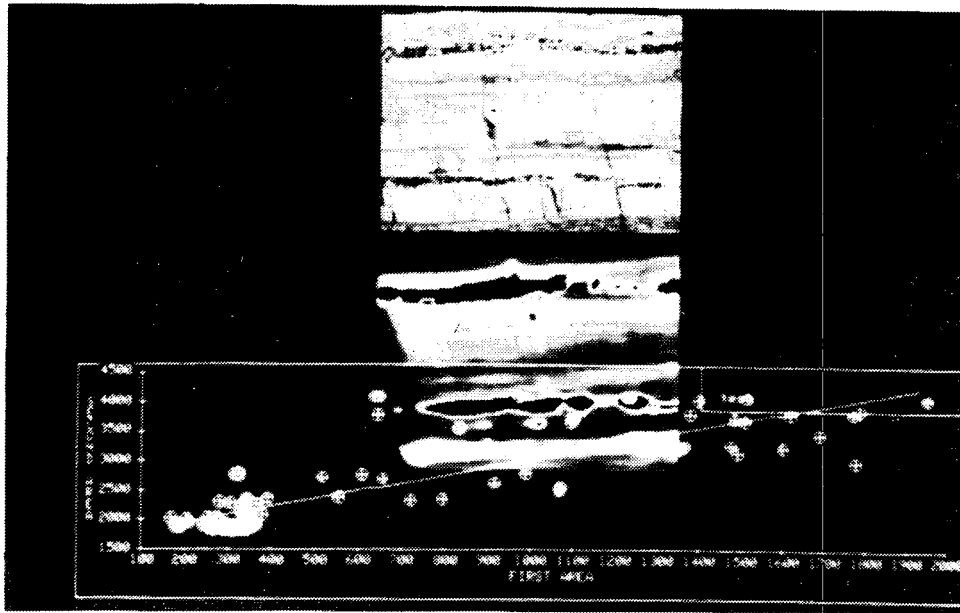
Figure 6-44. Pixel image comparison between a square on the reflectance map (top), and CT image (bottom). Coal is Lower Kittanning (nonmarine).
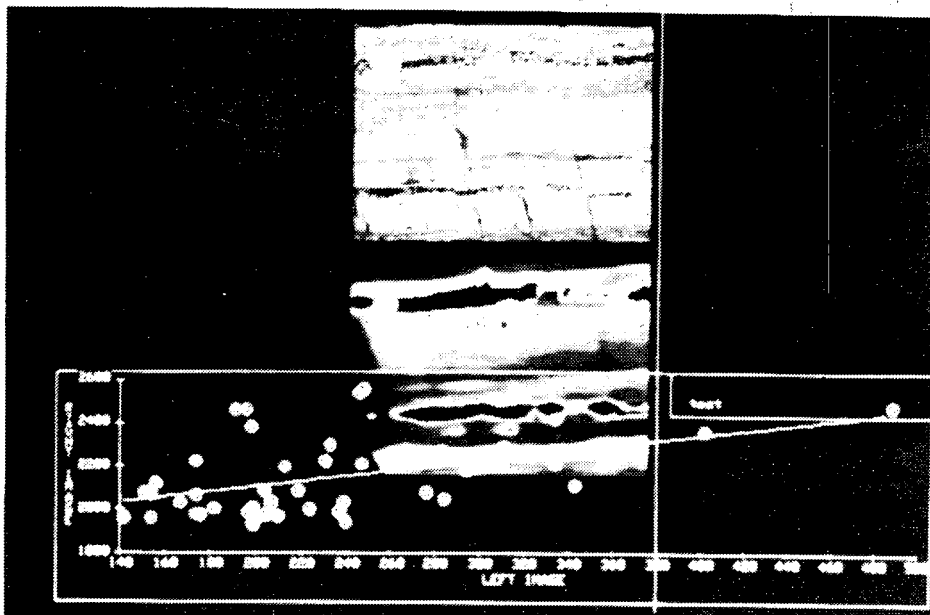
Figure 6-45. Pixel value comparisons between arbitrary shapes in the same two images used in Figure 6-44
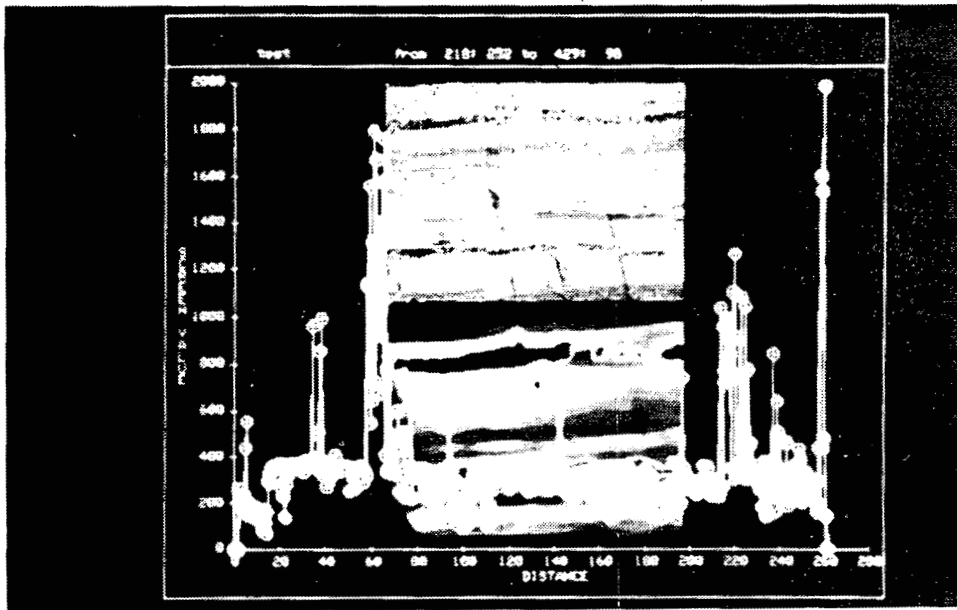
Figure 6-46. Pixel value along line drawn on reflectivity map
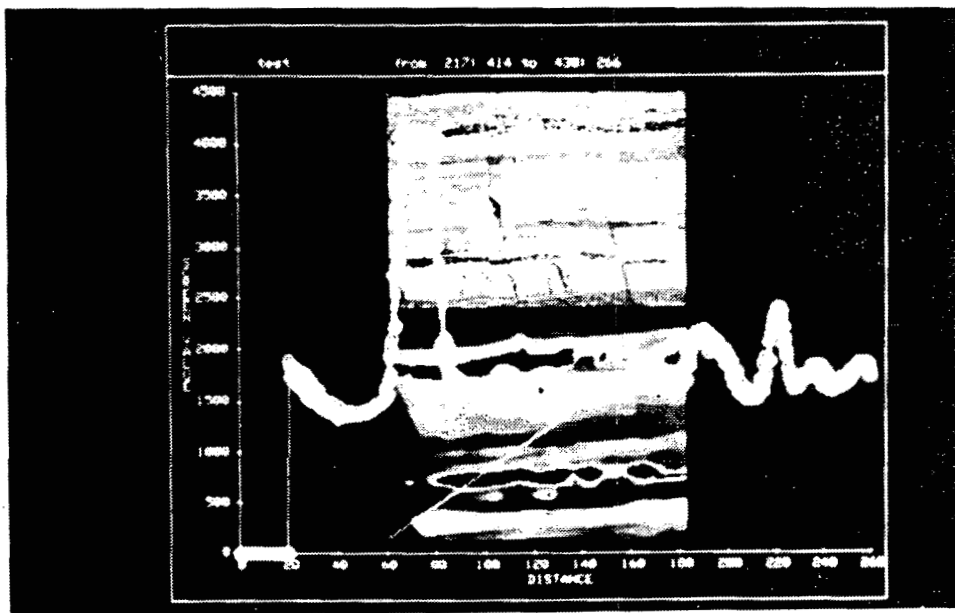
Figure 6-47. Pixel value along line on CT image. The position of the line relative to the image is the same as in Figure 6-45.
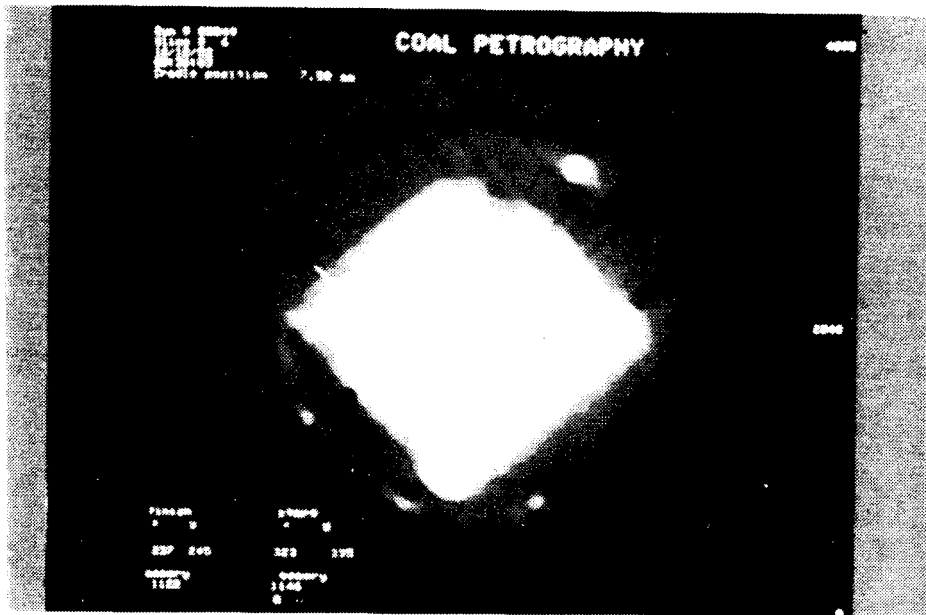
Figure 6-48. CT image of Illinois #6 coal with a line drawn for mineral comparisons

CT Numbers Along the Line
Drawn in Figure 4a
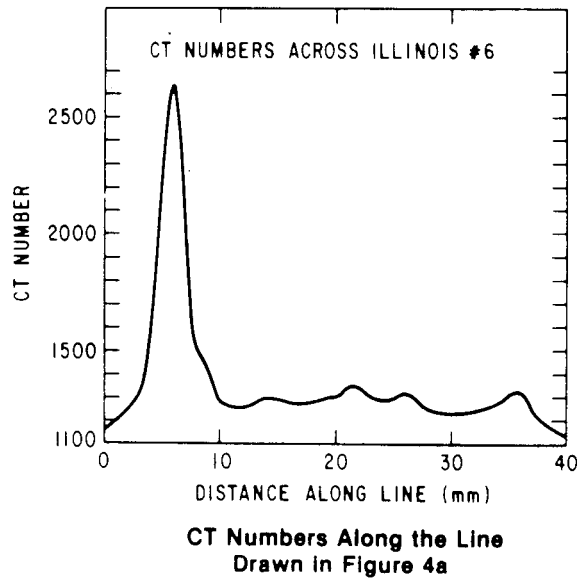
Figure 6-49. CT numbers along the line drawn in Figure 6-48
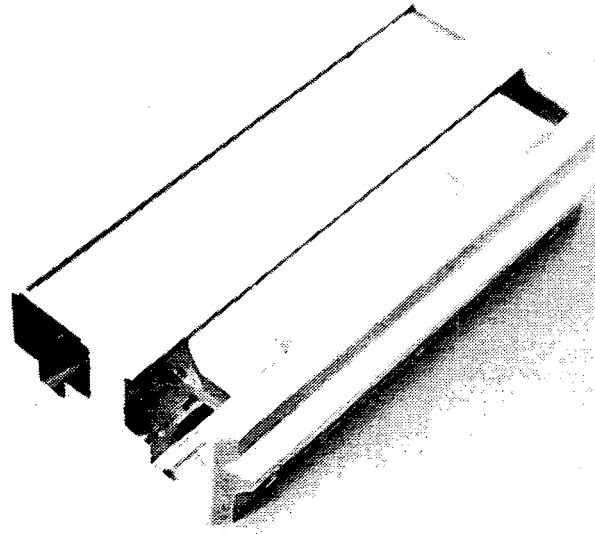
Figure 6-50. Coal holder for SEM microscope scans
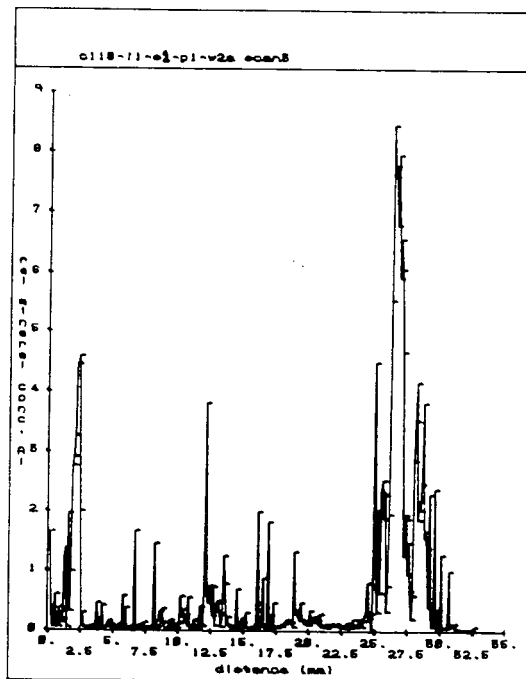
Figure 6-51. Aluminum scan on Illinois #6 coal
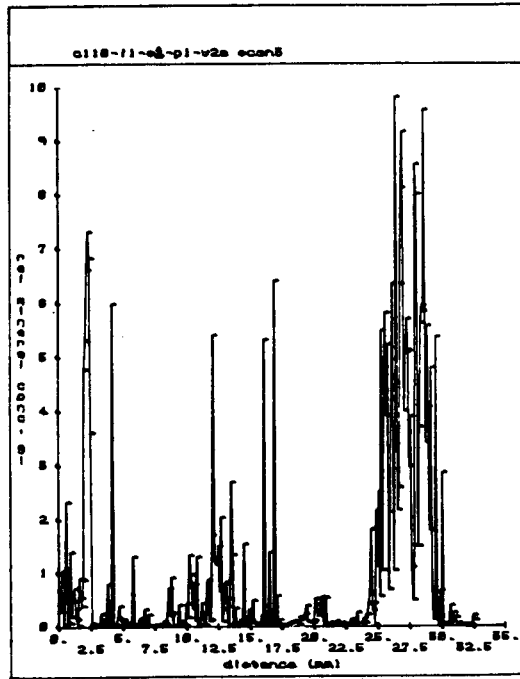
Figure 6-52. Silicon scan on Illinois #6 coal
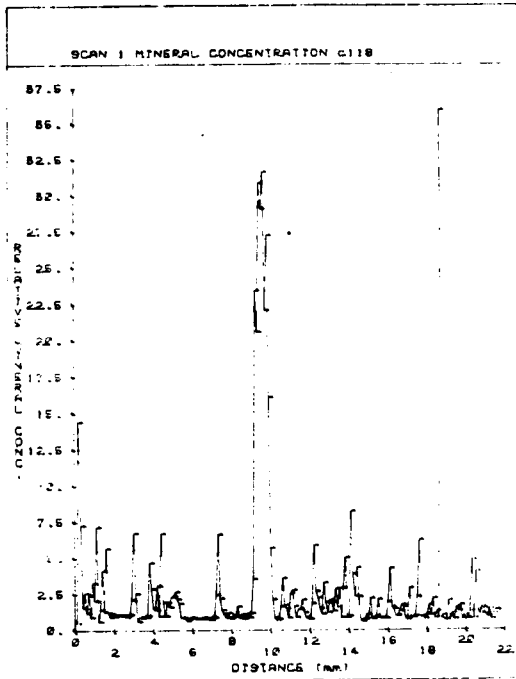
Figure 6-53. Microprobe Scan 1
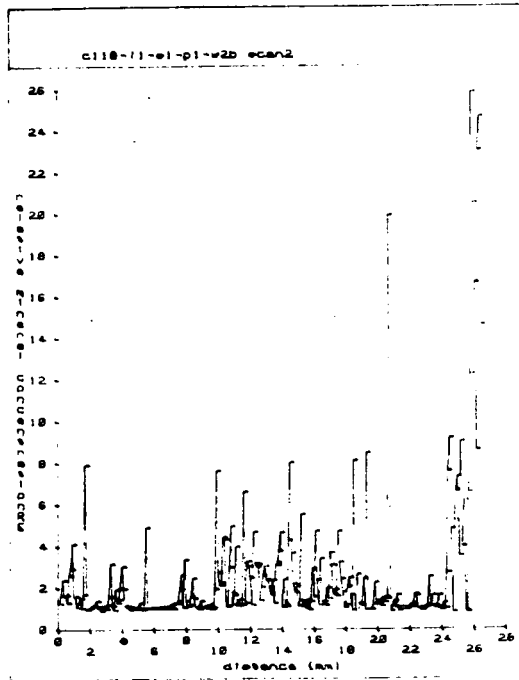
Figure 6-54. Microprobe Scan 2
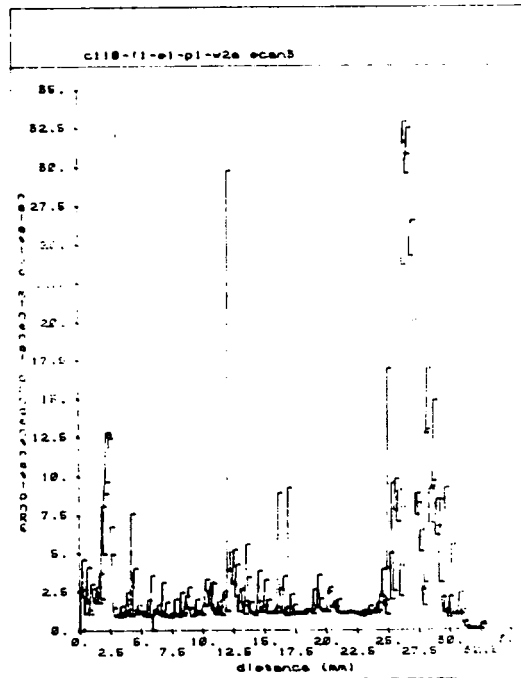
Figure 6-55. Microprobe Scan 3
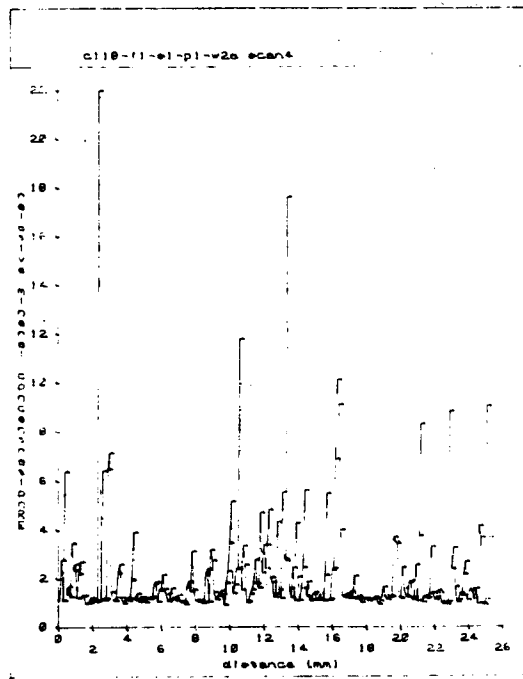
Figure 6-56. Microprobe Scan 4
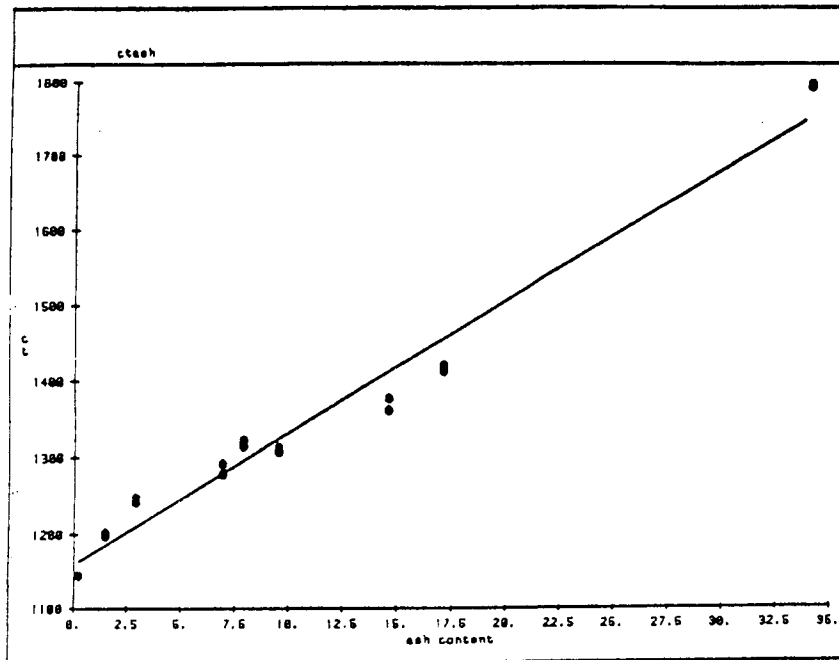
Figure 6-57. Comparison of CT values with ash content
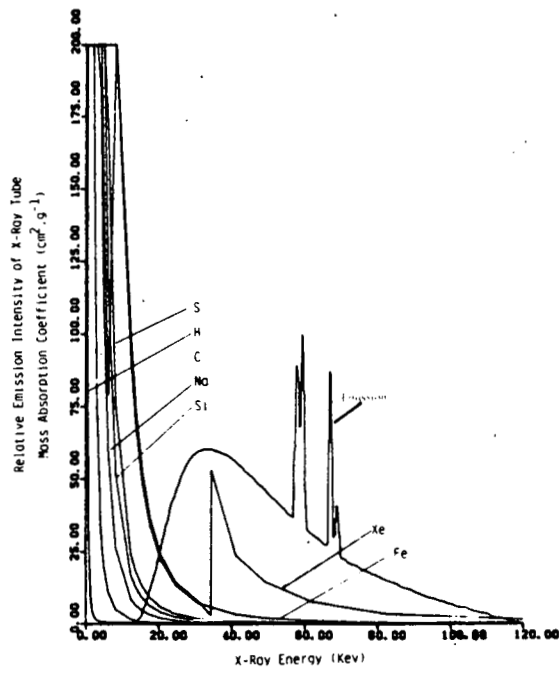
Figure 6-58. X-ray mass absorption coefficients for common coal elements and for xenon; x-ray tube emission curve
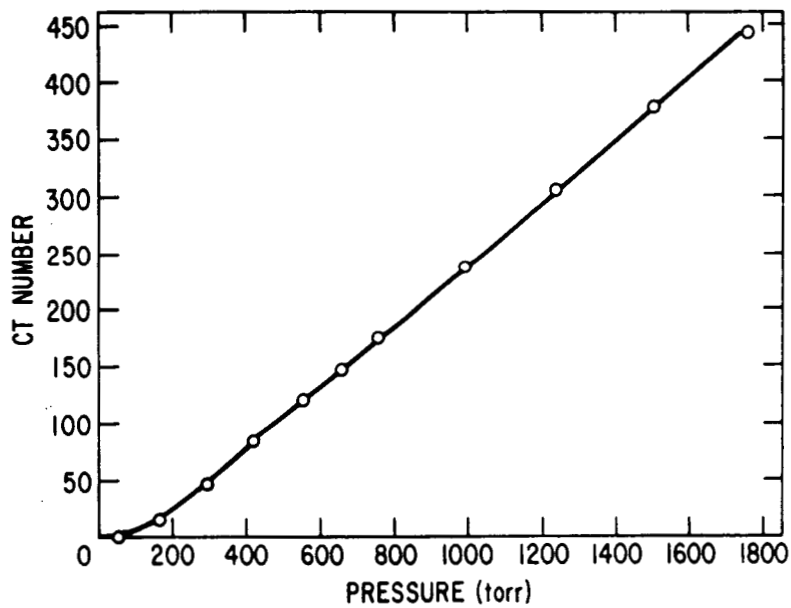
Figure 6-59. CT number as a function of xenon gas pressure
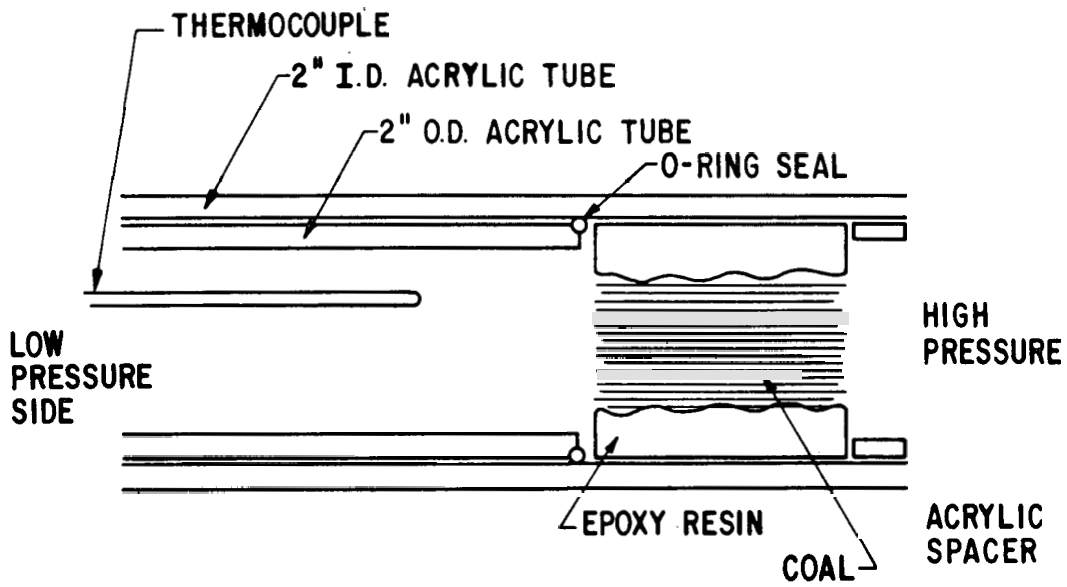
Figure 6-60. Schematic of xeon diffusion apparatus
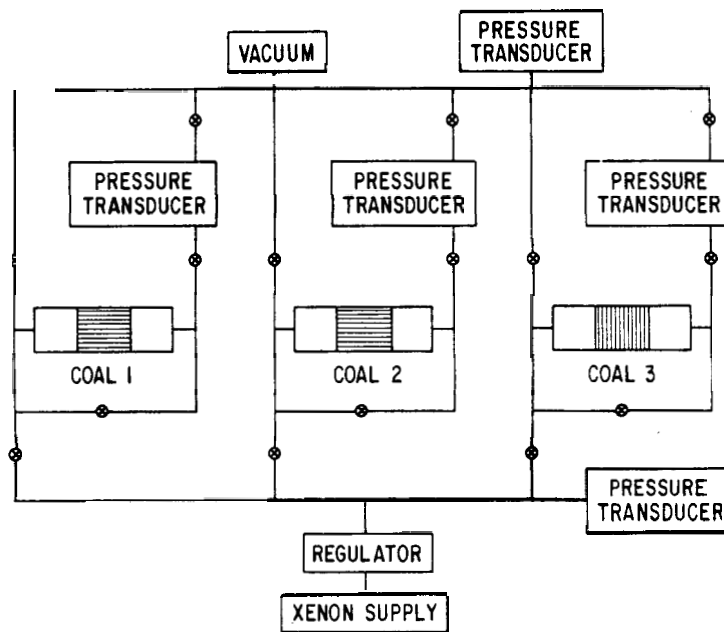
Figure 6-61. Schematic of gas connections in the xenon apparatus

VESSEL 2 PRESSURE HISTORY
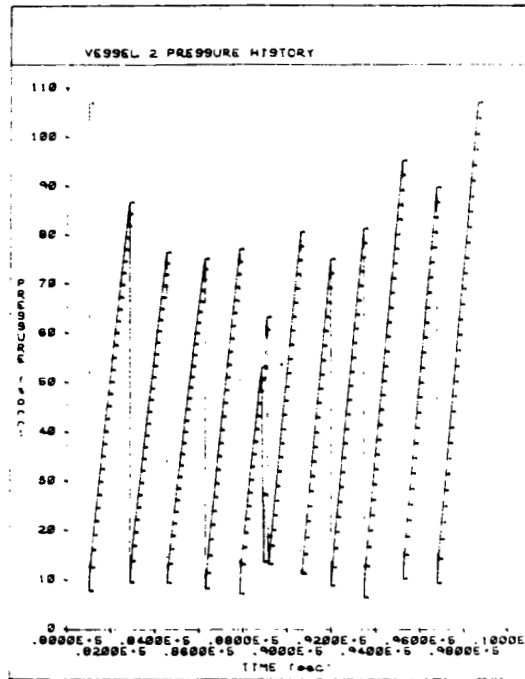
Figure 6-62. Pressure history for vessel #2

6-69
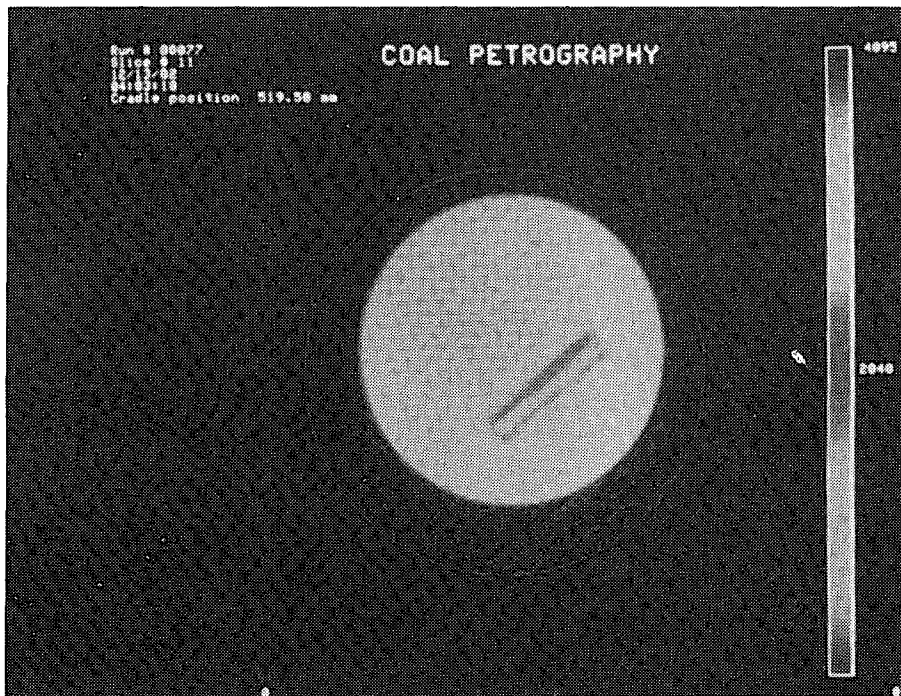
Figure 6-63. CT images showing change in position of CT image within computer zone of reconstruction
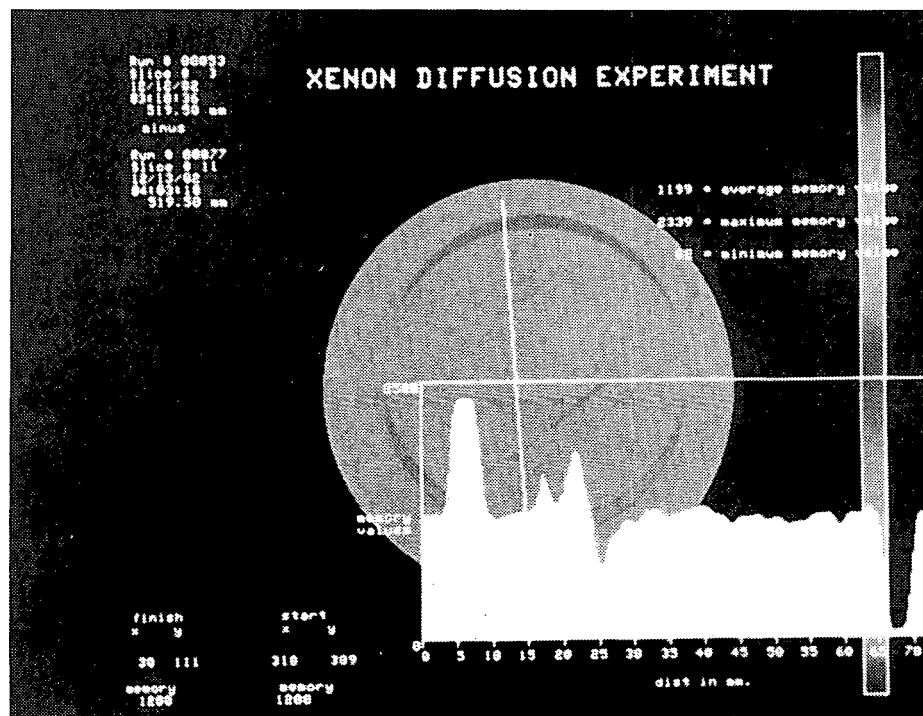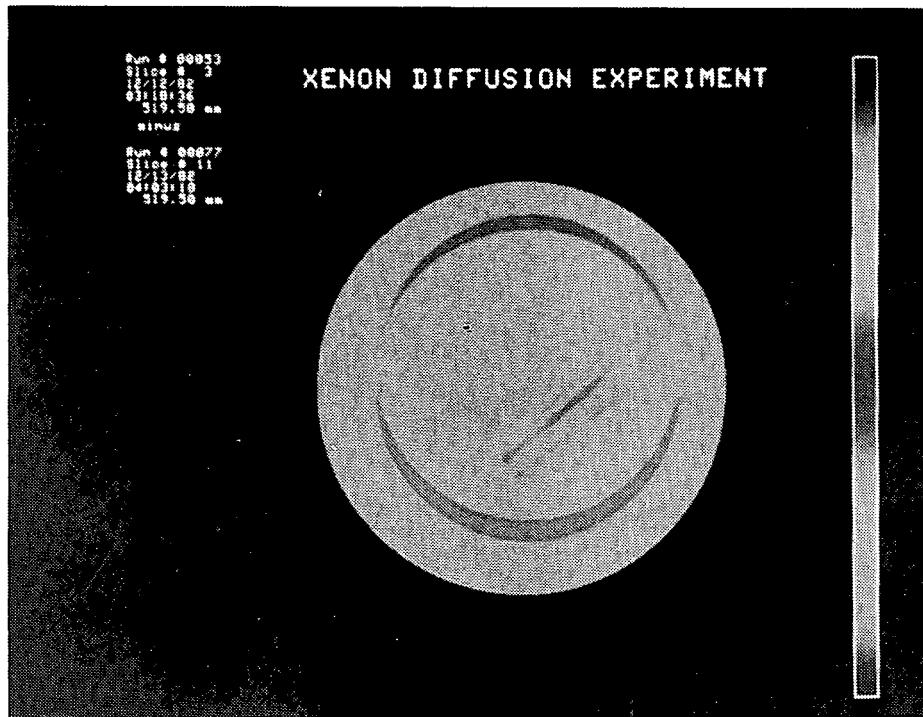
Figure 6-64. Artifact crescents caused by subtraction of misaligned images
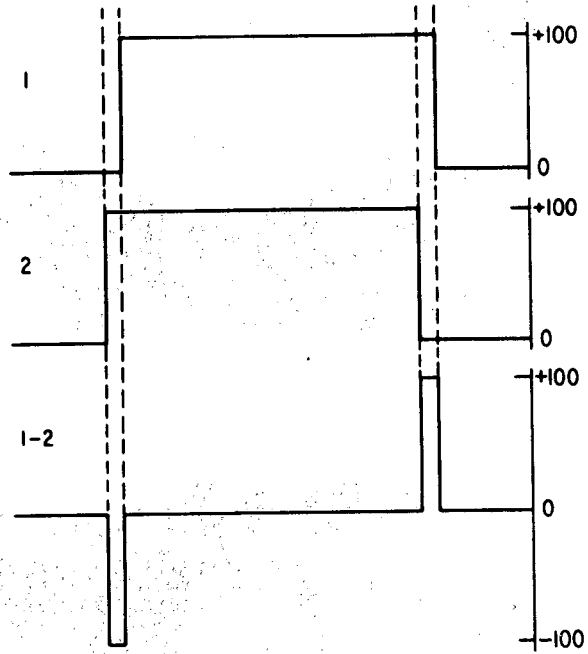
Figure 6-65. Origin of difference artifacts caused by image misalignment
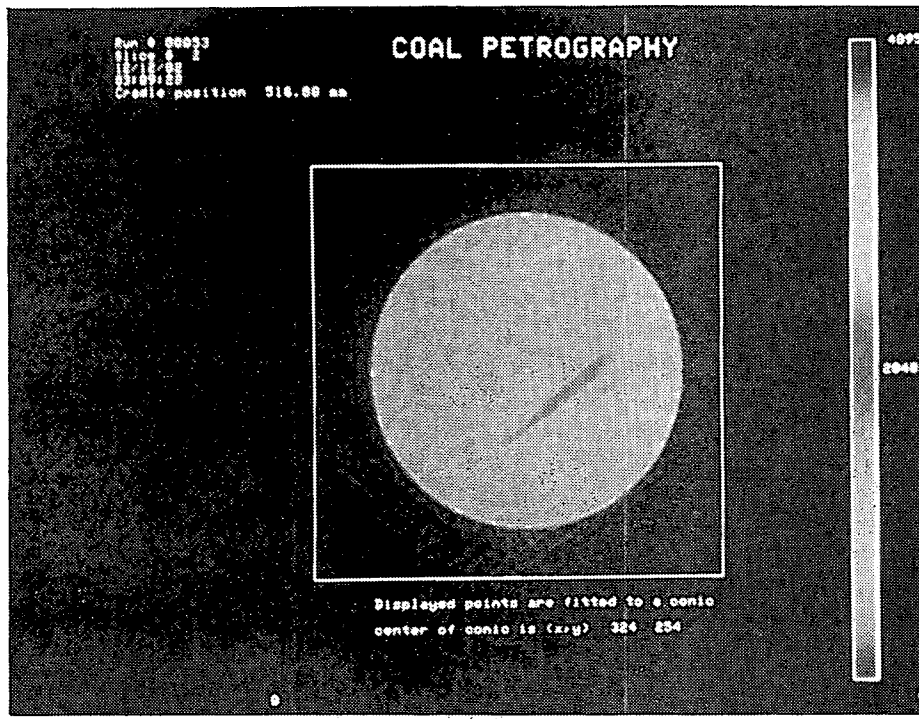
Figure 6-66a. CT image of acrylic tube with peripheral points
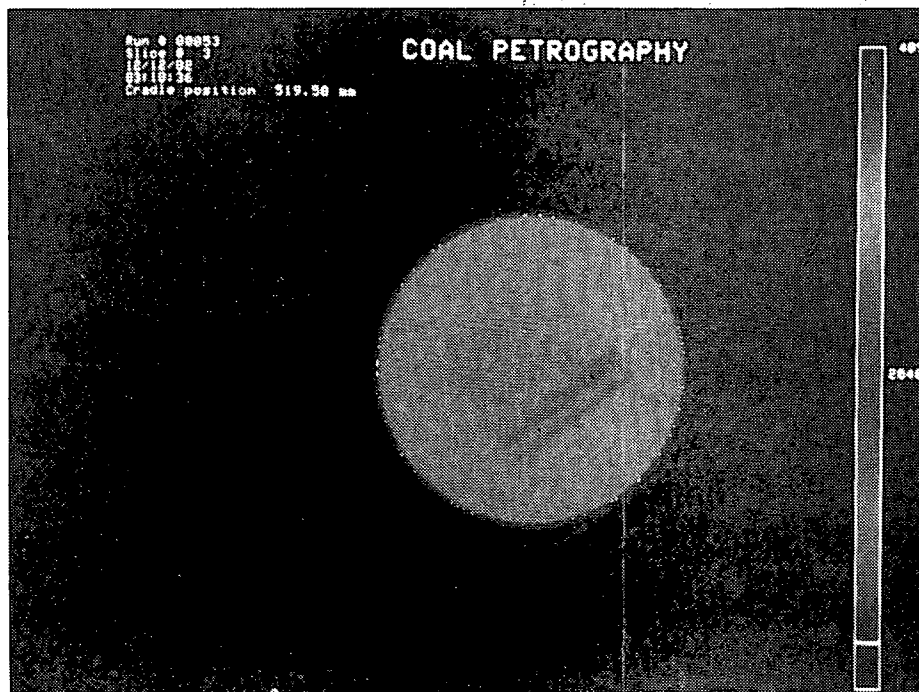
Figure 6-66b. Center of circle in CT image calculated from highlighted points
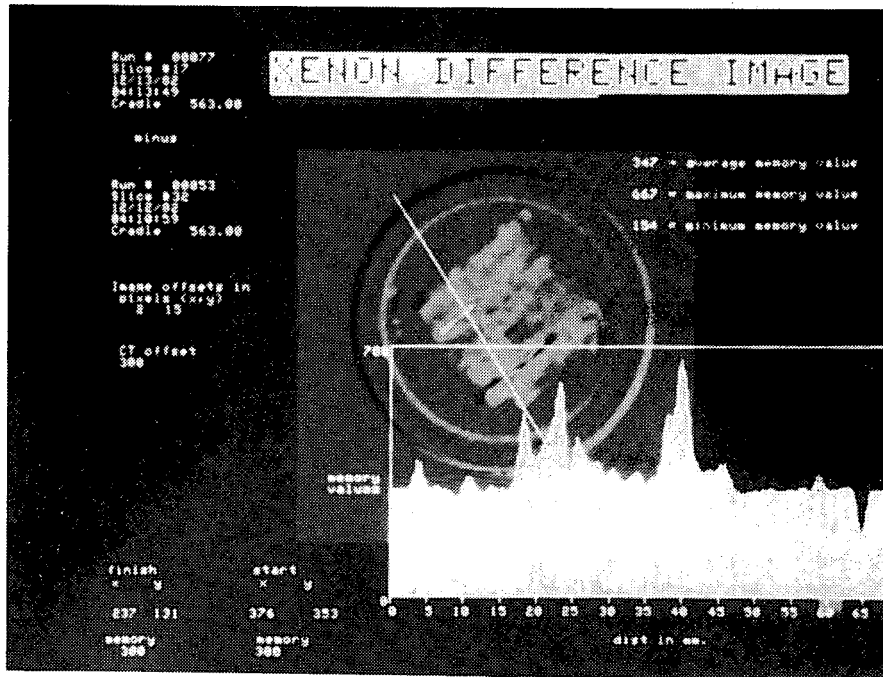
Figure 6-67. Xenon difference image with CT values along a line
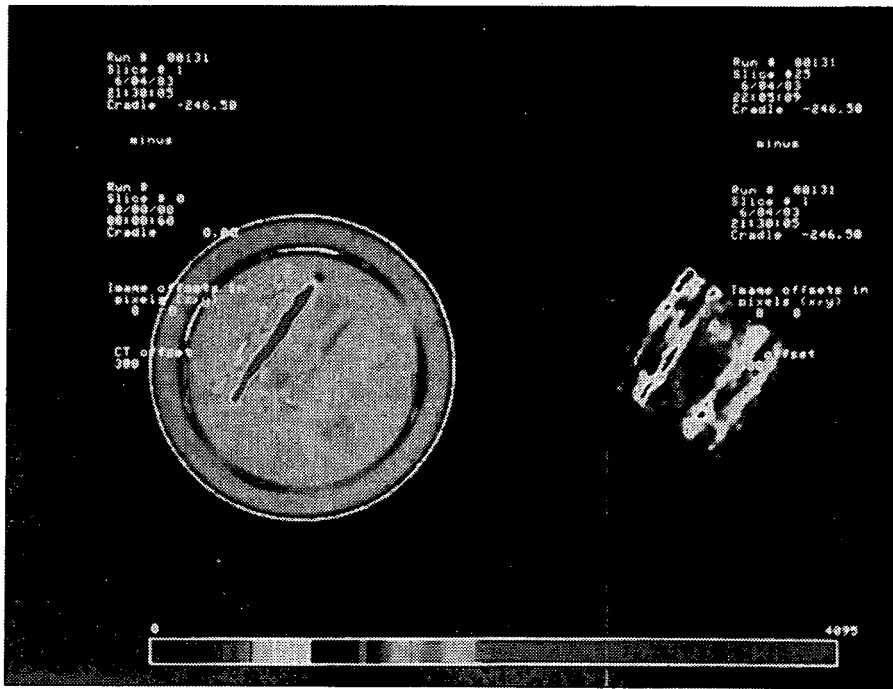
Figure 6-68. CT image of coal (left) and xenon difference image (right)
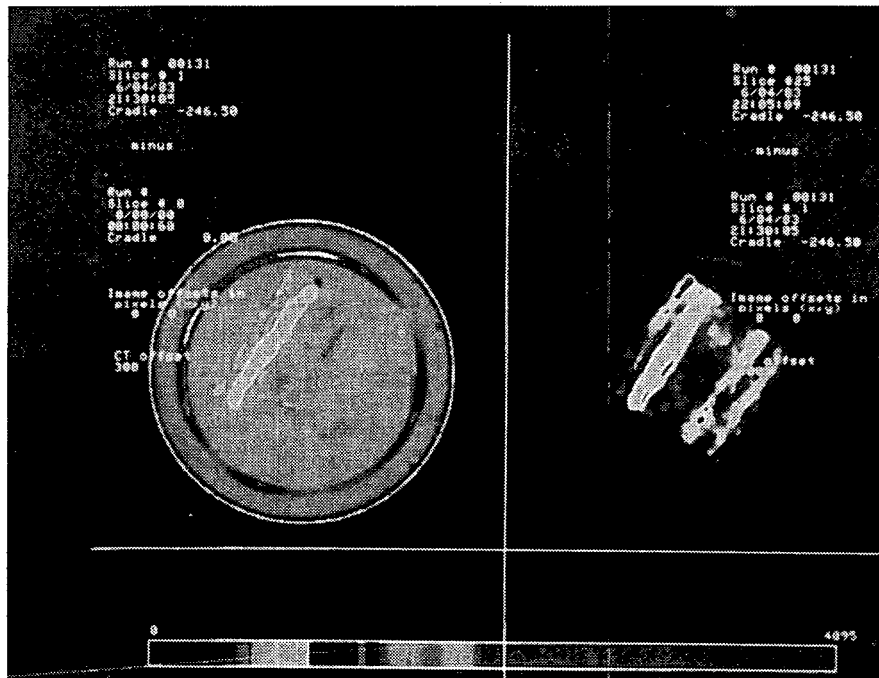
Figure 6-69. White polygon drawn on left image and applied to right image
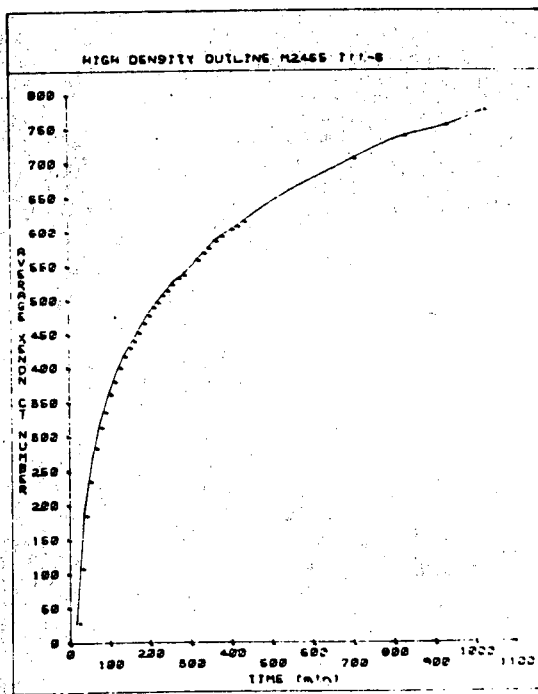
Figure 6-70. Xenon penetration into Illinois #6 coal
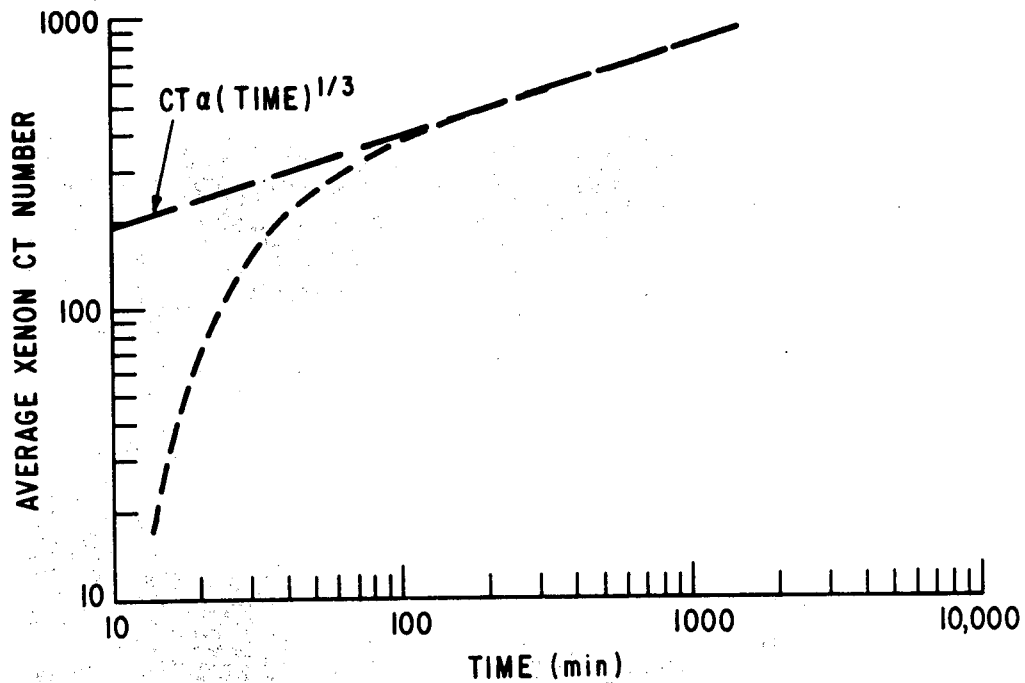
FULL LOG PLOT OF CT NUMBER AGAINST TIME
FOR HIGH DENSITY REGION OF m2465

Figure 6-71. Log-log plot of CT number against time for xenon infusion
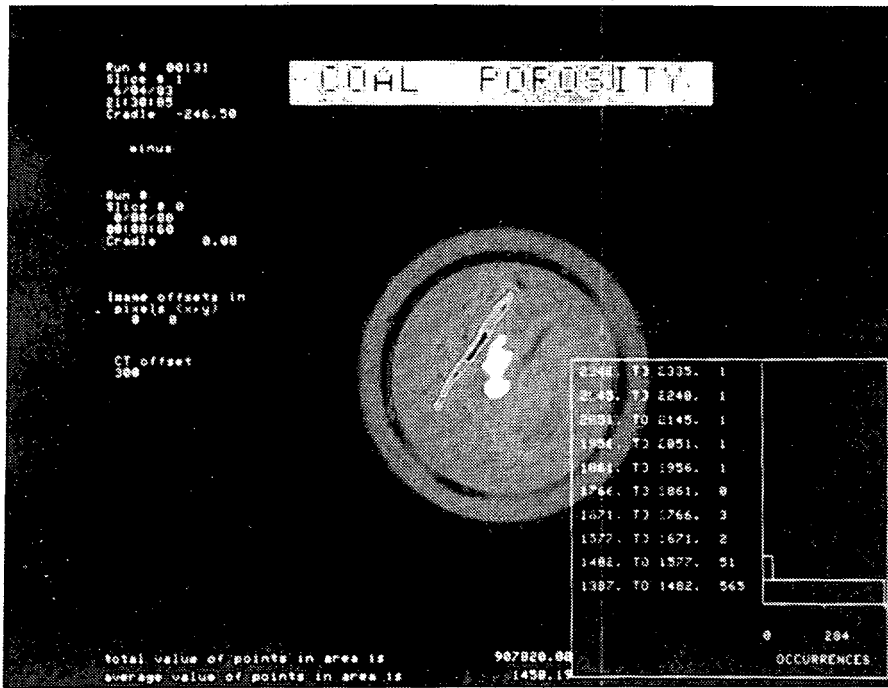
Figure 6-72. Low-density region outline on CT image
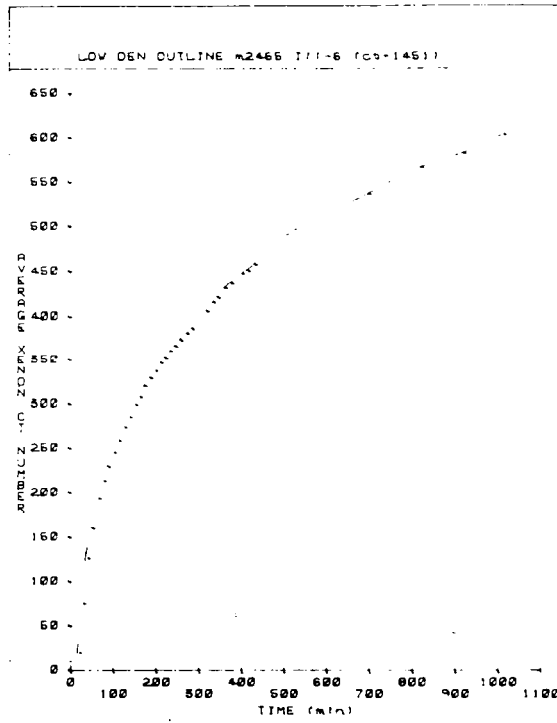
Figure 6-73. Xenon penetration of low-density region of Illinois #6 against time
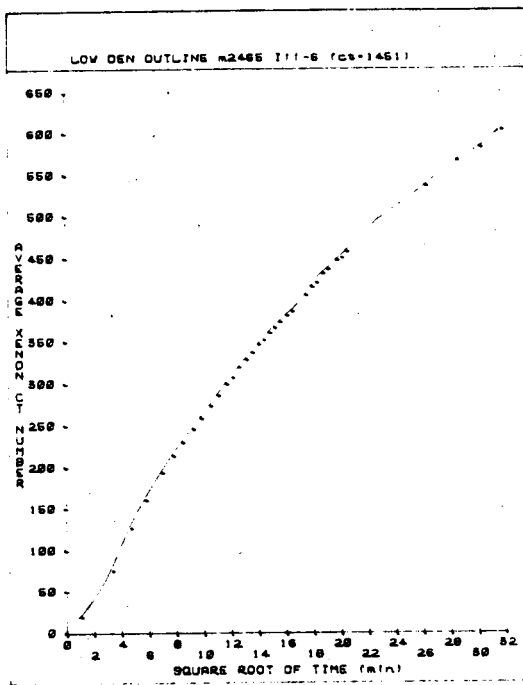
Figure 6-74. Data of Figure 6-73 plotted against the square root of time
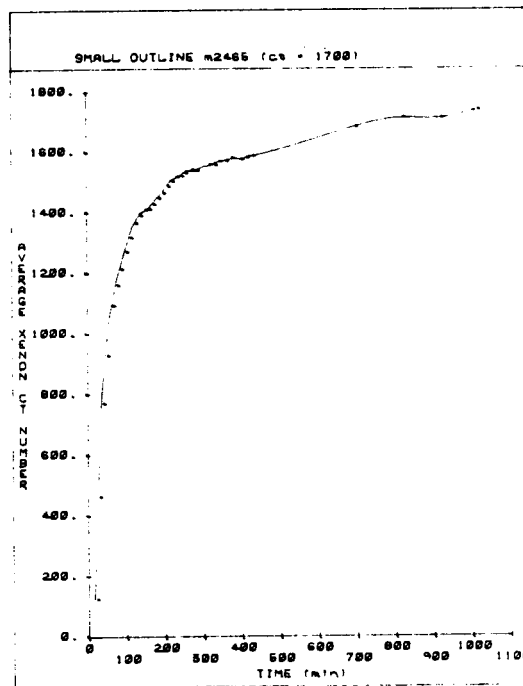
Figure 6-75. Xenon pentration as a function of time for a high penetration region

Figure 6-76. Xenon difference image at 0 min, parallel bedding planes

Figure 6-77. Xenon difference image at 24 min, parallel bedding planes
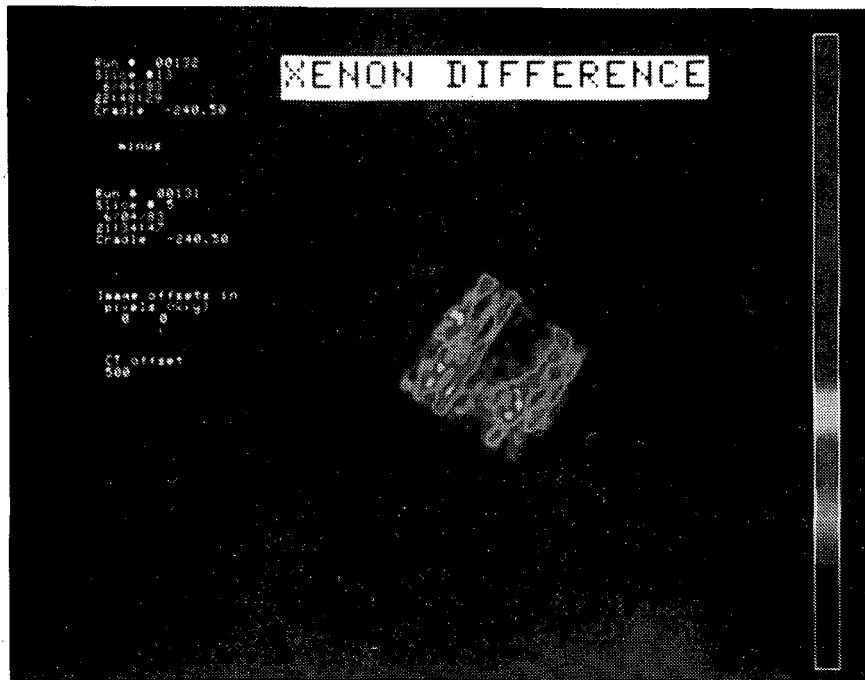
Figure 6-78. Xenon difference image at 74 min, parallel bedding planes

Figure 6-79. Xenon difference image at 122 min, parallel bedding planes
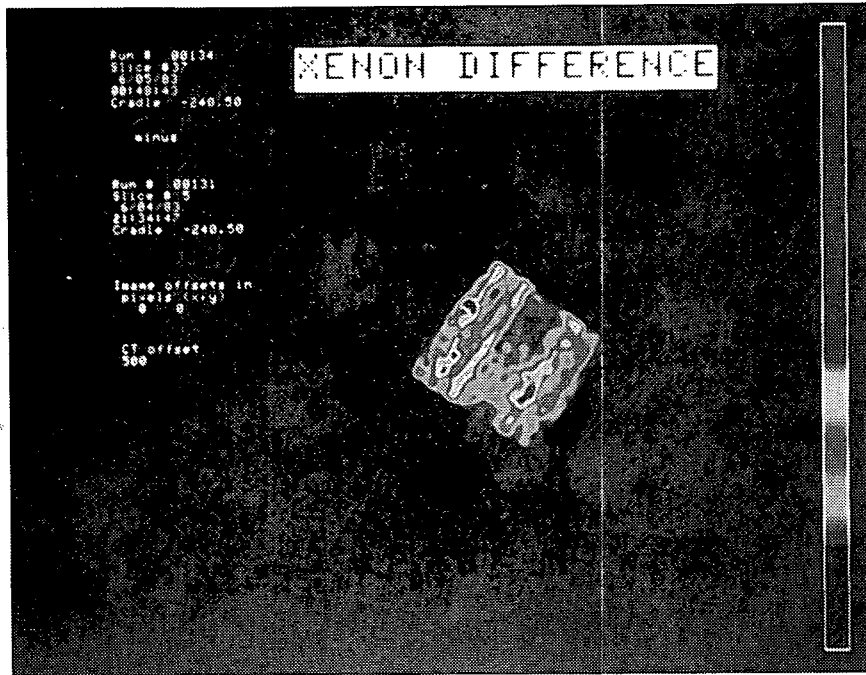
Figure 6-80. Xenon difference image at 194 min, parallel bedding planes
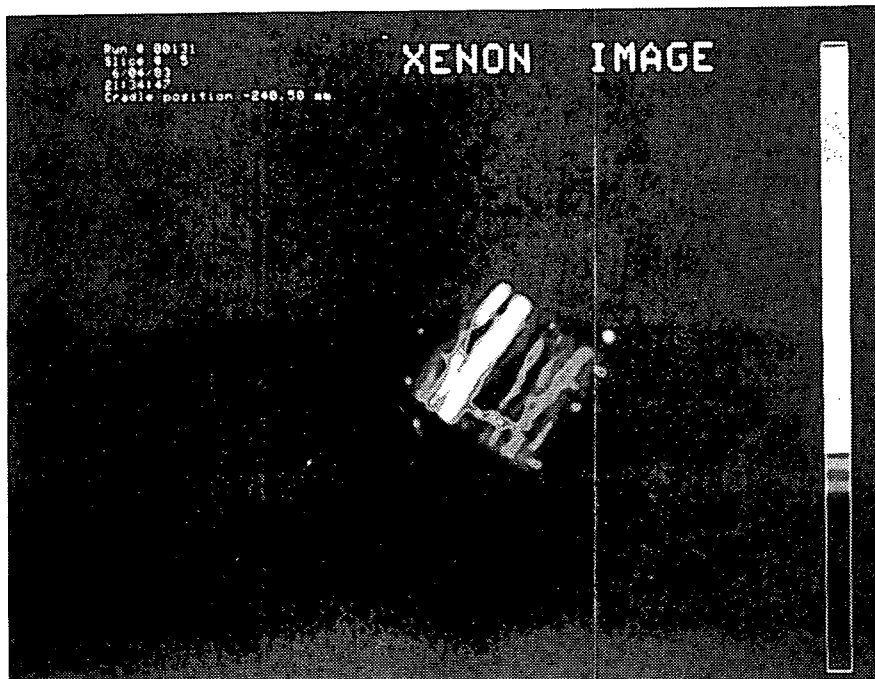
Figure 6-81. CT image of coal before xenon penetration
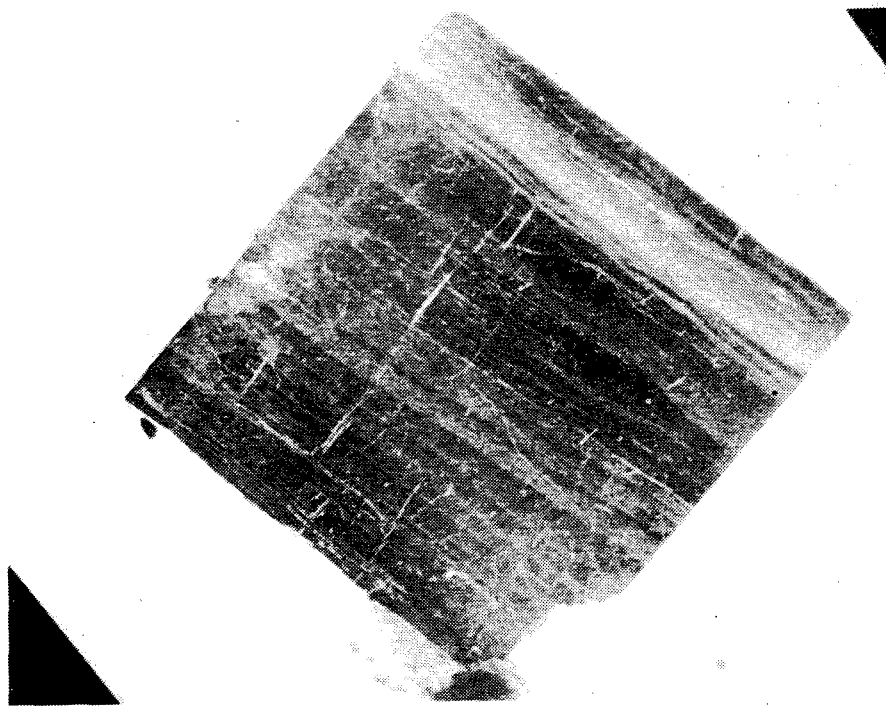
Figure 6-82. Optical picture of coal plane near the CT plane imaged in Figure 6-81
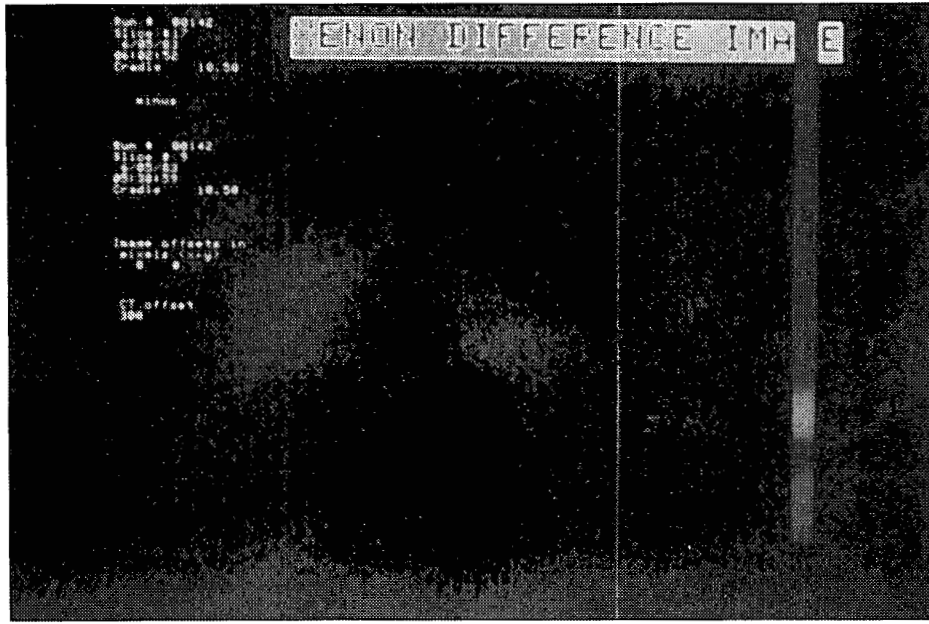
Figure 6-83. Xenon difference image at 0 min, perpendicular bedding planes
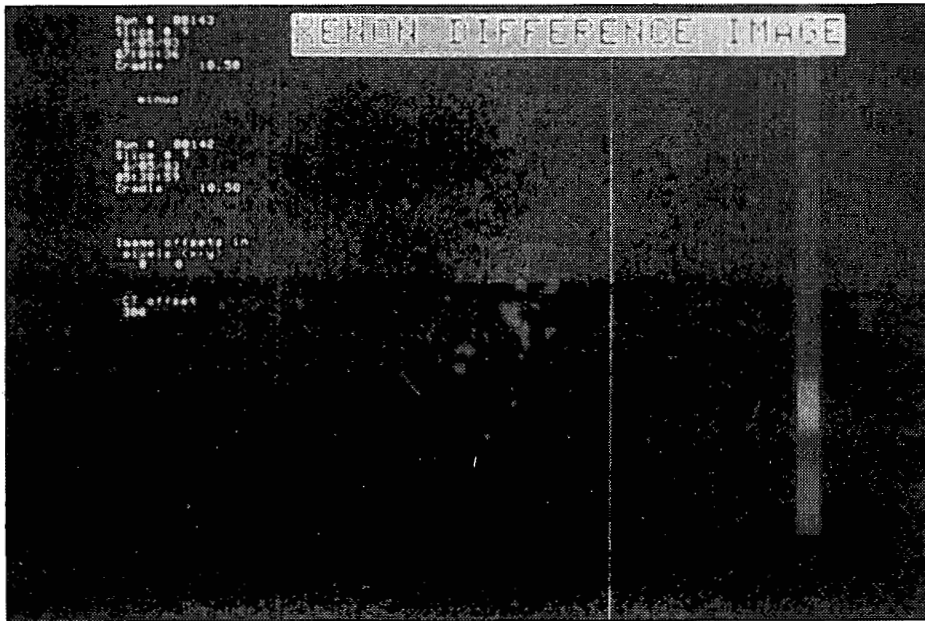
Figure 6-84. Xenon difference image at 60 min, perpendicular bedding planes
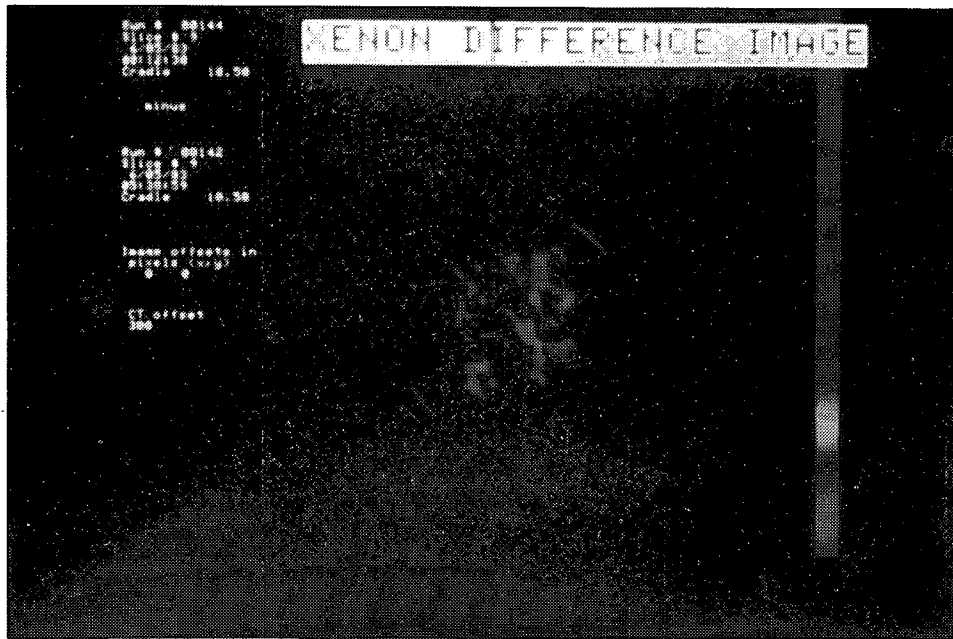
Figure 6-85. Xenon difference image at 120 min, perpendicular bedding planes
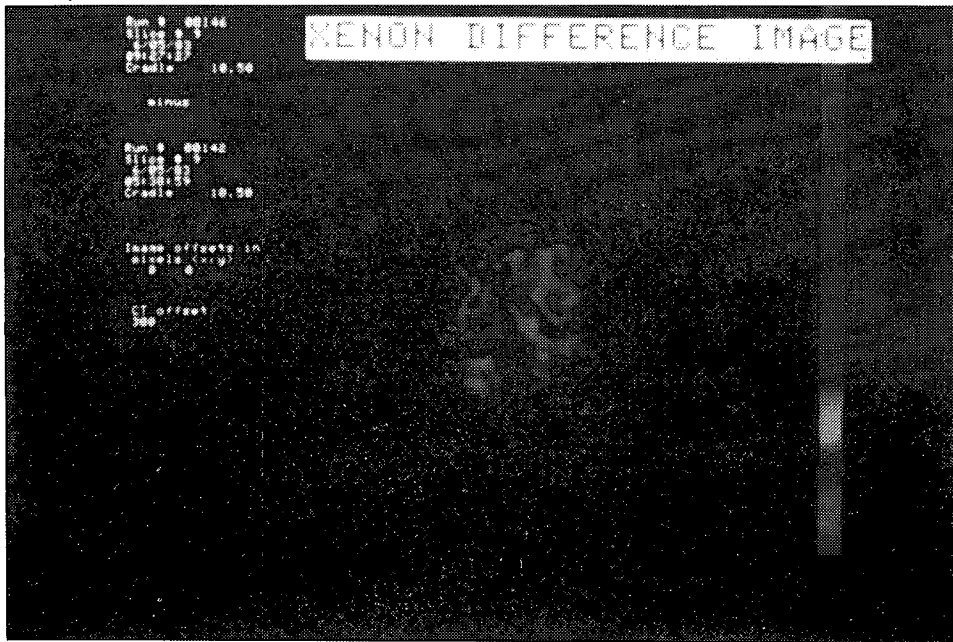
Figure 6-86. Xenon difference image at 200 min, perpendicular bedding planes
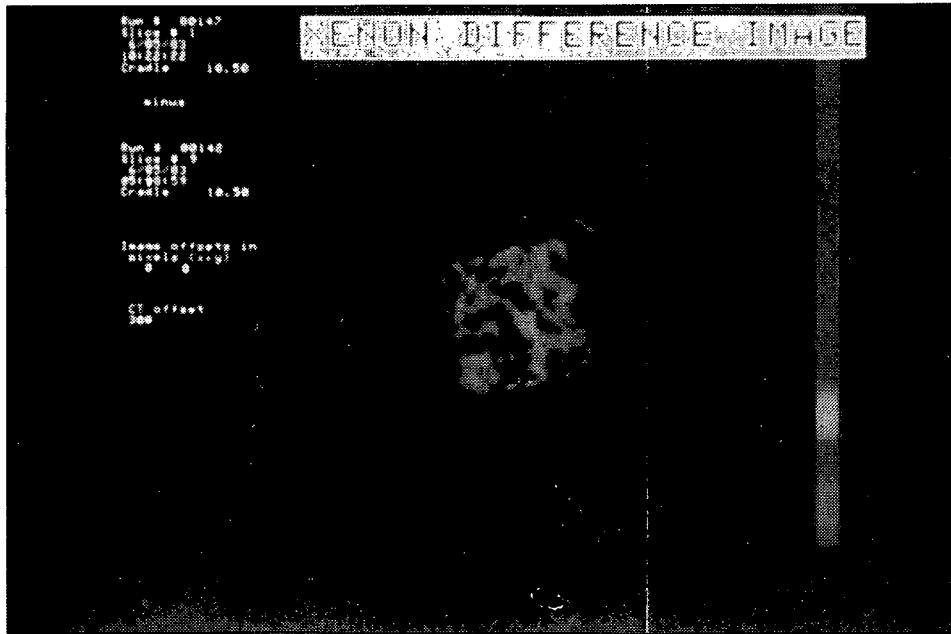
Figure 6-87. Xenon difference image at 260 min, perpendicular bedding planes

Figure 6-88. CT image of coal before xenon penetration
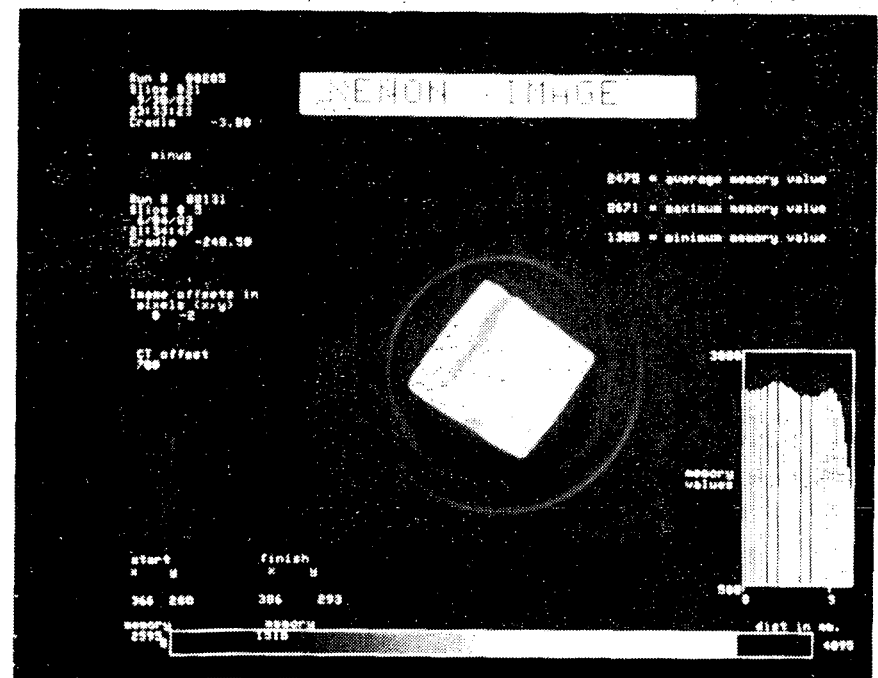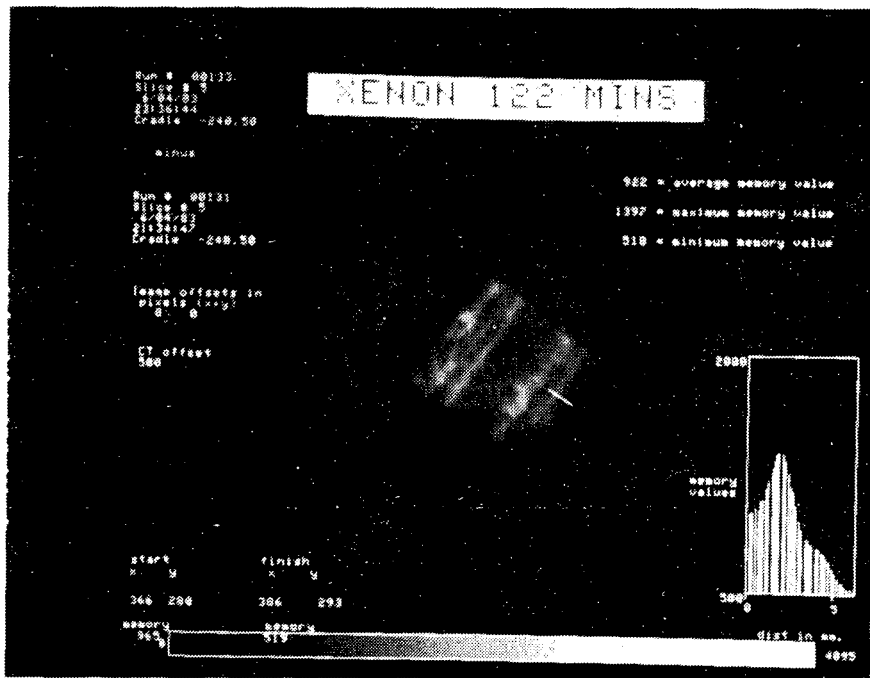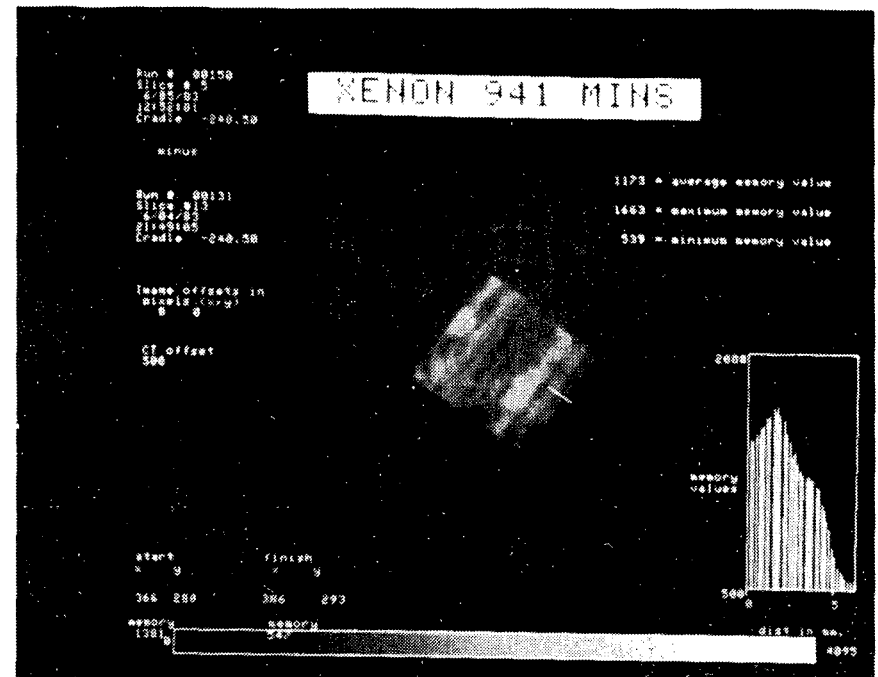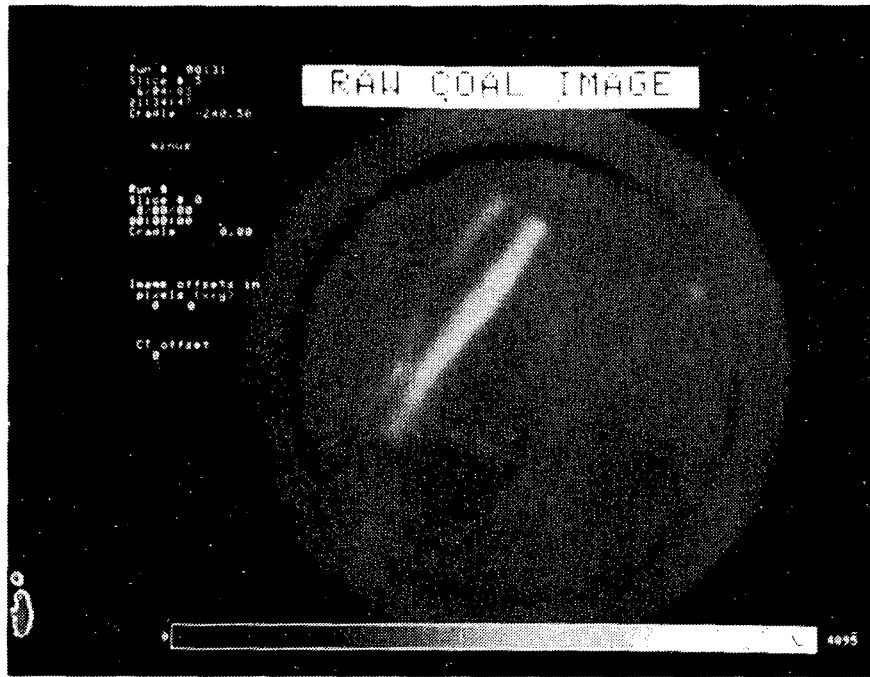
Figure 6-89. Xenon penetration along a chosen graphics line
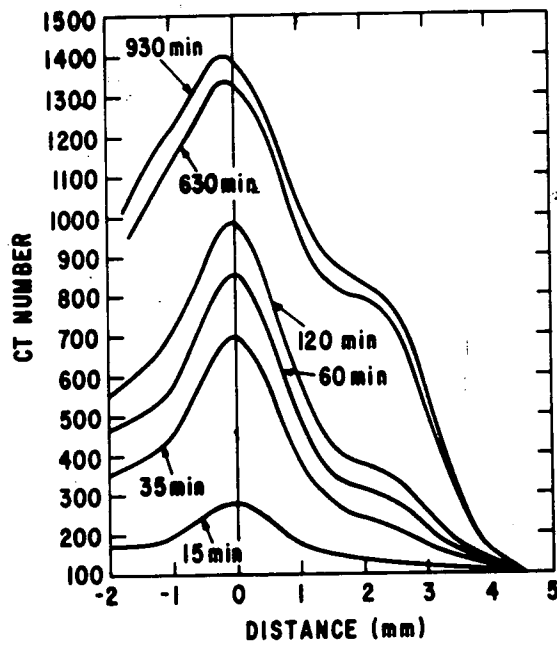
Figure 6-90. Xenon penetration across bedding planes as a function of time
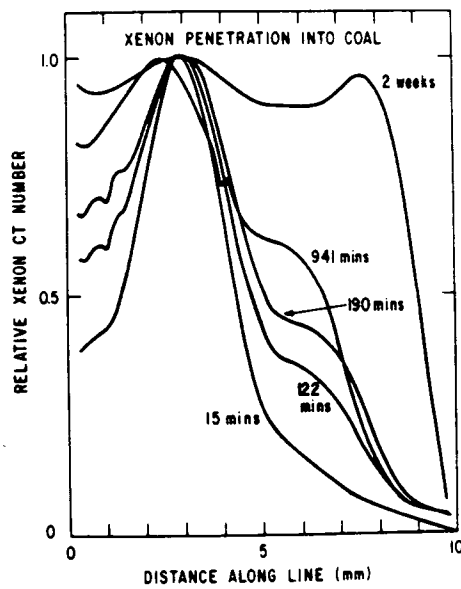
Figure 6-91. Normalized graph of xenon penetration in Figure 6-90

Figure 6-92. Line across xenon phantom image
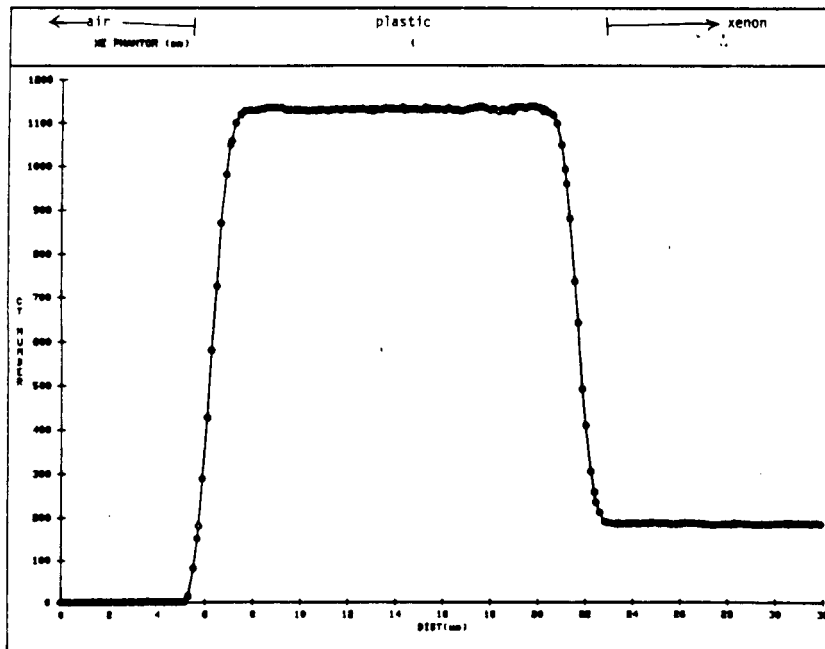
Figure 6-93. CT numbers along the line in Figure 6-92

6-88
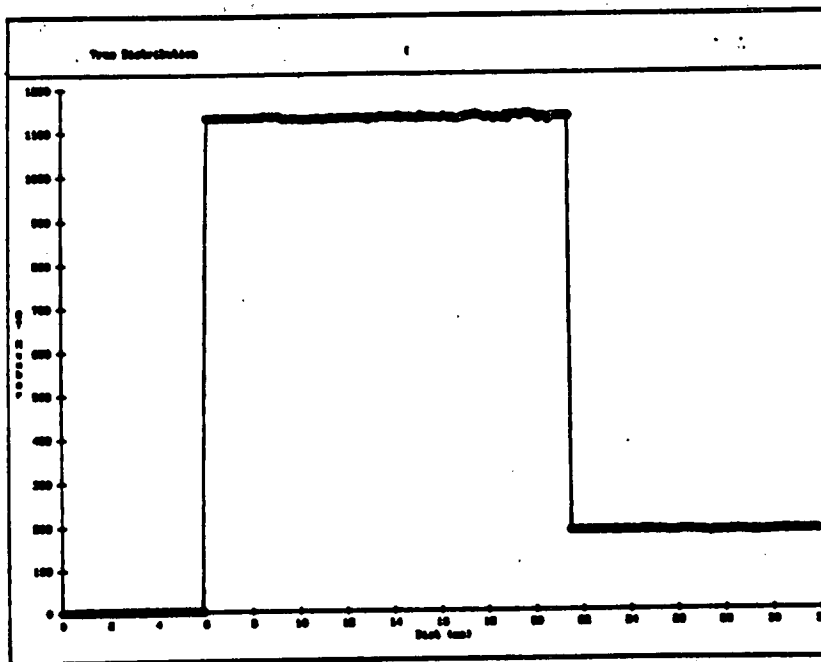
Figure 6-94. Assumed xenon phantom initial true electron density distribution
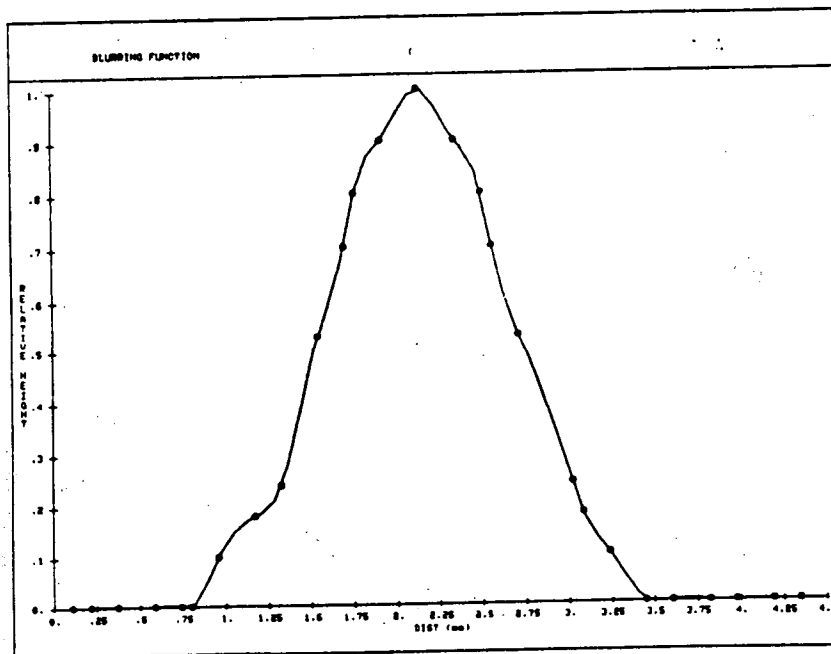
Figure 6-95. Normal-line blurring function
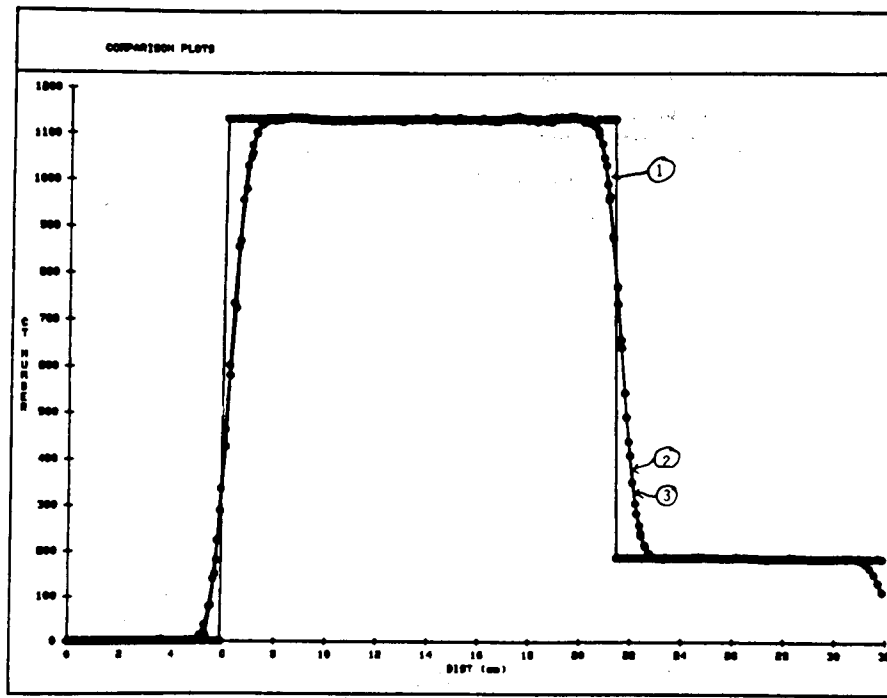
Figure 6-96. Comparison of (1) assumed true line shape, (2) observed line shape, and (3) calculated line shape
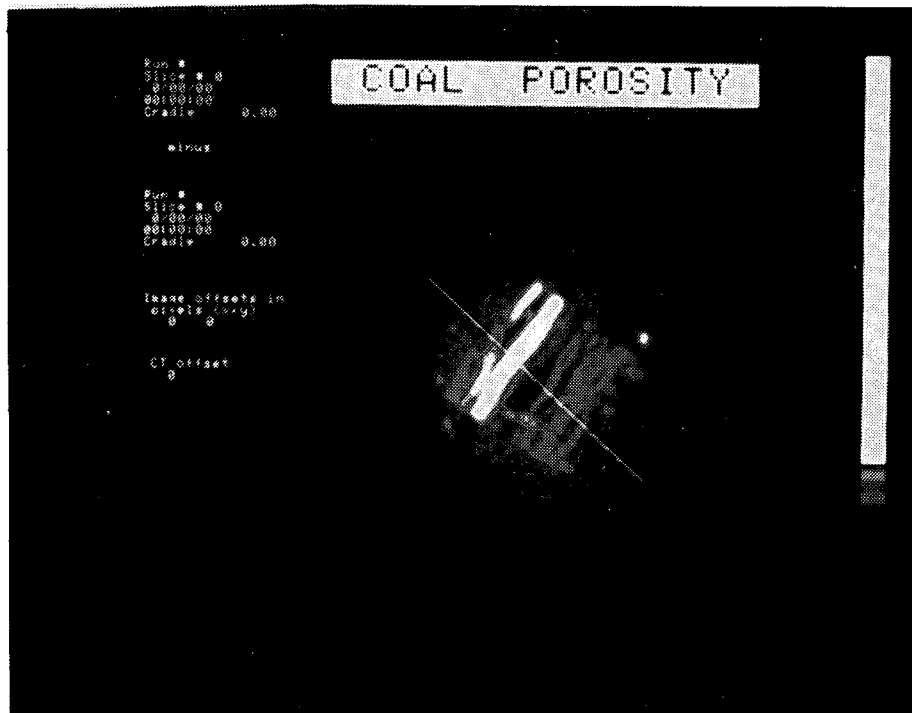
Figure 6-97. Xenon coal image with graphics line for deconvolution test
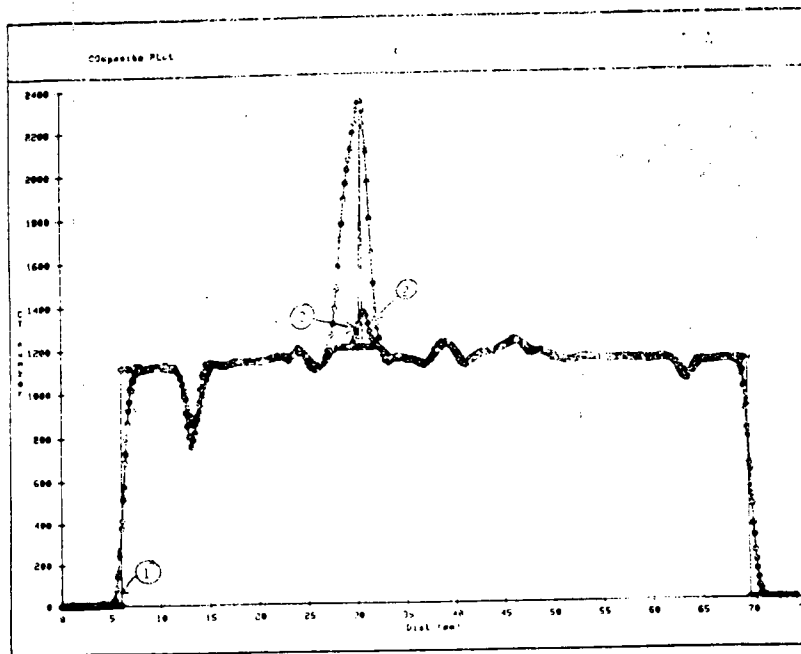
Figure 6-98. Comparison of (1) assumed initial distribution to fit only the edges, (2) observed distribution, and (3) calculated distibution
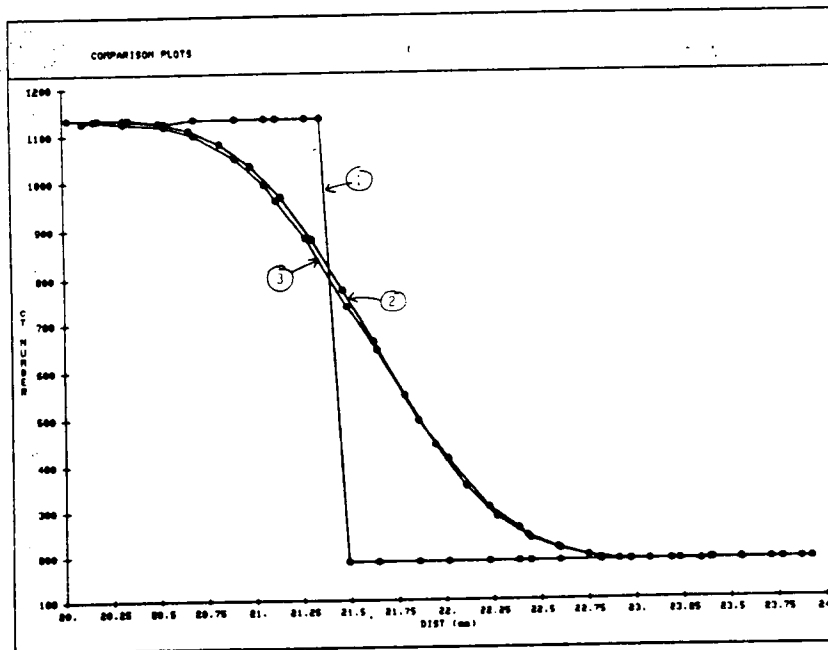
Figure 6-99. Blowup of edge of Figure 6-98
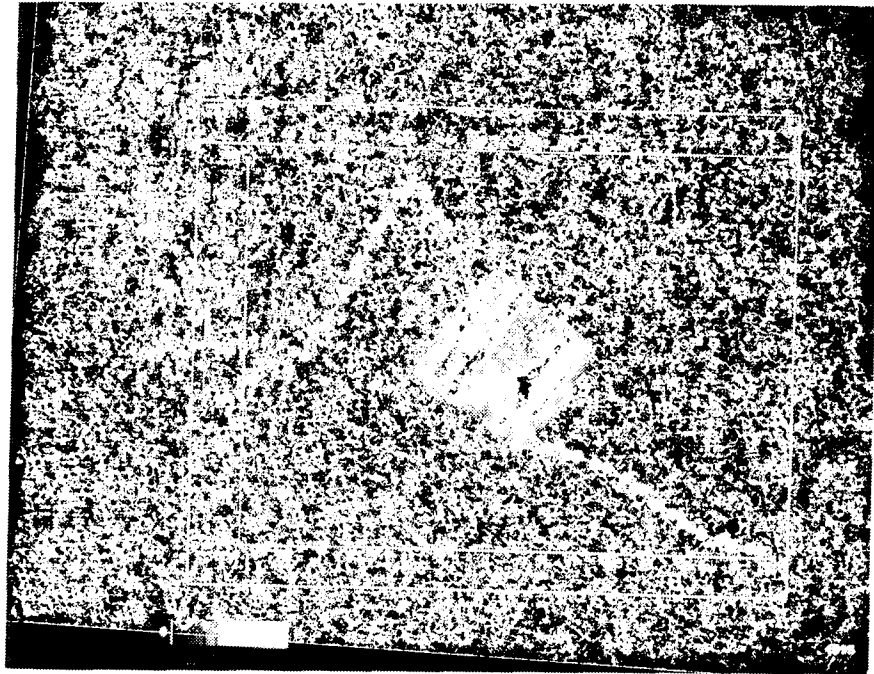
Figure 6-100. CT difference image of xenon diffusion into Illinois #6 coal. The CT numbers along the line at the edge of the coal have been displayed in the plot.
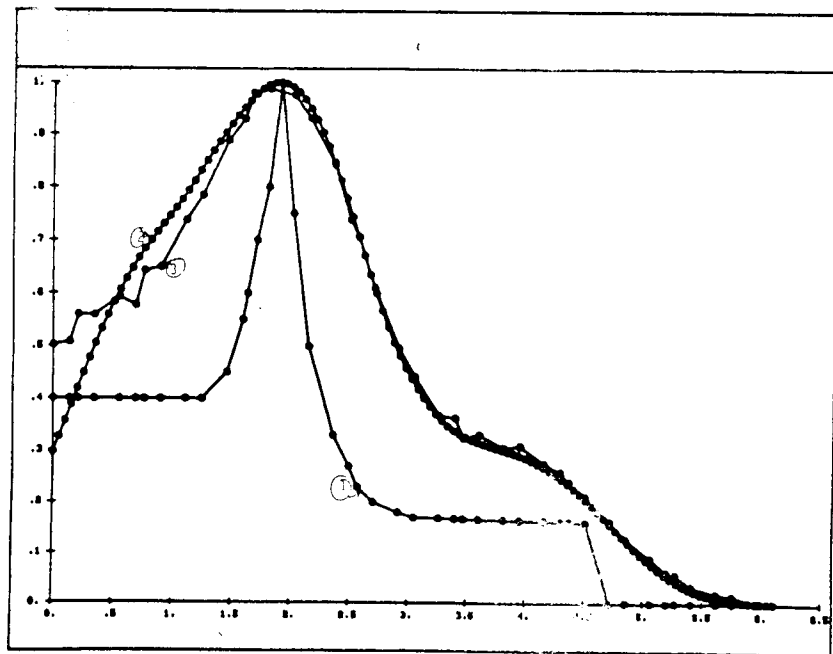
Figure 6-101. Xenon CT number: (1) assumed initial distribution, (2) calculated distribution, and (3) observed distribution
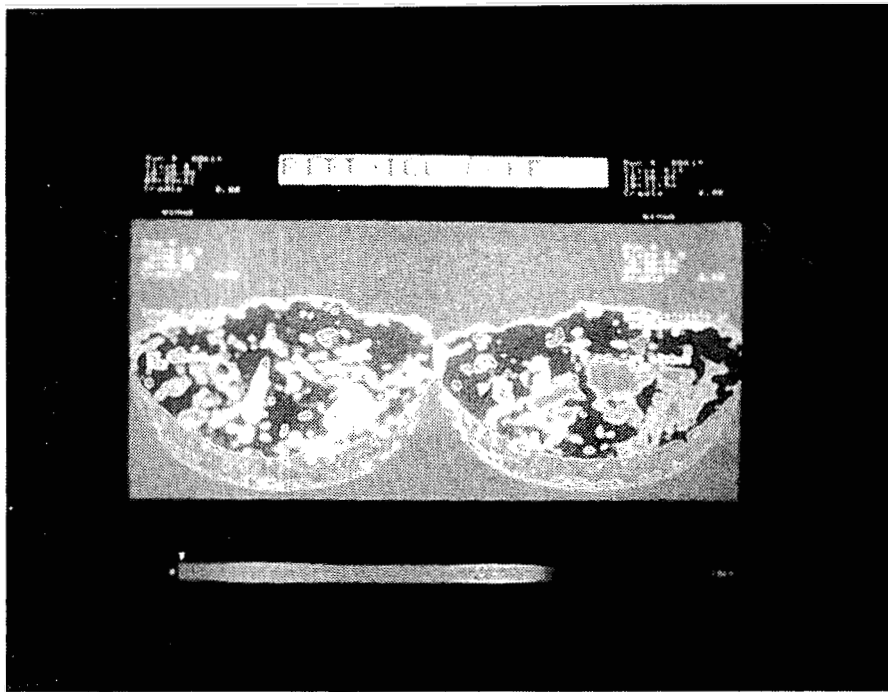
Figure 6-102. CT images of a 50/50 mixture of Pittsburgh #8 coal and Illinois #6 coal during a coking operation. The image on the left-hand side shows the probe for gas analysis.

Table 6-1

STATISTICAL SUMMARY OF CT IMAGES OF COAL

Coal I.D.	Seam	Class	CTMC	δ	Skew (pk)
C237 L1	Winifrede	Bituminous lvA	1205	97	173
C123 L1	Illinois #6	Bituminous hvB	1250	100	159
C290 L1	Mercer (Upper)	Bituminous	1210	86	133
C289 L1	Mercer (Lower)	Bituminous	1250	441	770
C267 L1	Lower Kittanning (Marine)	Bituminous	1205	26	42
C268 L3	Lower Kittanning (Non-marine)	Bituminous	-	538	892
C269 L1 P3	Ohio #6	Bituminous hvC	1220	114	204
C160 L1	San Juan #8	Bituminous hvC	1389	42	29
C245 L1	Wyodak	Subbituminous C	1305	24	28
C259 L1	Rosebud (W.E.)	Subbituminous B	1370	115	175
C276 L1	Dietz #1 (U)	Subbituminous B	1242	42	65
C285 L1	Dietz #1 (L)	Subbituminous B	1227	59	100
C232 L1	Beulah Zap	Lignite	1312	116	185

Table 6-2

COAL SAMPLES PREPARED FOR PETROGRAPHIC ANALYSIS

Coal I.D.	Seam	Class
C237 LI	Winifrede	Bituminous lvA
C123 LI	Illinois #6	Bituminous hvB
C290 LI	Mercer (Upper)	Bituminous
C289 LI	Mercer (Lower)	Bituminous
C237 LI	Lower Kittanning (Marine)	Bituminous
C267 LI	Lower Kittanning (Non-marine)	Bituminous
C268 LI P3	Ohio #6	Bituminous hvC
C160 LI	San Juan #8	Bituminous hvC
C245 LI	Wyodak	Subbituminous C
C259 LI	Rosebud (W.E.)	Subbituminous B
C276 LI	Dietz #1 (U)	Subbituminous B
C285 LI	Dietz #2 (L)	Subbituminous B
C232 LI	Beulah Zap	Lignite
C095 LI	Reading Anthracite	Anthracite

Table 6-3

CT IMAGES CHOSEN FOR PETROGRAPHIC STUDIES

Rank	Seam	Coal I.D.	CT Run #	Slice
Bituminous	Lower Kittanning (Non-Marine)	C268-LI	00016	6
Bituminous	Lower Kittanning (Non-Marine)	C267-L2	00013	16
Bituminous	Pittsburgh #8	C104-L1	00028	12
Bituminous	Illinois #6	C123-L1	00028	6
Subbituminous	Dietz #2	C285-L2	00035	12
Subbituminous	Upper Wyodak	C245-L1	00036	8
Subbituminous	San Juan #8	C160-L1	00033	4
Lignite	Buelah Zap	C232-L2	00027	6

Table 6-4

OBSERVED CT NUMBER RANGE
FOR VITRAIN, CLAY, AND PYRITE

Region Type	CT Range
vitrain	1200-1280
clay	1600-2000
pyrite	3900

Table 6-5

EXAMPLE OF STANDARD REFLECTANCE ANALYSIS OF COAL

```
**********************************************
**                                          **
**    The Pennsylvania State University     **
**           Coal Research Section          **
**                                          **
**********************************************
```

REFLECTANCE ANALYSIS FOR PSMC-116   6-18-84

Operator: DFB

Standard: 1.351 & 0.940
R.I. Oil: 1.518
Wavelength: 546 nm

REFLECTANCE OF VITRINITE
Mean Max. Ro: Av. Peak
   PELLET A   1.287%
   PELLET B   1.262%
  Mean Reflectance: 1.274%
Standard Deviation: 0.043

Mean Random (pol) Ro:
   PELLET A   1.189%
   PELLET B   1.053%
  Mean Reflectance: 1.121%
Standard Deviation: 0.098

1/2-VTYPE AND VTYPE TABLES FOR VITRINITE

1/2-VTYPE	COUNTS	% of TOTAL	VTYPE	COUNTS	% of TOTAL
11.25	0	0.0	11	3	3.0
11.75	3	3.0			
12.25	24	24.0	12	63	63.0
12.75	39	39.0			
13.25	30	30.0	13	34	34.0
13.75	4	4.0			

Table 6-5 (Continued)

EXAMPLE OF STANDARD REFLECTANCE ANALYSIS OF COAL

FREQUENCY TABLE FOR VITRINITE   PSMC-116

```
 1     1.16     1.00    *
 1     1.17     1.00    ●
 0     1.18     0.00
 1     1.19     1.00    *
 3     1.20     3.00    ***
 3     1.21     3.00    ***
 8     1.22     8.00    ********
 4     1.23     4.00    ****
 6     1.24     6.00    ******
12     1.25    12.00    ************
10     1.26    10.00    **********
 8     1.27     8.00    ********
 6     1.28     6.00    ******
 3     1.29     3.00    ***
 9     1.30     9.00    *********
 9     1.31     9.00    *********
 7     1.32     7.00    *******
 4     1.33     4.00    ****
 1     1.34     1.00    *
 1     1.35     1.00    ●
 2     1.36     2.00    **
 1     1.37     1.00    *
```

PSMC-116

```
vitrinite  ------------------  96.9 %
fusinite  -------------------   0.0 %
semifusinite  ---------------   0.8 %
macrinite  ------------------   0.0 %
micrinite  ------------------   1.5 %
exinite  --------------------   0.8 %
resinite  -------------------   0.1 %
                               -----
                               100 %
```

```
reactives  ----------------------------------  97.7 %
semi-inerts  --------------------------------   2.3 %
inerts  -------------------------------------   0.0 %
                                               -----
                                               100 %
```

Table 6-6

SUMMARY OF MACERAL CONTENTS OF COALS
BY STANDARD REFLECTANCE MAPPING

C-285	Reflectance Range	Digital Range	Maceral Distribution
Fusinite ------	2.0 -- 1.1	156 - 201	0.5 %
Semi-Inerts ---	1.1 -- 0.7	201 - 221	5.2 %
Vitrinite -----	0.7 -- 0.4	221 - 236	93.4 %
Liptinites ----	0.4 -- 0.2	236 - 246	0.9 %

C-268	Reflectance Range	Digital Range	Maceral Distribution
Fusinite ------	3.5 -- 1.6	81 - 176	3.3 %
Semi-Inerts ---	1.6 -- 1.2	176 - 196	6.4 %
Vitrinite -----	1.2 -- 0.7	196 - 221	89.6 %
Liptinites ----	0.4 -- 0.2	236 - 246	0.7 %

C-232	Reflectance Range	Digital Range	Maceral Distribution
Fusinite ------	2.6 -- 1.1	126 - 201	9.8 %
Semi-Inerts ---	1.1 -- 0.6	201 - 226	33.4 %
Vitrinite -----	0.6 -- 0.3	226 - 241	56.8 %
Liptinites ----	--- -- ---	--- - ---	0.0 %

C-267	Reflectance Range	Digital Range	Maceral Distribution
Fusinite ------	4.0 -- 2.8	56 - 116	1.1 %
Semi-Inerts ---	2.8 -- 1.1	116 - 201	9.2 %
Vitrinite -----	1.1 -- 0.7	201 - 221	81.6 %
liptinites ----	0.4 -- 0.2	236 - 246	8.1 %

Table 6-8 (Continued)

SUMMARY OF MACERAL CONTENTS OF COALS
BY STANDARD REFLECTANCE MAPPING

C-123	Reflectance Range	Digital Range	Maceral Distribution
Fusinite -------	3.8 -- 1.3	66 - 191	1.3 %
Semi-Inerts ---	1.3 -- 0.75	191 - 219	2.6 %
Vitrinite -----	0.75 - 0.4	219 - 236	94.0 %
Liptinites ----	0.4 -- 0.2	236 - 246	2.1 %

C-245	Reflectance Range	Digital Range	Maceral Distribution
Fusinite -------	2.0 -- 0.8	156 - 216	2.7 %
Semi-Inerts ---	0.8 -- 0.45	216 - 239	4.7 %
Vitrinite -----	0.45 - 0.25	239 - 244	91.4 %
Liptinites ----	--- -- ---	--- - ---	1.2 %

C-104	Reflectance Range	Digital Range	Maceral Distribution
Fusinite -------	3.5 -- 1.5	81 - 181	5.1 %
Semi-Inerts ---	1.5 -- 0.8	181 - 216	9.6 %
Vitrinite -----	0.8 -- 0.5	216 - 231	83.8 %
Liptinites ----	--- -- ---	--- - ---	1.5 %

C-160	Reflectance Range	Digital Range	Maceral Distribution
Fusinite -------	3.0 -- 1.4	106 - 186	2.1 %
Semi-Inerts ---	1.4 -- 0.7	186 - 221	5.1 %
Vitrinite -----	0.7 -- 0.35	221 - 239	91.9 %
Liptinites ----	0.35 - 0.2	239 - 246	0.9 %

Table 6-6 (Continued)

SUMMARY OF MACERAL CONTENTS OF COALS
BY STANDARD REFLECTANCE MAPPING

C-285

Most of the liptinite reflectances clustered around 0.3 percent. The upper and lower ranges 0.4 % to 0.2 % represent the extreme variation of the liptinite group. Please keep in mind the low percentage of liptinites in all samples analyzed. You may encounter a higher liptinite percentage in your analysis due to edge effects, cracks, etc. Although I have included the liptinite reflectance ranges for most of the samples you may have to discount the group as a whole if epoxy overlap is too high.

C-268

Semifusinite and vitrinite greatly overlap in reflectance with semifusinite reflectances as low as 0.80 typicaly encountered. The gap in reflectance between 0.7 and 0.4 could be covered under the vitrinite range, however no spot reflectances fell within this gap. I have therefore kept this gap open and will leave the evaluation to your judgement.

C-232

There were no liptinite macerals noted in this sample; In addition the fusinite and semi-inerts made up an exceptionaly high perportion of the maceral composition.

C-267

This sample has the highest and most prominent liptinite composition. Sporinite is the dominite liptinite maceral at 7.1 percent. The sporintie macerals are large enough to perhaps discriminate out. Most liptinite reflectance readings in this case clustered around 0.35 to 0.4 percent reflectance. You may wish to change the maceral bounds accordingly.

C-123

This sample had well defined fusinite and semifusinite. The vitrinite range should also be exceptionaly good in this sample.

C-245

The vitrinite reflectance in this sample is low enough to totaly obscure any liptinite reflectance. The main cluster of vitrinite reflectance ranged from 2.8 to 3.5 percent.

Table 6-6 (Continued)

SUMMARY OF MACERAL CONTENTS OF COALS
BY STANDARD REFLECTANCE MAPPING

C-104

The fusinite range should be well defined by the values given. The liptinite macerals in this sample were quite small in size. No maceral large enough to be accurately measured was observed.

C-160

This sample has good reflectance ranges for fusinite, semi-inerts and vitrinite. Minimal overlap between these groups was observed.

Table 6-7

COALS USED FOR ASH CONTENT COMPARISON WITH CT VALUES

Coal Bank No.	Coal Type	Ash Content
(C267)	Lower Kittanning (Marine)	1.43%
C268	Lower Kittanning (Non-Marine)	33.66%
C232	Beulah Zap	5.47%
C123	Illinois #6	6.31%
C104	Pittsburgh #8	14.35%
C160	Navajo	15.40%
C285	Upper Deck	2.29%
C245	Wyodak	7.16%

Table 6-8

SURFACE AREA MEASUREMENTS USING Xe, CO_2, AND N_2

Sample	N_2 (-106 °C)	Xe (-111 °C)	CO_2 (-78 °C)
Glass Beads	0.67	0.96	0.56
Hypersil	166.3	114.1	123.7
Illinois #6	12.9	18.9	206
Lignite	0.90	15.4	179.3

Section 7

VISUALIZATION OF GASIFICATION AND COMBUSTION

7.1 PYROLYSIS AND GASIFICATION

One of the main objectives of this experimental program is to observe the internal dynamics of coal structures during pyrolysis and gasification. The approach to the problem that will be used in this work is to fit a coal gasification apparatus into the aperture of a CT machine and construct the apparatus in such a way that x-ray imaging of the coal inside the furnace can be done during reaction.

7.1.1 Experimental Equipment

The CT furnace built for this program is shown in Figure 7-1 and schematically in Figure 7-2. The device is cylindrical with a length of 60 cm and a diameter of 40 cm. The heating elements were four semicylindrical 1050W wire-wound elements (Lindberg #506 KSP) arranged as two cylinders at the center of the furnace. The wires in the elements were potted in ceramic. The furnace construction around each of the two cylinders was conventional, with the furnace elements fitted inside a zirconium oxide refractory sleeve 2.5 cm thick, and this in turn fitted inside a double-walled stainless steel containment vessel. The two walls of this vessel were separated by a 6 cm space filled with bubbled alumina ball insulation. The outer steel wall was wrapped with copper coils for cooling water. Blank ceramic heating elements were used to fill out the inner bore of the furnace and a 15 cm-long solid ceramic cylinder closed off each end. The unique feature of this furnace is a gap of 2 cm between the two heating element cylinders corresponding to an x-ray transparent section in the furnace outer wall. The x-ray beam has access to the inside of the furnace for the full 360° circumference.

The body of the furnace was designed to operate at near-atmospheric pressure. However, it was envisioned that high-pressure operation may be desirable at some later date. As the weak point in high-pressure operation is clearly the window, it was decided to test out

possible window designs for high-pressure operation in this furnace. With a heavy metal outer shell on each furnace half, high-pressure operation would be a practical possibility. The design chosen was for a carbon fiber outer ring to contain the pressure and low-density silica-alumina felt to insulate the carbon ring from the internal temperatures. The carbon ring was made by wrapping carbon fibers around a cylindrical former, and then impregnating with epoxy. The carbon ring was made by Advanced Composite Products, East Haven, Connecticut. The ring had a wall cross section of 2.5 cm × 1.25 cm. The 2.5 cm length gave adequate clearance for the x-ray beam which, at its maximum, is 1 cm wide and in our usual operating mode is 1.5 mm. The 1.25 cm radial thickness is much greater than that necessary to retain the 200 psig specification pressure, but the ring was made that thick to give it mechanical strength for handling and to provide flat surfaces for o-ring seals on either side.

The temperature rating of the carbon composite ring is 100 °C. It was protected from higher temperatures by 5 cm of ceramic felt insulation on the inside, by conduction to the heavy metal plates on either side, and by air cooling from the outside.

The coal to be imaged is placed in a silica-alumina boat which can be traversed through the plane of the x-ray beam. Although the x-ray window has an effective width of only ca. 1 cm, the full length of a piece of coal or char can be scanned by traversing the boat through the beam. The boat is moved by a hollow ceramic rod that penetrates the vessel wall via a Konex connector and which is then attached to a motor-driven probe mechanism with position feedback control. The motor and feedback mechanism are functionally identical with the mechanisms used to position the patient cradle in the usual medical application of the CT machine. The coal boat position can therefore be set and recorded by the main CT computer. Not only must the traversing mechanism move the coal, but it must also be able to reposition the coal accurately within the beam. As a test of reproducibility, a cone-shaped plastic shape was placed in the boat and imaged; then the boat was moved away from zero, returned to the nominal starting position, and reimaged after every move. Figures 7-3a-d show the results.

A graphics software line has been drawn on each of the images, and the CT numbers along it have been plotted out. If reproducibility was exact, then all circles would have the

same diameter. In fact, the diameters fall into two groups. The largest diameter error corresponds to a longitudinal error of 1.6 mm. However, eliminating backlash by approaching the zero position from the same direction may reduce this error to 0.01 mm. Because of this reproducibility, the coal boat was used in this set of experiments merely to position the coal and not to move it and then reposition it at the "same" position. This reproducibility problem was solved for later experiments by a redesign of the boat, as will be described.

Temperatures within the furnace are measured by seven metal-clad Type-K thermocouples. They enter from either end of the furnace body housed in ceramic shields. These thermocouples measure the radiation temperature within the furnace. A traverse with one thermocouple along the axis of the furnace showed no variations larger then 5 °C for a 20 cm central section of the furnace operating at 800 °C.

Power to the furnace was supplied by two SCRs (Control Systems Research Model 661) governed by a dual channel programmable controller (Control Systems Micristar). Two of the Type-K thermocouples were used to provide feedback to the controller. A schematic of the controller network is given in Figure 7-4.

The atmosphere within the furnace was monitored using a quadrupole mass spectrometer gas analyzer (Spectrum Scientific Model SM100). The sampling was done through a ceramic tube which reached to the upper center of the furnace region, i.e., above the coal boat. The gas line connections for the mass spectrometer are shown in Figure 7-5.

Gas mixtures were supplied to the furnace from an outside manifold. A schematic of this is shown in Figure 7-6.

The Type-K thermocouples and the readings from the flow controllers were fed into a data handling system based upon a HP-85 computer. The data was stored on floppy disks for subsequent evaluation in Schenectady. A schematic of the data handling system is given in Figure 7-7.

Although the x-ray window has been made as transparent to x-rays as was possible given the pressure and temperature constraints on the window, there is clearly some absorption by the window, its insulation and the coal boat. This absorption is wavelength-

dependent with more low-energy x-rays being lost than high-energy x-rays. For an object of a particular composition, this absorption can change the CT number observed from the CT value observed outside the furnace. Calibration of the CT values against density, normally done in the open air, had to be repeated with the standards resting on the boat inside the furnace. A calibration graph for inside the furnace is given in Figure 7-8. The CT numbers inside the furnace are 15 to 20 units lower than measured outside, but the sensitivity to density changes appear to have remained essentially unchanged (i.e., 0.01 g/cm^3/CT no.).

7.1.2 Pyrolysis of Illinois #6

In this experiment the furnace first was stabilized at 850 °C with an atmosphere of nitrogen. The furnace was then opened, and a cubic piece of Illinois #6 coal (4 × 4 × 4 cm) was placed in the boat so that when the furnace was closed the mid-plane of the piece of coal would be at the plane of imaging of the CT machine. During the time the furnace was open, and for 4 min after it was closed, the flow of nitrogen was raised to 2 l/s. This was done to quickly sweep the oxygen out of the system. The oxygen concentration was being monitored by the mass spectrometer, and after a few minutes the nitrogen flow was reduced to ca. 2 l/min. At this flow rate, there is no apparent cooling of the furnace by the incoming gas, the thermocouples reading essentially the same as in the static gas case. As soon as the coal was exposed to a high temperature, it started to lose water; at higher temperatures, it devolatilized and charred. The CT pictures taken during the time when these processes might be expected to be taking place are shown in Figures 7-9 to 7-16. The color bar has been chosen so that the reds and yellows correspond to the range of CT numbers expected for raw Illinois #6 coal, while the blues and greens have been arranged to match the density of the char. It can be readily seen from these images that the pyrolysis is penetrating into the coal as a thin front leaving char behind it. As would be anticipated, the shape of the front as it penetrates into the coal starts off squarish, then becomes more circular as the front approaches the center of the coal. The shape of the char left behind the pyrolysis front is much more irregular than the original shape of the coal or, indeed, of the pyrolysis front itself. It appears that the thermal forces acting upon the coal are not affected significantly by either the bedding plane structure of the coal or by the presence of cracks or fissures close by in the char. It may have been expected that the pyrolysis front

would conform more to the outline of the fissures in the coke if the heat flow into the coal was mainly down the cracks in the char envelope.

A set of black and white images from this pyrolysis is shown in Figures 7-17 to 7-24. It is clearer in the black-and-white set that immediately between the unaltered coal and the char there is a very low density ring. This gap probably contains a rapidly moving mixture of gas, tars, and mineral matter being transported from the decomposing surface of the coal onto the inner wall of the char. Figures 7-9 to 7-16 show the same images as in Figures 7-17 to 7-24, and in both series, a software-generated line has been drawn on the images with the CT numbers along this line plotted on the accompanying graphs. In Figures 7-25 to 7-32, that portion of the line corresponding to the gap between coal and char has been expanded in the X-direction. The CT numbers at the bottom of the gap are always about 300. This corresponds to a density less than 0.3 g/cm^3 and is lower than what would be expected if the coal simply liquified at the pyrolysis interface, and then charred at the char interface; however, it is much higher than would be expected if the gap were simply filled with gas.

The gap between the coal and the char is about 2 mm full width half maximum (fwhm), and the shape of the gap does not appear to change during the course of the pyrolysis. This size feature is on the border of what is reproduced faithfully by the CT machine. Figure 7-33 shows the CT number drop-off from the edge of a piece of coal sitting in air; the drop is essentially complete in 1.2 mm. It appears then that the gap seen by the CT is approximately the true time-averaged profile and is not the result of a much narrower gap of considerably lower density.

The material being lost from the pyrolyzing coal surface is either deposited on the inner wall of the char or passed through the char to the outside world. It would be expected that permanent gases formed during the pyrolysis at the coal face would pass through the char, but the fate of high molecular tars is not so obvious. These tars could slowly crack and deposit within the char on their way out. In that case, the CT numbers of the char layers towards the edge of the char should rise as a function of time. While in the last image of the time sequence (e.g., Figure 7-32) the density of the char rises from the center towards the edges; it does not appear from the sequence of images that those layers of char formed

during the earlier stages of the pyrolysis gain density as the pyrolysis continues. In the sequence of images (Figures 7-25 to 7-32) where the CT values at the edge of the char are emphasized, the CT number for a position stays quite constant once the char has been formed. The heavy tar molecules formed at the pyrolysis front appear to either crack very rapidly to immobile char or else they do not crack at all during their passage to the outside. Their passage to the outside may take place via cracks penetrating to the pyrolysis zone rather than by diffusion through the bulk of the char.

The passage of the pyrolysis front through the coal leaves behind it a spherical pattern of lower and higher density within the final char. This spherical pattern has essentially destroyed the original horizontal bedding plane pattern within the coal. However, the effect of the passage of the pyrolysis front is not to totally randomize the mineral matter within the coal, if only because a very small fraction of the coal/char composite is molten at any one time. Regions of the coal that were high in mineral matter give rise to regions in the char that are also high in mineral matter. In fact, in the sequence of images (Figures 7-34 to 7-41), where a double look-up-table has been used to simultaneously show detail in the coal and the char, there are several high-density regions, probably small high-pyrite regions, that survive in position after the front has passed.

The coal clearly swells during the early stages of the pyrolysis. The extent of the swelling at the end of the pyrolysis depends on what value is taken for the area covered by the char. For comparison with the ASTM free swelling index, it is probably more correct to take the outside geometric area of the coal and ignore the fissures and cracks that are present in the char. On this basis, the area has increased by a factor of ca. 1.6, giving the coal an FSI of 2.5. This is at the low end of what would be expected for Illinois #6 coal. However, the temperature profile and sample preparation was not, of course, that required for the ASTM test.

The coal suffers a loss of mass during the pyrolysis process. Figure 7-42 shows the total CT number for the entire image as a function of time, and Figure 7-43 shows the average CT number for the central area of what is assumed to be the original coal. The CT number total drops to 60.8% of its original value. The ASTM proximate analysis of the coal (Table 7-1) gives the fixed carbon plus the ash to be 58.1% by weight of the original coal;

hence the CT number drop is in the range that would be expected.

The time dependence of the weight loss of the coal (Figure 7-43) shows that little loss occurred until the pyrolysis front arrived. The weight loss that did occur was about 9% of the original density. The proximate analysis shows 8.7% water in this coal, so water loss is a reasonable mechanism for the density drop in the coal prior to the arrival of the pyrolysis front.

The mass spectrometric data taken during the course of the experiment showed that methane, water, and CO_2 are the major permanent gases. Ethylene was also observed. Hydrogen was not scanned. Carbon monoxide could not be distinguished from N_2 in our system. The methane evolution peaked around 550 s into the run, dropped to 41% of the peak after a further 10 min and disappeared after another 35 min. Given the estimated time constant of ~10 min for turning over the gas content of the furnace, it appears that the major gas evolution stops when the pyrolysis front reaches the center of the coal. From both the char weight loss curve and the mass spectrometer data, it appears that, once formed, the char is unreactive under these pyrolysis conditions.

7.1.3 Analysis of Pyrolysis Experiments

The progress of the pyrolysis front into the coal should be capable of interpretation in terms of such parameters as the thermal diffusivity of the coal, the heat capacity of the coal, heats of reaction, heats of volatilization, etc.

Figure 7-44 shows a plot of the square of the diameter of the coal circles during the pyrolysis. The diameters were calculated by measuring the area of the pixels within the region covered by the coal and determining the diameter of the circle that has the same area. For the middle of the image sequence, where the coal image is almost exactly circular, this procedure is quite accurate. It clearly is an approximation for the early stages when the coal image is more square. As Figure 7-44 shows, there is a very good linear relationship between d^2 and time. Such a finding is quite common in combustion problems like oil droplet burnup, and it might be quite surprising to see that it effectively holds for the pyrolysis of Illinois #6 under these conditions. This finding may make analytical solutions of the pyrolysis sequence more tractable. Because of the geometrical constraints of the prob-

lem, a numerical solution was first attempted.

The commercially available finite element analysis package, ADINAT, was used to simulate the progress of the pyrolysis front into the coal. This program used the thermal properties of the material to solve for the time-dependent temperature distributions within the coal. The following properties of the system must be given before a solution can be attempted:

1. Density of the material as a function of temperature

2. Thermal conductivity as a function of temperature

3. Heat capacity as a function of temperature

4. Heat of pyrolysis of the coal

The density function was determined from a TGA analysis on a sample of this coal. The result of the experiment, done at two different heating rates, is shown in Figure 7-45. The TGA results show a mass drop to 60% of the original mass, which agrees with the 60% drop in CT number. The mass values were converted to density assuming 1.3 g/cm^3 as the density of the original coal. The density curve used in ADINAT is shown in Figure 7-46. The water loss and pyrolysis curves have been approximated by a series of straight lines. The thermal conductivity curve (Figure 7-47) for the coal and char was taken from Table 2 of Reference 20. The relationship between heat capacity and temperature for coal and char (Figure 7-48) was taken from Reference 21 with a correction for 9% water below 100 °C. The gaseous products of pyrolysis are broken into two groups: light gases and tars. The temperature dependence of Cp for the light gases is given in Table 7-2. In the case of the tars, we assume the elemental composition is similar to that of coal and that a typical molecular weight is 400 amu (atomic mass units). This gives an approximate formula of $C_{33}H_{26}$ for the tar. To this hypothetical molecule we have assigned a heat capacity three times the heat capacity of biphenyl ($C_{12}H_{10}$). The tar heat capacity relationship used in ADINAT is

$$Cp = 2.93 \times T + 37 \; J/kg \; °K$$

The relative proportions of the different products formed during pyrolysis are taken from Reference 22, viz,

56%	by weight of the coal forms	char
32%		tars
6%		water
2%		methane
2%		carbon monoxide
2%		carbon dioxide

The heat of pyrolysis of the coal was taken as a first approximation to be zero. Badzioch et al. (Reference 20) found no evidence for net endothermicity or exothermicity for the coals they tested. Other authors (Reference 23) have used a small value (700 J/g).

ADINAT was used in its 2-D form. A network of node points was set up in a 1.1 × 1.1 cm square representing a quarter of the coal. A mesh of 20 × 20 node points (Figure 7-49) was first tested and compared to a mesh of 10 × 10. No apparent difference in the resulting temperature contours was found; therefore, the coarser mesh was used because considerable savings in computer time resulted.

The ADINAT package has been linked to a GE proprietary software package called the Computer Aided Thermal Engineering System (CATE). CATE allows the user to

create the finite element model, attach boundary conditions and material properties, run ADINAT, and display the results. All input and output for the CATE system is via an interactive graphics nondriver interface. The model temperatures generated by ADINAT are used by CATE to create isotherm maps (Figure 7-50) or color-filled density images (Figure 7-56). The color images are readily comparable to CT images. A simplified series of thermal profiles from CATE is shown in Figures 7-51 through 7-55, where the square outline represents the top right-hand corner of the coal in the CT image.

The contour labeled 1 represents the 100 °C line, and the contour labeled 2 represents the 425 °C line. At 100 °C all the water is expected to be steam, and at 425 °C the pyrolysis is expected to be occurring (Figure 7-45). These figures show the water/steam front preceding the pyrolysis front into the coal and show the transition with time from the essentially square profile to the circular profile. Temperature profiles taken at different times can be used to determine the rate of temperature rise at any time within the coal. For example, using Figures 7-53 and 7-54 it can be calculated that the temperature 1 cm away from the center of the coal is rising at about 1 °C/s after the coal has been exposed to the furnace environment for 300 s. The complete 2-D temperature map can be convolved with the density function (Figure 7-46) to provide a time history of the density of the coal. A sequence of these images is shown in Figures 7-56 to 7-59. The red regions correspond to the density of coal, while the blue regions have the density of char. The yellow band shows the narrow region within which the pyrolysis is occurring. The ADINAT images cover only the top right-hand quadrant of the coal CT image not the entire image. There is therefore a considerable change in scale between the two types of image.

The ADINAT results confirm the experimental finding of a very narrow region in the coal within which the pyrolysis is occurring. The calculations also show the interior of the coal becoming sufficiently hot to drive out the water considerably before the pyrolysis front arrives. Because of the low water content of this coal, the water front was not experimentally proved. Experimentally, the CT values in the coal dropped before the arrival of the pyrolysis front, but the coal image was so uneven it was difficult to detect a "front" for this process. However, in a subsequent experiment a sample of lignite was taken through the same thermal step. Figure 7-60 shows a CT image taken during its pyrolysis. This image clearly shows two rings penetrating into the coal. On the basis of the present results, it

is reasonable to assign the inner ring to water devolatilization and the outer to pyrolysis.

So far in the ADINAT analysis we have assumed literature values of the parameters and have not used any adjustable parameters to achieve the images in Figures 7-51 to 7-55. A quantitative comparison between the experiment and ADINAT can be made by measuring the areas in the ADINAT temperature profiles and comparing their rate of change with the rate of change of the coal area in the CT image. This comparison is given in Figure 7-61 (Model B). This figure shows that the ADINAT results fall off faster than the experiment shows. Considering that a 3-D version of ADINAT would certainly drop off even faster than the 2-D version, this suggests that some alteration of the literature values will be necessary to fit the data. In particular, the effective thermal conductivity for this coal may be lower by a factor of 2 to 3.

7.2 CATALYZED AND UNCATALYZED CARBON DIOXIDE GASIFICATION EXPERIMENTATION

For all subsequent experiments the ceramic boat assembly used to traverse the coal across the plane of the x-ray beam was designed to produce minimal backlash when moving the boat back and forth. The backlash was measured by reimaging an object whose position in the beam could be determined by its image shape (e.g., a plastic conic section in this case). The boat is moved by a rod which passes through the walls of the furnace. At one end the rod is attached to the ceramic boat; at the other end, it is attached to a lead-screw traversing mechanism run by the CT computer. The rod was originally ceramic but was replaced with molybdenum. The rod also had a flat piece of molybdenum plate welded onto the end at right angles to the rod. This plate fitted into a slot molded into the end wall of the ceramic boat. The boat is made of 360-m Moldable Ceramic. The tests with this boat and rod design showed that the backlash was at most 1 pixel and usually not even that.

7.2.1 Run 444 – Illinois #6, Steam Gasification, Uncatalyzed

In this experiment, Illinois #6 coal char was gasified in steam. The partial pressure of steam employed was 0.4 atm with the balance consisting of nitrogen. The char, actually consisting of a large and a small lump, was gasified at 850 °C for 2 h, raised to 900 °C for

2 h, 950 °C for 2.5 h, and 1000 °C for 1 h.

Figure 7-62 shows a CT slice of the region from which most of the data were extracted. As before, we have plotted CT values along a line throughout the course of the experiment. Figure 7-63 shows a CT comparison of the char used in this experiment from a time early on in the course of the test until a time close to the end.

Figures 7-64 to 7-67 show the progress of gasification on the larger lump at 850, 900, 950, and 1000 °C, respectively. In general, most of the gasification occurred at the edges, though considerable internal reactivity took place at more elevated temperatures. In order to make this quantitative, rates of gasification were determined at 10-pixel (2.65 mm) intervals throughout the course of gasification. In many instances, movement of the char, a likely consequence of crack development and propagation, resulted in an apparent weight gain at a given voxel element. Table 7-3 reports average rate constants as a function of location in the char. Locations in the table correspond to those which appear in Figures 7-64 to 7-67. At each temperature and position, pixel values were determined at four or five different time intervals. For each time interval, isothermal rate constants were calculated. These were averaged for a given temperature and appear as entries in the table. Points where a significant weight gain occurred (a consequence of char translation) or where two or more slight weight gains occurred in a given temperature/ position interval, were discarded as meaningless in rate calculations, and a "+" sign appears in the table. If a slight weight gain was observed in a single point (i.e., <5 CT units), then the rate was calculated assuming no weight loss, and this was averaged into the total rate constant.

In general, the rates reveal greater reactivity at elevated temperatures as expected. Rates are quite reasonable based on our experience in this area (Reference 24). Where a given locus had three or more good data points, an Arrhenius plot of log (rate) vs. inverse absolute temperature was made, and appears in Figure 7-68. Note that the four good lines are reasonably parallel, indicating a consistent activation energy of roughly 50 kcal/mole. For example, at location 80 with four good data points, the slope yields 51.6 kcal/mole for an apparent activation barrier. This is typical of a chemically, rather than a diffusionally, limited regime. Even though the activation energies are reasonably similar in penetrating the char from the surface to a depth of nearly 1 cm, the absolute rates clearly drop in the

core. One might expect that if the rates dropped internally, this would be a reflection of diffusion limitations. This is apparently not the observation. The near-constant activation energies reflect a consistent chemically limiting mechanism, while the lowered reactivity indicates a diminished number of active sites. We can speculate that at the surface of the char there are more surface discontinuities, cracks, and edge defects in the char pseudo-lattice which propagate inward.

Another unexpected observation is the apparent lack of edge recession in this trial. Over the course of the experiment, one edge propagated inward at a rate of 0.004 mm/min; two others receded at 0.001 mm/min, while the fourth edge failed to recede at all, even while being held at temperatures from 850 °C to 1000 °C for over 8 h.

7.2.2 Run 448 – Illinois #6, Rubidium Carbonate as Plug, Carbon Dioxide Gasification

In this experiment, an Illinois #6 coal was pyrolyzed at 700 °C for 2 h under nitrogen and cooled. A hole approximately 5 mm was drilled into the char and subsequently packed with powdered rubidium carbonate. The sample was heated to 850 °C under nitrogen. Carbon dioxide was then admitted to the furnace, and gasification commenced.

Figure 7-69 shows the coal at the onset of gasification (left) and at the completion of the trial (right). The salient features include the apparent disappearance and downward migration of the catalyst into the char, and the wake of gasification in its path. Presumably the dominant driving force for catalyst migration was gravity, as gasification appears to have been enhanced mainly at the original position of the catalyst as well as directly vertically below the catalyst origin.

In an effort to make this more quantitative, CT values along a vertical line passing through the catalyst plug were plotted as a function of time. The vertical line appears in Figure 7-70 and is plotted in Figure 7-71. The dominant feature in Figure 7-71 appears in the locations at position 80 to 100, the original catalyst location. Thus the catalyst at 850 °C spanned approximately 5.3 mm. The decrease in density at this spot over time took place at an apparent rate of 8.8×10^{-3}/min, or 2.4 times that observed when the catalyst was solution impregnated (see Figure 7-72). This is likely a consequence of both melting and migration of the catalyst as well as loss of material through gasification. The rate of

recession of the catalyst maximum was 0.04 mm/min, again 2.2 times that observed in the solution-impregnated char. This most likely reflects the higher local concentration of high-density salt in the drilled plug along with the effects of gravity in enhancing downward mobility into the char.

Further into the char, at position 120, the catalyst migrated and appeared approximately 22 min after gasification was initiated, as evidenced by a local maximum in CT values at this time. This was followed by gasification at an apparent rate constant of 1.46×10^{-3}/min, a more realistic value based on our previous experience with catalytic gasification rates (Reference 24).

At a spot above the catalyst, position 45 to 50, gasification rates were 4.5×10^{-4}/min, and edge recession was only 5×10^{-3}/min, or eight times slower than the catalyzed front.

7.2.3 Run 450 – Illinois #6 with Dispersed Catalyst; Carbon Dioxide Gasification

In this trial, a lump of Illinois #6 coal had been prepyrolyzed to 700 °C for 2 h under nitrogen several weeks earlier. The resultant char had been suspended in a saturated solution of rubidium carbonate and the solution allowed to evaporate, leaving salt on the periphery of part of the char. Figure 7-73 shows the prepared char on the CT boat; the deep red and yellow region along the base of the char reveals the extent of penetration of catalyst.

Gasification in carbon dioxide was performed at 850 °C in the CT, with the progress monitored throughout. Figure 7-74 shows two slices separated by 80 min. Movement of the catalyst, edge recession, and general broadening of the cracks is evident. A particularly useful way of visualizing these phenomena is to plot CT values along a given line over a period of time. The line employed in this test appears at the base of the char in Figure 7-73, and is plotted in Figure 7-75 at three different times. On the left edge of the char (Figure 7-76), there is considerable recession of the maximum along with some broadening. Specifically, the rate of edge recession is 1.8×10^{-2} mm/min. The maximum apparent gasification rate constant occurs at position 38 along the line, yielding 3.8×10^{-3}/min. This value is a composite of weight loss due to gasification as well as migration of the catalyst into the char. The other edge of the coal did not reveal as obvious

an edge recession (Figure 7-77), but gasification at position 147 yielded an apparent rate constant of 3.8×10^{-3}/min identical to the opposite edge. Finally, note that throughout the center of the char there was relatively little gasification. More significant was that from position 40 to position 125 inclusive: the char actually everywhere gained weight, presumably from migration of the catalyst into the center. Indeed, even at dead center the average CT value rose 6.5% at a specific rate constant of 7.3×10^{-4}/min.

7.2.4 Run 424-426 – CO_2 Gasification, Illinois #6 Catalyzed

In this experiment, lump Illinois #6 was placed in the furnace, where it underwent rapid pyrolysis at 850 °C. After stabilizing for 2 h, carbon dioxide (1 atm) was admitted and the Boudouard gasification was followed by CT. Isothermal rates at 850, 900, 950, and 1000 °C were determined over an 8 h period.

Figure 7-78 shows the char at the outset of gasification and at the termination.

The char was generally unreactive throughout, although some loss of material along the edges was apparent. Very little edge recession or movement of the char was observed. In order to quantify the gasification, a line was drawn through the coal and CT values were determined along the same line throughout the test. Figure 7-79 shows which line was employed, and Figure 7-80 represents a plot of several values along the line taken at 900 °C. Similar plots exist for each temperature examined.

The most reactive position along the line, position 130, just inside the edge, revealed a CT value/time profile which appears in Figure 7-81. These data do not appear to follow Arrhenius behavior, and rate constants were typically in the range of 1 to 3×10^{-3}/min. In the center of the char, the average CT value over a small, 138 pixel region was measured and showed greatly reduced rates ranging from 2×10^{-5}/min at 850 °C to 5×10^{-4}/min at 1000 °C. This is well below the maximum rate that was observed at the edge of the char.

Some locations in the char showed actual increases in CT values. This may represent changes due to minute movements or could represent true densification phenomena, a notion under study in upcoming trials.

7.2.5 Run 436 – Lignite Gasification in Carbon Dioxide

In this experiment, North Dakota A lignite was heated in carbon dioxide with isothermal gasification monitored at 850, 900, 950, and 1000 °C. Figure 7-82 shows the char at 850 °C at the onset of gasification. The horizontal line through the image is that which was used for analyses as described below. Figure 7-83 shows the char before and at the end of gasification. Clearly the char has been gasified extensively, with considerable edge recession, surface rounding, and crack formation/propagation. Notice that over 5 h elapsed between the slices.

Figure 7-84 shows a composite of data along the line of interest. For display purposes, the zero in CT values has been offset by 1000. Thus, a value of 1000 indicates the absence of material at that location. Note that at either edge of the char most of the matter became depleted in time, and edge recession occurred. Figure 7-85 is somewhat less complex than Figure 7-84, showing only those data points at 900 °C; Figure 7-84 showed data from 850 to 1000 °C inclusive. Note the minimal edge recession in this figure, and also extensive weight loss at positions 60 and 210 at either edge.

As with the Illinois coal gasification, gasification rate constants were determined at 10-pixel intervals along the line shown in Figure 7-82. These are listed in Table 7-4. An Arrhenius plot of data obtained near the edge of the coal (position 65) yielded $E_a = 64$ kcal/mole, again typical of a chemically limited process. In general, data were insufficient to obtain Arrhenius data throughout the char, as apparent weight gains due to char movement were pervasive.

Table 7-5 reveals that considerable and highly temperature-dependent edge recession occurred. This is further borne out in Figure 7-86, which shows how the edge moved from position 55 to position 62 in just over an hour. (Recall that one pixel on this scale is equal to 0.265 mm.)

7.2.6 Run 417 – Pittsburgh Coal, Uncatalyzed CO_2 Gasification

In this trial, Pittsburgh char was gasified in CO_2 under isothermal conditions at 850, 900, and 950 °C. Figure 7-87 shows the char along with the line used in analyses. Figure 7-88 shows two slices taken at the onset and 2 h into gasification, respectively. Beyond

some crack broadening at the center of the char, very little in the way of gasification has taken place. Figures 7-89 to 7-91 taken at 850, 900, and 950 °C further bear this out, where, except for a few locations, little evidence for gasification is noted. This is in contrast to the Illinois char, where extensive gasification was noted. It is possible that there are significant differences in the char structures which result in inherent differences in chemical reactivity or diffusion profiles, or that the gasification process is dominated by adventitious and indigenous catalysts which are somehow not present in the Pittsburgh coal. Certainly the Illinois coal is noted for high salt content which has well-characterized catalytic behavior. In the absence of additional data, the reason for the apparent differences in reactivity between these chars remains speculation.

7.3 STEAM GASIFICATION EXPERIMENTS

Four further gasification trials were undertaken with steam in nitrogen as the reacting gas. Neat, nitrogen-saturated water was admitted to a steam generator located at the aft end of the furnace outside the CT. Pure steam was admitted to the furnace, where mixing with the furnace atmosphere took place by a molybdenum fan welded to a molybdenum rod just prior to the furnace boat. Partial pressure of steam ranged from 0.30 and 0.37 atm, with the balance consisting of nitrogen.

The steam generator consisted of a stainless steel vessel 11 in. long and 1 1/4 in. in diameter. This hollow vessel was filled with small-diameter ceramic beads and wrapped with Thermolyne flexible electric heating tape. Nitrogen gas was constantly circulated through the steam generator vessel into the furnace. A reservoir of distilled water, deaerated with bubbling nitrogen, served as the supply water for the generator. Water was pumped from the reservior with a speed-controlled peristaltic pump at a predetermined set rate (1 to 2 cc/min). There were two type-K thermocouples used to monitor the system: one was located inside the vessel and the other within the heating tape. Limits were set on the thermocouple in the vessel, so an alarm sounded if the temperature within the vessel dropped below 200 °C. This assured that only steam entered the furnace. As water entered the generator, it flashed to steam and was carried into the furnace by the flow of nitrogen gas. The water flow was not started until the temperature of the furnace was above 150 °C, which provided further assurance that only steam was used in the gasification process.

A Micromonitor 500 Gas Analyzer (GC) from Microsensor Technology was used in these experiments to monitor the furnace atmosphere. The GC probe was the same as the mass spectrometer probe. The GC measured nitrogen, oxygen, carbon monoxide, carbon dioxide, and methane.

Gas was drawn from the sample probe through a Fiberfax fiber inline filter, and then passed through a condensor, which had a glass reservoir at its bottom level to collect liquids. The gas then passed through another inline filter that contained Drierite beads and Fiberfax fiber to trap any carryover tars or moisture. The GC took samples at predetermined time intervals (usually every 15 min). Exhaust gas was then pumped back into the exhaust piping of the furnace.

The coals had been equilibrated with pure nitrogen over a period of several hours to ensure that true gasification, rather than oxidation by residual air, took place.

The four trials included steam gasification of a North Dakota A lignite from the North American Coal Corporation, Bismark, North Dakota (C-114H); steam gasification of a Pittsburgh HvA bituminous coal (C-83A-1) from the Eastern Coal Association Fed #2 Mine, a catalyzed lignite (C-114G) which contained two plugs of rubidium carbonate catalyst; and a Reading anthracite(C-101A) from Pottsville, Pennsylvania, which contained three plugs of rubidium carbonate catalyst. Analytical data on these coals appears in Table 7-6. The uncatalyzed coals were used without additional preparation. The catalyzed coals were prepared by drilling 0.125 in. holes approximately 0.25 in. into the top surface of the coal, followed by manually filling the holes with rubidium carbonate powder. Unlike catalytic data from previous experiments, here pyrolysis took place in the presence of catalyst. Specific temperature profiles were recorded for each sample.

7.3.1 Run 504 – Uncatalyzed Lignite Gasification with Steam

A pentagonal-shaped lump of North Dakota A lignite was heated in humidified nitrogen according to the temperature/time profile in Figure 7-92. The partial pressure of steam was 0.37 atm.

Figure 7-93 reveals the gas evolution profile monitored by mass spectrometry. During pyrolysis which took place during the temperature ramp to 850 °C, evolution of carbon

dioxide and methane coincided. It is likely that carbon dioxide resulted from thermal de-
carboxylation of inherent lignite functional groups along with those generated by oxygen
chemisorbed during sample preparation. Methane is a product from thermolytic degrada-
tion of the organic matrix. As expected, methane evolution ceased as carbonization
reached completion. Carbon dioxide evolution increased with temperature due to char
gasification as follows:

$$C + H_2O = CO + H_2 \text{ (Primary gasification)}$$

$$CO + H_2O = CO_2 + H_2 \text{ (Water-gas shift reaction)}$$

$$2CO = C + CO_2 \text{ (Boudouard gasification)}$$
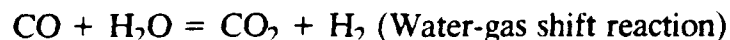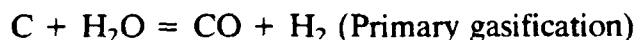
In this instance, carbon dioxide evolution occurred primarily through the shift reaction.
The sudden drop-off of carbon dioxide after 350 min is due to the depletion of carbon
from the sample.

During the pyrolysis stage of the sequence (T <850 °C) the pentagonal shape of the
lump was preserved, though a near-isotropic linear shrinkage of 26% occurred, illustrated
in Figure 7-94. As described earlier, mass transfer from the core of the lump took place in
spherical contours. One consequence of this is the void which results in the center of the
lump, an apparently general phenomenon in most of the coals studied by CT. In addition
to volume reduction, the average density decreased 28%. The original lump was highly
uniform, with most pixels clustered within a very narrow range around 1190. The pyro-
lyzed coal was much less uniform, with pixel values in the bulk showing values which
ranged throughout the 800s. The void had values down to 0, as is apparent in Figure 7-94.
Qualitatively similar pyrolytic phenomena were observed in carbon dioxide gasification of
the same type of lignite.

Figure 7-95 shows a sequence of slices taken during the gasification. The process is
characterized by a loss of material from the edges, with very little change occurring inside

the char, at least until the external regions were depleted of organic matter. Figure 7-96 shows plots of CT values along the horizontal line in Figure 7-95 for five slices taken over 90 min at 900 °C. Essentially no material was lost from the center of the char at 900 °C, while the outer surface strongly diminished in density.

Analyses based on edge recession are difficult to apply here since ash was left nearly in place, only slightly rafted into the center of the core. The shoulders that appear at the base of the curves in Figure 7-96 are probably due to porous ash buildup. Noteworthy is that the hole in the center of the char showed virtually no translation over the course of the experiment. A more useful exercise is to compare isodensity lines as a function of time. A sample of this appears in the table below:

RATE OF RECESSION FOR ISODENSITY LINES IN CO_2 AND STEAM

Temperature (°C)	Rate of Recession Steam	Rate of Recession Carbon Dioxide
850	9.0×10^{-3} mm/min	4.5×10^{-3} mm/min
900	5.3×10^{-2} mm/min	1.2×10^{-2} mm/min
950	2.3×10^{-1} mm/min	7.0×10^{-2} mm/min
1000	-----	1.4×10^{-1} mm/min

Isodensity contours for CT values clustered at 500 are illustrated in Figure 7-97. Figure 7-98 reveals that the Arrhenius law is followed for these data, with log (rate) being a linear function of inverse absolute temperature.

The gasification of run 436 took place in 1 atm carbon dioxide and provides an opportunity to compare carbon dioxide vs. steam gasification. In the table above isodensity rates are compared. As expected (Reference 24), rates in steam are somewhat greater than those in carbon dioxide, although apparent activation energies which determine slopes in Figure 7-97 are comparable.

7.3.2 Run 510 – Uncatalyzed Pittsburgh #8 Gasification in Steam

In this trial, a lump of Pittsburgh #8 coal was gasified in humidified nitrogen. Steam partial pressure of 0.30 atm was used throughout. Figure 7-99 shows the temperature/time profile of the experiment. The data are best described in two parts: pyrolysis and gasification. Figure 7-100 shows the gas evolution profile.

The pyrolytic profile is illustrated in Figure 7-101. The rectangular lump of the highly volatile, highly swelling coal is initially fairly uniform, with CT values ranging from 1200 to 1400, typical of a porous, mineral-laden Eastern bituminous coal. As the pyrolysis proceeds, the gradual fragmentation, melting, and recombination into a cylindrical semicoke takes place. The dominant morphological changes occur in the 350 to 550 °C range, although the temperature inside the core likely lags behind the externally measured furnace atmosphere temperature. Again the phenomenon of an internal void was realized, and the generality of this effect must be considered a likelihood. The loss of volatile matter accompanied by the dimensional swelling results in greatly reduced densities, manifest in CT numbers which are typically in the range of 250 to 450.

Gasification rates as a function of position appear in Table 7-7. Plots of log (rate) vs. inverse absolute temperature appear linear as before, and activation energies determined from slopes of the lines are roughly identical at 55 ± 10 kcal/mole. These indicate a chemically limiting pathway, but must be carefully considered in light of the rapidly progressing front associated with shrinkage and edge recession. In particular, this coal showed general shrinkage at the elevated temperatures. This is illustrated in Figure 7-102, which shows CT numbers plotted along a constant horizontal line through the char at 1000 °C at four different times. The line through the doughnut-shaped slice reveals the central void and two maxima associated with each part of the char. Both external edges recess with time, the apparent result of loss of material due to gasification. On the other hand, at the center of the core, there is an increase in density with time, and the char apparently shrinks, showing a decrease in core radius. This is readily seen in Figure 7-103. The shrinkage phenomenon is probably due to ultimate densification caused by the semicoke-to-coke transformation. A slight increase in methane evolution at the higher temperature was observed, and it is likely that other products of coking would be oxidized by the steam.

As with the Illinois and lignite coals, the Pittsburgh char shows relatively higher reactivity in steam than in CO_2.

7.3.3 Run 516 – Rb_3CO_3 Catalyzed Lignite Gasification in Steam

In this experiment, North Dakota A lignite was predrilled to create two holes which were packed with rubidium carbonate. The coal was pyrolyzed in humidified nitrogen, with a partial pressure of 0.36 atm steam. Figure 7-104 shows the temperature/time profile, and Figure 7-105 shows the gas evolution profile. The catalyzed lignite shows two maxima associated with methane evolution, while the uncatalyzed lump shows only a single, though much larger, maximum. The significance or generality of this result is not known at this time.

The pyrolysis sequence, ranging from room temperature to 750 °C showed a loss of volatile matter, with slight shrinkage, but not nearly enough to compensate for the loss of material from the coal. As a consequence, the char generally decreased in density, with considerable uniformity. Some cracking occurred.

The catalyst showed morphological changes during the pyrolysis, as appears in the sequence in Figure 7-106. It is likely that the catalyst movement was due to loss of admixed organic matter from the coal rather than a true melting. Throughout the course of gasification to completion, the catalyst showed no propensity toward spreading, as is evident in Figure 7-107.

During the gasification, the char cracked and crumbled, and eventually spilled onto the tray. Because of the gross movement, quantitative rate data were obviated. Even the role of the catalyst was obscured in the gasification process. The coal was much more reactive than previous samples, although the presence of adventitious catalytic matter in these coals is well documented.

7.3.4 Run 525 – Rb_2CO_3 Catalyzed Steam Gasification of Reading Anthracite

In this trial, a lump of Reading anthracite was predrilled with three holes, which were packed with rubidium carbonate. The coal was heated according to the temperature/time profile in Figure 7-108 in humidified nitrogen with a steam partial pressure of 0.34 atm.

The pyrolysis portion of the run was generally uneventful, with a nearly isotropic reduction in density from an average CT value of 1475 at the ambient temperature to 1386 at 800 °C. The 6% loss of density compares well with the 8% combined volatile matter and moisture content of the coal (Table 7-6). Some minor morphological changes in the catalyst were observed, possibly due to decarbonation of the salt or moisture loss. Figure 7-109 reveals the gas evolution profile for this trial, showing methane outgassing during the early stages of pyrolysis, and CO/CO_2 evolution due to gasification at the elevated temperatures. The latter species become more pronounced at the more elevated temperature as the gasification becomes more vigorous.

The gasification sequence was monitored in several ways, with particular emphasis on catalyst mobility. Figure 7-110 reveals the degree of penetration of the catalyst into the char at 850 and 1000 °C. Recall that, at room temperature, the catalyst simply filled the three small holes which appear as voids in Figure 7-110. The catalysts have apparently migrated considerably into the coal in the immediate region by the cavities. This is more quantitatively borne out in Figure 7-111, which shows CT values along a horizontal line through the three cavities which appear in Figure 7-110. Initially the catalyst filled the voids, and appeared as three spikes in the figure. After several hours at temperature, the appearance of voids at the same location indicates that the catalyst has disappeared into the char. The growth of shoulders on the char surface adjacent to the holes reveals that the catalyst has penetrated considerably in the vicinity of the holes.

What is not apparent from these figures is the degree of catalyst penetration throughout the char and into regions which are quite remote from the holes. Figure 7-112 brings this phenomenon out more clearly with a different look-up-table. Here the catalyst, appearing red in the figures, penetrates deeply into the char, with an apparent increase in densification. Because the coal does not shrink, the increase in density must be due to the catalyst presence.

The increase in density is remarkably uniform with depth. In particular, the catalyst penetration does not appear to gradually seep into the coal from top to bottom, but rather appears to become quickly isotropic. For example, consider Figure 7-113. Here, the weight gains are quantified as a function of time at depths of 24, 29, 34, and 40 mm beneath the

surface of the coal. The salient features of this figure are the overall weight gain with time, and, especially, the little difference among the four curves taken at different depths. It is possible that the catalyst has dispersed throughout the coal by a vapor phase intermediate such as the reduced metal. Carbothermic reduction of the metal ion could account for this. The neutral hydroxide salt would also be expected to have appreciable vapor pressure and could accommodate this mechanism. An alternate mechanism for catalyst dispersion would be via activated diffusion across a concentration gradient.

Another cause for speculation is the lack of catalyst dispersion and apparent densification in the catalyzed lignite gasification described earlier. Here it is possible that the dispersion of the catalyst did indeed take place, but was masked by the much greater reactivity and near complete burnout of the char. The presence of indigenous catalytic material, as well as the higher porosity of the lignite, could mediate the catalyst mobility.

Finally, the coal was removed from the furnace and examined. Photos of the surface appear in Figures 7-114 through 7-115. Note that the predrilled holes are largely intact, with no edge recession and a large void which had been filled with catalyst. Also, the surface shows penumbric ellipses of ash about the holes which are of different character from the remainder of the char surface. It is possible that these are rubidium-enriched ashes, or that the presence of higher concentrations of the salt resulted in more complete gasification. Another feature of the elliptical penumbric ash deposits is the eccentricity. In all three holes, the ash spread 15% more in the direction parallel to the bedding planes than in the perpendicular direction.

These studies clearly show the advantages of CT for studying the pyrolysis and gasification of coals, especially for fixed bed gasifier systems. Estimates can be obtained for how quickly the coal heats up upon entry into the gasifier, how quickly the volatiles are blown off, and what the effective area of the coal is to combustion gases and to gasification reactions.
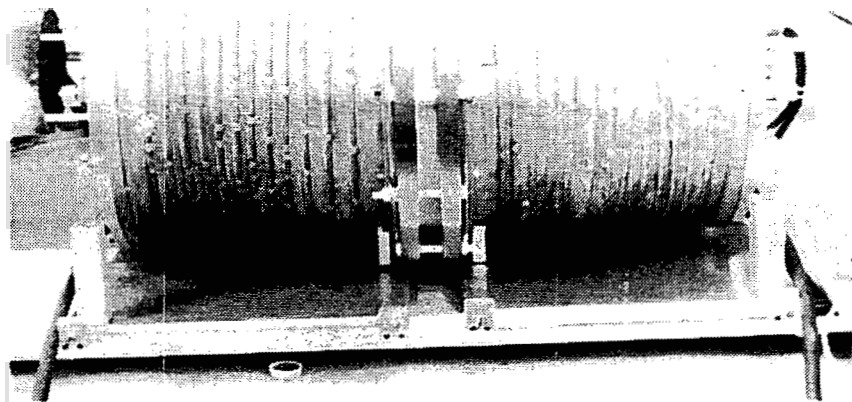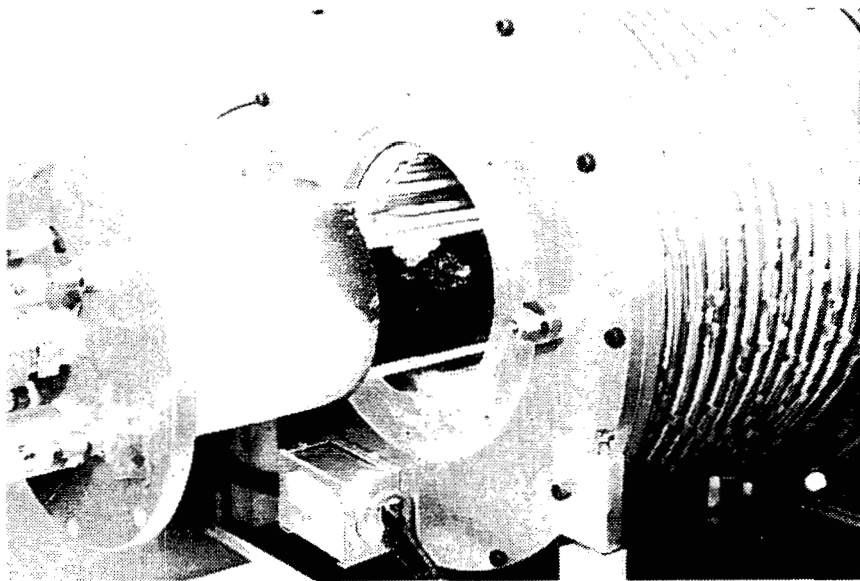
Figure 7-1. Photographs of CT furnace
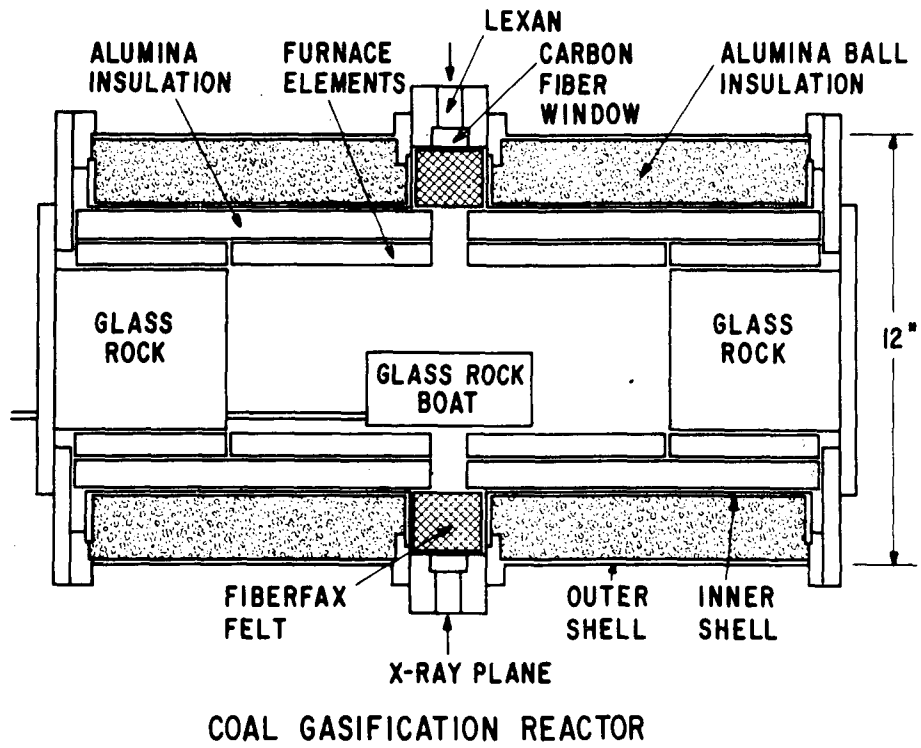
Figure 7-2. Schematic of CT furnace
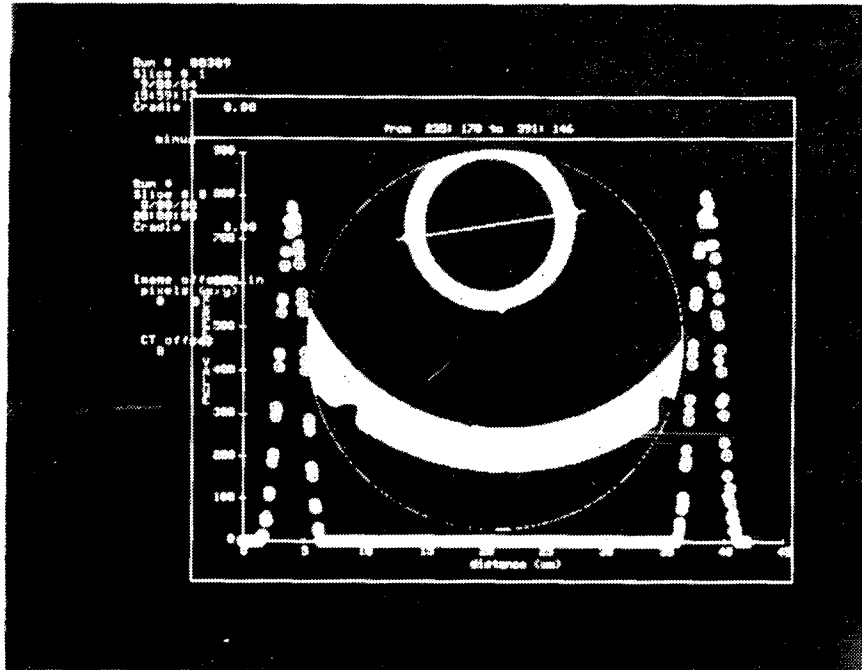
Figure 7-3a. CT image of plastic cone
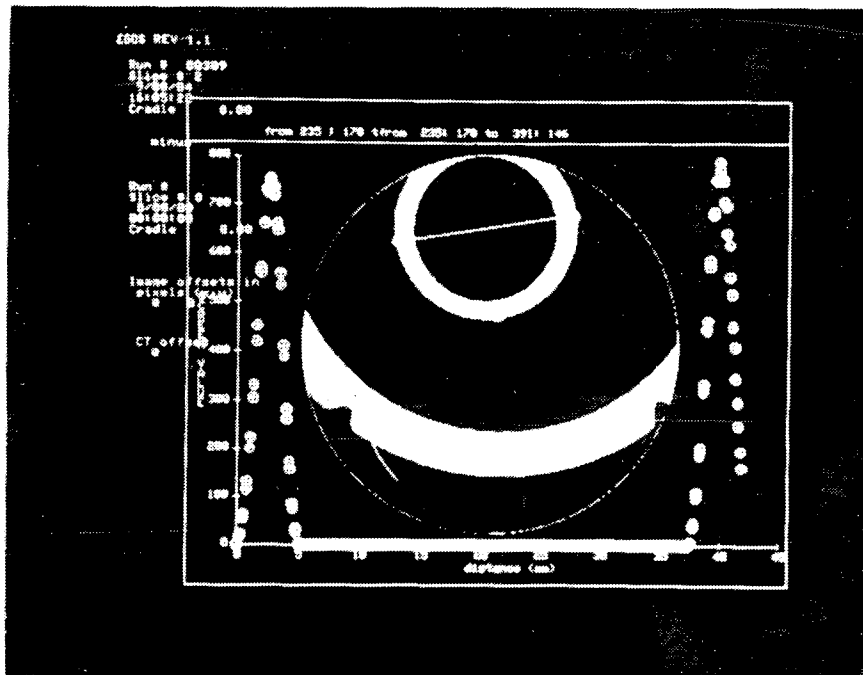
Figure 7-3b. CT image of plastic cone after first move
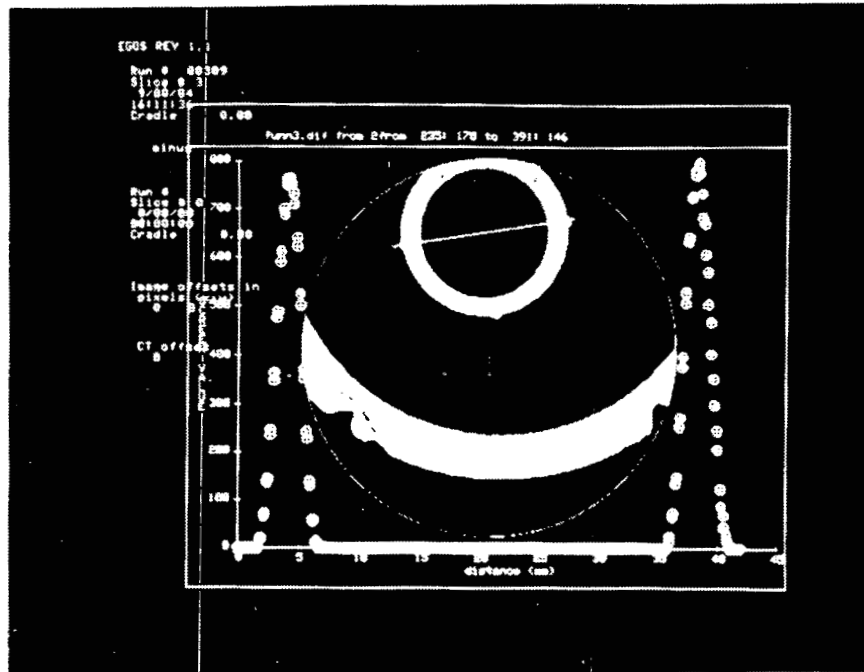
Figure 7-3c. CT image of plastic cone after second move
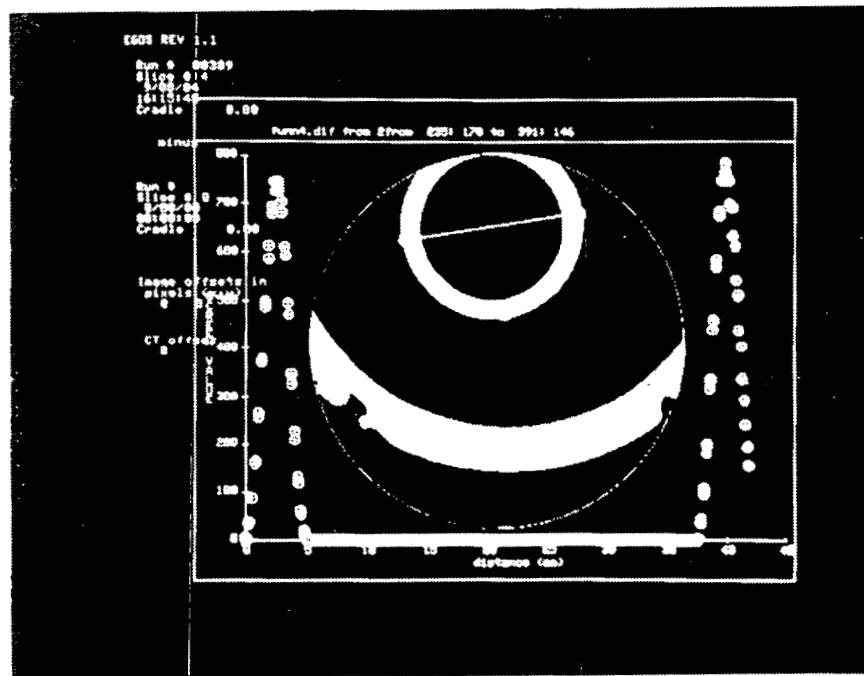
Figure 7-3d. CT image of plastic cone after third move
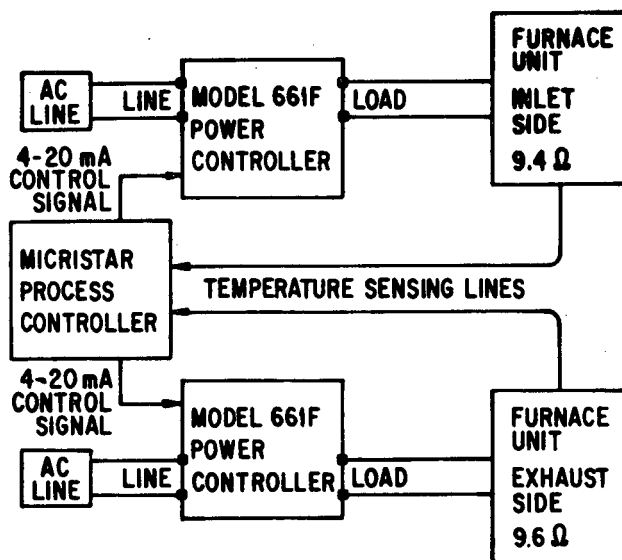
Figure 7-4. Electrical connections for furnace
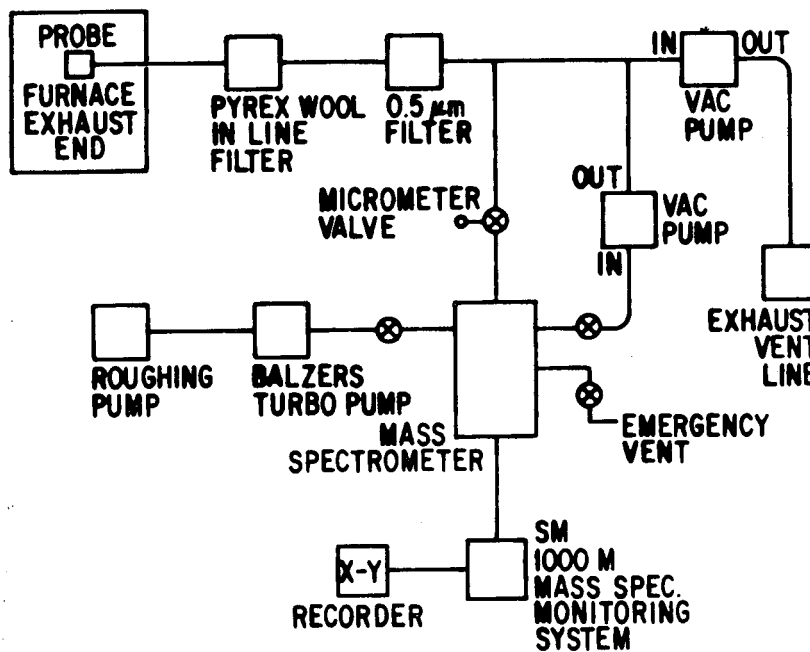
Figure 7-5. Gas connections for mass spectrometer
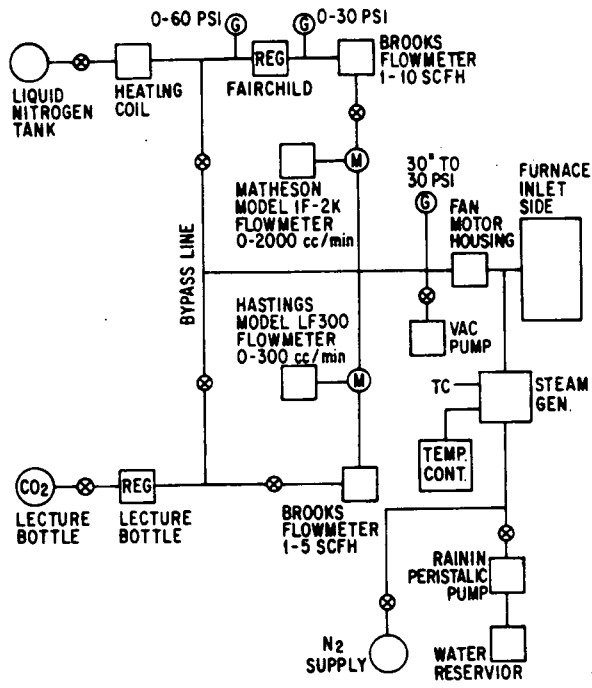
Figure 7-6. Gas supply system for furnace
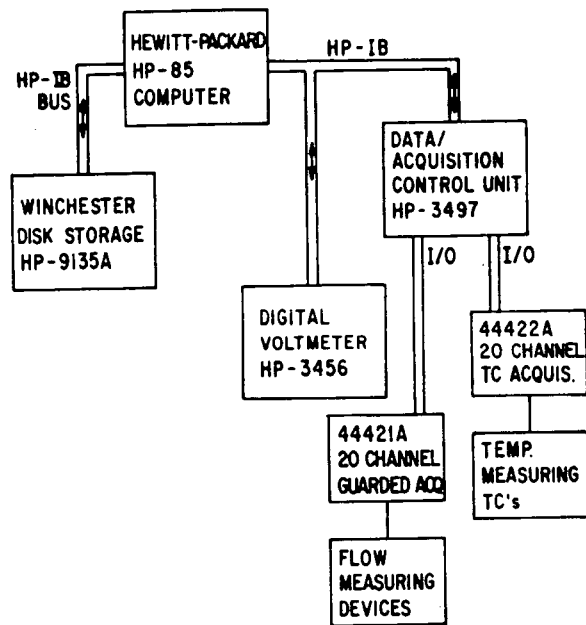
Figure 7-7. Data acquisition for furnace
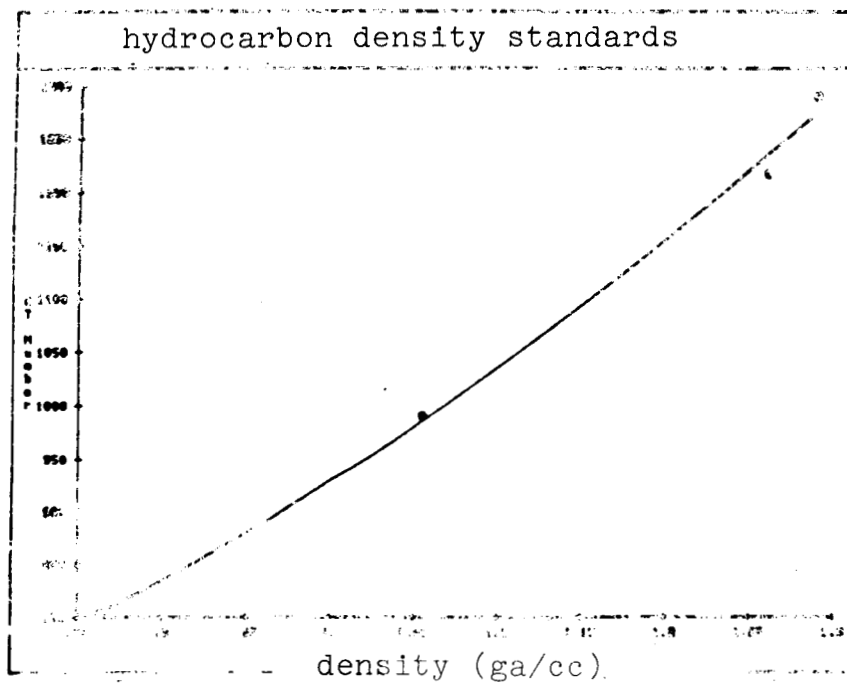
FIGURE 7-8. Calibration graph of density standards within furnace.
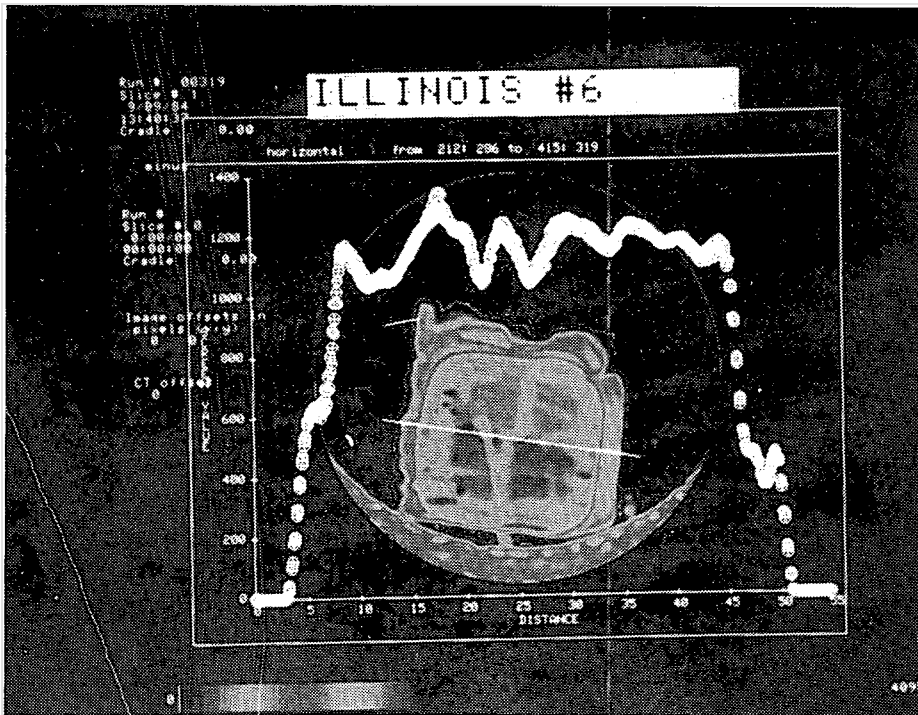
Figure 7-9. Illinois #6 pyrolysis, 850 °C, 120 s, Color LUT
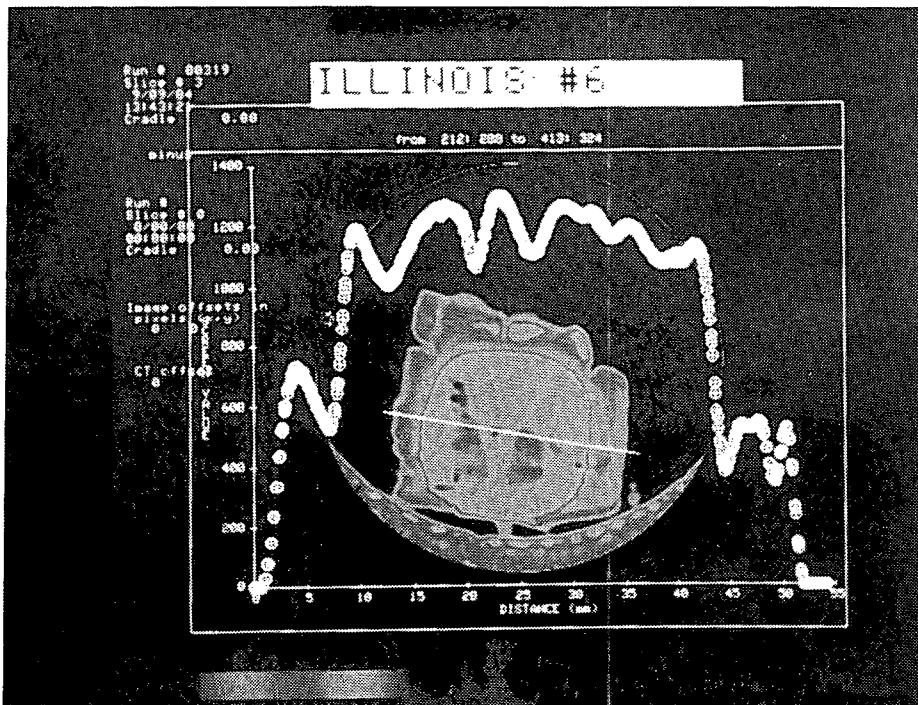
Figure 7-10. Illinois #6 pyrolysis, 850 °C, 284 s, Color LUT
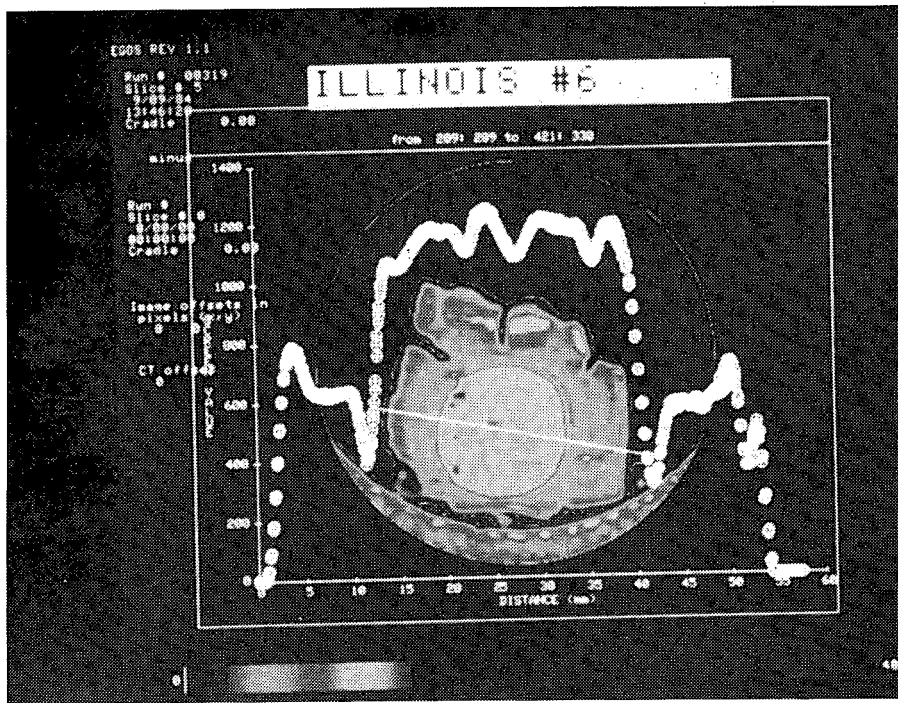
Figure 7-11. Illinois #6 pyrolysis, 850 °C, 473 s, Color LUT

Figure 7-12. Illinois #6 pyrolysis, 850 °C, 535 s, Color LUT
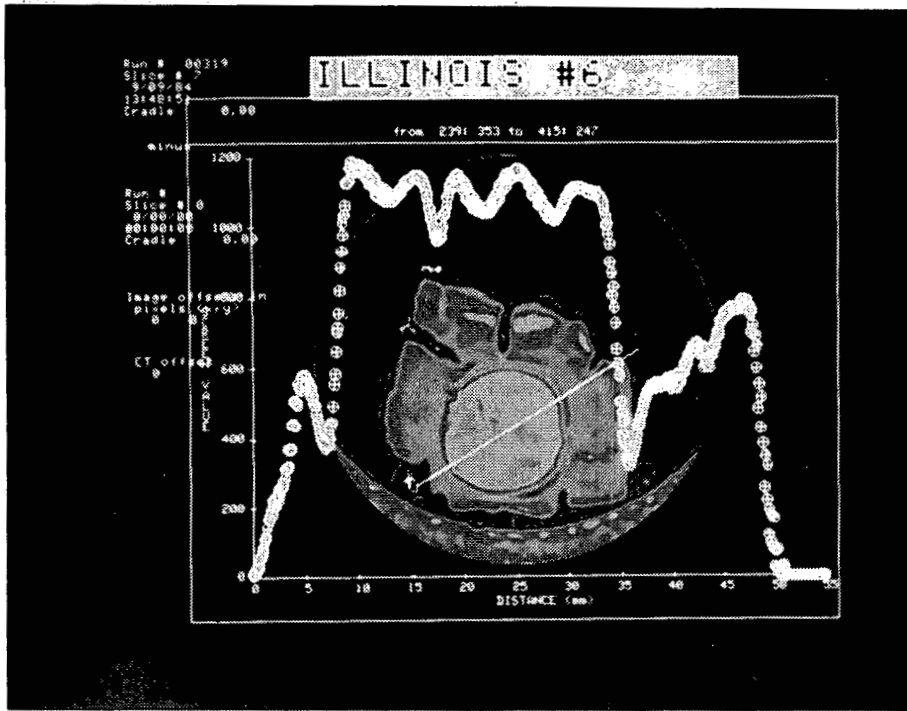
Figure 7-13. Illinois #6 pyrolysis, 850 °C, 614 s, Color LUT
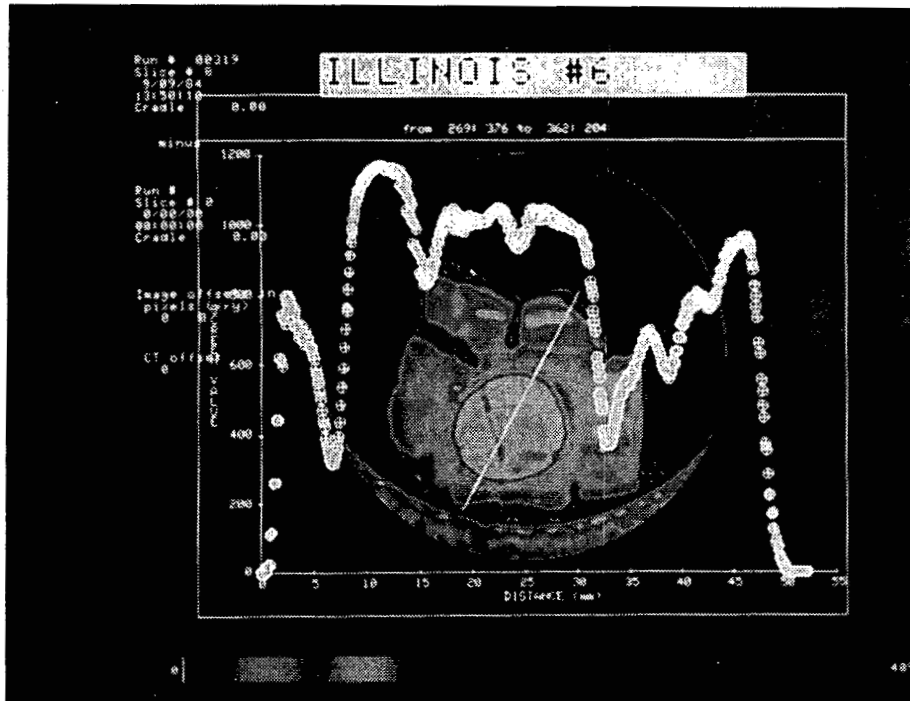
Figure 7-14. Illinois #6 pyrolysis, 850 °C, 693 s, Color LUT

7-35
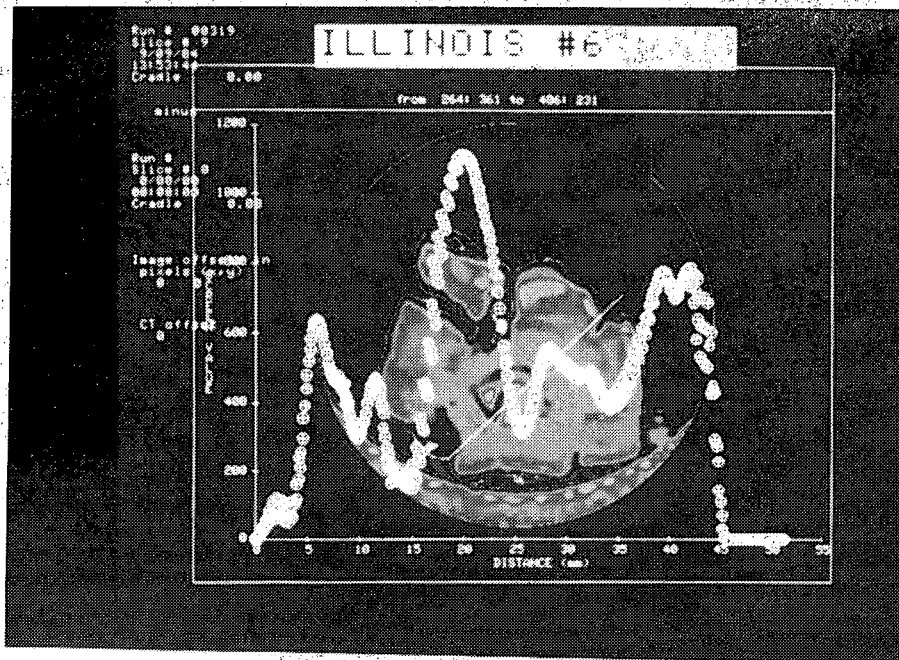
Figure 7-15. Illinois #6 pyrolysis, 850 °C, 907 s, Color LUT
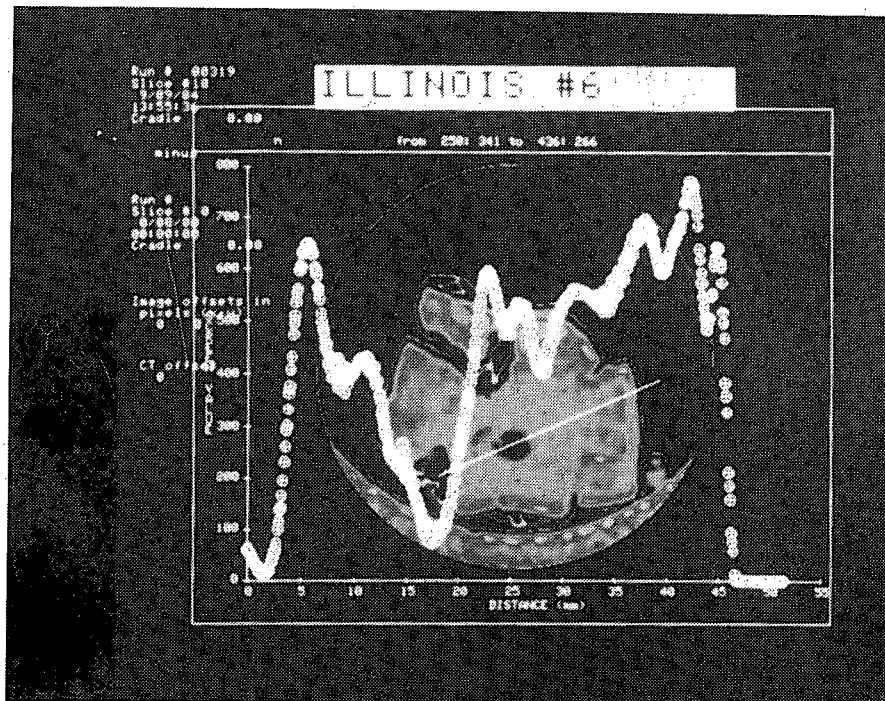
Figure 7-16. Illinois #6 pyrolysis, 850 °C, 1019 s, Color LUT
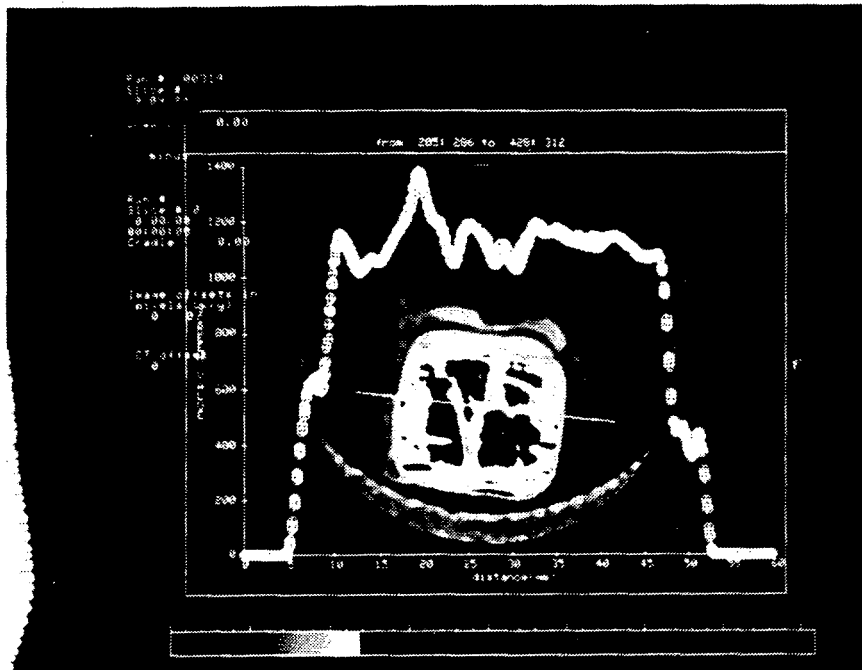
Figure 7-17. Illinois #6 pyrolysis, 850 °C, 120 s, Full line
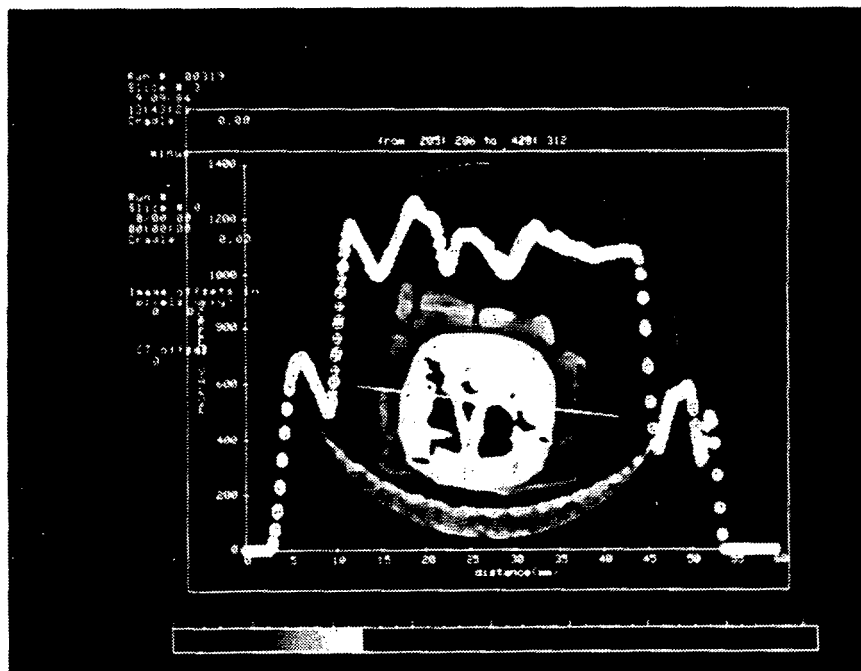
Figure 7-18. Illinois #6 pyrolysis, 850 °C, 284 s, Full line
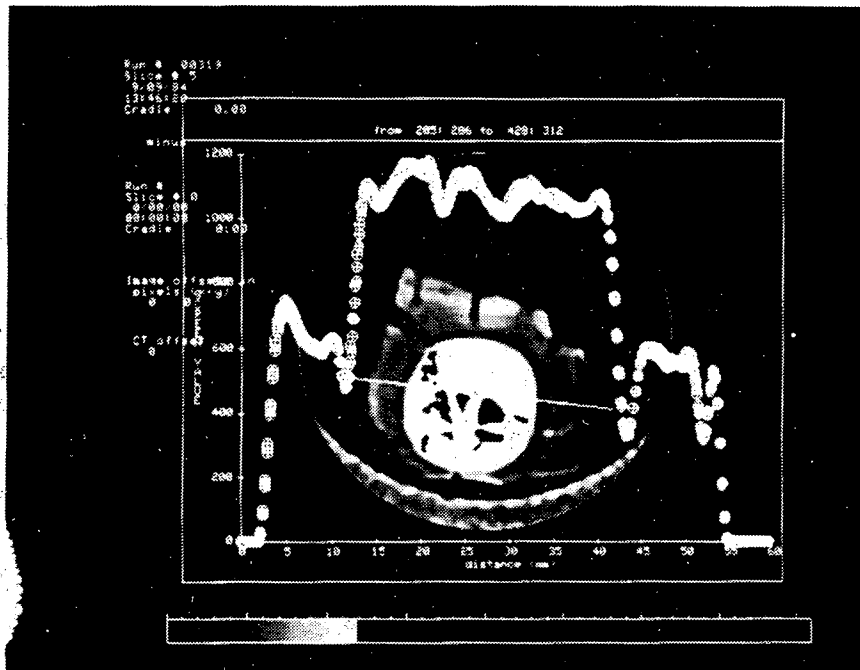
Figure 7-19. Illinois #6 pyrolysis, 850 °C, 473 s, Full line
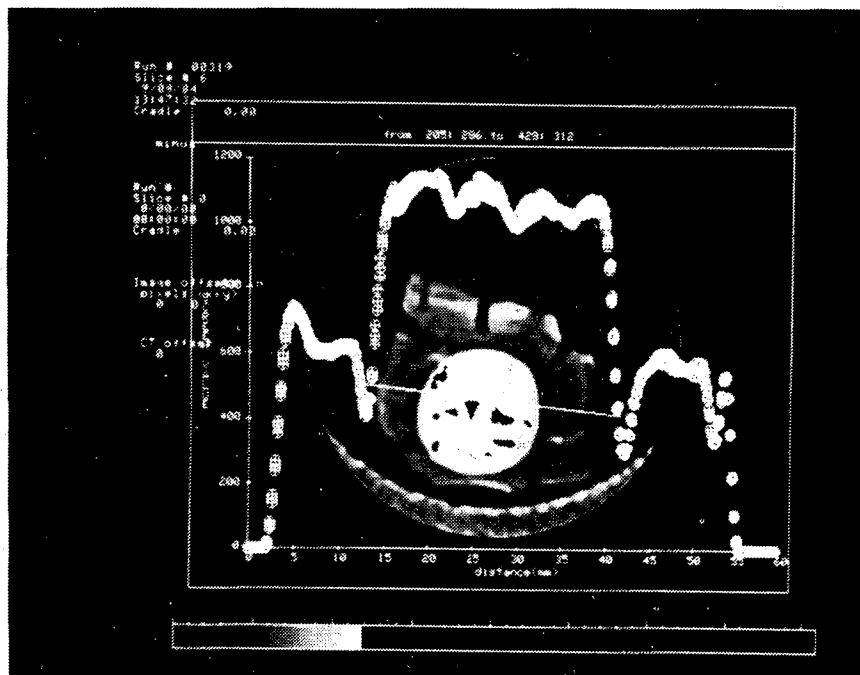
Figure 7-20. Illinois #6 pyrolysis, 850 °C, 535 s, Full line
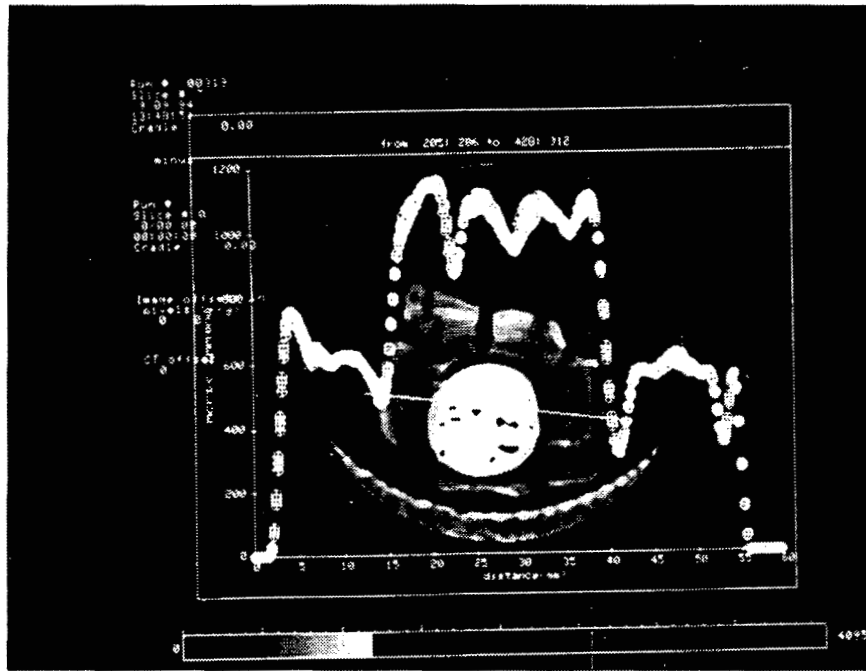
Figure 7-21. Illinois #6 pyrolysis, 850 °C, 614 s, Full line
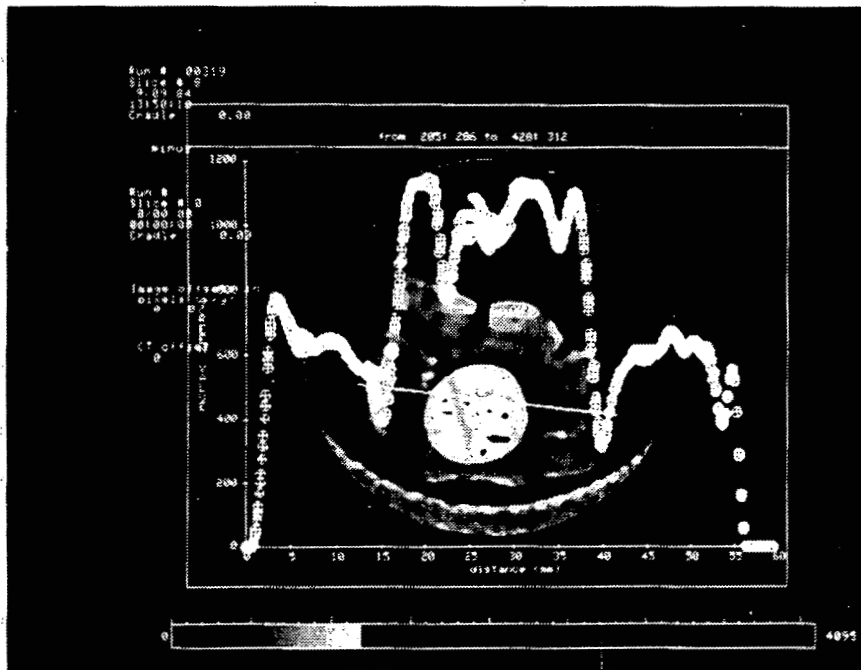
Figure 7-22. Illinois #6 pyrolysis, 850 °C, 693 s, Full line
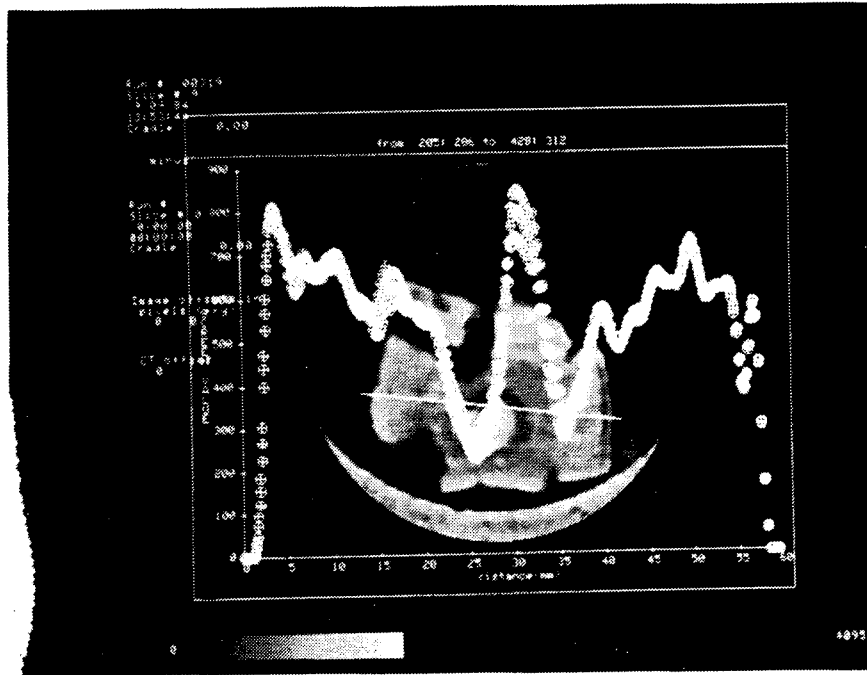
Figure 7-23. Illinois #6 pyrolysis, 850 °C, 907 s, Full line
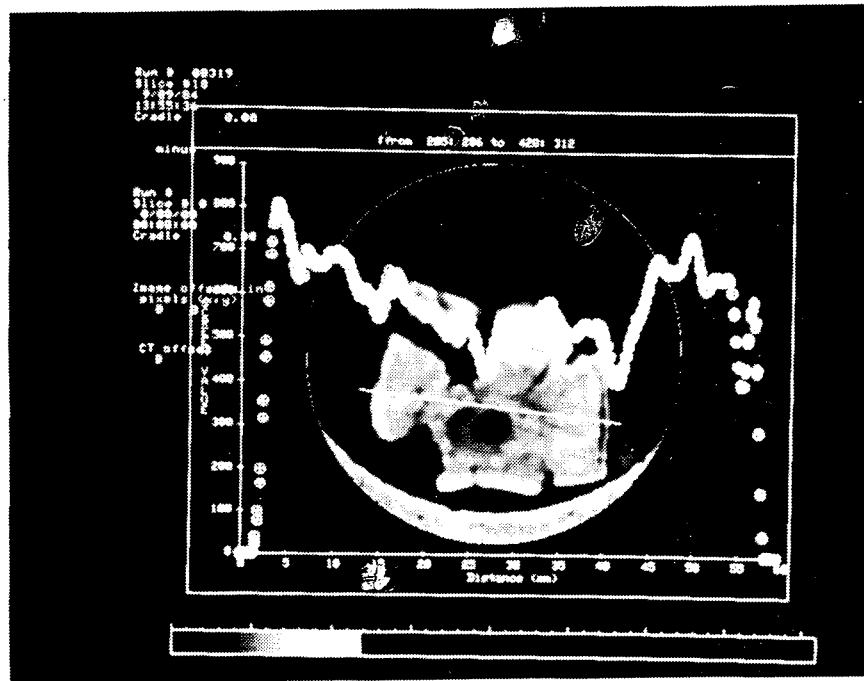
Figure 7-24. Illinois #6 pyrolysis, 850 °C, 1019 s, Full line
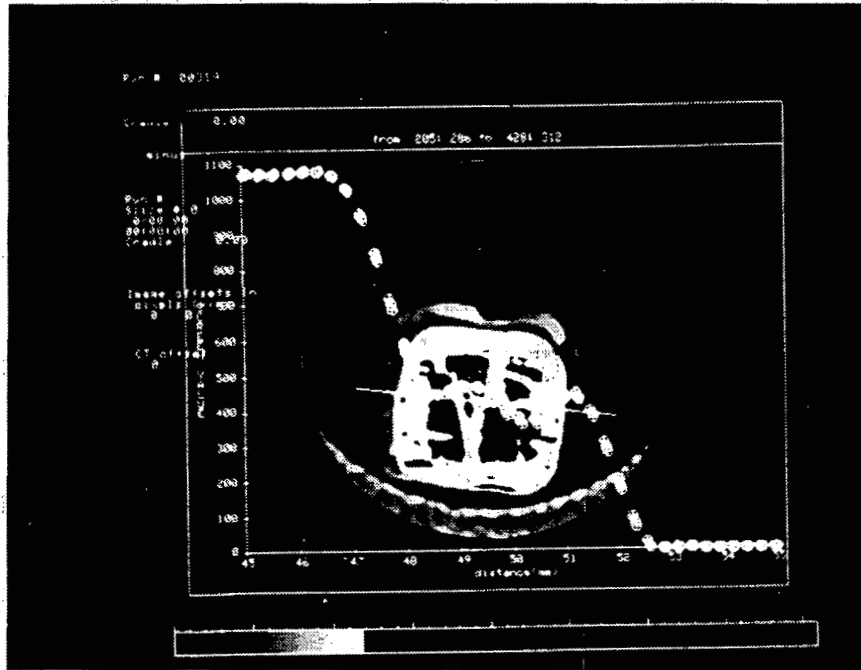
Figure 7-25. Illinois #6 pyrolysis, 850 °C, 120 s, Edge Expanded
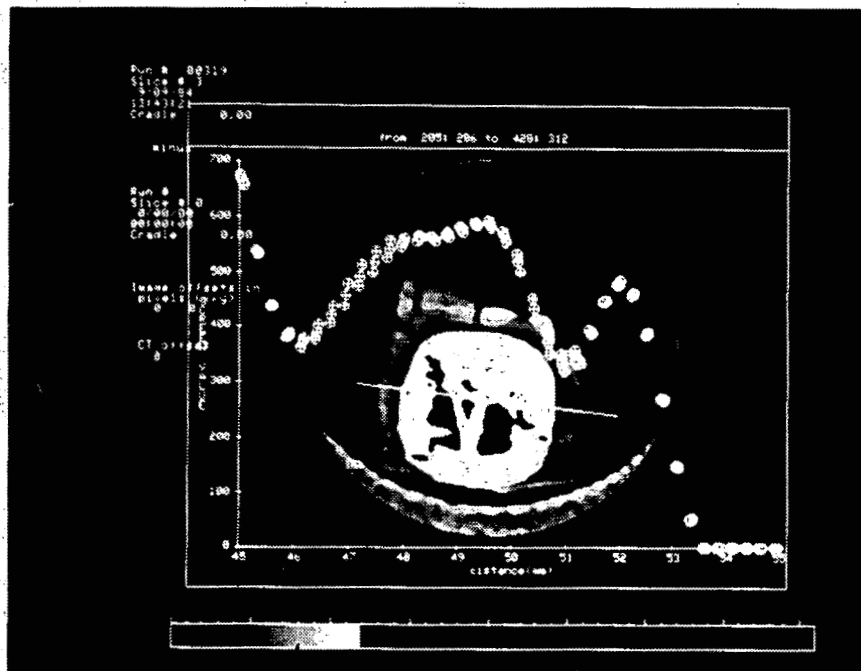
Figure 7-26. Illinois #6 pyrolysis, 850 °C, 284 s, Edge Expanded
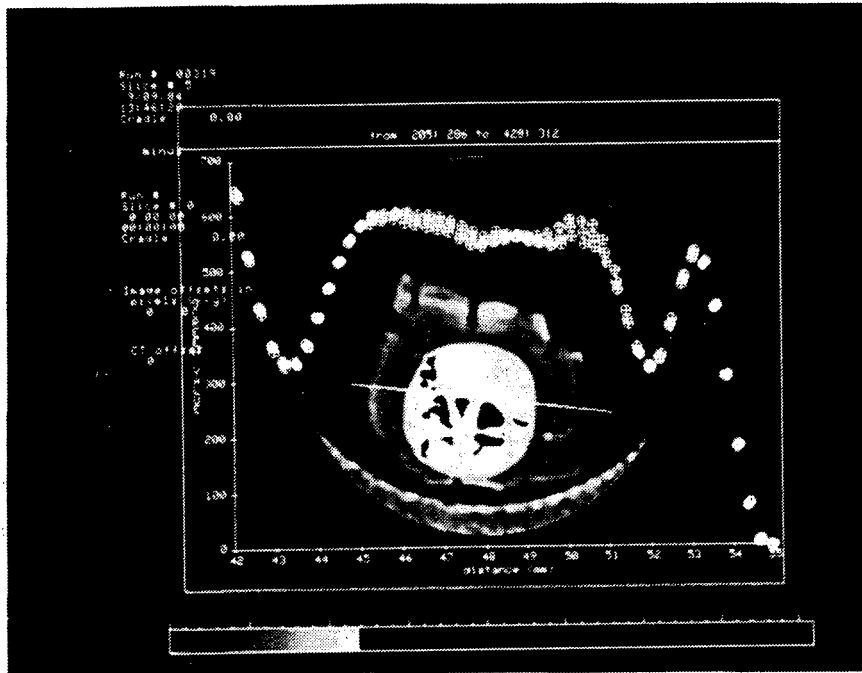
Figure 7-27. Illinois #6 pyrolysis, 850 °C, 473 s, Edge Expanded
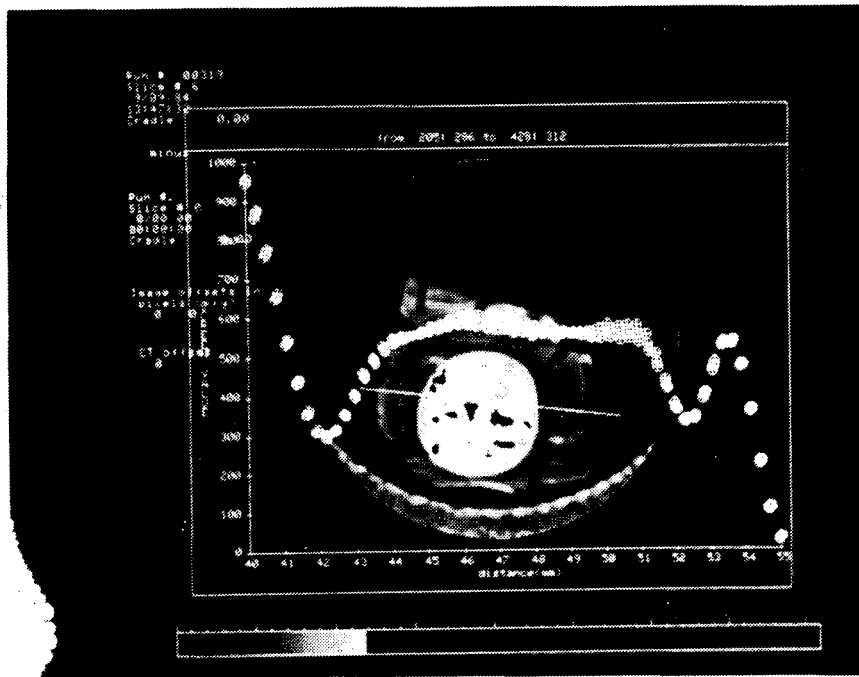
Figure 7-28. Illinois #6 pyrolysis, 850 °C, 535 s, Edge Expanded
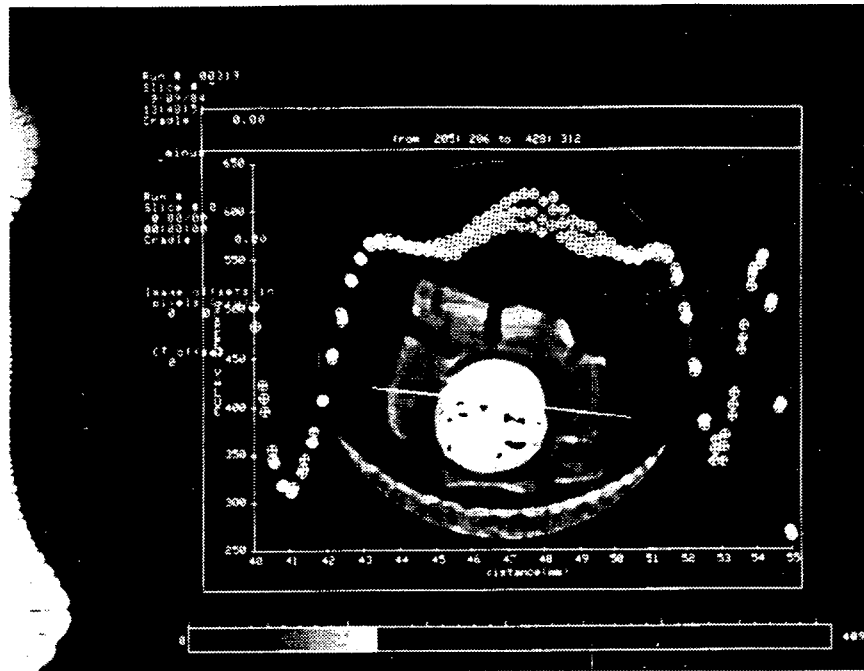
Figure 7-29. Illinois #6 pyrolysis, 850 °C, 614 s, Edge Expanded
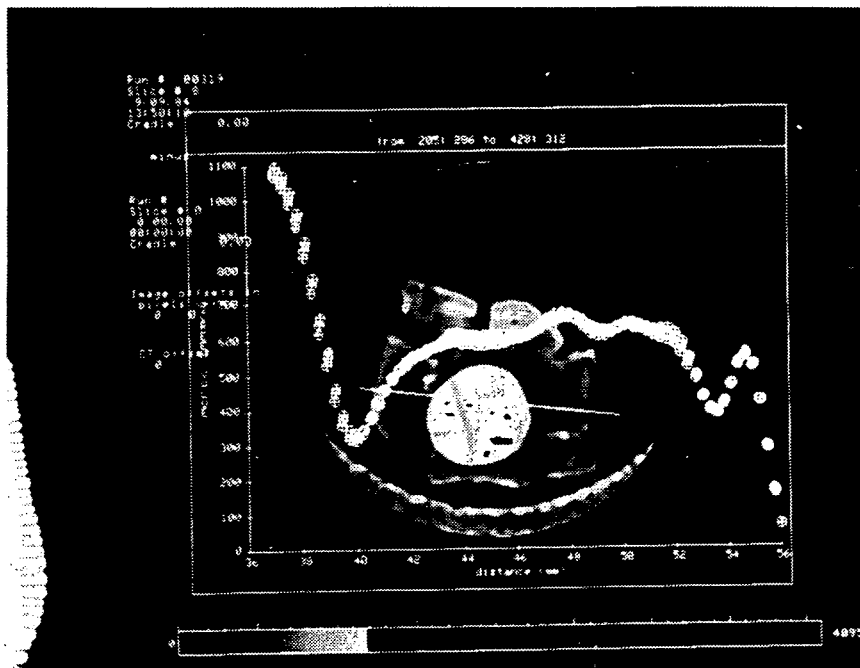
Figure 7-30. Illinois #6 pyrolysis, 850 °C, 693 s, Edge Expanded
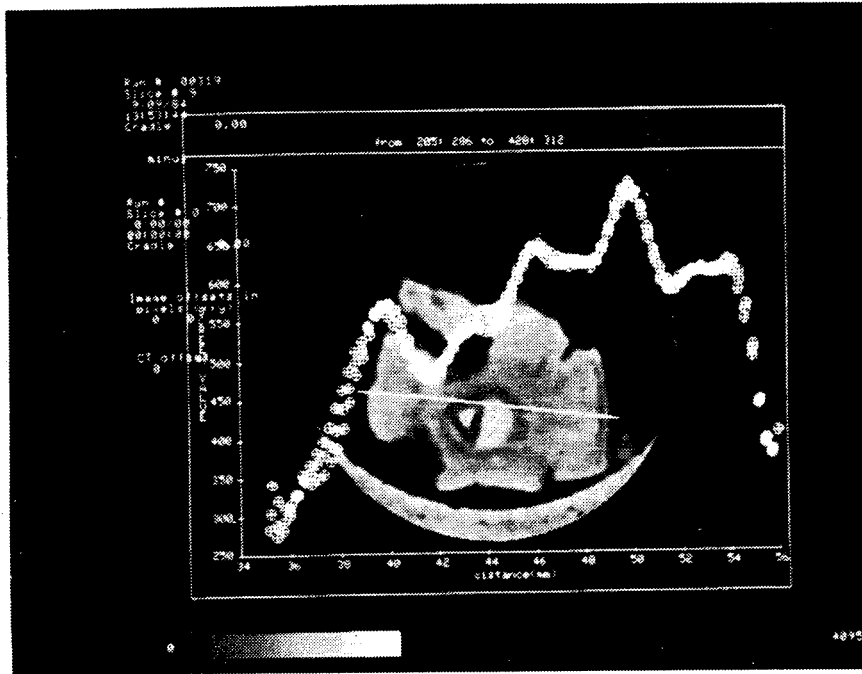
Figure 7-31. Illinois #6 pyrolysis, 850 °C, 907 s, Edge Expanded
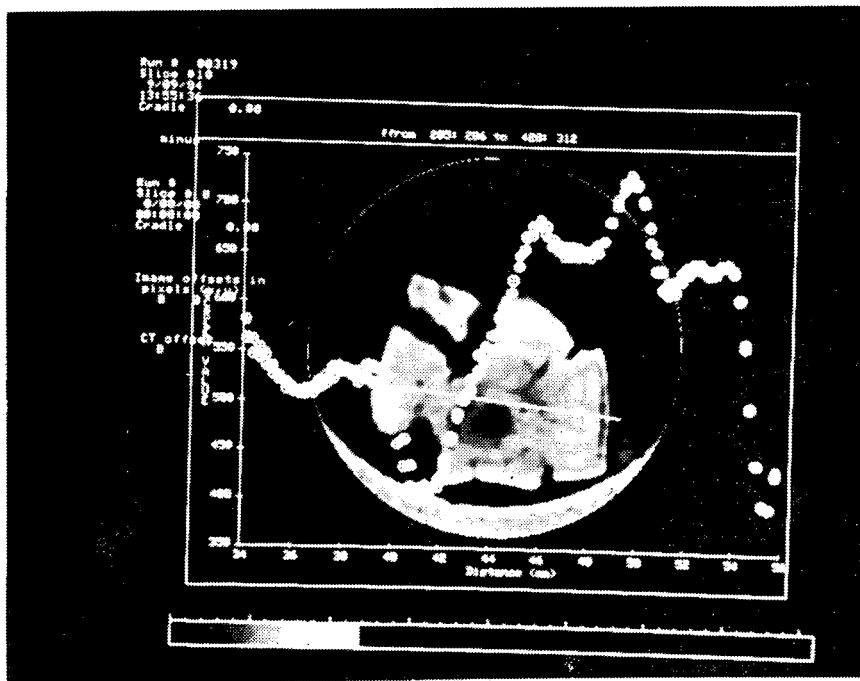
Figure 7-32. Illinois #6 pyrolysis, 850 °C, 1019 s, Edge Expanded
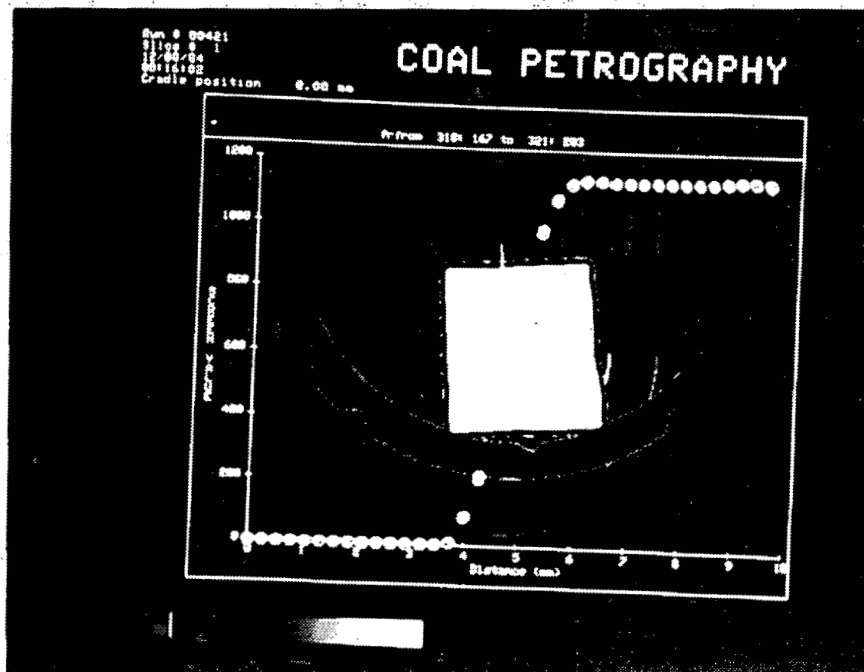
Figure 7-33. CT number at edge of coal
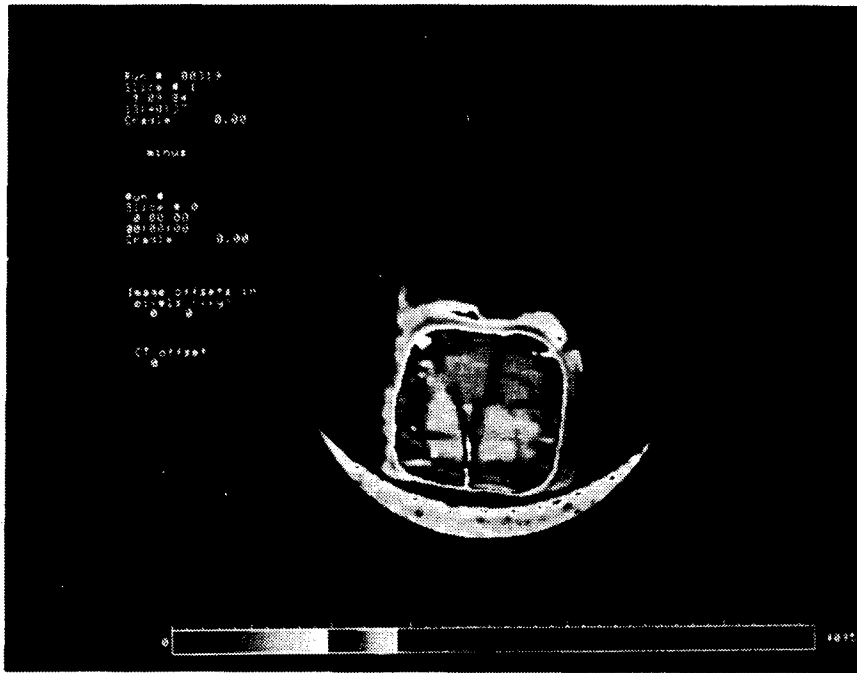
Figure 7-34. Illinois #6 pyrolysis, 850 °C, 120 s, Double LUT
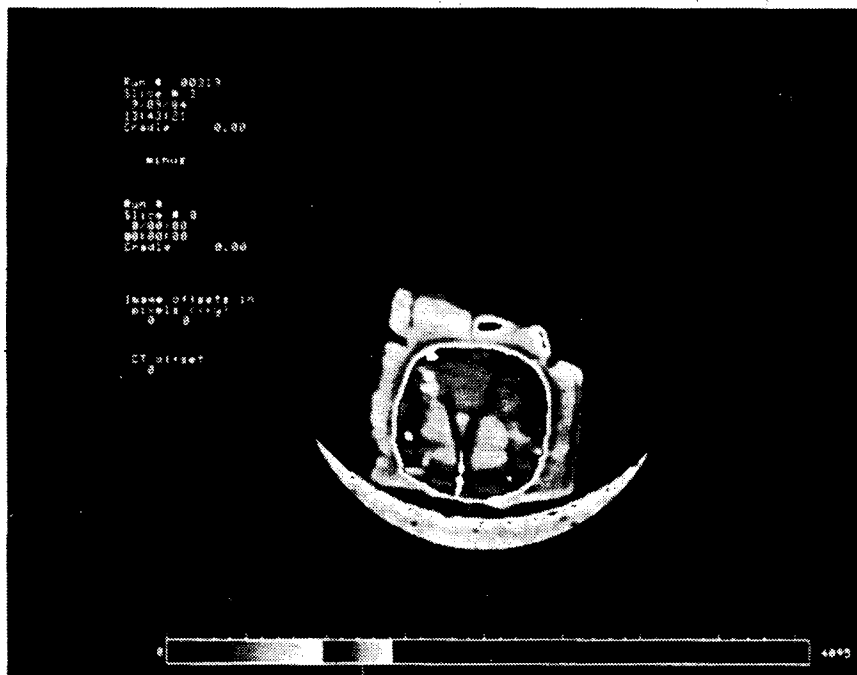
Figure 7-35. Illinois #6 pyrolysis, 850 °C, 284 s, Double LUT
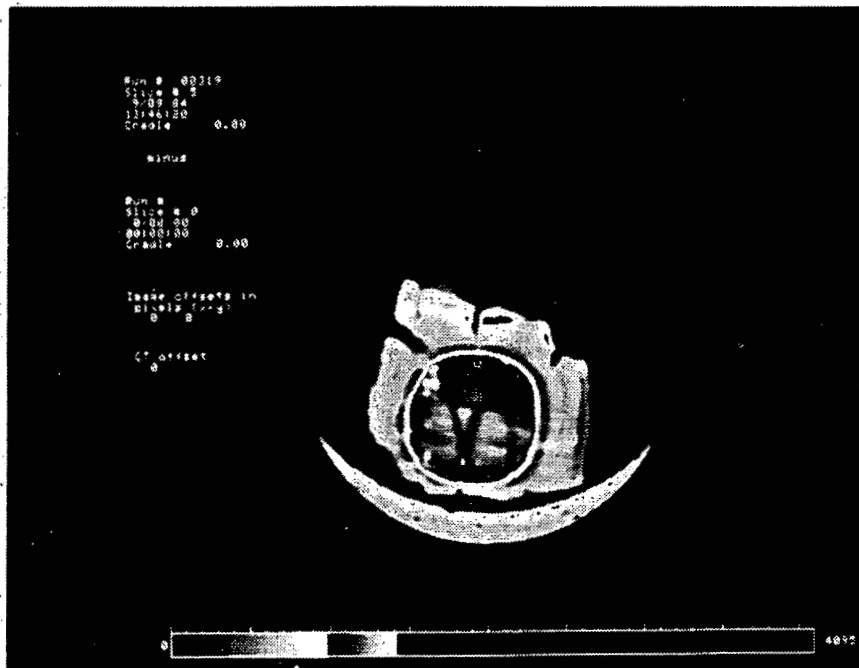
Figure 7-36. Illinois #6 pyrolysis, 850 °C, 473 s, Double LUT
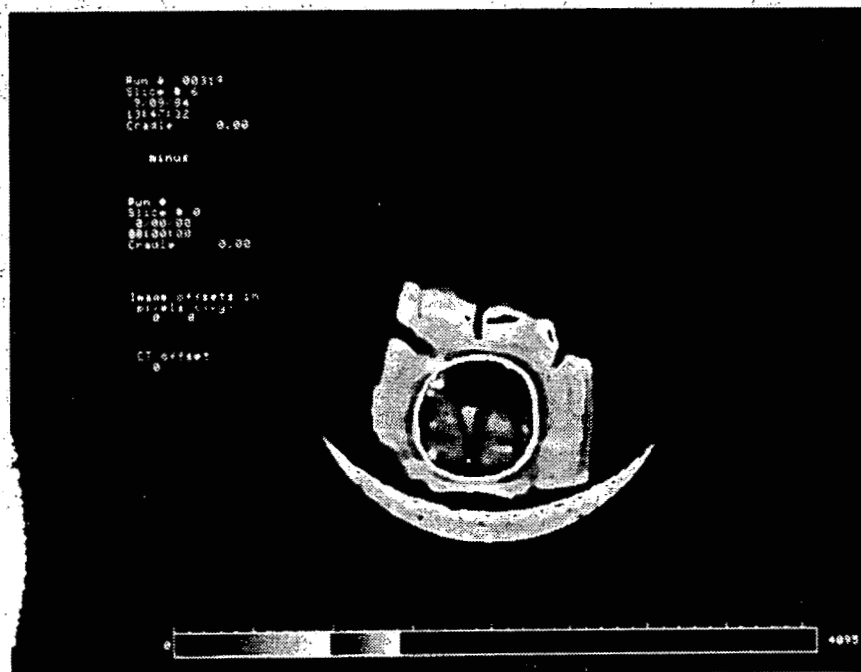
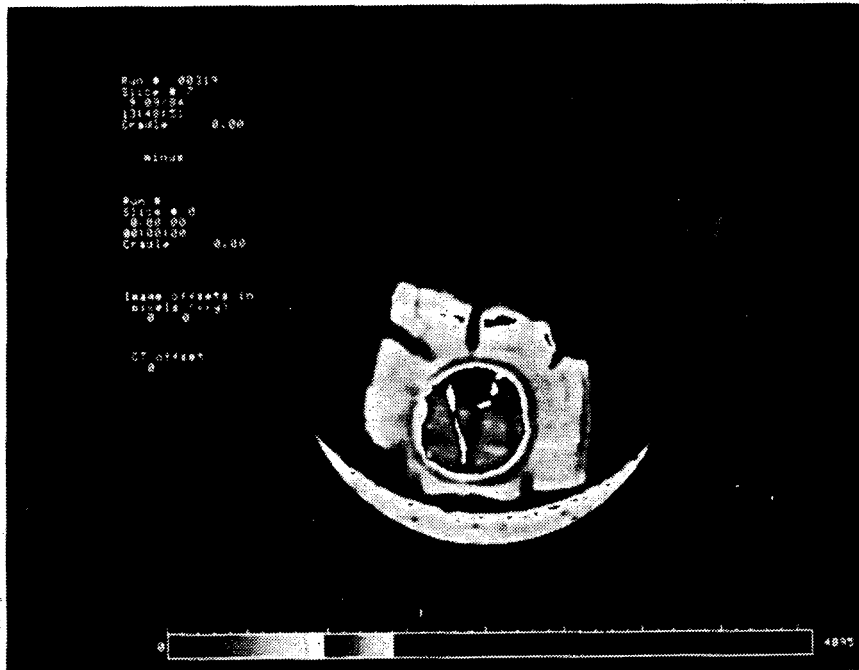
Figure 7-37. Illinois #6 pyrolysis, 850 °C, 535 s, Double LUT

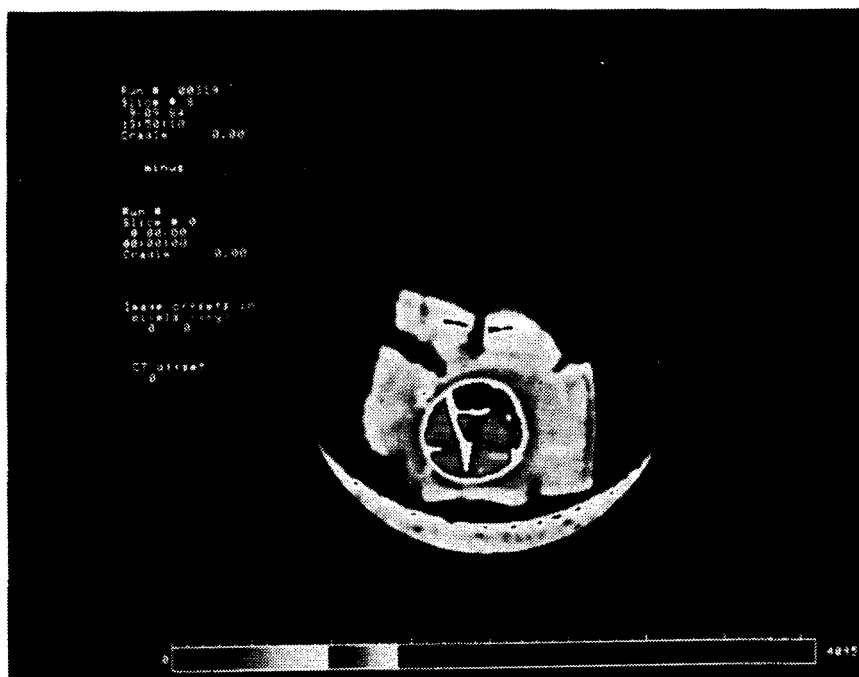**Figure 7-38.** Illinois #6 pyrolysis, 850 °C, 614 s, Double LUT

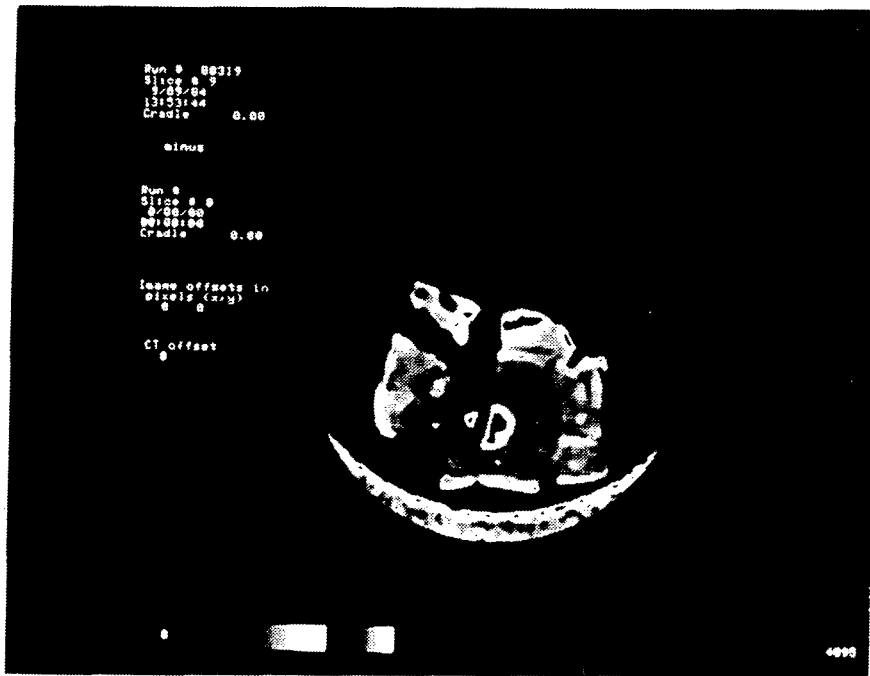**Figure 7-39.** Illinois #6 pyrolysis, 850 °C, 693 s, Double LUT

Figure 7-40. Illinois #6 pyrolysis, 850 °C, 907 s, Double LUT
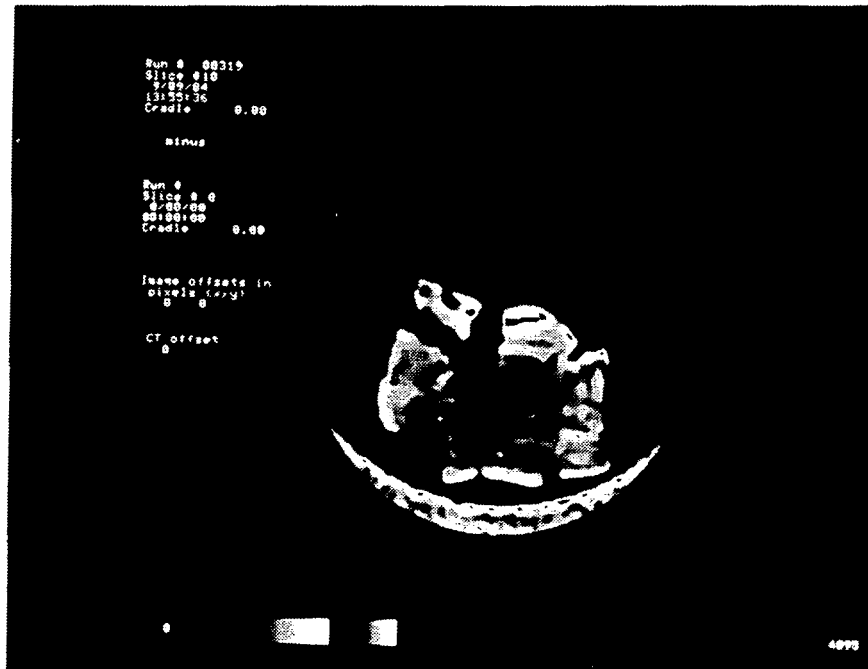

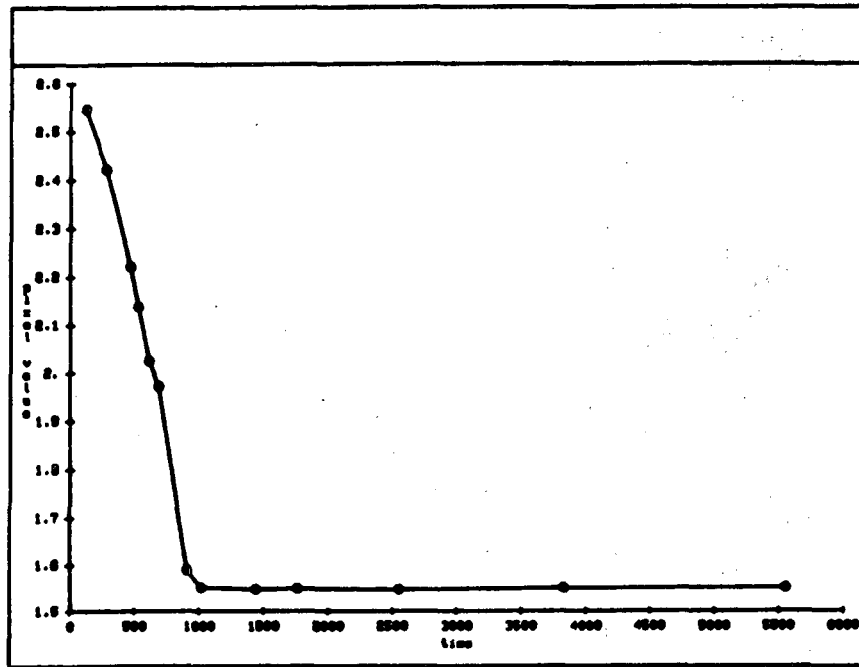**Figure 7-41.** Illinois #6 pyrolysis, 850 °C, 1019 s, Double LUT

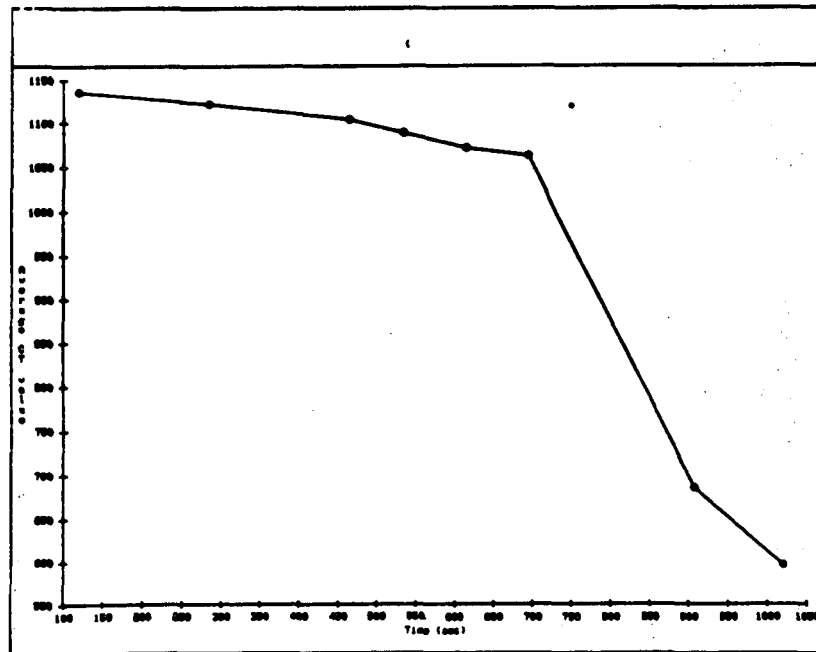**Figure 7-42. Relative CT number total as a function of time**

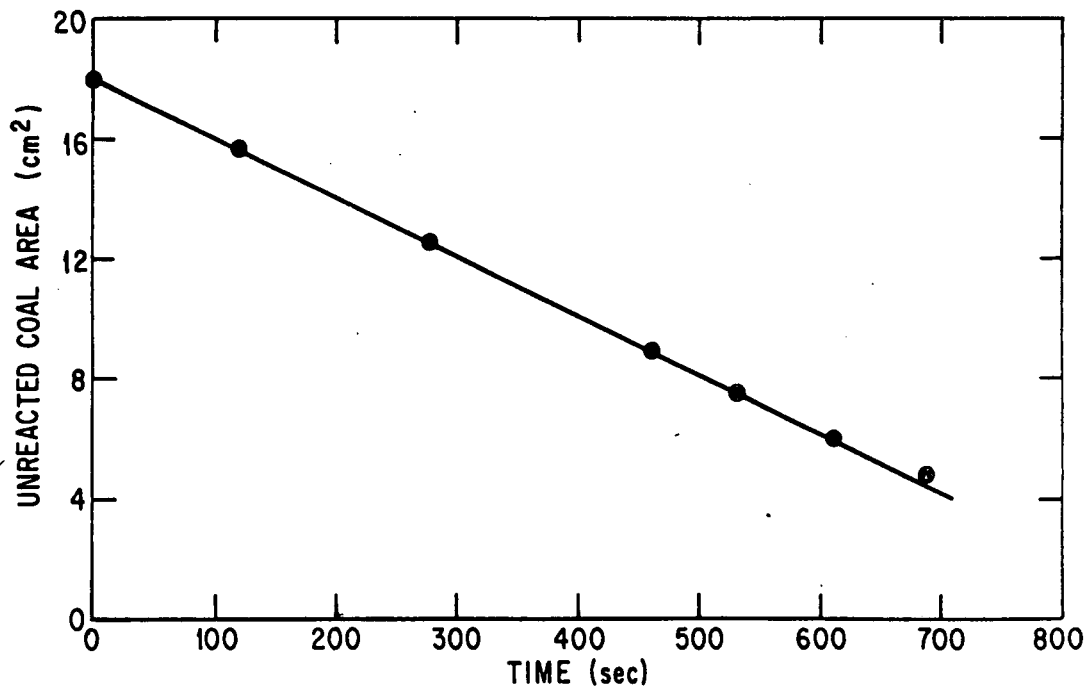**Figure 7-43. CT number for "unaltered" coal vs. time**

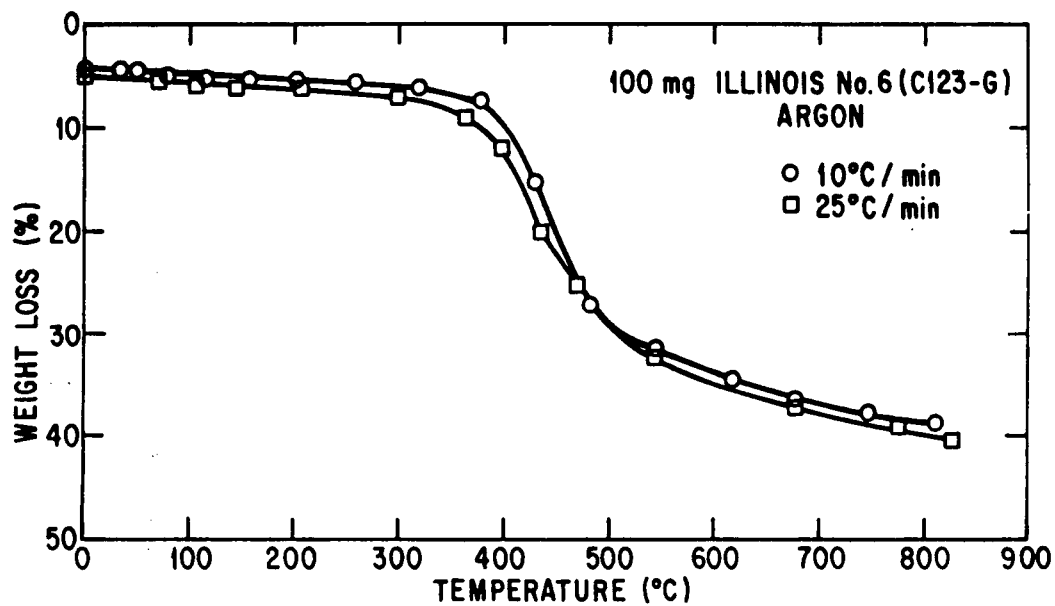Figure 7-44. Pyrolysis – unreacted coal area vs. time

Figure 7-45. Weight loss of Illinois #6 vs. temperature
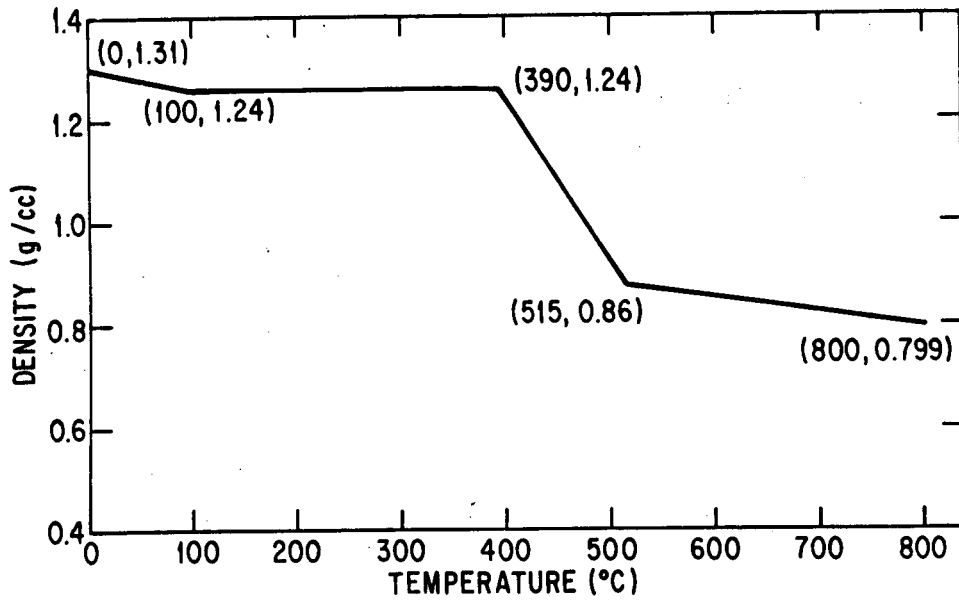
Figure 7-46. Density variation in Illinois #6 vs. temperature
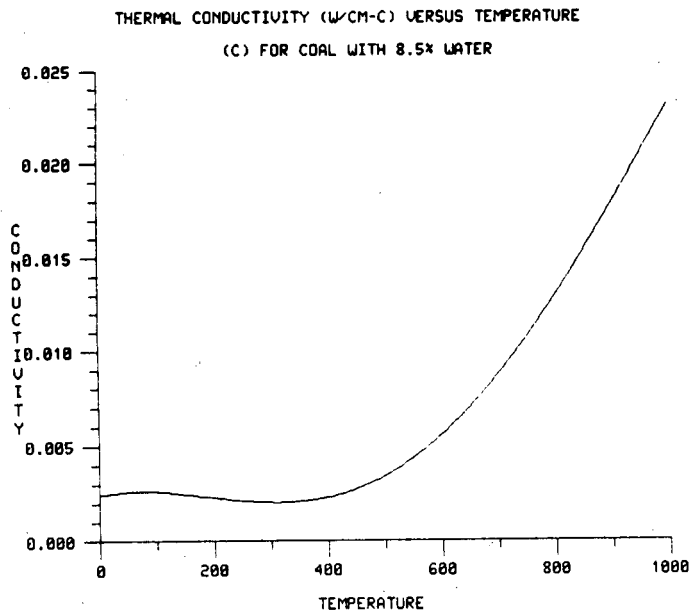
Figure 7-47. Thermal conductivity of coal and char as used in ADINAT

SPECIFIC HEAT (J/GM-C) VERSUS TEMPERATURE (C)
FOR COAL WITH 8.5% WATER
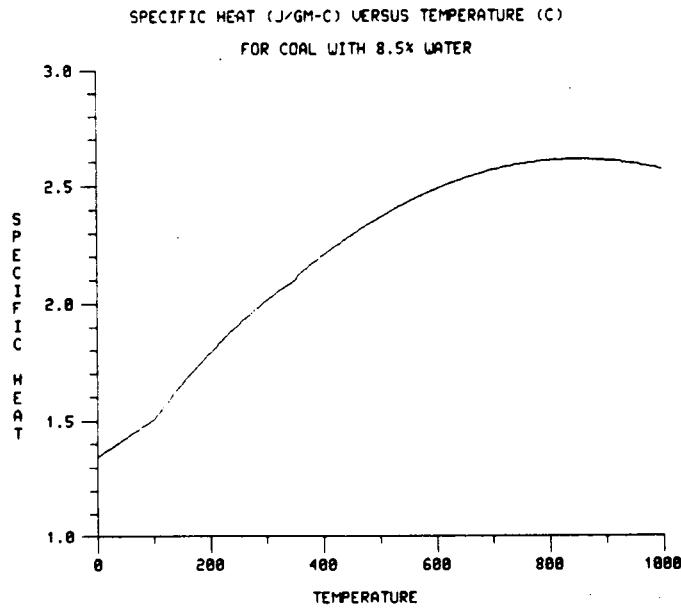
Figure 7-48. Heat capacity of coal and char as used in ADINAT
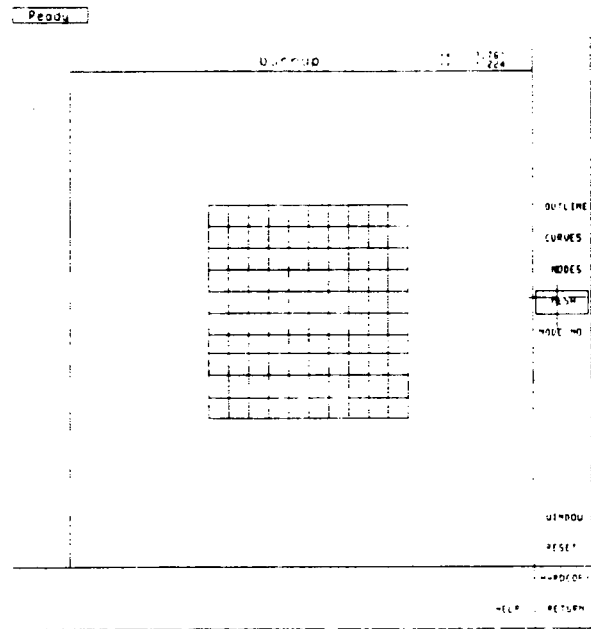
Figure 7-49. Grid pattern used in ADINAT for one coal quadrant
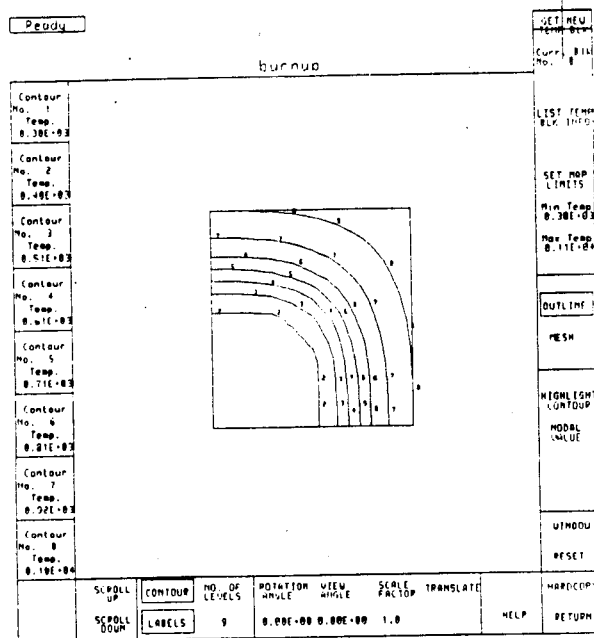
Figure 7-50. ADINAT temperature contours 240 s after 850 °C start
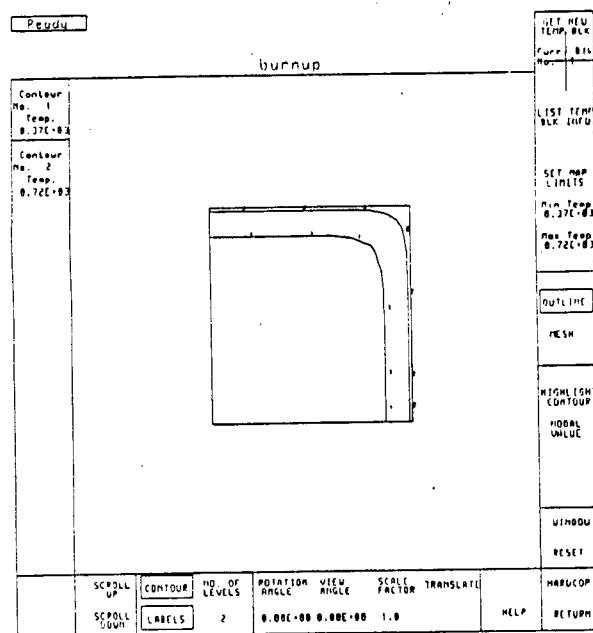
Figure 7-51. ADINAT steam and pyrolysis contours at 30 s
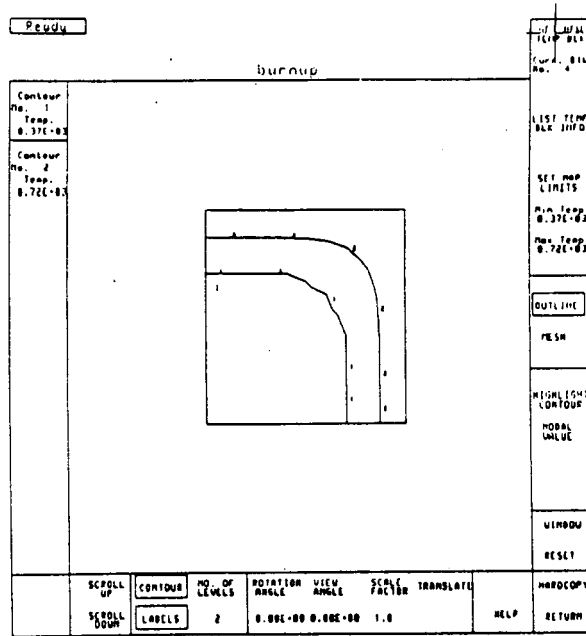
Figure 7-52. ADINAT steam and pyrolysis contours at 120 s
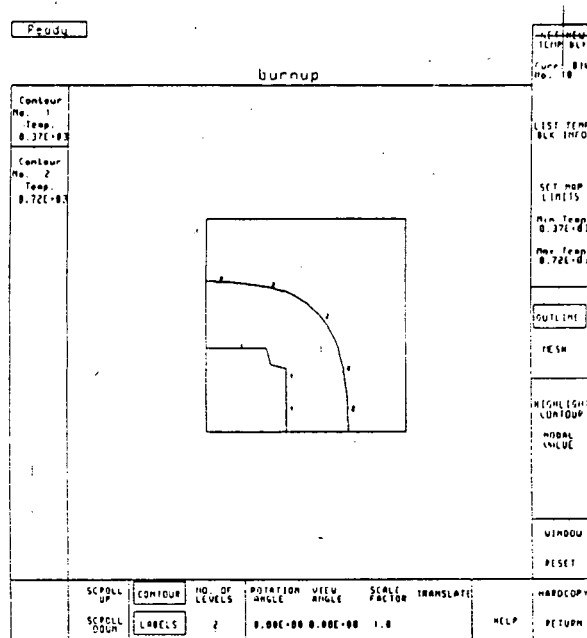
Figure 7-53. ADINAT steam and pyrolysis contours at 300 s
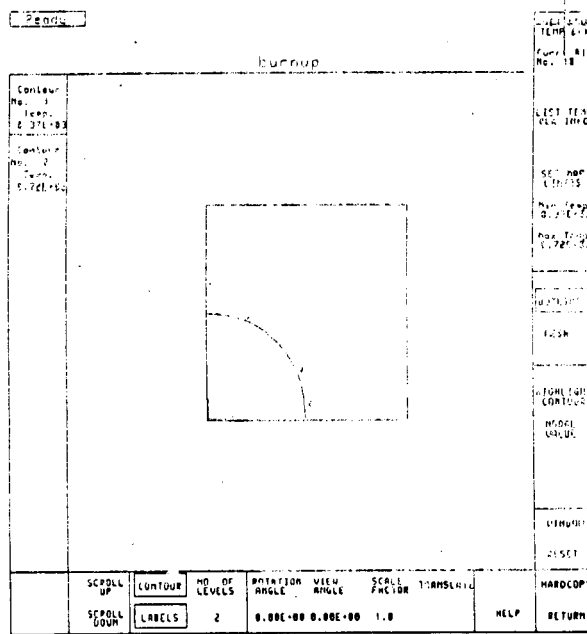
Figure 7-54. ADINAT steam and pyrolysis contours at 540 s
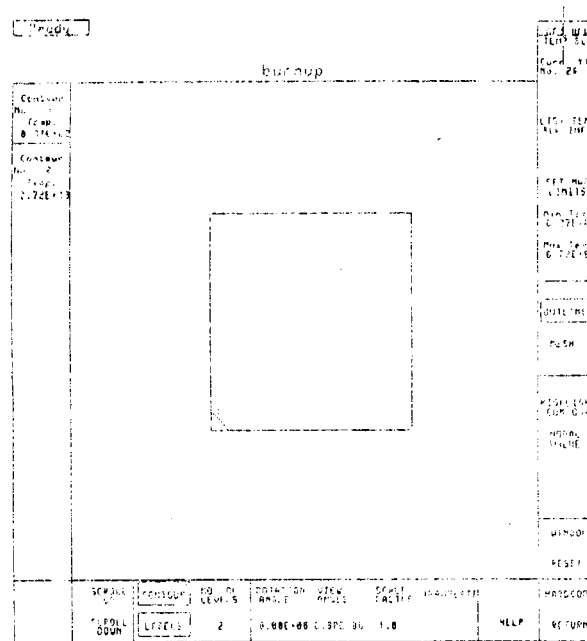
Figure 7-55. ADINAT steam and pyrolysis contours at 780 s

7-56
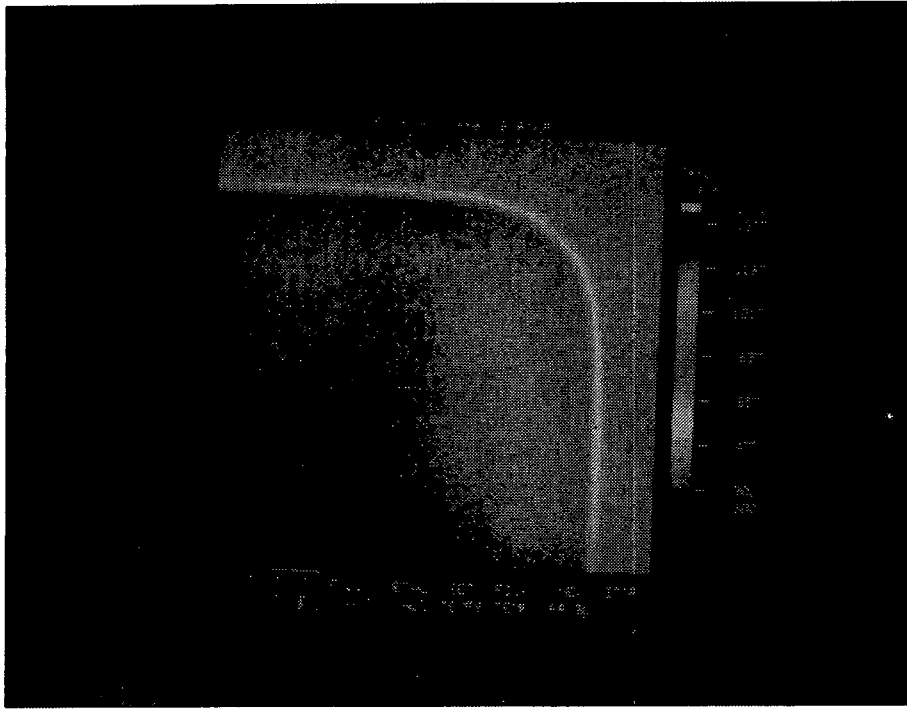
Figure 7-56. ADINAT density image at 120 s
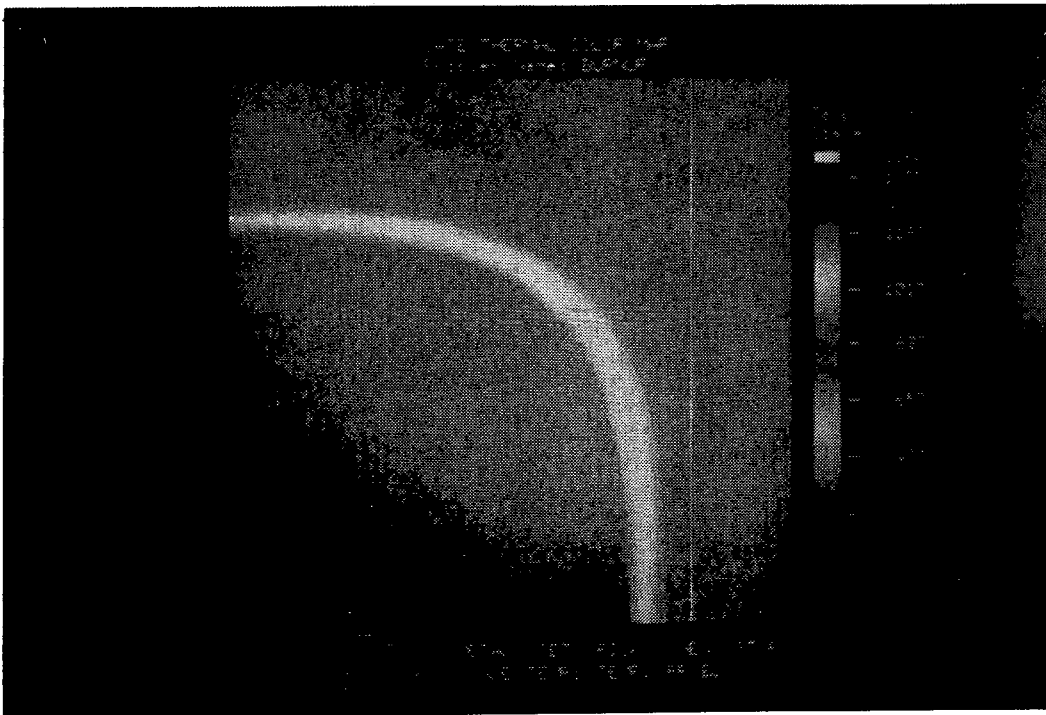
Figure 7-57. ADINAT density image at 270 s
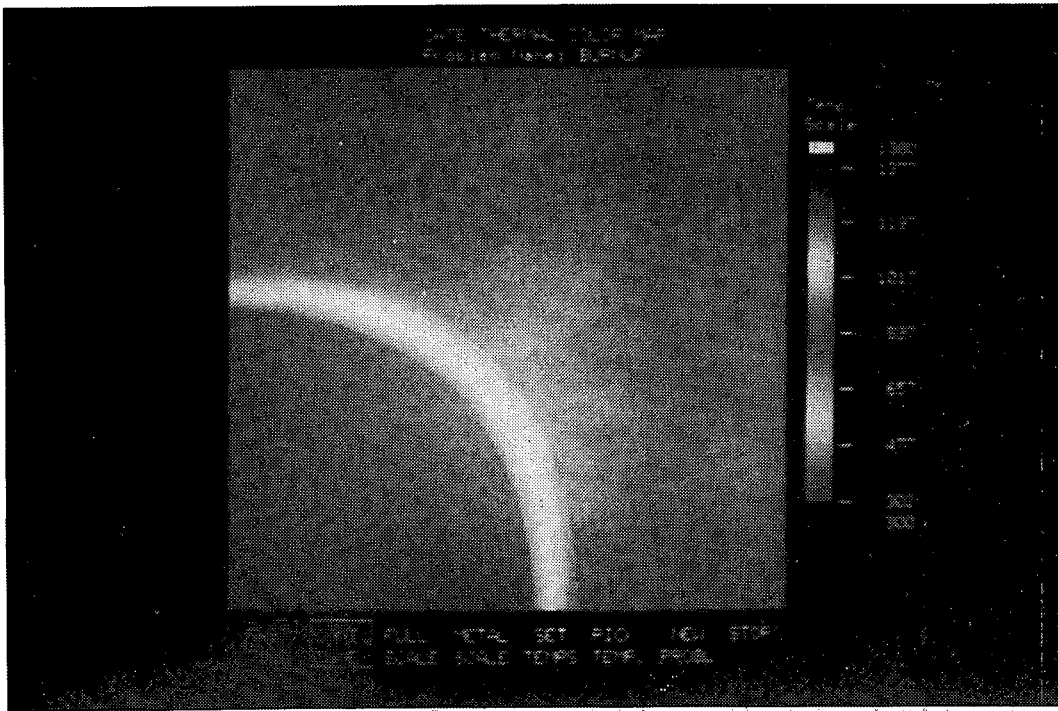
Figure 7-58. ADINAT density image at 450 s
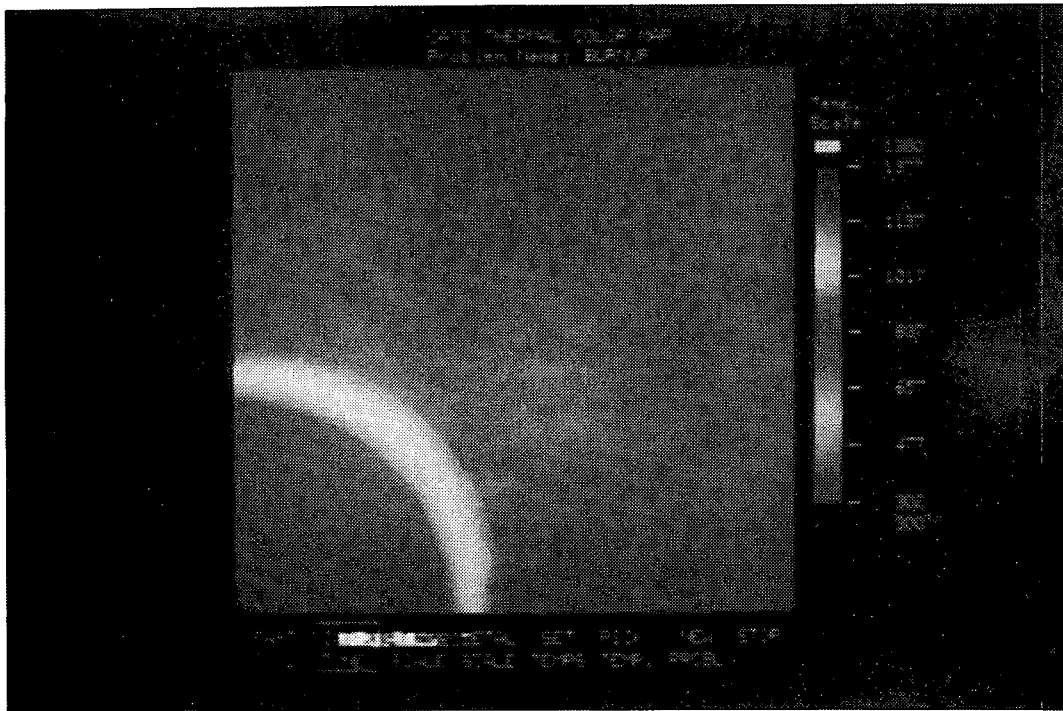
Figure 7-59. ADINAT density image at 540 s
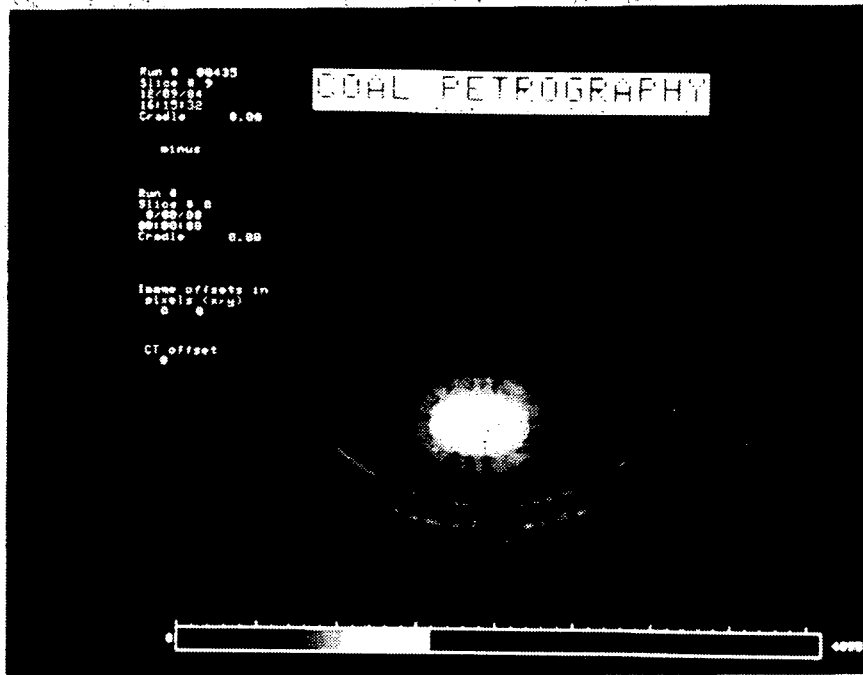
Figure 7-60. CT image of lignite during pyrolysis
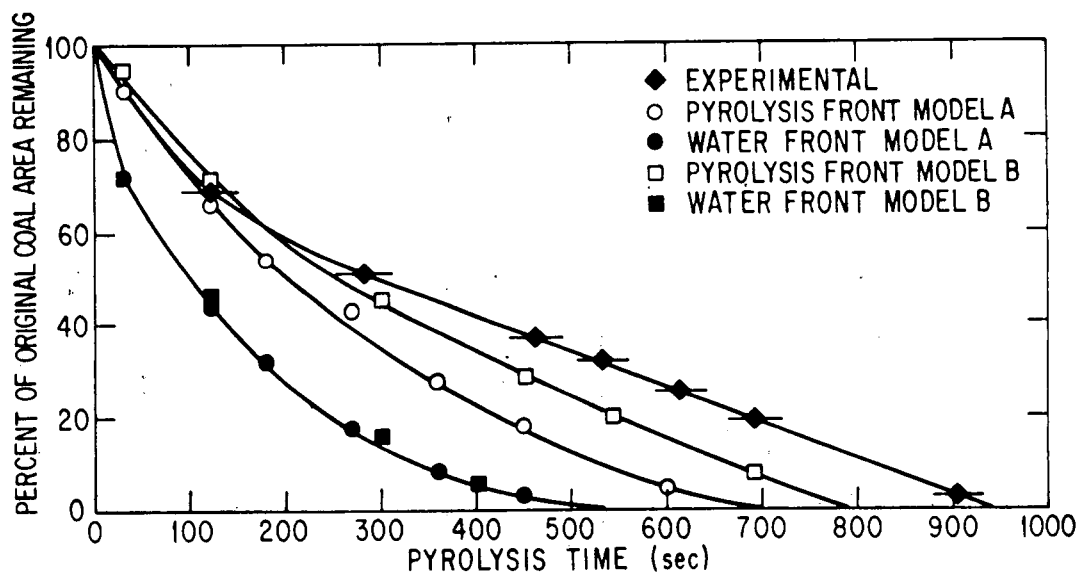
Figure 7-61. Comparison of CT and ADINAT results
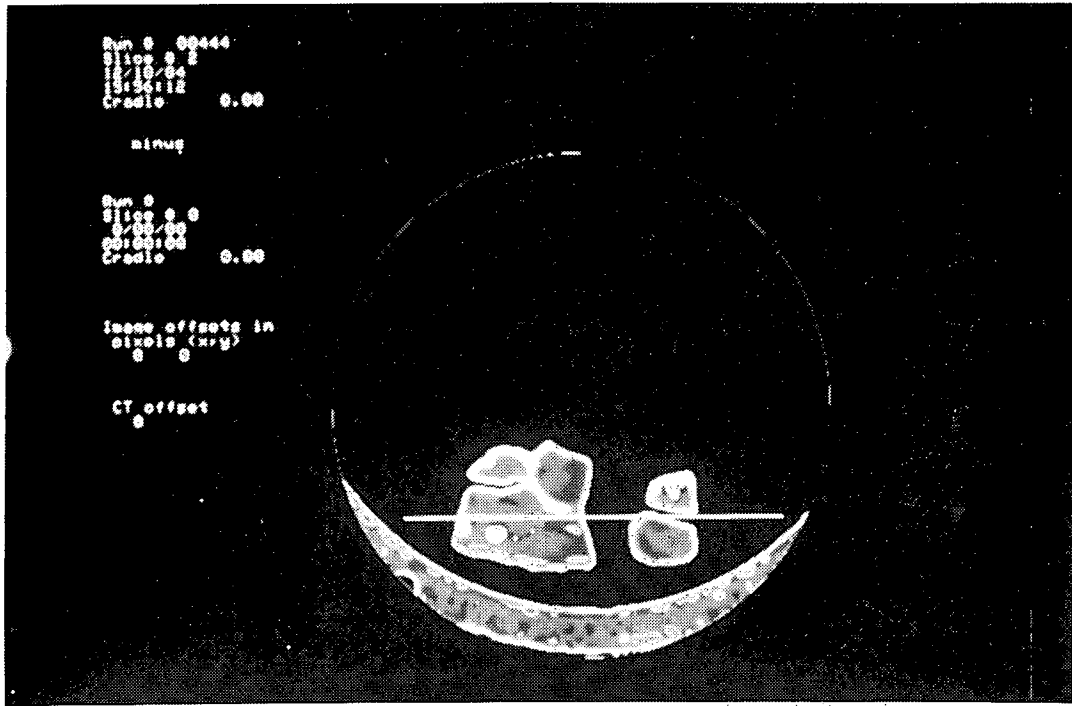
Figure 7-62. Illinois #6 plate taken at the onset of gasification in steam. The horizontal line through the slice was the one used in analysis (Run 444).
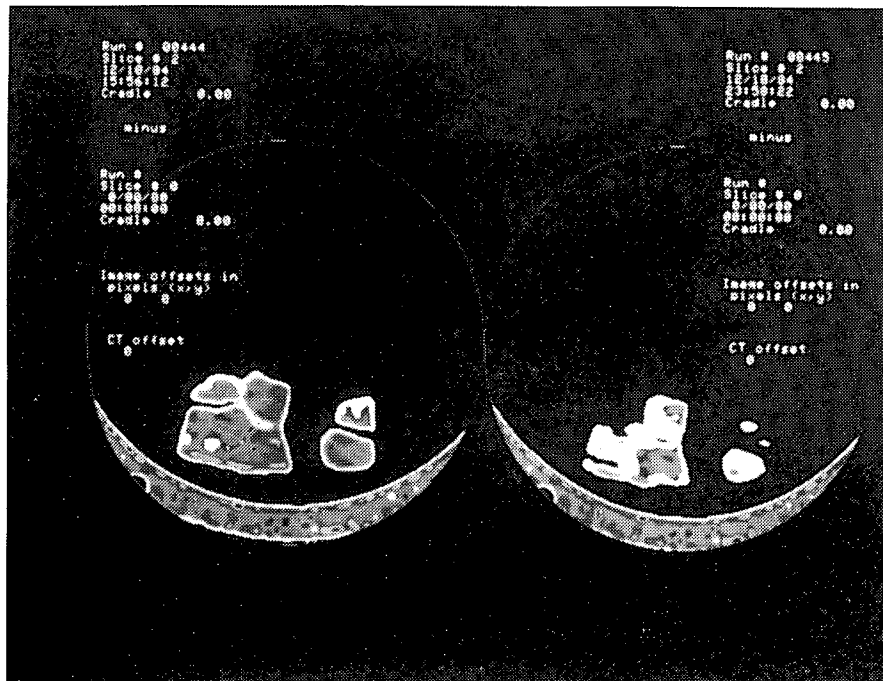
Figure 7-63. Illinois #6 char at the onset and near the end of steam gasification (Run 444)
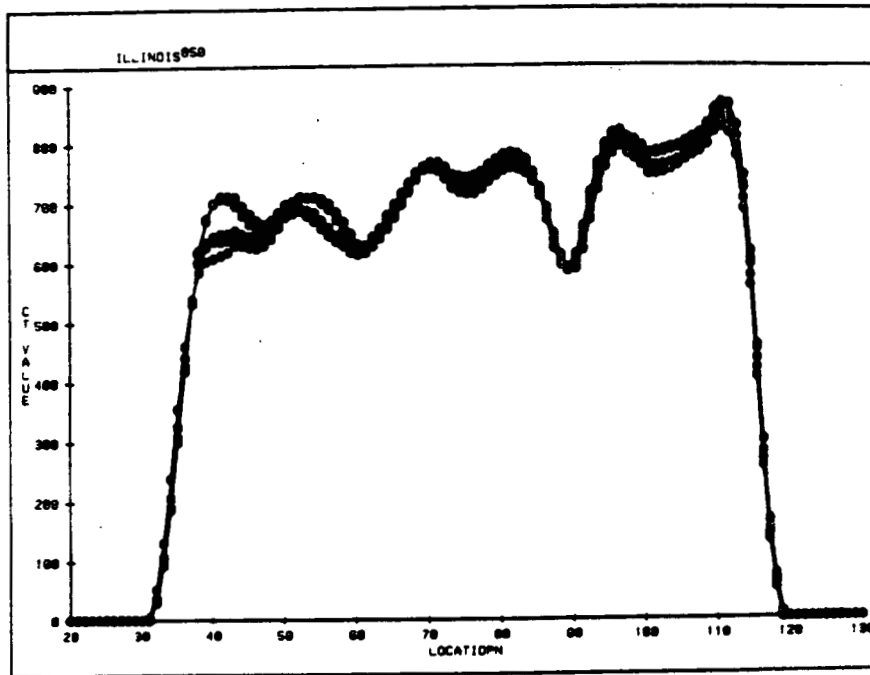
Figure 7-64. Plots of CT values along the line shown in Figure 7-63, taken during isothermal gasification at 850 °C
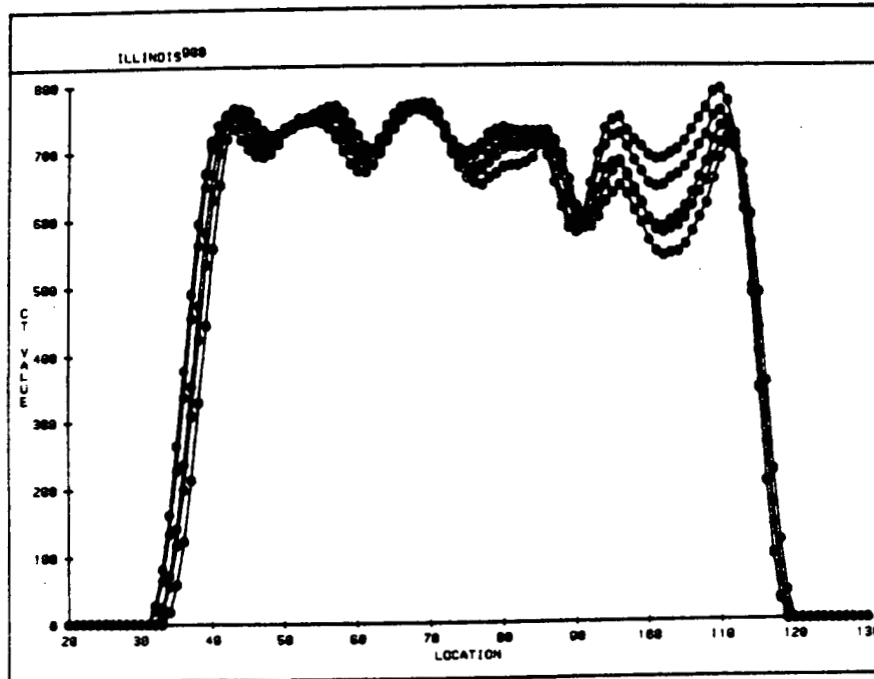
Figure 7-65. Plots of CT values along the line shown in Figure 7-63, taken during isothermal gasification at 900 °C
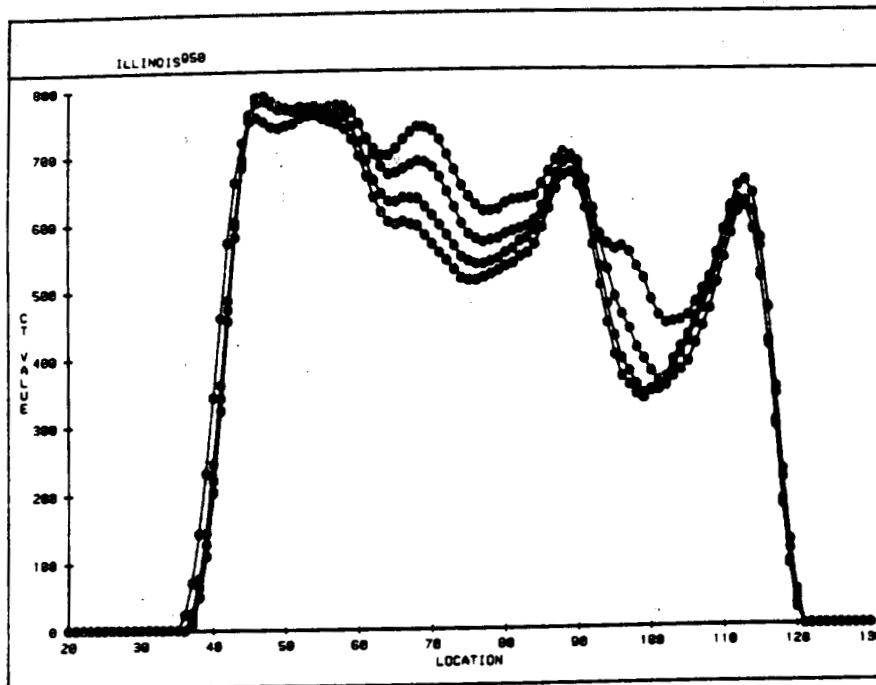
Figure 7-66. Plots of CT values along the line shown in Figure 7-63, taken during isothermal gasification at 950 °C
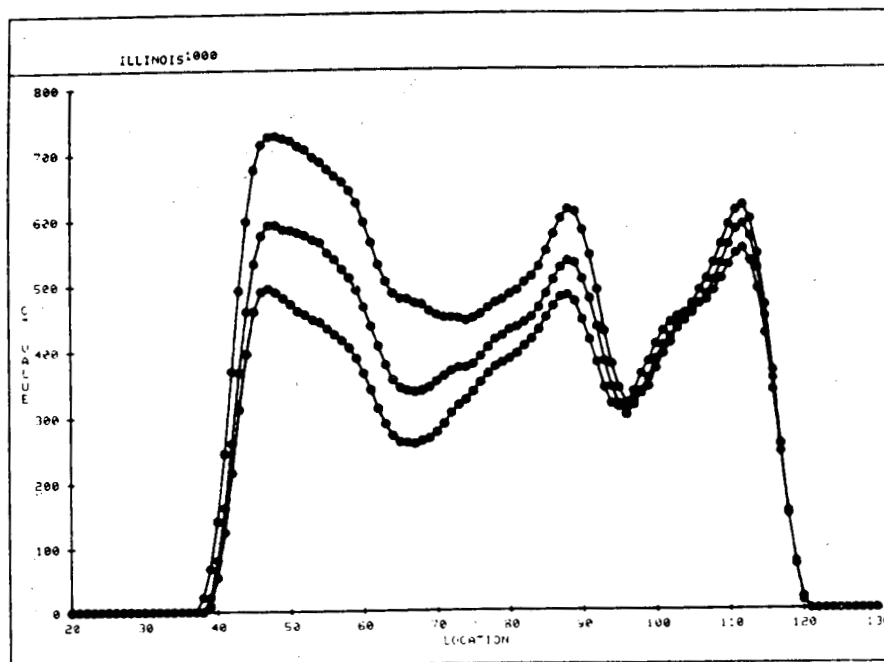
Figure 7-67. Plots of CT values along the line shown in Figure 7-63, taken during isothermal gasification at 1000 °C
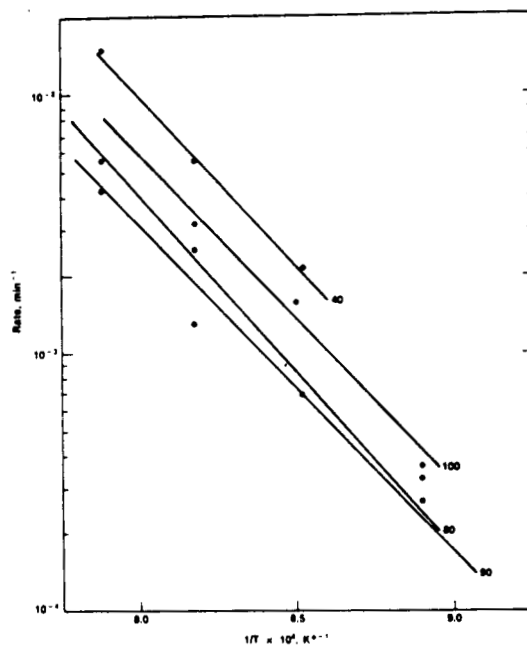
Figure 7-68. Arrhenius plots of log rate vs inverse absolute temperature showing how steam gasification occurs as a function of position in the coal. Note that rates are greatest near the edges of the char, but activation energies determined from the slopes of the lines are roughly constant.
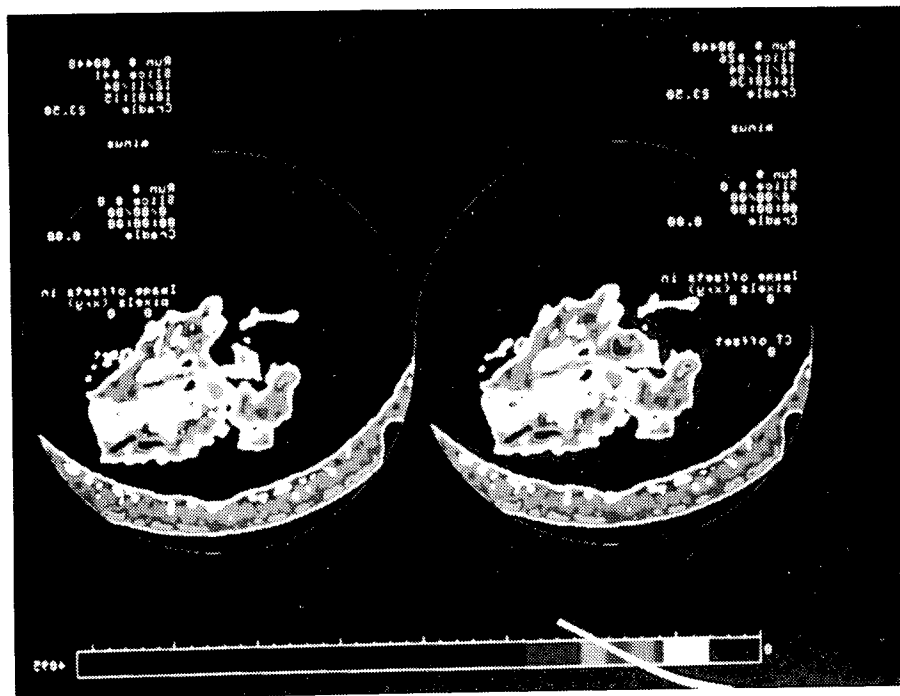
Figure 7-69. Plate of Illinois #6 char containing rubidium carbonate as a plug. In the left-hand figure, taken at the outset of gasification, the catalyst shows up as a dark red spot. The left-hand slice, taken an hour and a half later, shows that the rubidium has dissappeared and gasification has occurred in its wake.
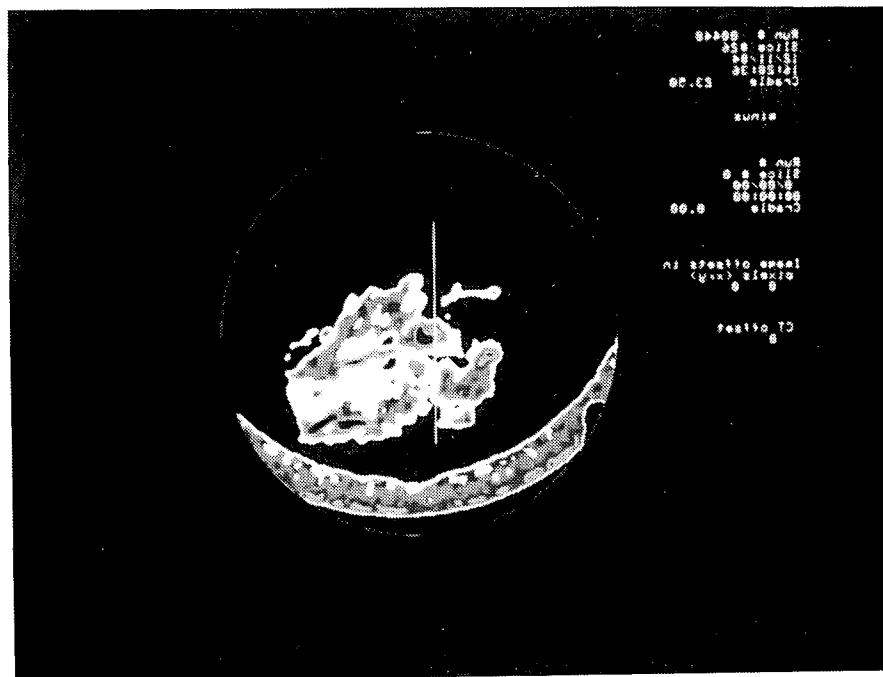
Figure 7-70. Plate of Illinois #6 char containing the rubidium carbonate plug, indicating the vertical line through the catalyst core which was used in analysis (see text).
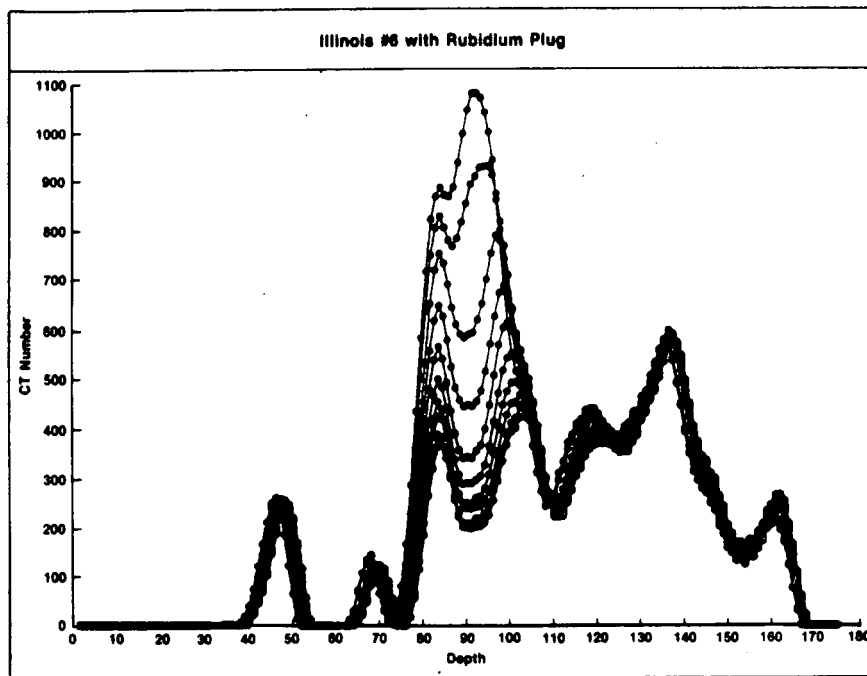
Figure 7-71. Plot of CT values along the vertical line illustrated in Figure 7-70 . Note that the catalyst appears initially at a depth of 90 and gradually dissappears into the char.
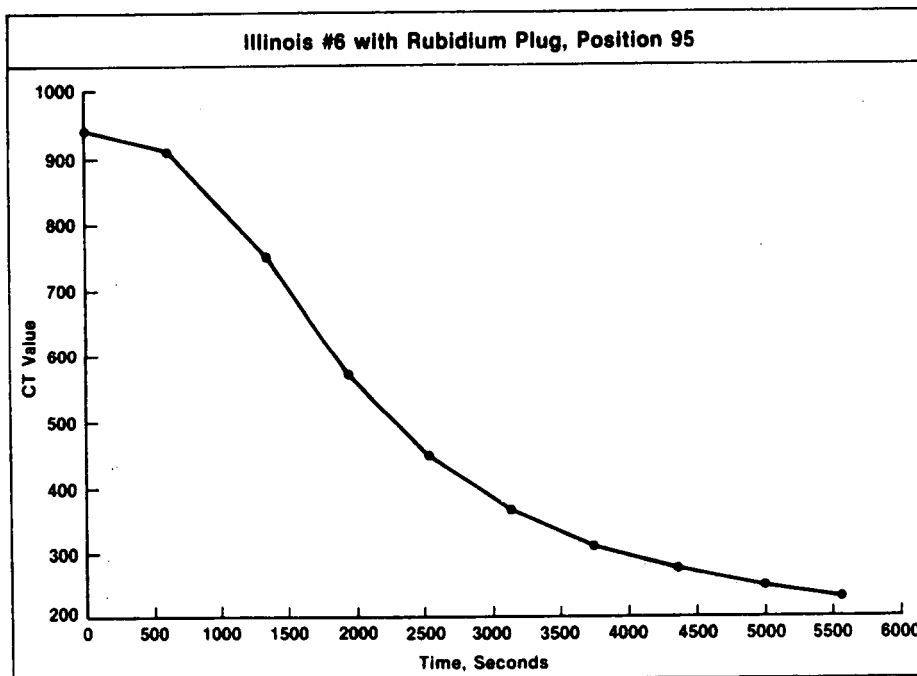
Figure 7-72. Plot of CT value as a function of time at position 95
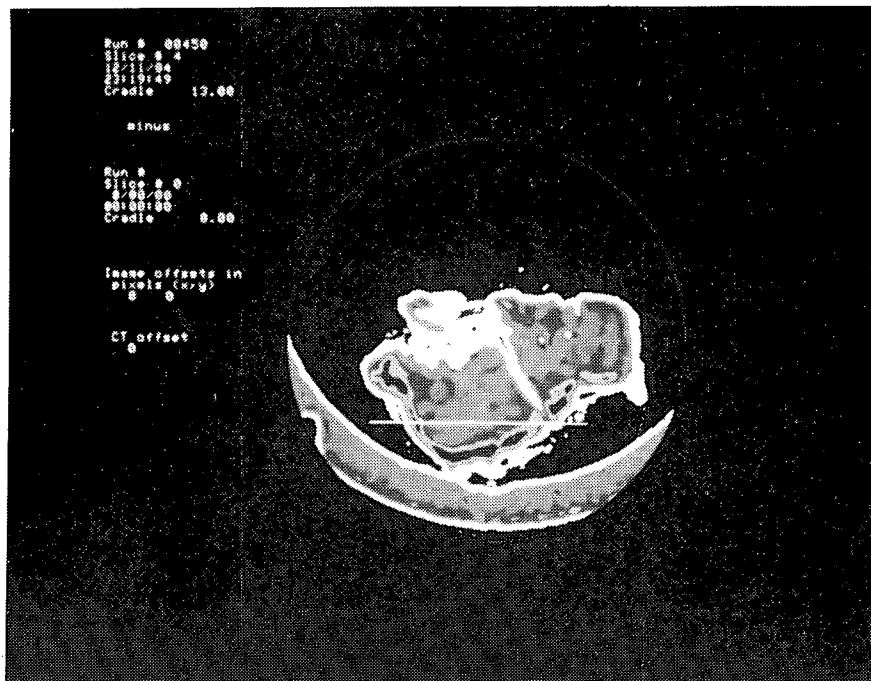
Figure 7-73. Plate of Illinois #6 char which had been solution-impregnated with rubidium carbonate. This shows up as a dark red rim along the base of the char. The horizontal line in the figure was that used for analysis (see text).
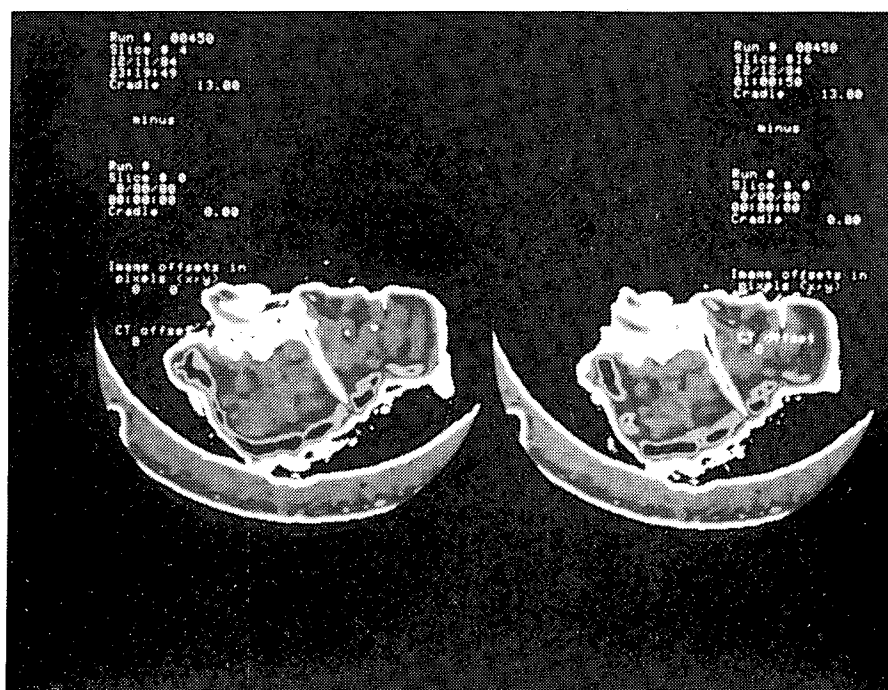
Figure 7-74. Plate of Illinois #6 solution impregnated char at the outset of gasification and after ~1 h at 850 °C
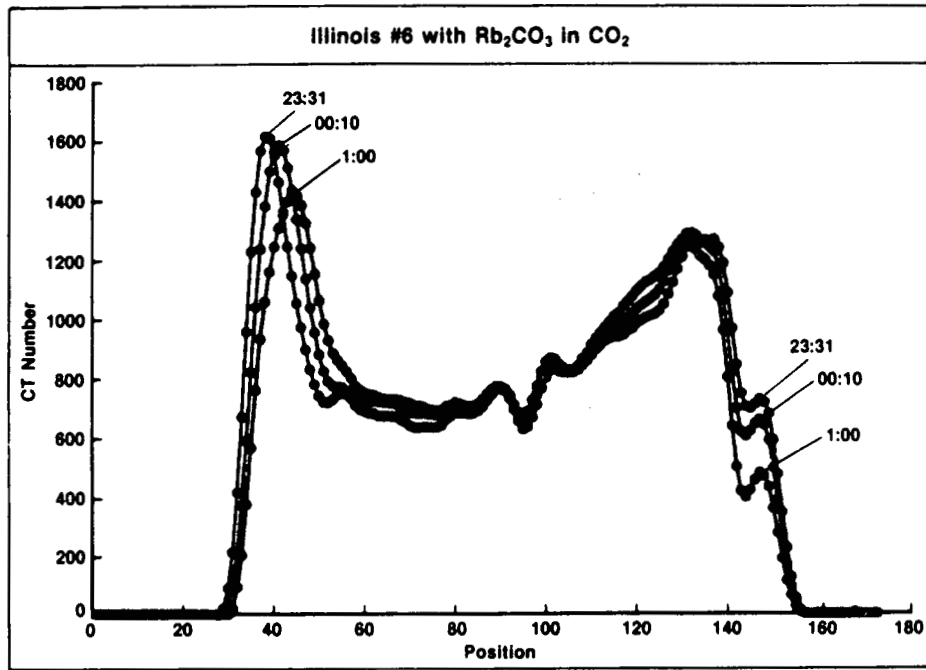
Figure 7-75. Plot of CT values of the rubidium carbonate solution-impregnated Illinois #7 char at three different time intervals. Note that the gasification process is dominated at the edges where catalyst was present.
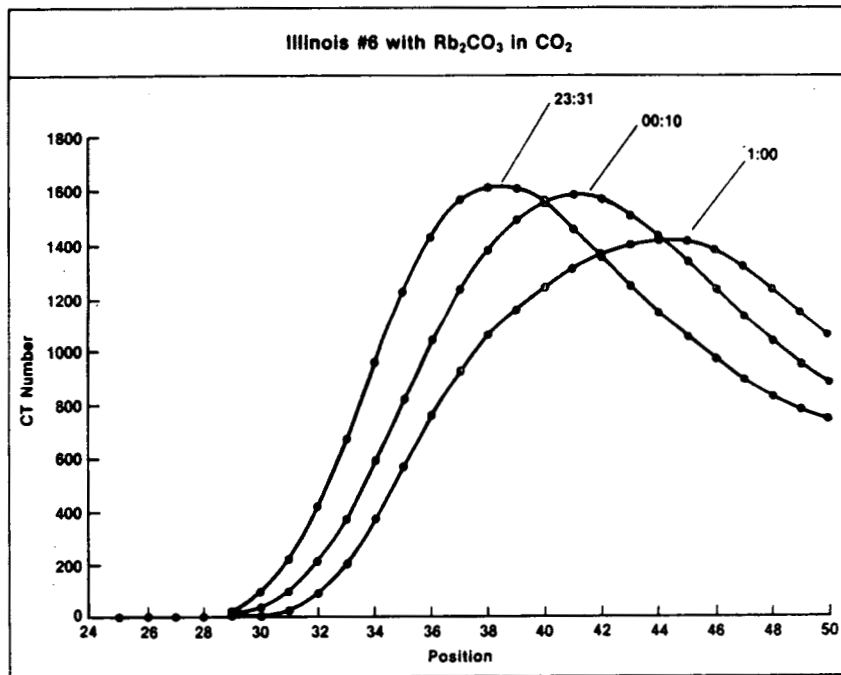
Figure 7-76. Plot of the left side of the Illinois #6 char as it gasified
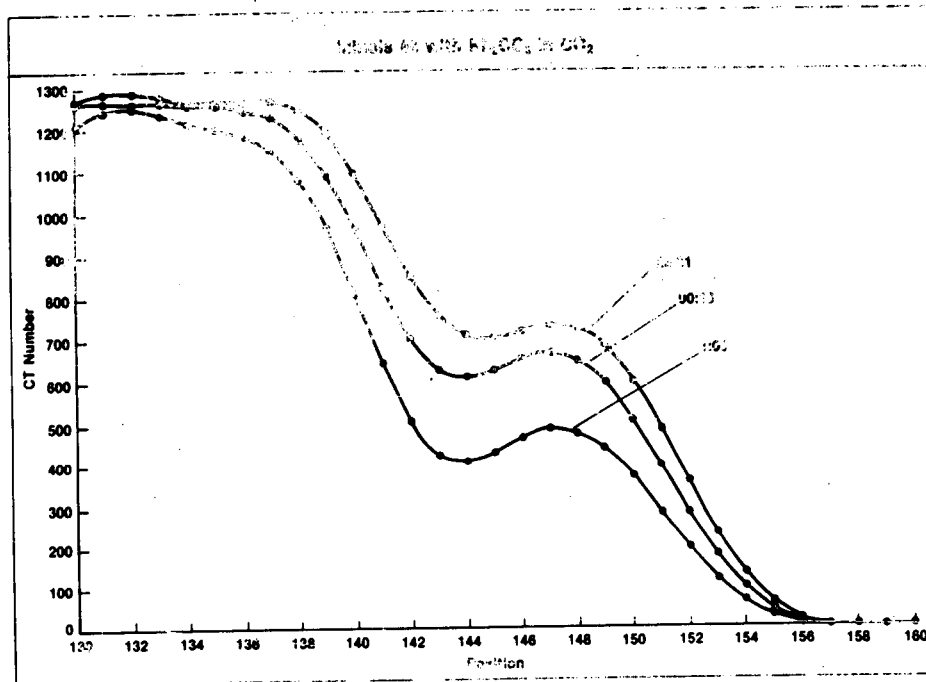
Figure 7-77.   Plot of the right side of the
Illinois #6 char as it gasified
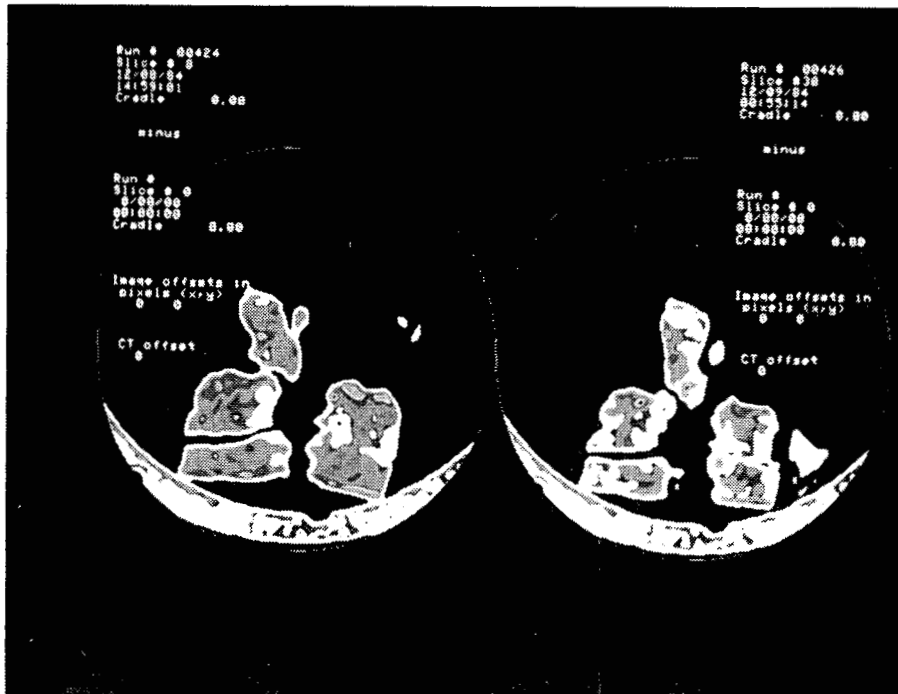
Figure 7-78. Plate of Illinois #6 char (left) at the outset of gasification in carbon dioxide and (right) after 10 h
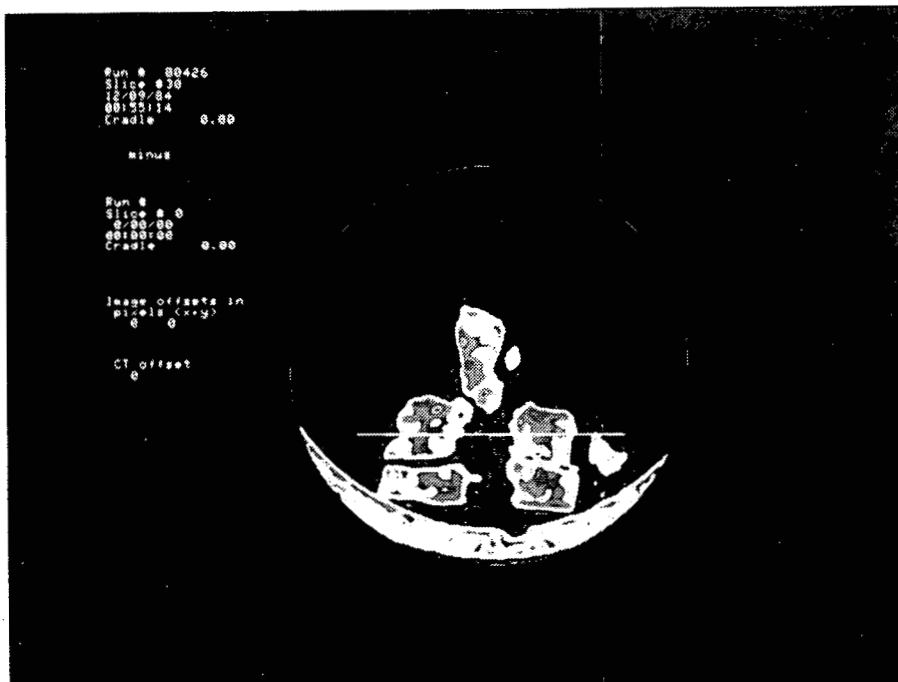
Figure 7-79. Plate of Illinois #6 char indicating line used for analyses (see text)
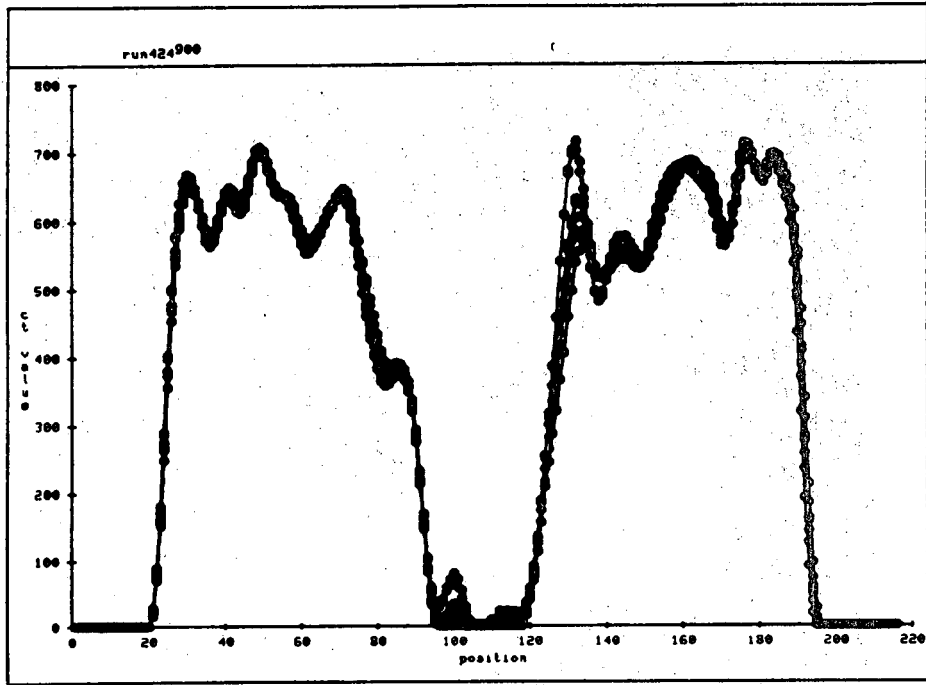
Figure 7-80. Plot of CT values along the line illustrated in Figure 7-79, showing CT values at 900 °C
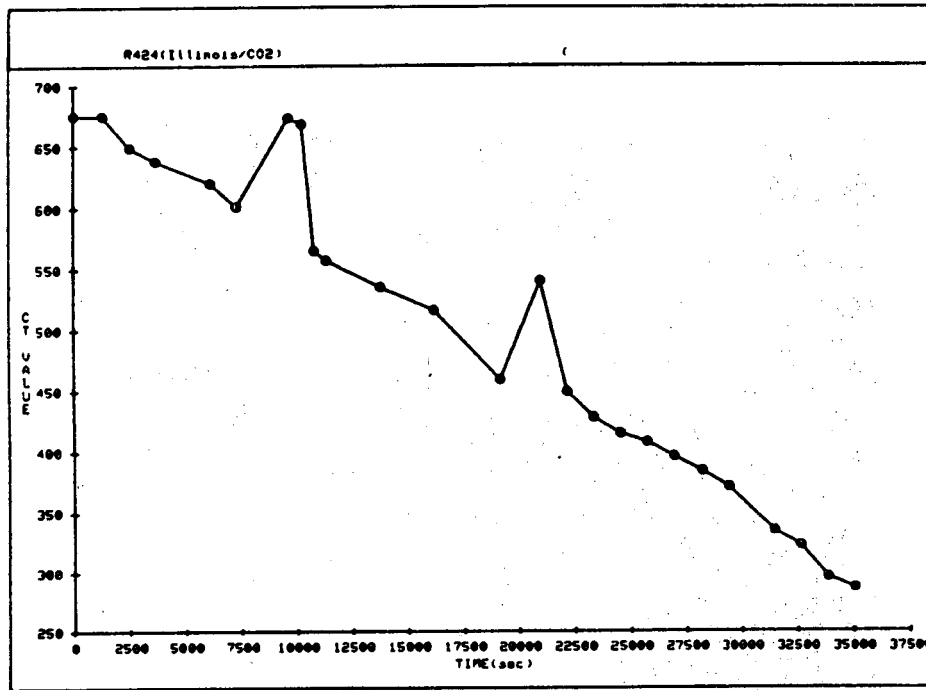
Figure 7-81. Plot of CT values as a function of time at location 130 along the line illustrated in Figure 7-79
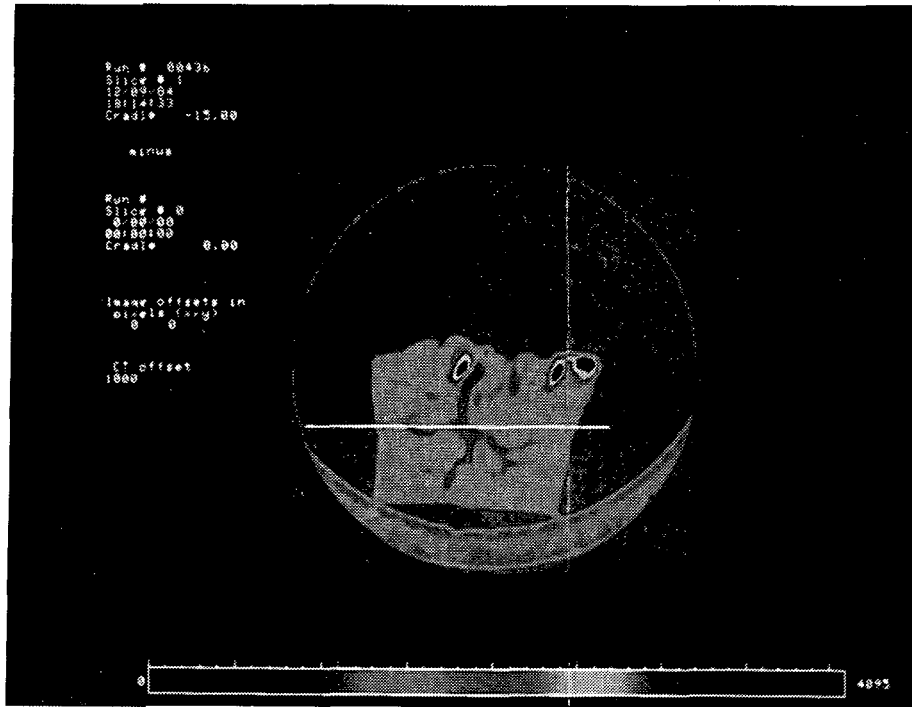
Figure 7-82. Plate of lignite char at the outset of gasification, indicating the line used for analyses (see text)
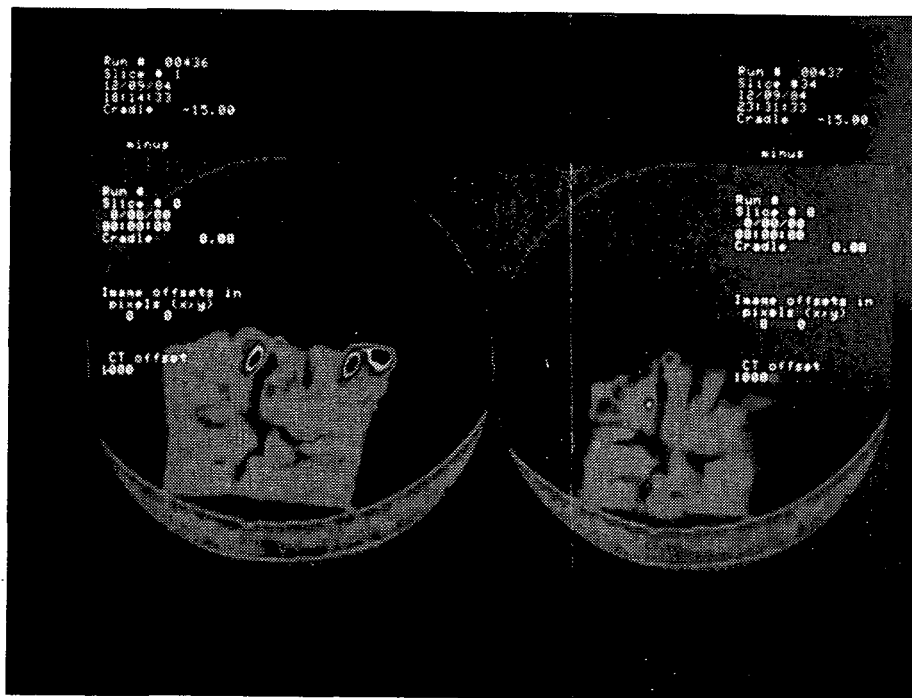
Figure 7-83. Plate of lignite char (left) at the onset of carbon dioxide gasification and (right) after ~5 h
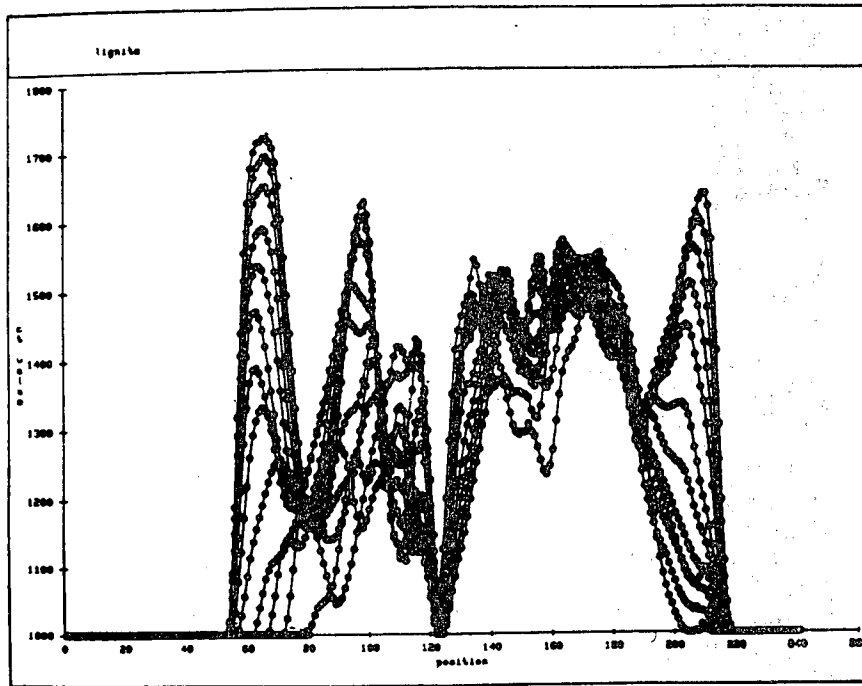
Figure 7-84. Composite of plots of CT values along the line illustrated in Figure 7-83, taken at temperatures from 850 °C to 1000 °C. Note that on either edge the most dramatic losses of material occurred.
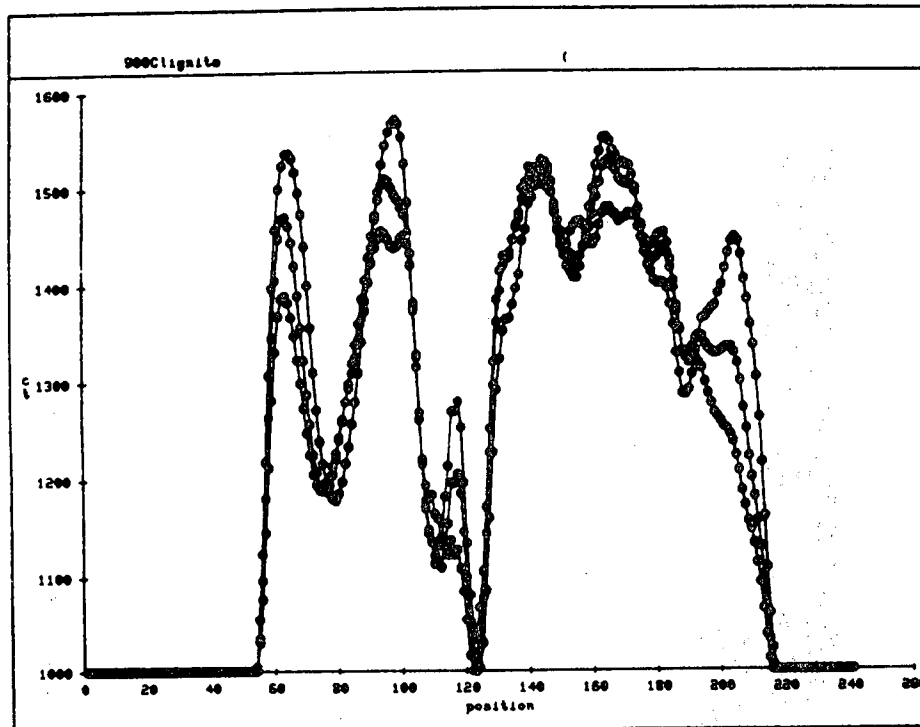
Figure 7-85. Composite of plots of CT values along the line illustrated in Figure 7-83, taken at 900 °C. Very few changes were observed between positions 100 and 160, while the edges showed extensive weight loss without recession.
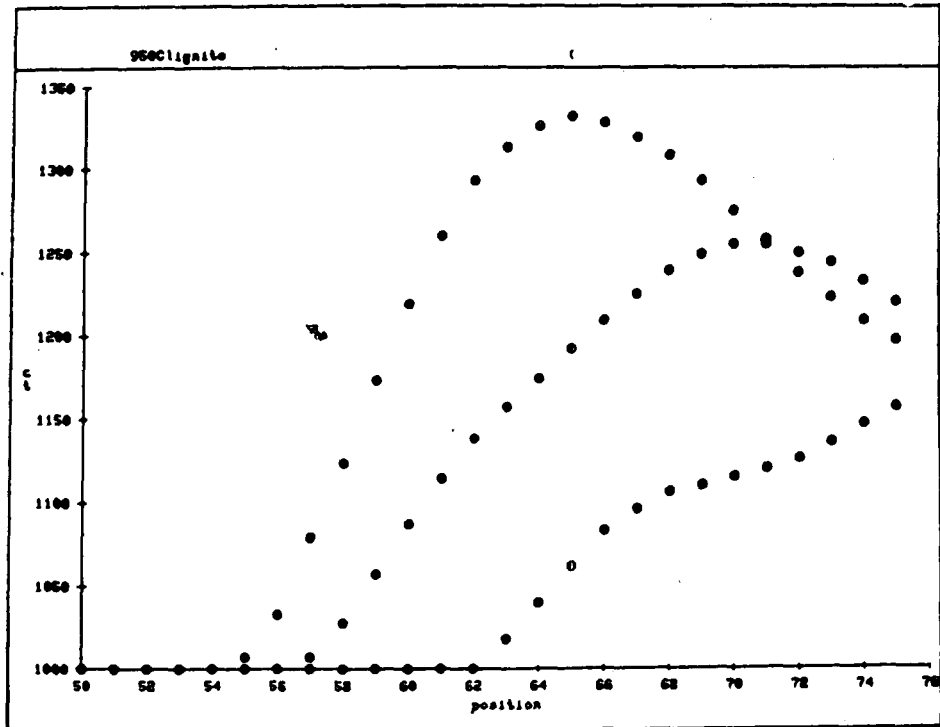
Figure 7-86. Plot of edge recession at 950 °C. Note that in Figure 7-85 above, little edge recession at 950°C was observed, while at 950 °C, this edge is receding at rate of 3.2×10^{-2} mm/min.
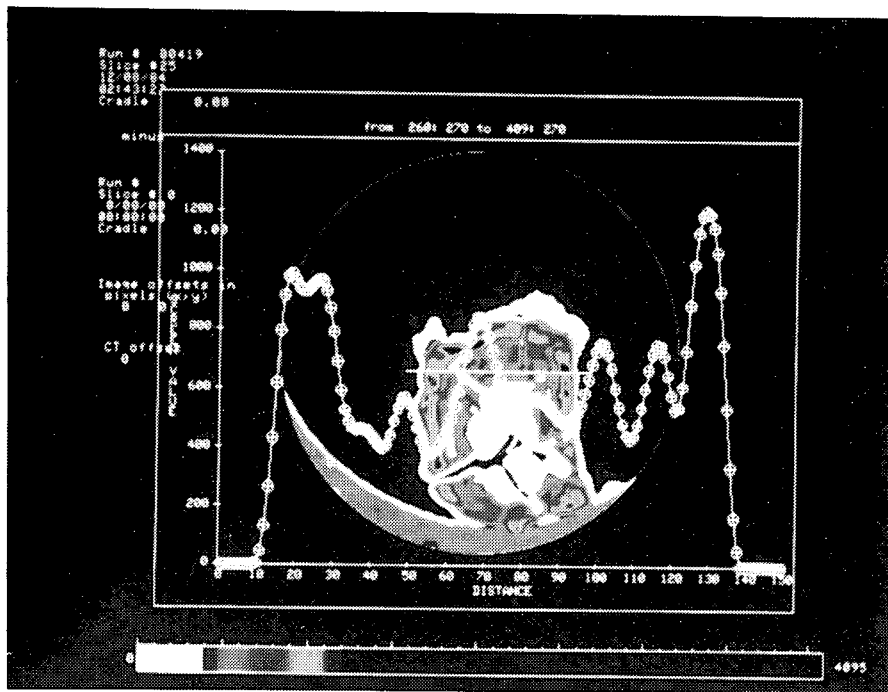
Figure 7-87. Plate of Pittsburgh coal char, taken at the outset of gasification in carbon dioxide. The horizontal line is that used for analyses (see text), and a plot of values along that line is superimposed on the image.
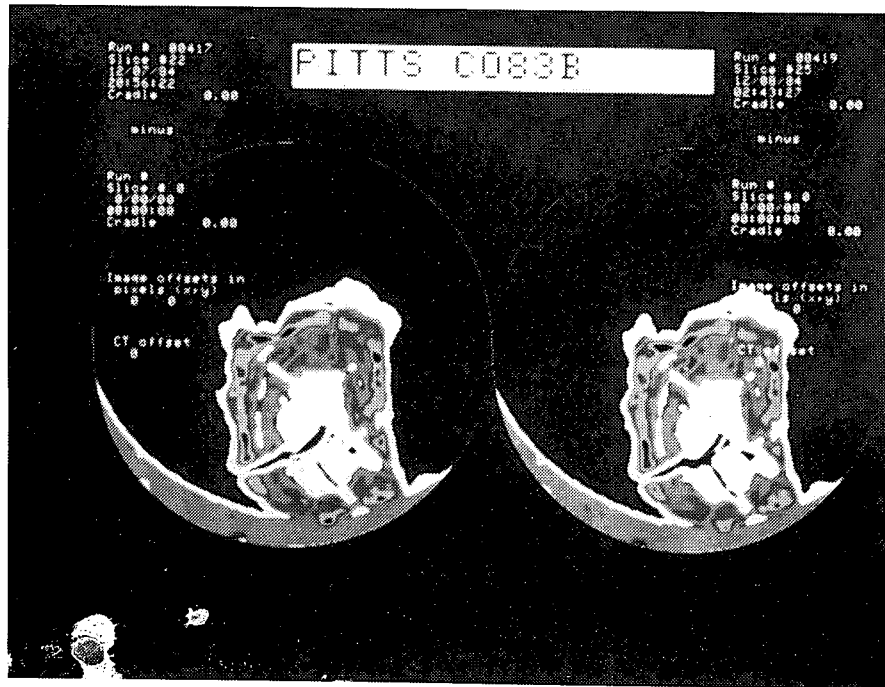
Figure 7-88. Plate of Pittsburgh coal chars, taken (left) at the outset of gasification in carbon dioxide and (right) after ~6 h
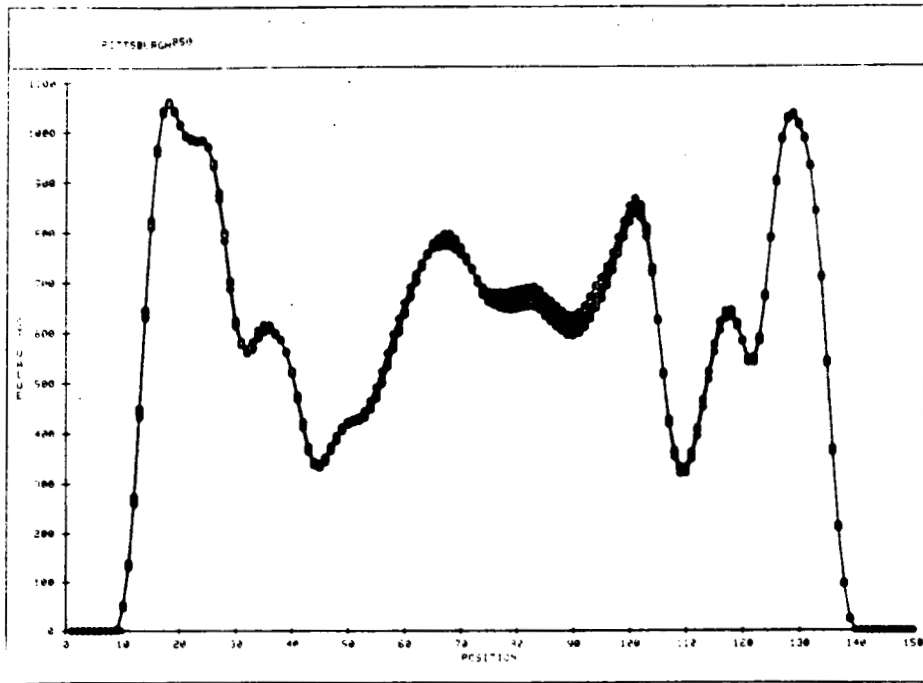
Figure 7-89. Plot of CT values along the line illustrated in Figure 7-87, taken at 850 °C
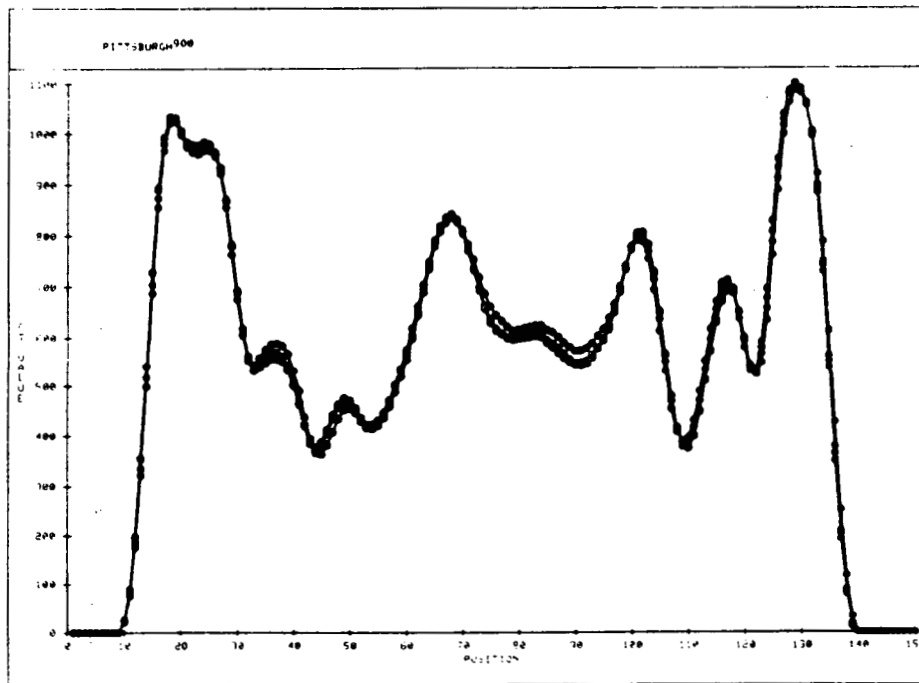
Figure 7-90. Plot of CT values along the line illustrated in Figure 7-87, taken at 900 °C
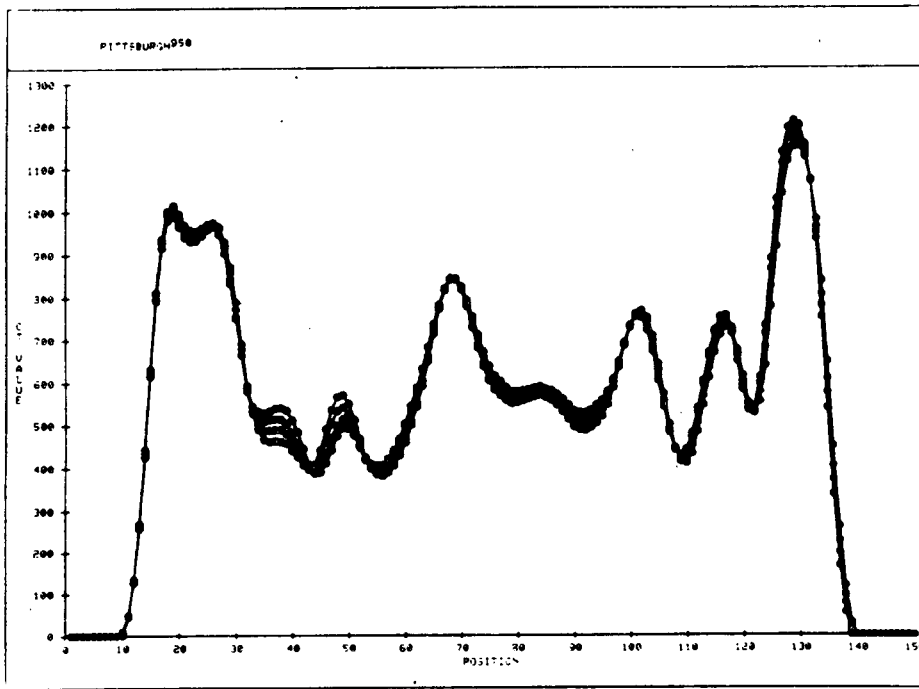
Figure 7-91. Plot of CT values along the line illustrated in Figure 7-87, taken at 950 °C
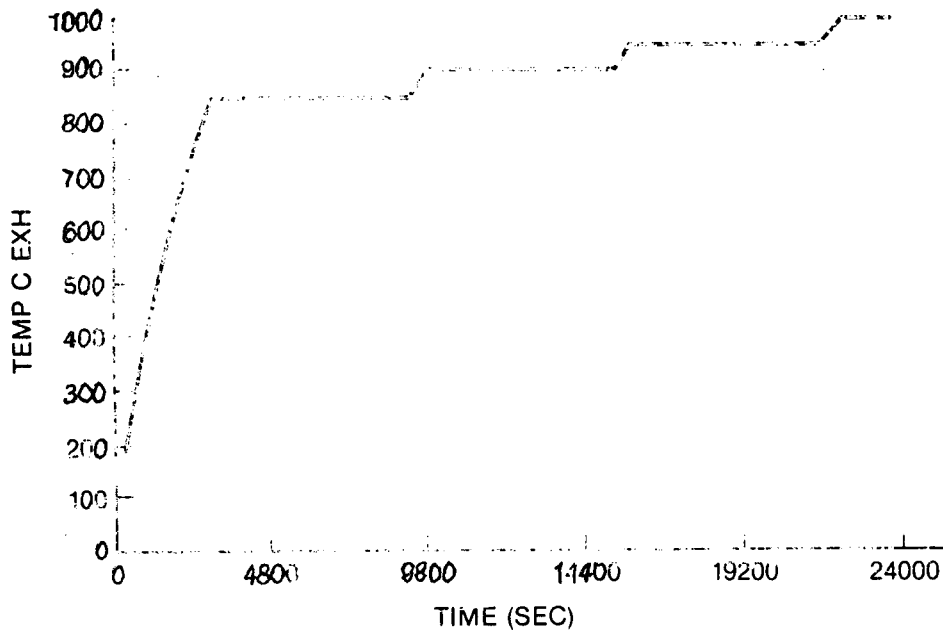
Figure 7-92. Temperature/time profile for North Dakota A lignite steam gasification
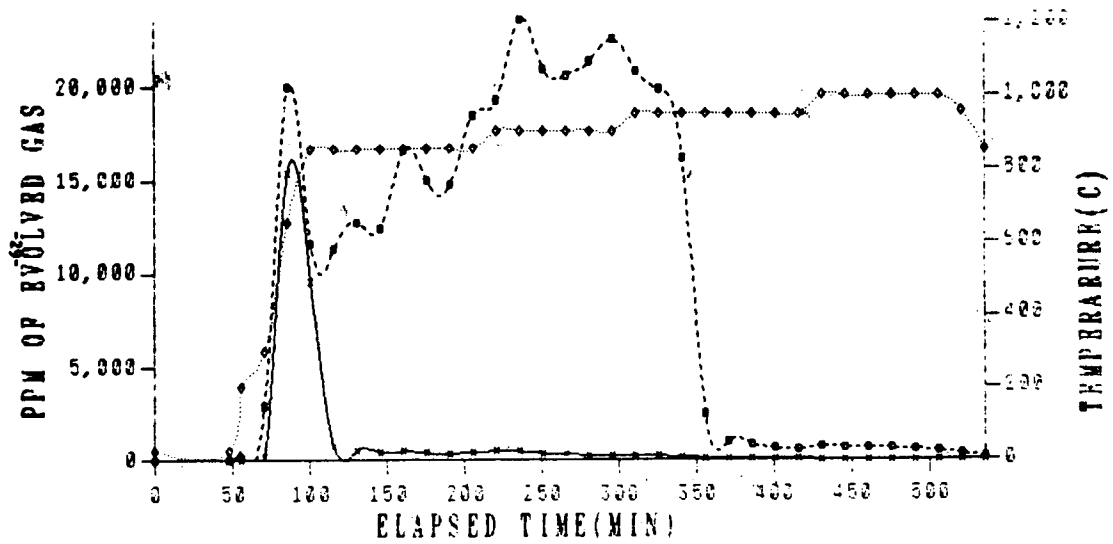
Figure 7-93. The gas evolution profile monitored by mass spectrometry, for North Dakota A lignite steam gasification
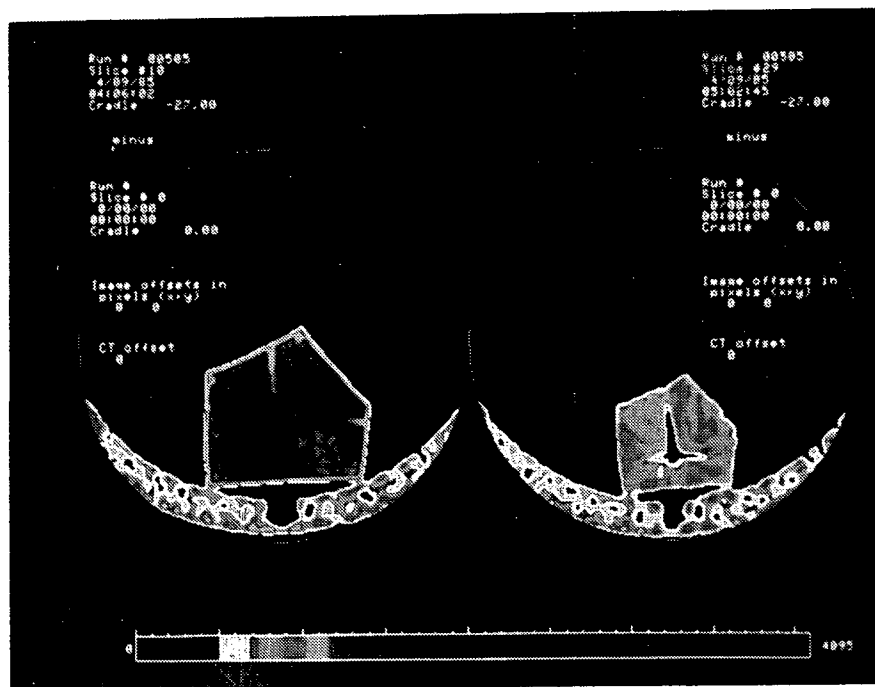
Figure 7-94. Pyrolysis of North Dakota A lignite. During the pyrolysis stage of the sequence (T < 850 °C), the pentagonal shape of the lump was preserved, though a near isotropic linear shrinkage of 26% occurred.
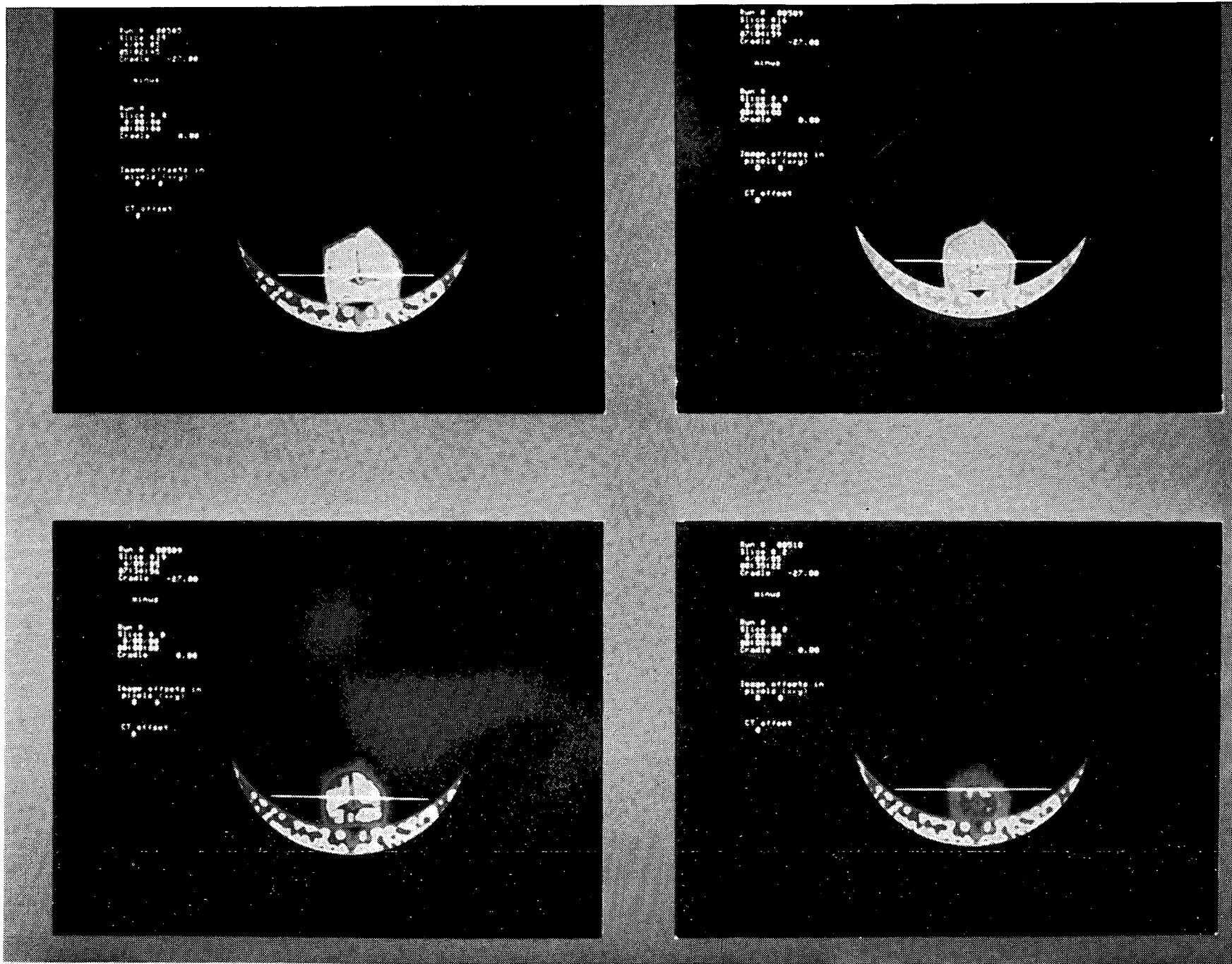
Figure 7-95. A sequence of slices taken during the gasification of North Dakota A lignite in steam
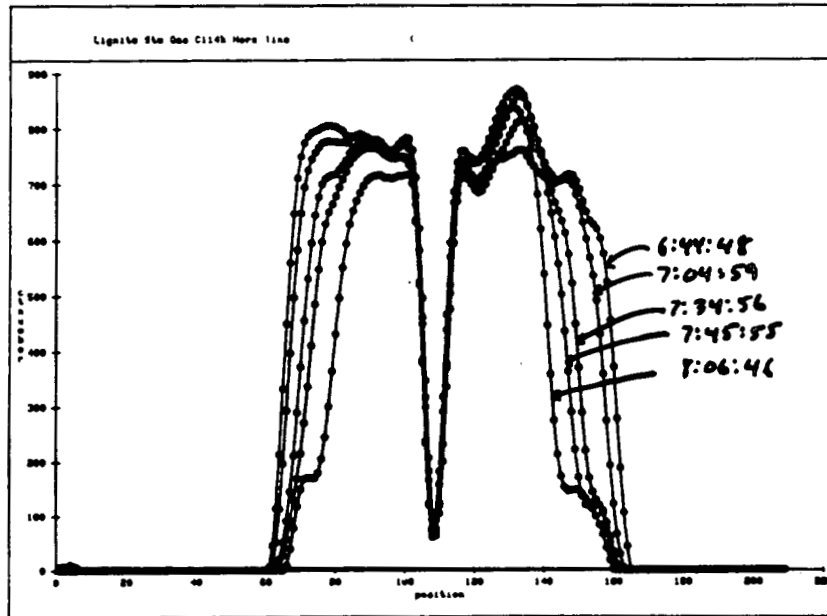
Figure 7-96. Plots of CT values along the horizontal line in Figure 7-95 for five slices taken over 90 min at 900 °C
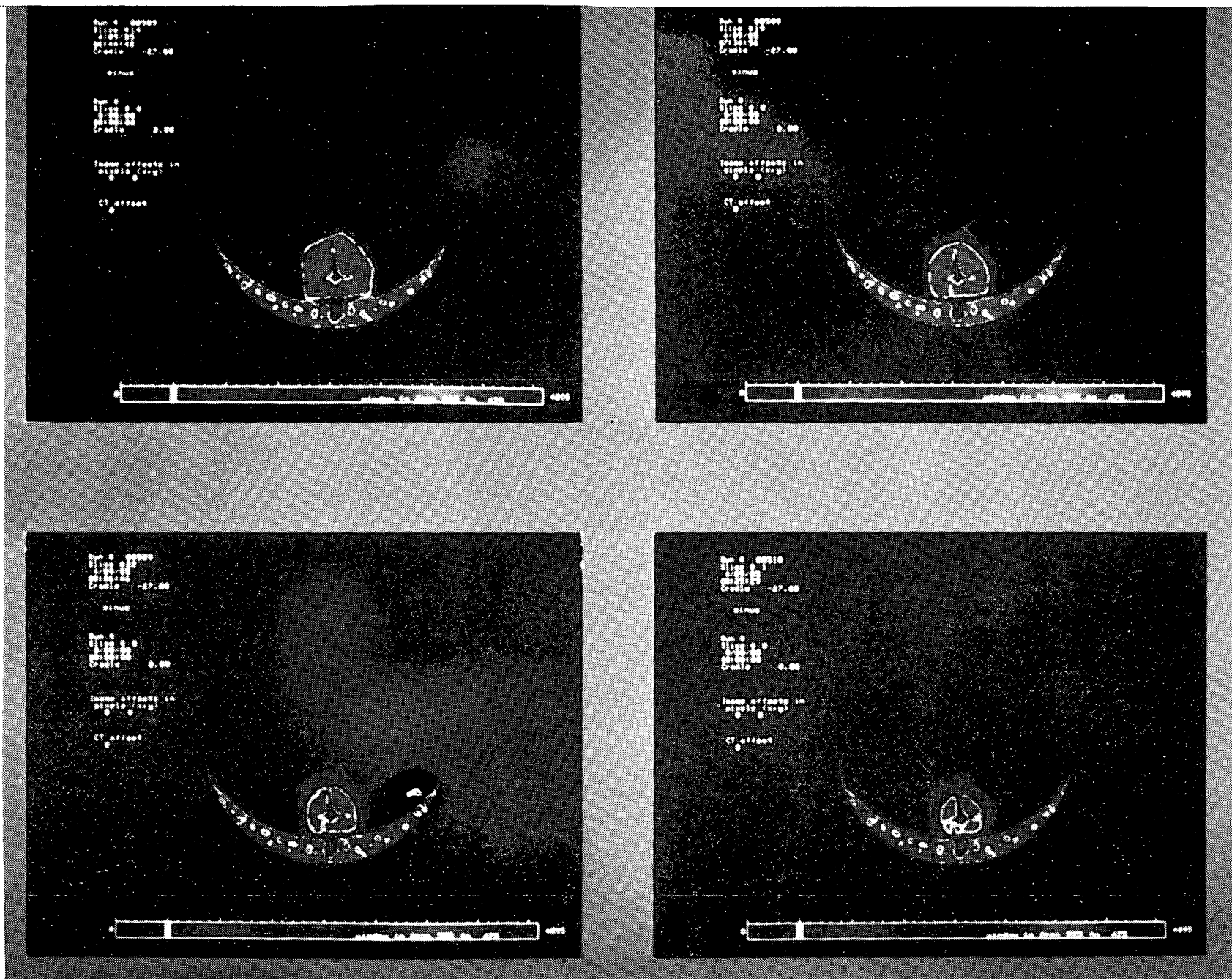
Figure 7-97. Isodensity contours for CT values clustered at 500 for North Dakota A lignite steam gasification
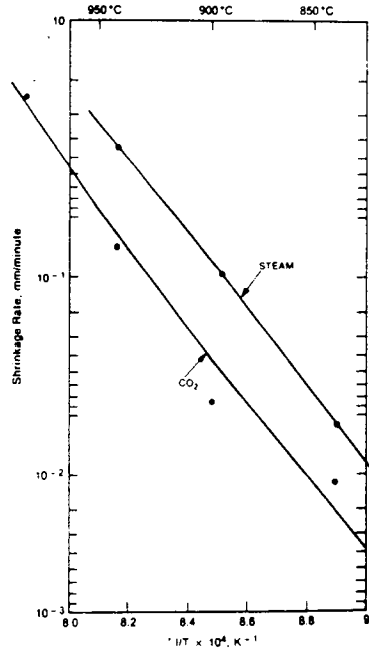
Figure 7-98. The Arrhenius law is followed for these data, with log (rate of isodensity contour shrinkage) being a linear function of inverse absolute temperature
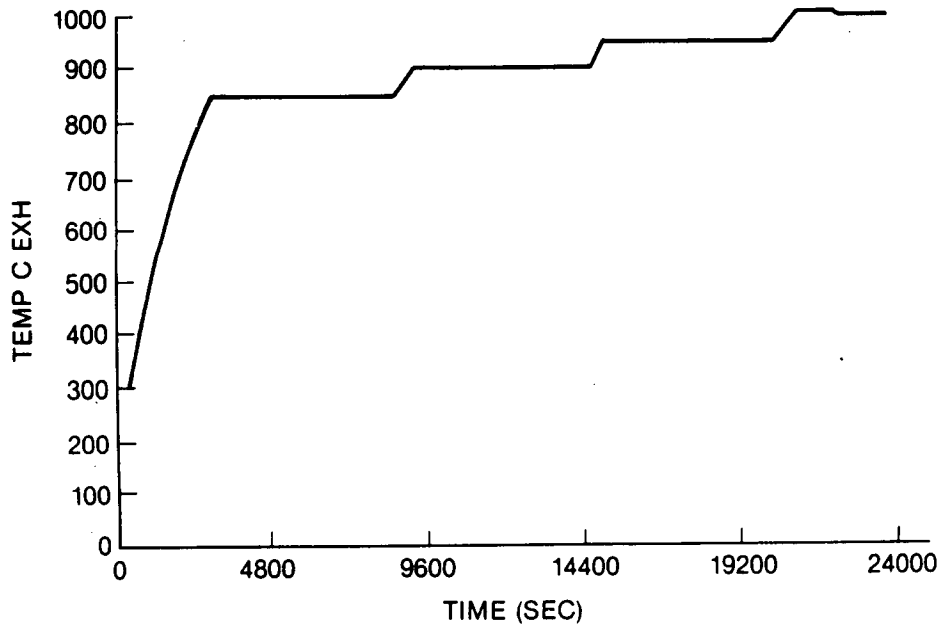
Figure 7-99. Temperature/time profile for uncatalyzed Pittsburgh #8 coal gasification in steam

7-81
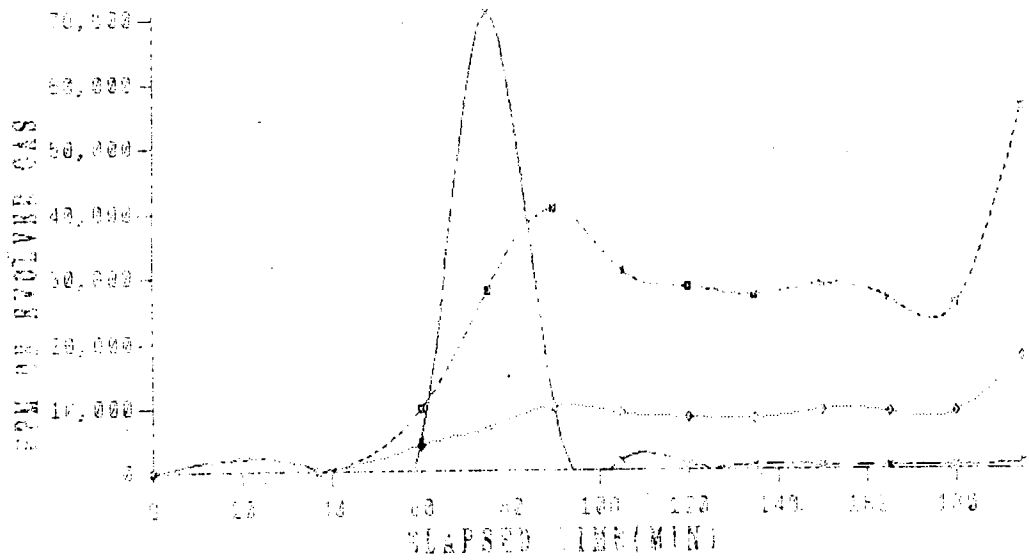
Figure 7-100   Gas evolution profile for uncatalyzed Pittsburgh
#3 coal gasification in steam
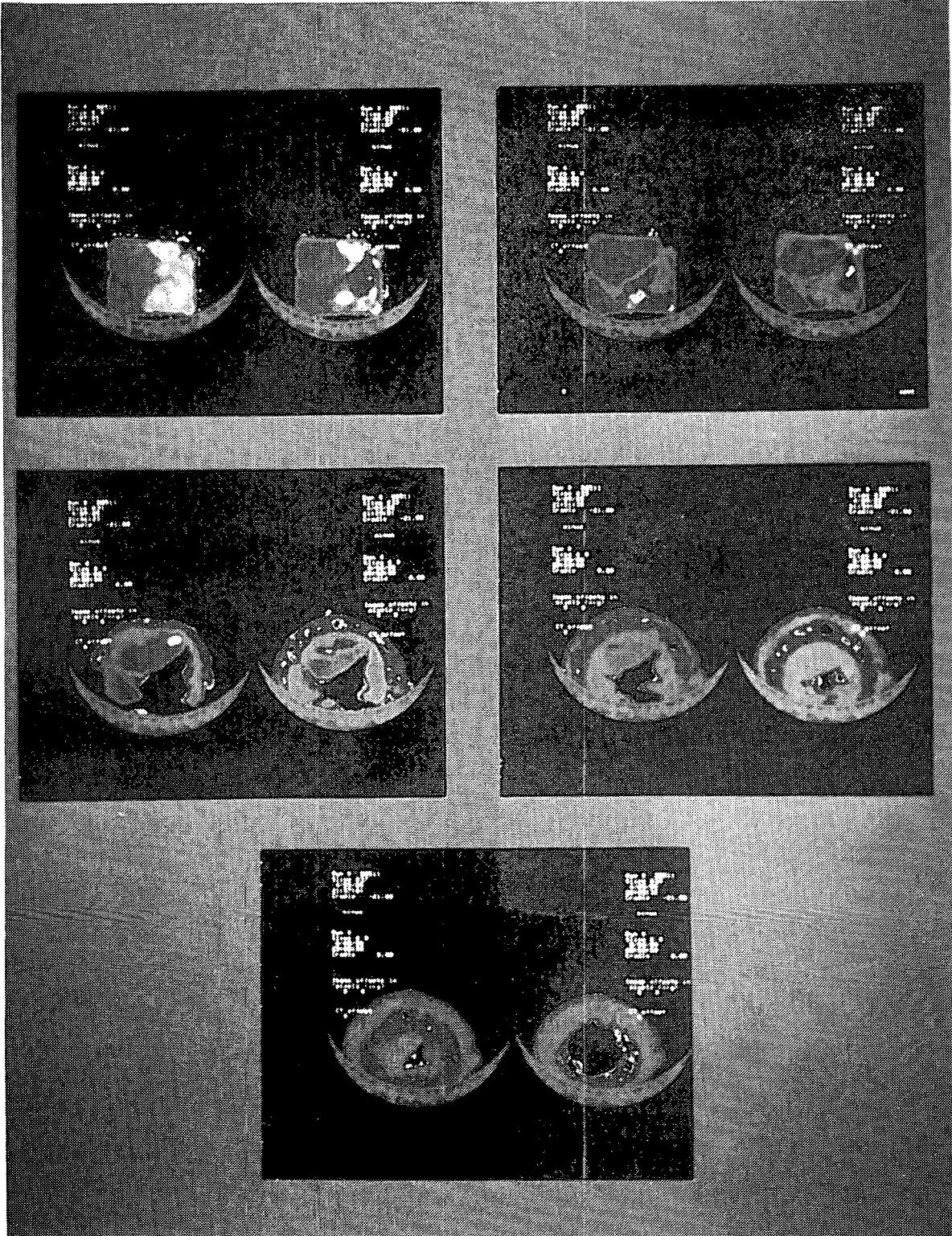
Figure 7-101. Morphological changes in Pittsburgh coal undergoing pyrolysis in the range 300 to 600 °C
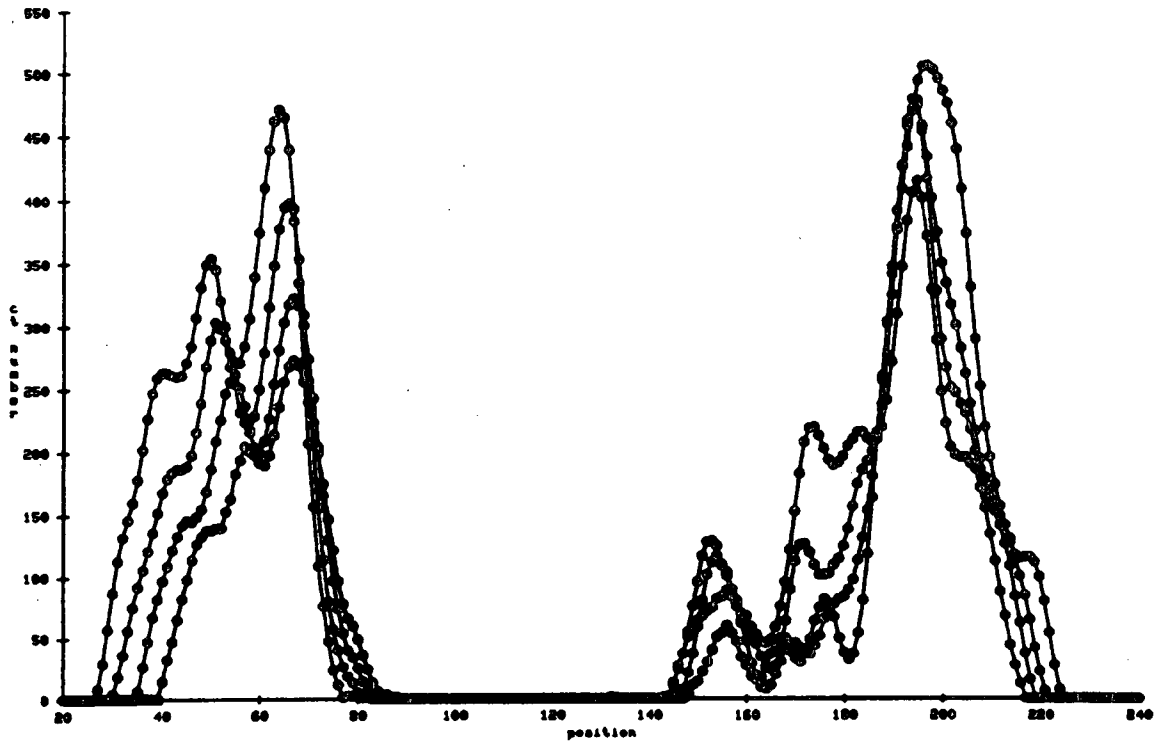
Figure 7-102. CT numbers plotted along a constant horizontal line through the char at 1000 °C at four different times. The line h through the doughnut-shaped slice reveals the central void and two maxima associated with each part of the char.
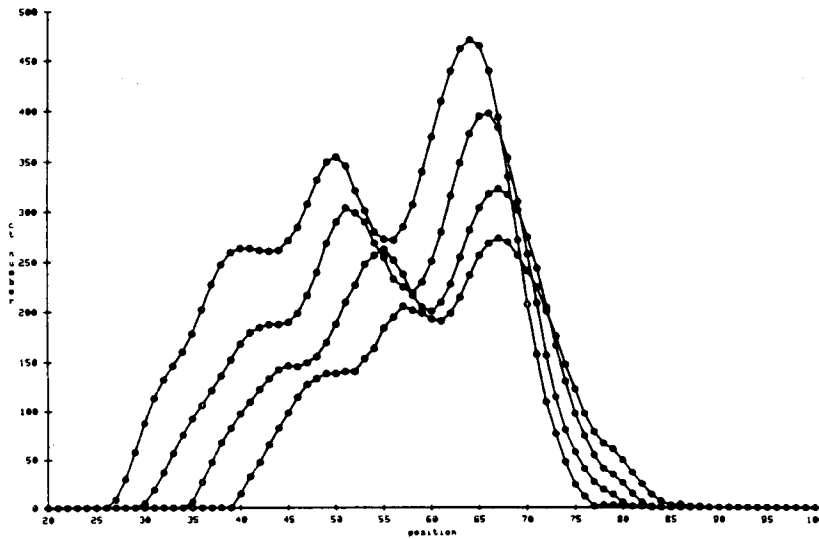
Figure 7-103. Same as Figure 7-102, but of the slice through just the left-hand side of cylindrical core
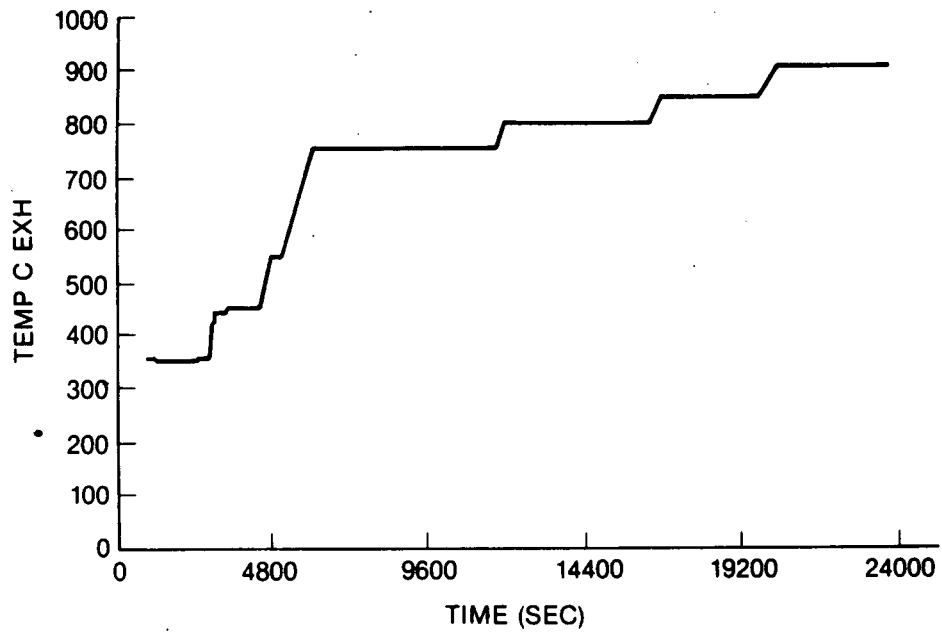
Figure 7-104. Temperature/time profile for rubidium carbonate catalyzed steam gasification of North Dakota A lignite coal
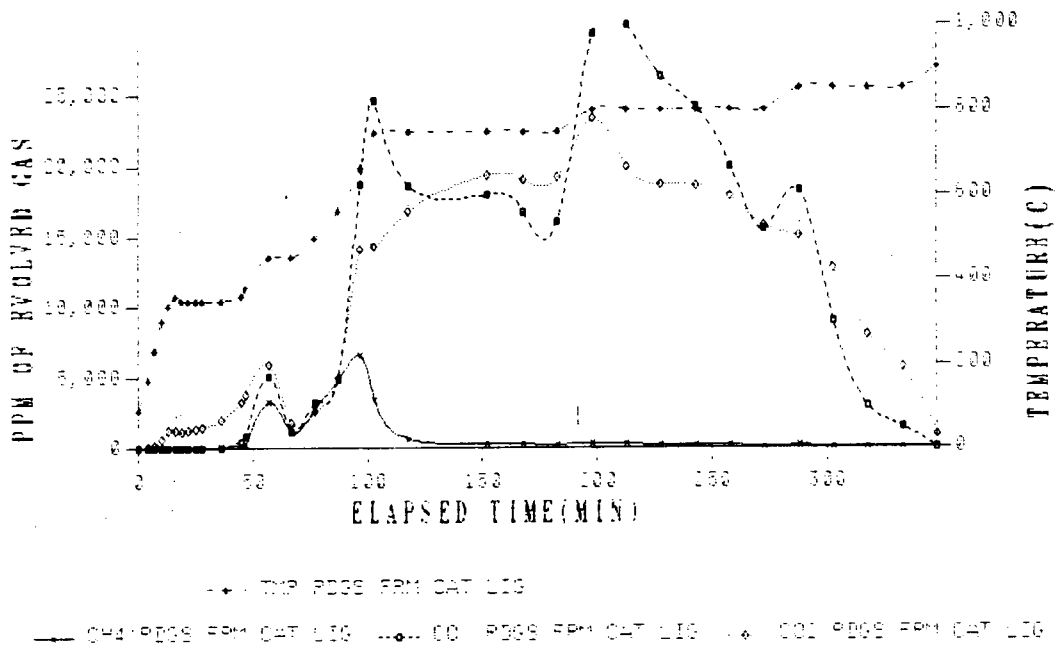
Figure 7-105. Gas evolution profile for rubidium carbonate catalyzed steam gasification of North Dakota A lignite coal
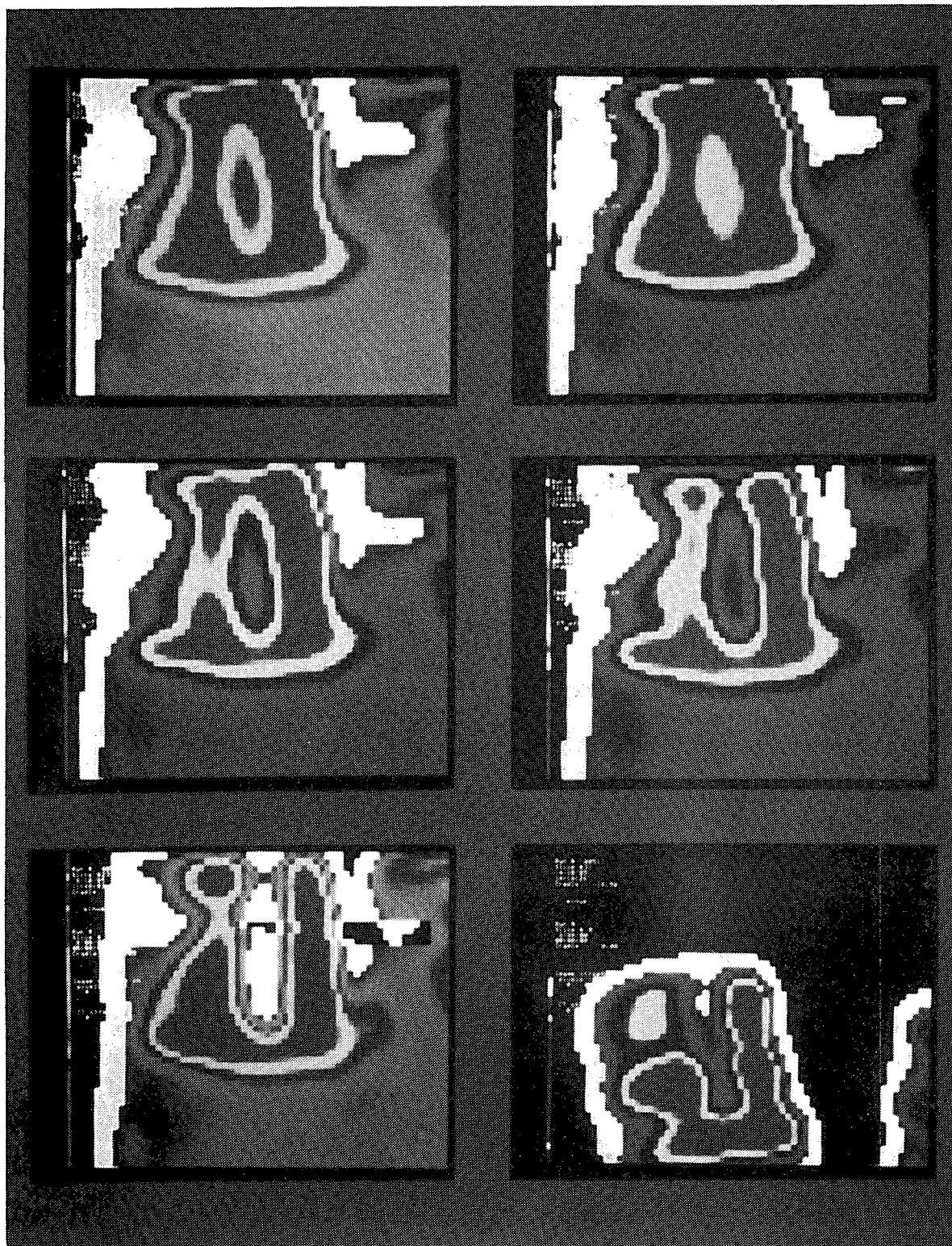
Figure 7-106. Morphological changes of the catalyst during the pyrolysis of lignite
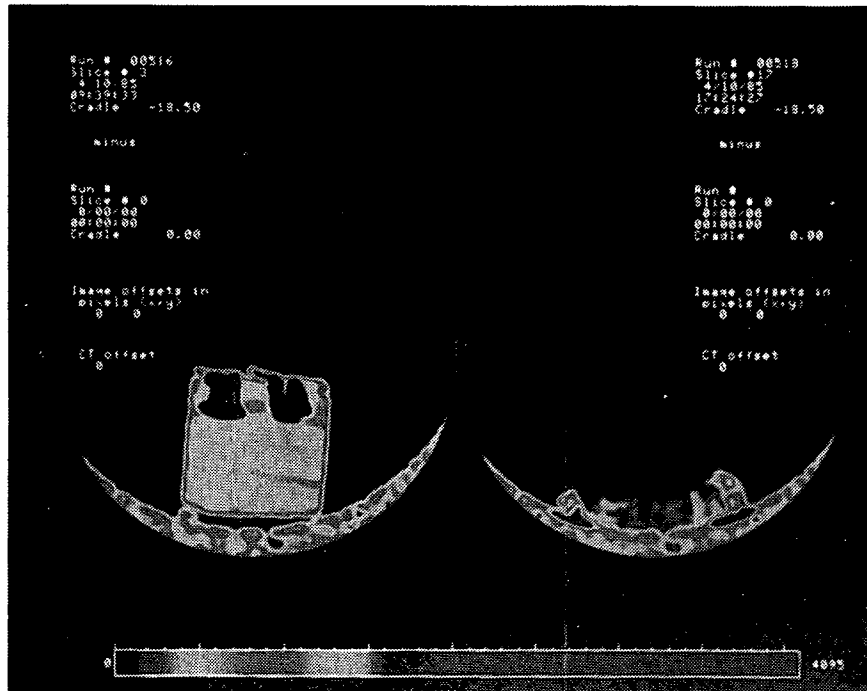
Figure 7-107. Even after gasification is complete, the catalyst appears to retain its morphological integrity during lignite steam gasification.
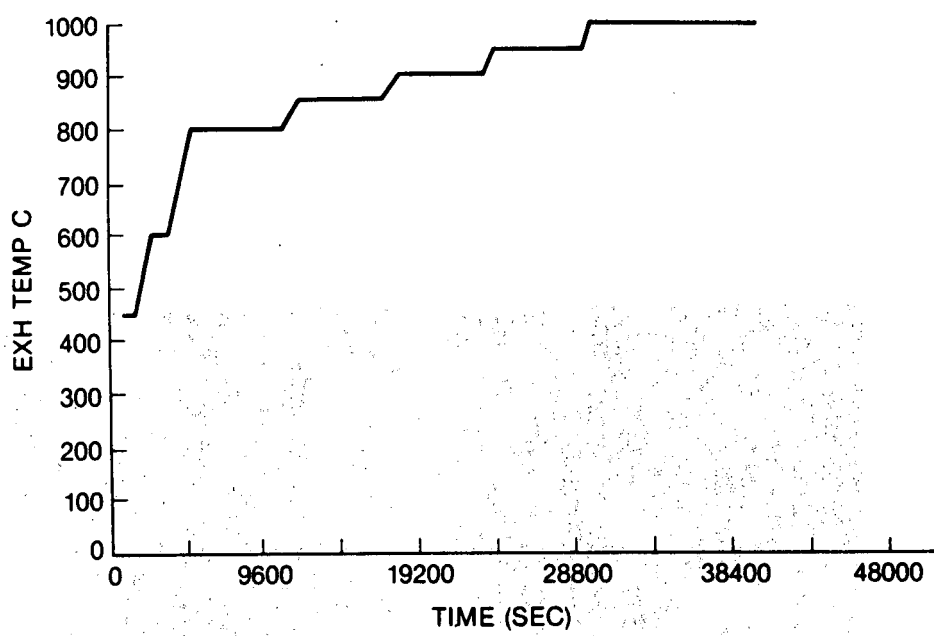
Figure 7-108. Temperature/time profile for rubidium catalyzed gasification of Reading anthracite in steam
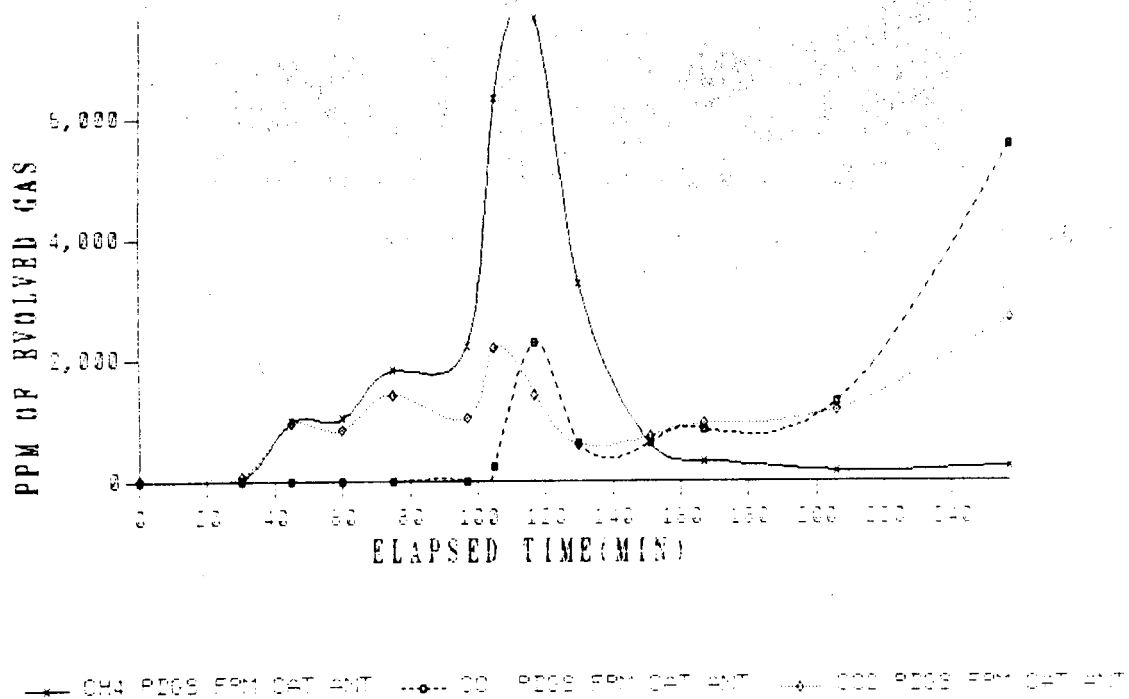
Figure 7-109. Gas evolution profile for rubidium catalyzed gasification of Reading anthracite in steam
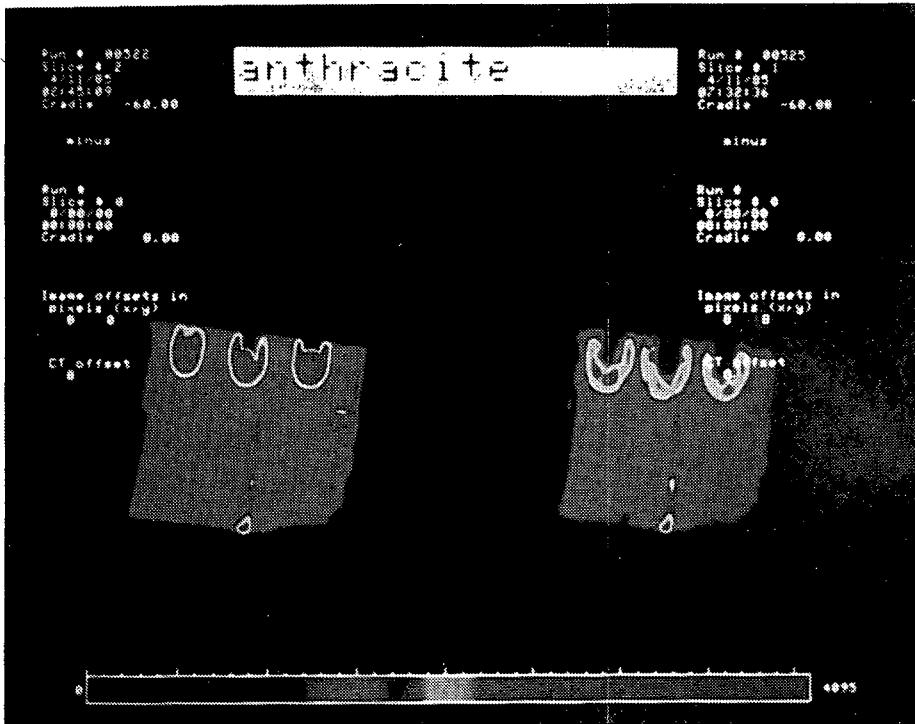
Figure 7-110. The degree of penetration of catalyst into anthracite char at 850 °C (left) and 1000 °C (right)
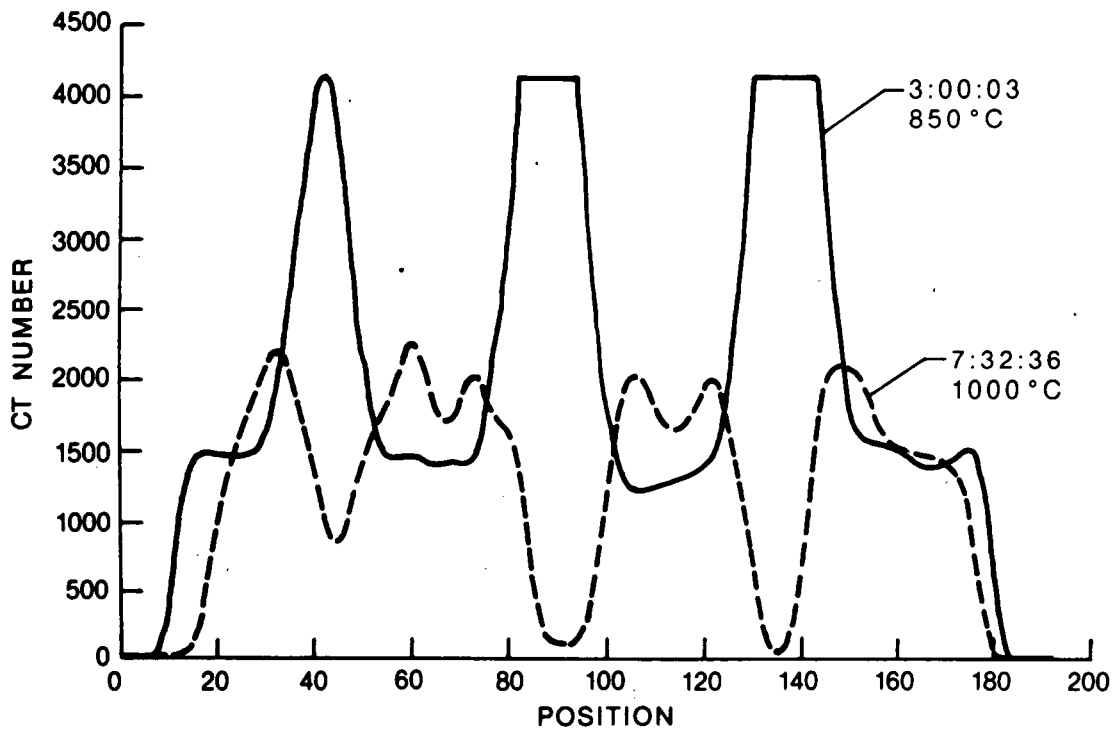
Figure 7-111. CT values along a horizontal line through the three cavities which appear in Figure 7-110
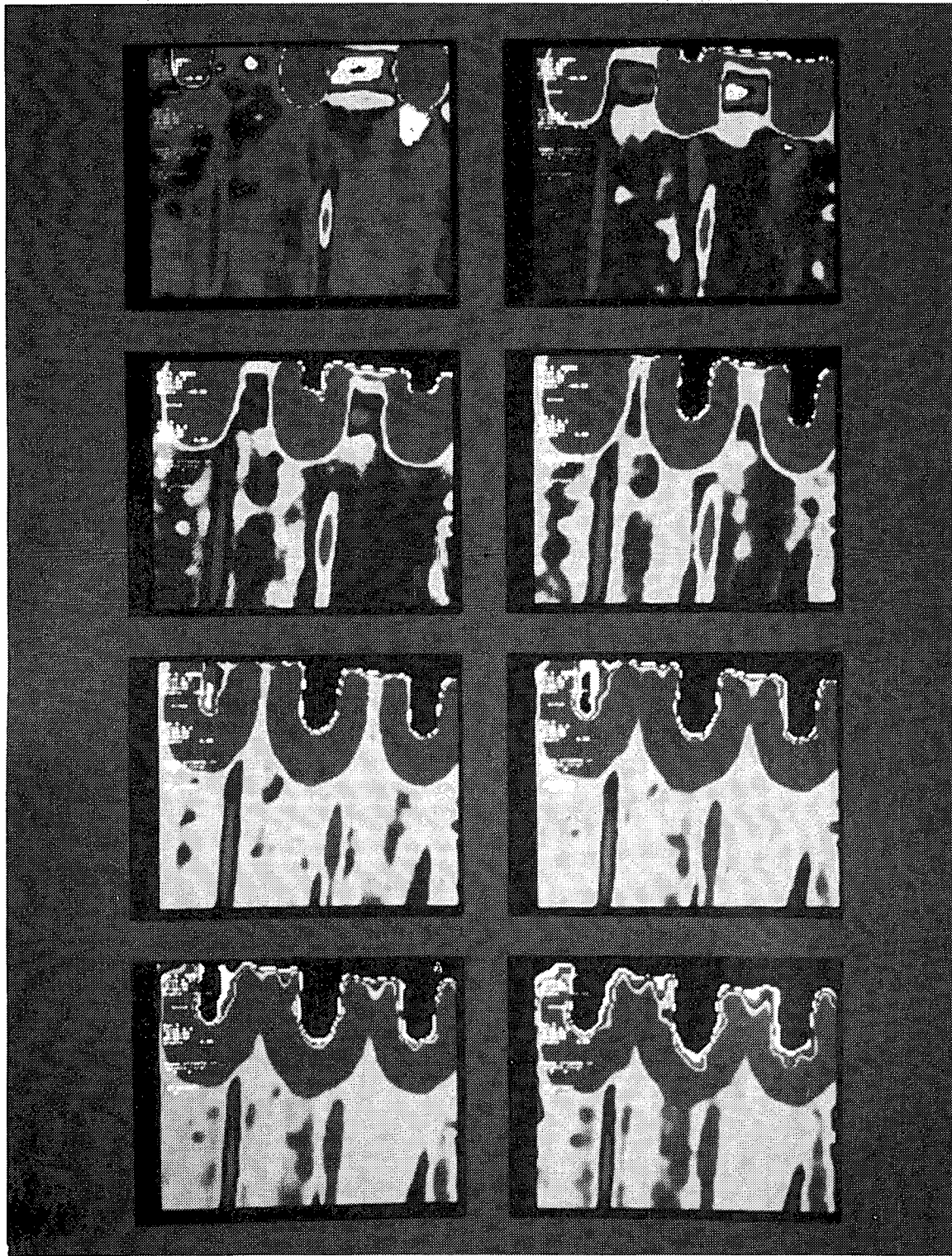
Figure 7-112. Catalyst penetration into anthracite char is more clearly illustrated in a different look-up-table (color scheme)
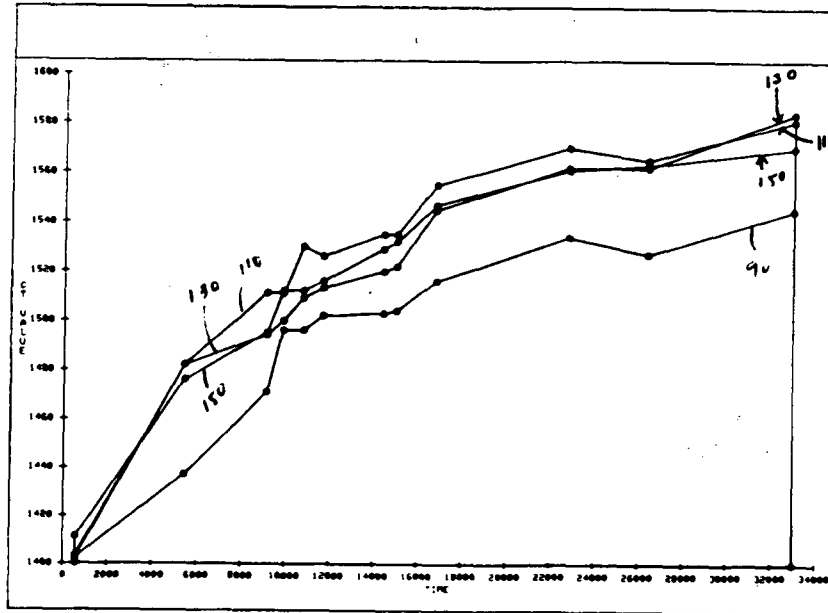
Figure 7-113. Weight gains are quantified as a function of time at depths of 24, 29, 34, and 40 mm beneath the surface of the coal. The uniformity of weight gain as a function of depth beneath the catalyst indicates the rapidity of catalyst mobility.

Figure 7-114. Char surface after gasification was complete, revealing that the three predrilled holes were intact
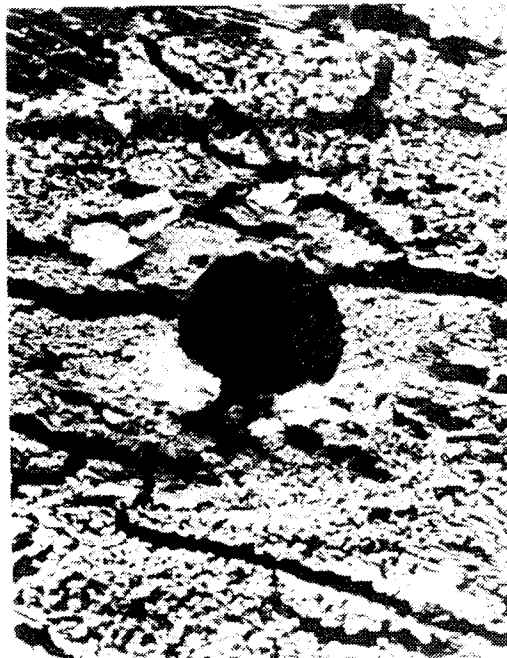
Figure 7-115. Closeup of area shown in Figure 7-114, revealing a penumbric ash which is elliptical and 15% eccentric along the bedding plane

Table 7-1

ANALYSIS OF ILLINOIS #6 (C123)

ULTIMATE ANALYSIS

	As Received	Dry
%Moisture	8.71	0
%Carbon	70.00	76.68
%Hydrogen	4.77	5.22
%Nitrogen	1.59	1.74
%Chlorine	0.37	0.40
%Sulfur	0.67	0.73
%Ash	6.31	6.91
%Oxygen (diff.)	7.58	8.32

PROXIMATE ANALYSIS

	As Received	Dry Basis	MAF
%Moisture	8.71	0	
%Ash	6.31	6.91	
%Volatile	33.15	36.31	
%Fixed Carbon	51.83	56.78	
	100.00	100.00	
Btu/lb	12362	13542	14547
%Sulfur	0.67	0.73	

Table 7-2

GASEOUS HEAT CAPACITIES OF COMMON PYROLYSIS GASES

Heat Capacity (C_p) of Pyrolsis Gases (273 °K - 1500 °K)

$C_p = A + bT + cT^2$ $\qquad$ C_p = cal/mole °K

	a	$b \times 10^3$	$x\,10^7$
H_2	6.9469	−0.1999	4.808
CO	6.420	1.665	−1.96
CO_2	6.214	10.396	−35.45
H_2O	7.256	2.298	2.83
CH_4	3.381	18.044	−43.00
C_2H_6	2.2	38.78	−93.43

Table 7-3

RATE CONSTANTS FOR GASIFICATION OF ILLINOIS #6 CHAR (RUN 444)

Position	Temperature			
	850	900	950	1000
40	+	$2.14 \times 10^{(-3)}$	$5.43 \times 10^{(-3)}$	$1.52 \times 10^{(-2)}$
50	+	+	+	$7.70 \times 10^{(-3)}$
60	+	+	$1.35 \times 10^{(-3)}$	$8.93 \times 10^{(-3)}$
70	+	+	$3.17 \times 10^{(-3)}$	$9.05 \times 10^{(-3)}$
80	$2.74 \times 10^{(-4)}$	$6.98 \times 10^{(-4)}$	$2.50 \times 10^{(-3)}$	$4.34 \times 10^{(-3)}$
90	$3.30 \times 10^{(-4)}$	+	$1.15 \times 10^{(-3)}$	$5.70 \times 10^{(-3)}$
100	$3.70 \times 10^{(-4)}$	$1.61 \times 10^{(-3)}$	$3.23 \times 10^{(-3)}$	+
110	+	$1.16 \times 10^{(-3)}$	+	$2.20 \times 10^{(-3)}$

Table 7-4

RATE CONSTANTS FOR GASIFICATION OF LIGNITE (RUN 436-438)

Position	Temperature			
	850	900	950	1000
60	$2.04 \times 10^{(-3)}$	$5.00 \times 10^{(-3)}+$	$2.30 \times 10^{(-3)}$	
70	$2.33 \times 10^{(-3)}$	$7.19 \times 10^{(-3)}$	$1.37 \times 10^{(-2)}$	
80	$4.56 \times 10^{(-4)}$	+	+	
90	+	+	+	+
100	+	$2.44 \times 10^{(-3)}$	$2.39 \times 10^{(-2)}$	$1.67 \times 10^{(-3)}$
110	$3.40 \times 10^{(-3)}$	$4.44 \times 10^{(-3)}$	+	+
120	$3.58 \times 10^{(-3)}$	+	+	+
130	+	+	+	+
140	+	+	+	+
150	+	+	+	+
160	$4.75 \times 10^{(-4)}$	+	$9.47 \times 10^{(-3)}$	+
170	+	+	$1.77 \times 10^{(-3)}$	$1.30 \times 10^{(-2)}$
180	$4.22 \times 10^{(-4)}$	+	+	$1.54 \times 10^{(-3)}$
190	$1.00 \times 10^{(-3)}$	+	+	$1.90 \times 10^{(-2)}$
200	$7.51 \times 10^{(-4)}$	$7.48 \times 10^{(-3)}$	$1.96 \times 10^{(-2)}$	
210	$3.60 \times 10^{(-3)}$	$1.14 \times 10^{(-2)}$		

Table 7-5

RATE OF EDGE RECESSION,
LIGNITE (RUN 436)

Temperature	Rate (mm/min)
850	0.0
900	$4.5 \times 10^{(-3)}$
950	$3.2 \times 10^{(-2)}$
1000	$6.4 \times 10^{(-2)}$

Table 7-6

ANALYTICAL DATA ON COALS
USED IN STEAM GASIFICATION

LIGNITE
ULTIMATE ANALYSIS

	As Received	Dry
%Moisture	31.10	0
%Carbon	43.45	63.06
%Hydrogen	2.96	4.29
%Nitrogen	0.76	1.11
%Chlorine	0.01	0.01
%Sulfur	0.74	1.07
%Ash	8.07	11.71
%Oxygen (diff.)	12.91	18.75

PROXIMATE ANALYSIS

	As Received	Dry Basis
%Moisture	31.10	0
%Ash	8.07	11.71
%Volatile	45.22	65.63
%Fixed Carbon	15.61	22.66
	100.00	100.00
Btu/lb	6922	10046
%Sulfur	0.74	1.07

Table 7-6 (Continued)

ANALYTICAL DATA ON COALS
USED IN STEAM GASIFICATION

PITTSBURGH #8

ULTIMATE ANALYSIS

	As Received	Dry
%Moisture	2.36	0
%Carbon	79.59	78.44
%Hydrogen	5.45	5.58
%Nitrogen	1.33	1.36
%Chlorine	0.07	0.07
%Sulfur	3.81	3.90
%Ash	6.09	6.24
%Oxygen (diff.)	4.30	4.41

PROXIMATE ANALYSIS

	As Received	Dry Basis	MAF
%Moisture	2.36	0	
%Ash	6.09	6.24	
%Volatile	39.08	40.02	
%Fixed Carbon	52.47	53.74	
	100.00	100.00	
Btu/lb	13941	14278	15228
%Sulfur	3.81	3.90	

Table 7-6 (Continued)

ANALYTICAL DATA ON COALS
USED IN STEAM GASIFICATION

READING ANTHRACITE
ULTIMATE ANALYSIS

	As Received	Dry
%Moisture	3.72	0
%Carbon	78.29	81.31
%Hydrogen	2.08	2.16
%Nitrogen	0.58	0.60
%Chlorine	0.02	0.02
%Sulfur	0.25	0.26
%Ash	13.71	14.24
%Oxygen (diff.)	1.35	1.41

PROXIMATE ANALYSIS

	As Received	Dry Basis	MAF
%Moisture	3.72	0	
%Ash	13.71	14.24	
%Volatile	4.32	4.49	
%Fixed Carbon	78.25	81.27	
	100.00	100.00	
Btu/lb	11540	11986	13976
%Sulfur	0.70	0.73	

Table 7-7

GASIFICATION RATES, MINUTES$^{(-1)} \times 10^3$
PITTSBURGH #8 IN STEAM

	Position				
Temp	30	40	50	60	70
850 °C	1.0	0.28	1.1	+	+
900 °C	3.1	1.3	0.83	+	+
950 °C	9.5	3.8	3.3	+	+
1000 °C	33.0	18.0	8.9	+	+

Section 8

FLUIDIZED BED EXPERIMENTS

Reactions and processes involving contact of a gas and a solid, particularly those involving highly exothermic reactions, are conveniently carried out in fluidized beds. Fluidized beds are unsurpassed in maximizing both gas solid contact and solids mixing. However, because fluidized beds involve at least two phases as well as poorly characterized dynamic processes such as bubble formation, they are very difficult to analyze and model.

Characterization of the fluid dynamics inside a fluidized bed reactor is essential in forming an accurate picture of the reaction processes involved. Experimental verification of flow patterns in a fluidized bed is very difficult. Solids are usually opaque to most low-energy electromagnetic radiation, preventing observation of the flow pattern by conventional techniques (i.e., visual observation using tracers and laser velocimetry).

Three techniques have provided experimental verification of flow patterns. The first is based on pressure fluctuations between two vertical locations and provides information on the frequency and velocity of bubbles (References 38, 28, 30, and 33). A more widely used technique uses capacitance probes that must be inserted into the bed. Changes in the capacitance of the bed can be correlated with bed density but only give information at one point. This has proven useful in obtaining local information such as heat transfer rates near heated and submerged surfaces (Reference 27). To determine the overall flow pattern, a capacitance probe must be moved to a large number of locations, or a series of probes must be used (References 31, 37, 25, and 29). The procedure is laborious and gives poor spatial resolution. In addition, it is always possible to disturb the flow in the proximity of the probe, producing artifacts.

The third technique is x-ray shadow photography. Rowe and coworkers have used this technique to visualize flow patterns inside fluidized beds (References 26, 34, 35, and 36). The technique is similar to the familiar medical x-ray transmission technique but is usually done with a shorter x-ray exposure time. Shadow radiography produces a 2-D projection of

a 3-D object. The shadowing hinders the ability to discern patterns at different depths in the object. The CT technique helps remove the shadowing ambiguities, but usually requires seconds exposure times. This limits the time scale of the features that can be imaged. All of our CT pictures were taken with 9 s exposure time.

The fluidized bed was contained in a cylindrical polyacrylic tube 150 mm long with an inside diameter of 43 mm. Gas distribution was accomplished by two crossed layers of nylon mesh with openings of 34 μm. A subbituminous coal (C285) was used for these experiments. Characteristics of the coal are given in Table 8-1. A −35 mesh (<500 μm) +200 mesh (>75 μm) fraction was used. The coal was fluidized by air at room temperature. Assuming spherical particles, the range of settling velocities in air is from 0.02 to 0.2 m/s. However, as noted in Table 8-1, 83.6% by volume of the sample was less than 115 μm, so that the settling velocities pertinent to the vast majority of the sample were in a much narrower range than the extremes quoted above. At the volumetric mean diameter of 47.1 μm, the settling velocity is 0.062 m/s, which is compatible with the range of observations for fluidization in these experiments. Pressure measurements were made with the same type of Validyne pressure transducers used in the xenon experiments. Experiments were performed on a static bed, a bed near minimum fluidity, and a bed well into the bubbling regime.

Figure 8-1a shows a CT scan of the bed obtained by allowing 28 g of fluidized material to settle by reducing the linear superficial gas velocity from 28.8 cm/s to zero. The static bed height was 2.7 cm. The polyacrylic container appears as the vertical red regions towards the edge of the figure. The picture represents a cross-sectional view through the bed along a diameter. The slice through the diameter was chosen to minimize wall effects which are present in a bed this small. The CT map was converted into a density map using the calibration standards used for coal. A range of densities was assigned a particular color, and the resulting image was displayed as in Figure 8-1a. In this figure and all the following CT images, increasing density is indicated by the color sequence blue <green <yellow <red. An area of uniform color represents a uniform density within the resolution set by the color assignment. Although the pictures are a convenient way of visualizing density gradients, a quantitative technique is to plot density vs. distance along a line though the image of the bed. Figure 8-2a is a plot of the bed density vs. position along the

vertical line shown in Figure 8-1a. The line is actually 3 pixels wide so that the curve appears to be a superposition of three curves. The density at the top of the bed was 0.54 g/cm³/cc and increased to 0.65 g/cm³/cc at the bottom. Figure 8-2b is a plot of bed density vs. position along the horizontal line in Figure 8-1b. This figure indicates the sensitivity of the technique. The average density near the bottom of the bed is ca. 0.640 g/cm³/cc, but fluctuations around the mean as small as 0.005 g/cm³/cc are observed.

Figure 8-1c is a CT scan of a bed with a superficial velocity of 0.048 m/s. At this velocity, visual examination indicated that the bed was well fluidized and expanded, producing a bed height of 32 mm with a pressure drop across the bed of 96.5 Pa. Examination of Figure 8-1c indicates that the bed density was fairly constant in the radial direction for a given height, but was a strong function of vertical position. Figure 8-2c is a plot of bed density vs. position along the vertical line in Figure 8-1c. At this flow rate, the material near the bottom of the bed had a density of 0.65 g/cm³/cc, similar to the static bed. The density decreased, moving from the bottom of the bed, and reached a value of 0.48 g/cm³/cc near the top of the bed.

At a linear superficial velocity of 0.288 m/s, the bed was well into the bubbling regime with 50 mm-high spouts visible at the top of the bed. Figure 8-1d is the CT scan under these conditions. The green and blue areas are low-density regions indicating a low concentration of solids (high void fraction). The pressure drop across the bed was 103 Pa, and the bed height was approximately 33 mm. Bed height was difficult to determine visually in the laboratory due to the spouting. However, a good estimate of bed height can be obtained from the CT image. The bed height is given as the position where there is a large decrease in density. This occurred at 33 mm for a linear velocity of 0.288 m/s. A low-density region in a scan implies that the volume elememt has a low solids content and a corresponding increase in the fraction of the gas present (i.e., a bubble). Since the coal powder used in this work was noncohesive and fluidized well at lower velocities (cf. Figure 8-1c), these low-density regions correspond to regions with high volumetric flow rates of fluidizing gas.

Figure 8-1d shows dramatically the bed circulation with the presence of high-velocity/low-density spouts, as when the superficial velocity was 0.288 m/s. The high-velocity region was annular, as evidenced by the dumbbell symmetry in Figure 8-1d. The

density gradient in the radial direction at a level 18 mm above the distributor is quantified in Figure 8-1d. The density near the walls was ca. 0.6 g/cm³/cc. It decreased to a minimum value of 0.27 g/cm³/cc at a distance of 12 mm from the wall, and then increased to 450 g/cm³/cc at the centerline.

The ability to readily obtain densities with millimeter spatial resolution is a great advantage of the CT technique. Knowing the density of the particles fluidized and the density of the bed as a function of position, it is possible to calcuate the void fraction (ϵ) at any location in the bed from the equation

$$\epsilon = 1 - \rho_{bed} / \rho_{particle} \qquad (8-1)$$

For the static bed, the bulk density of the bed (7 mm above the gas distributor) was 0.640 g/cm³/cc (Figure 8-1b). Using this value and the particle density from Table 8-1, the average void fraction is 0.51. This value is close to the 0.6 normally associated with a static bed. In the vertical direction, the void fraction decreases from 0.57 at the top of the bed to 0.51 at the bottom (Equation 8-1 and Figure 8-1a). The vertical gradient in void fraction can be explained as a result of the experimental procedure. The static bed was formed by allowing a fluidized bed to collapse. As the bed loses fluidization, the material at the bottom is compressed due to the weight of the material above. This compression results in a tighter packing and a higher density/lower void fraction.

Figure 8-1c confirms that at a flow rate of 0.048 m/s the system was fluidized. This corresponds to the spherical settling velocity for particles of 33 μm, close to the most probable particle size in the fluidized sample. Measurement of the bed height from Figure 8-1c yields a value of 32 mm (19% expansion over static bed), which agrees exactly with visual observation. The uniform density at the various levels indicates that there was no channeling in any one location of a characteristic time constant in the region of 9 s or longer. If such a region existed, it would show up as a low-density region due to the lower solids content.

The absence of sustained localized channeling does not imply that channeling was absent. The pressure drop required to lift the bed was about half the expected value for the weight of the coal charge. For example, a bed burden of 28 g of material with a cross

section of 58 cm^2 is expected to require a pressure drop of 186 Pa if uniformly lifted. The actual pressure drop measure was 96.5 Pa. This difference can be explained in terms of bypassing in the bed. Gas will tend to find the path of least resistance. In a low aspect bed, such as the one employed in this work, gas may temporarily find a direct path between the distributor and the free surface. Once this is established, there is very little pressure drop associated with flow through the channel. If these channels are stable, the pressure drop is lower than would be expected for uniform fluidization. The CT images indicated that there were no channels stable with characteristic time constants of 9 s or more. However, a sequence of transient channels randomly located throughout the bed could produce the same low-pressure drop but would not show up in the density map. This may be the case under the conditions for Figure 8-1c.

The vertical density gradient in the bed occurs because the material (gas and solids) at the bottom of the bed supports the weight of the material above, just as in the case of the static bed. The linear increase in density moving from the top of the bed to the bottom is expected because the weight of material increases linearly with depth.

The high velocity case is the most interesting. The CT image in Figure 8-1d confirms accepted theories of gas and solids motion in a fluidized bed. At high velocity, many bubbles are formed which contain little solid material. The gas bubbles are uniformly distributed very close to the distributor but coalesce and eventually form channels or jets inside the reactor as they move upward. At sufficiently high gas flow rates, the channels form a bypass region in the center of the bed. This region has a very high gas flow rate since most of the pressure drop across the bed occurs here. The presence of the central bypass region causes powder to circulate, constantly being drawn towards the centerline at the bottom, thrown into the free space above the bed, and returned to the bottom by moving along the walls. Figure 8-1d shows this circulation. The densities in these various regions allow measurement of the void fraction using Equation 8-1. The void fraction in the central high-velocity region is 0.79, and at the low-velocity wall regions is 0.53.
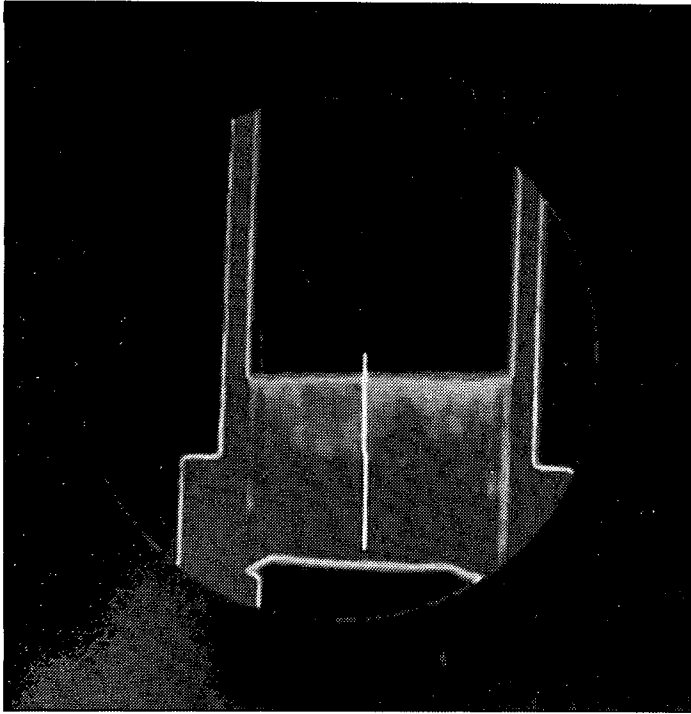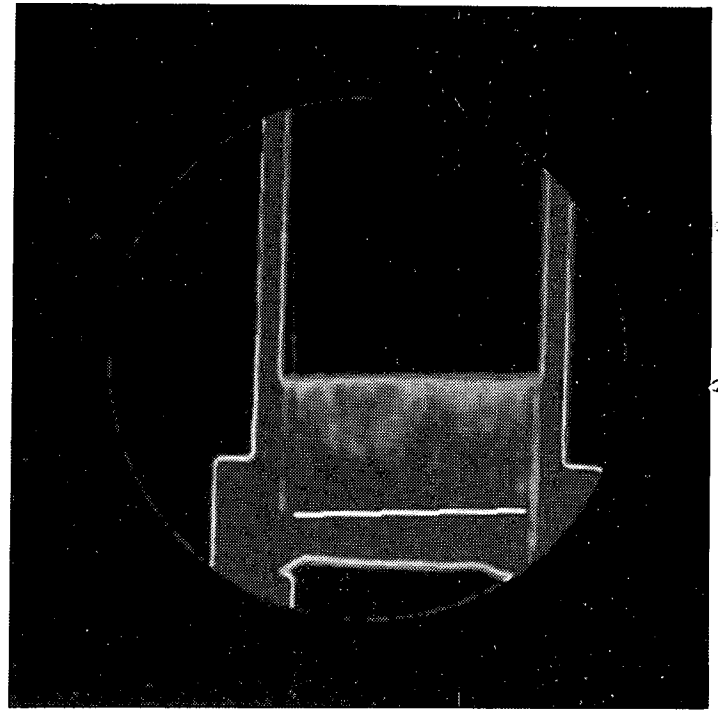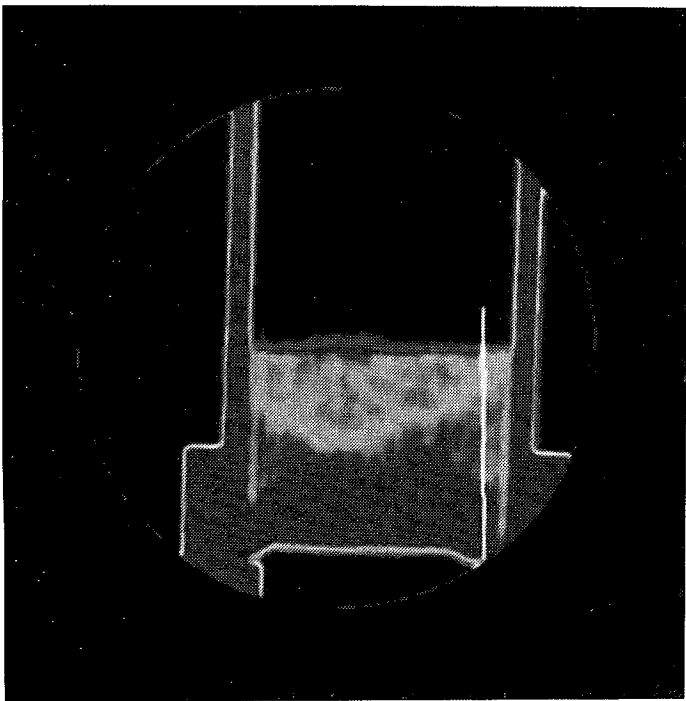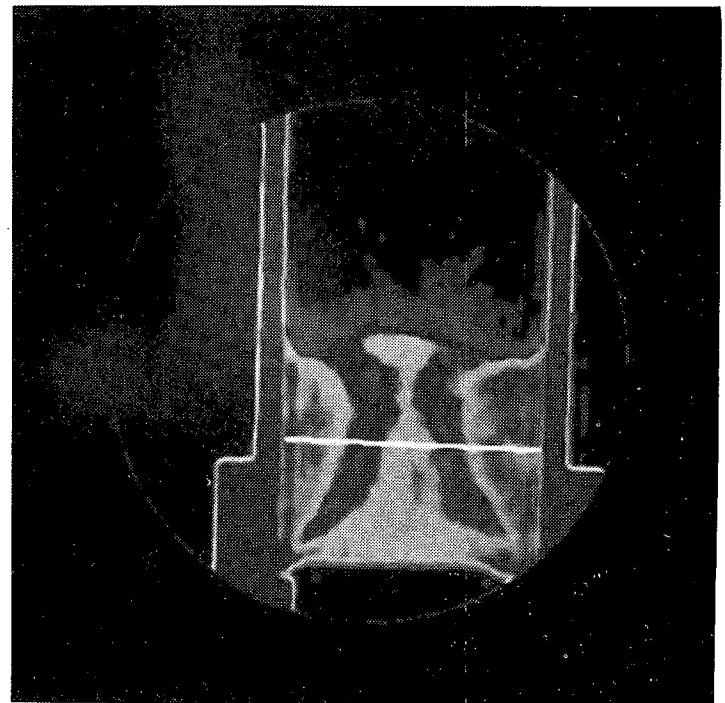
Figure 8-1. CT image of the Fluidized bed with a superficial gas velocity of (a) 0 m/s, (b) 0 m/s, (c) 0.048 m/s, (d) 0.288 m/s. Density differences are denoted by changes in color.
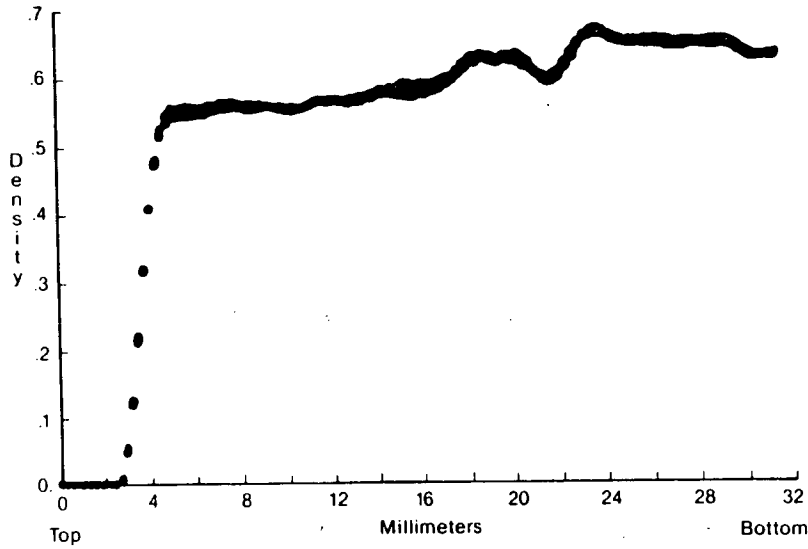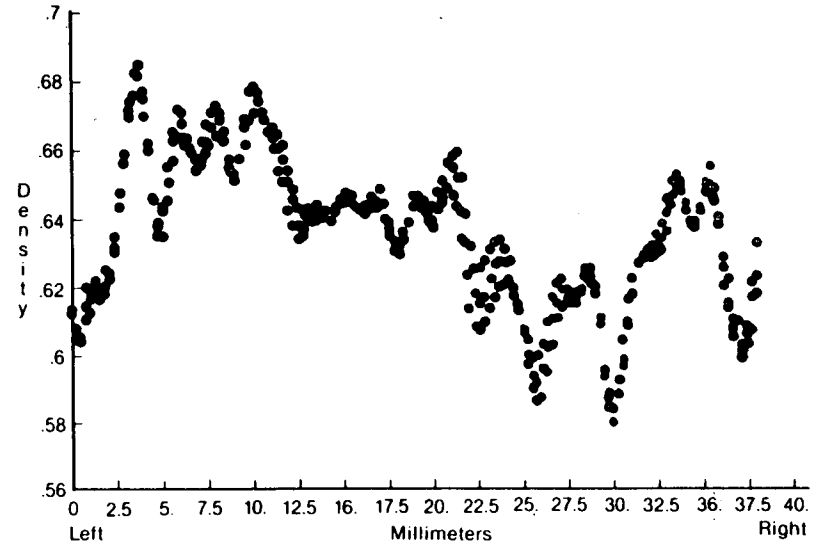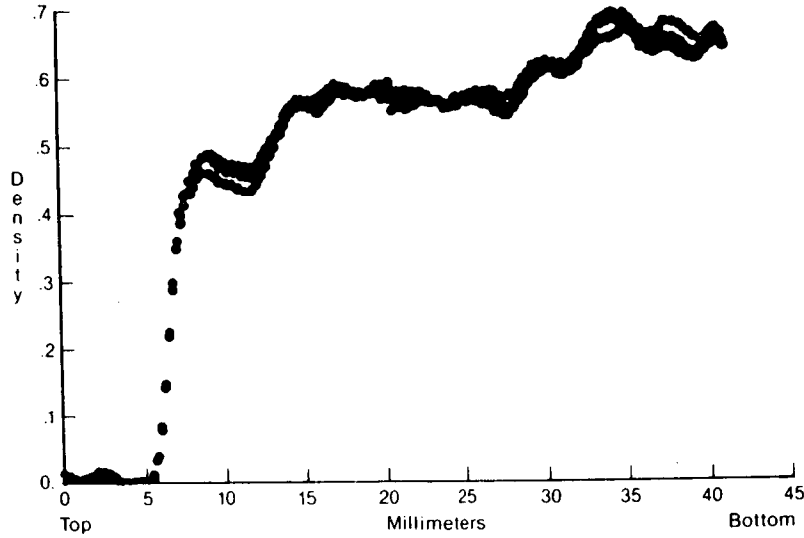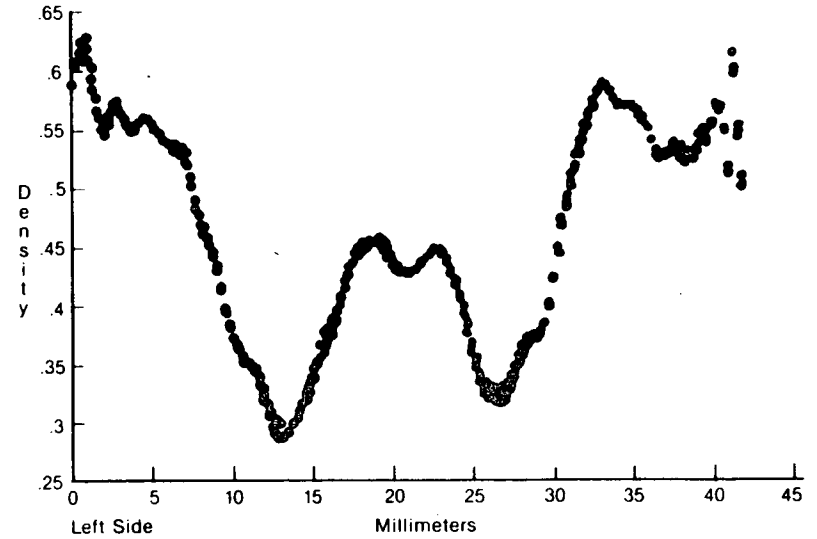
Figure 8-2. Plot of density vs position along the lines in Figure 8-1, (a) density along vertical line in Figure 8-1a from top to bottom, (b) density along horizontal line in Figure 8-1b from left to right (note scale change), (c) density along vertical line in Figure 8-1c measured from top to bottom, (d) density along horizontal line in Figure 8-1d measured from left to right.

Table 8-1

ANALYSIS OF DECKER (C285) COAL

	As Received	Dry
%Moisture	20.72	--
%Carbon	59.65	75.24
%Hydrogen	3.76	4.74
%Nitrogen	1.15	1.45
%Chlorine	0.01	0.01
%Sulfur	0.29	0.36
%Ash	2.29	2.89
%Oxygen (diff.)	12.13	15.31
%Volatile	29.25	36.89
%Fixed Carbon	47.74	60.22
Btu/lb	10117	12761
Density	264 Kg/m^3	

Particle Size Analysis

Diameter, μ	Volume % in Range
>400	0
400-305	4.7
305-210	8.6
210-115	3.0
115-20	47.1
<20	36.5

Section 9

MICROBIAL DESULFURIZATION

The removal of pyritic sulfur from pulverized suspensions of coal by microorganisms such as *Thiobacillus ferrooxidans* is well established (References 39, 40). In the laboratory up to 90% of the pyrite can be removed by bacteria under optimal conditions of pH, nutrient supply, and temperature (References 39 to 42). Reaction rates can be enhanced by the use of finely ground coal, generally 200 mesh or less, and a maximum of 20% pulp density. Such reaction conditions may be compatible with the emerging technology of coal-water slurries and, hence, have increased interest in the use of microorganisms as an alternative to the existing methods of pyritic sulfur removal.

Another approach involves the use of microorganisms to remove, or at least reduce pyritic sulfur from in situ deposits of coal. The rate of pyritic sulfur removal from in situ deposits does not need to be extremely fast because certain extensive coal deposits are not expected to be exploited for another 25 to 50 years. The crucial questions are to what extent the pyritic sulfur can be removed during this period and what factors affect it. Obviously the accessibility of the coal to aqueous solutions and the removal of the resulting acid mine drainage are of prime importance. However, a discussion of the hydrology and engineering of these aspects of in situ pyrite removal is outside the scope of this work. Here the possibility of using CT as a technique to observe the removal of pyrite from lump coal by microorganisms will be investigated. Pyrite can be readily seen in coal because the mineral has a much higher electron density than the surrounding coal.

The coal used was a highly volatile A bituminous type from the Lower Kittanning non-marine seam (C311). Composition analysis of the coal is given in Table 9-1 coal sample is known to have large and extensive inclusions of pyrite. Individual coal pieces were mounted in polyethylene jars. The bottoms of the jars were filled with a layer of epoxy in which three thin aluminum wires were embedded. These wires show up in the CT images and allow the jars to be repositioned accurately in the x-ray beam. The set of jars and lids were autoclaved to ensure sterility; then the coals were anchored in place above the registration

wires with more epoxy. The coals had been sterilized by heating to 120 °C overnight. The jars were sealed until inoculation.

T. ferrooxidans (ATCC 19859, ATCC 33020, and ATCC 13598), T. acidophilus (ATCC 27807), and Acidphilium cryptum (ATCC 33463) were obtained from the American Type Culture Collection. A. organovorum is a novel species of the Acidiphilium genus recently isolated in our laboratory and has been given the provisional designation ATCC 43141 (Reference 43).

Growth medium containing bacteria, or no added bacteria in the case of the controls, was introduced into the vessels containing the embedded coal. A 1/10 volume of bacterial culture was used as an inoculum and contained approximately 10^7 cells of T. ferrooxidans or approximately 10^8 cells of each of the acidophilic heterotrophs: T. acidophilus, A. cryptum, and A. organovorum. Growth media for the T. ferrooxidans or for the mixed culture was a standard minimal salts 9K medium, pH 2.2 with or without $FeSO_4$ (Reference 44). The acidophilic heterotrophs were cultured in NPYE medium with 1% (w/v) glucose. NPYE contained the following per liter: yeast extract, 1/100 volume of a 50 g/l stock solution; $FeSO_4$. 7 H_2O, 1/100 volume of 1 g/l stock solution and basal salts containing (NH_4) $2 SO_4$, 3 g + KCl, 0.1 g + $MgSO_4$. 7 H_2O, 0.5 g + $Ca(NO_3)$. 4 H_2O, 0.02 g + NaH_2PO_4, 6.8 g; pH adjusted to 3.0-3.5 with H_3PO_4. The basal salts and yeast extract were autoclaved separately. The $FeSO_4$. 7 H_2O solution was filter-sterilzed and added to the other solutions after they had been autoclaved.

X-ray CT scans of coals containing numerous pyritic inclusions were taken immediately after inoculation with the various biological growth media #1-7 (Table 9-2) and 4 months after inoculation. Figure 9-1 shows the sample from medium 6, which had no T. ferrooxidans inoculant. The left-hand CT image was taken at time zero, while the right image was taken after 4 months' incubation. The lump of pyrite appears as a solid white area in both images (circled in Figure 9-1), indicating that no gross depeletion of the pyrite inclusion had occurred.

Figure 9-2 shows a plot of pixel-by-pixel comparisons between the scans shown in Figure 9-1. Here CT values for each point (x,y) in the circled spot on the time zero image is compared with the corresponding (x', y') CT value after 4 months' incubation. For two

identical images, a straight line with slope = 1 is expected. Indeed, the resultant plot shows a nearly straight line with a slope of unity. Slight deviations from unity are likely to be the result of minute misalignment effects associated with removing and replacing the sample within the x-ray zone of reconstruction.

No changes in pyritic content were observed in media 4 through 7 where *T. ferrooxidans* cells were absent. When scans from time zero were subtracted pixel-by-pixel from the corresponding images after 4 months' incubation, essentially featureless images resulted. The fact that they are featureless indicates that no pyrite removal has occurred. It also demonstrates that acceptable realignment of the samples has occurred. This is in contrast to the ultimate porosity experiments where the coal structure collapsed and image subtraction were not meaningful.

In contrast to the results just described, we observed depletion of large pyritic inclusions when the lump coal was incubated in media containing *T. ferrooxidans* (media 1 through 3, Table 9-2). No obvious difference was observed between media containing *T. ferrooxidans* alone (media 1, Table 9-2) or media containing associated acidophilic heterotrophs in addition to *T. ferrooxidans* (media 2, Table 9-2). However, a significant difference was observed if the media contained added $FeSO_4$ (media 1, Table 9-2) compared to that with no added $FeSO_4$ (media 3, Table 9-2).

An example of the dissolution of a large pyritic inclusion buried 17 mm below the surface of a lump of coal in media containing *T. ferrooxidans* and added $FeSO_4$ (media 1, Table 9-2) is shown in Figure 9-3. The left-hand image consists of data taken at time zero, while the right-hand image was taken after 4 months' incubation. For clarity, the pyritic inclusions have been magnified 5X and appear as white spots and lighter regions in the rectangles beneath the 1X magnification images above them. The spots in the left-hand image appear much lighter and more solid (arrow, Figure 9-3), while the corresponding region in te right-hand image (arrow, Figure 9-3) includes grey throughout.

A quantitative determination of pyritic dissolution can be made from the pixl-by-pixel comparison shown in Figure 9-4. If the two image were identical, a straight line with slope = 1 would result, as in Figure 9-2. Were the images random, or even shifted one or two pixels with respect to one another (see the discussion on comparison of petrographic

images), the resulting plot of left vs. right would show scatter. The two lines that appear in Figure 9-4 are interpreted to consist of one line for an unaffected region (slope = 1) and a second region corresponding to the pyritic inclusion that showed a significant loss of material (slope 1.4).

T. ferrooxidans is an aerobic, chemoautotrophic bacterium which grows in extremely acidic environments (pH 1.0 to 3.0) such as acid mine drainage or mineral ore leach dumps. It oxidizes ferrous iron or reduced forms of sulfur including mineral sulfides to form sulfuric acid. The energy derived from this oxidation is used to fix carbon dioxide into all the necessary cell carbon via the Calvin cycle, much the same way that plants assimilate carbon dioxide.

T. acidophilus is a facultative chemoautotroph found in close association with *T. ferrooxidans* in acidic habitat. It is a gram-negative, aerobic bacterium thought to be capable of oxidizing elemental sulfur as a source of energy for fixing carbon dioxide. *T. acidophilus* also has the capability to grow heterotrophically, using organic materials as a source of energy as well as incorporating them into cell carbon.

We included a mixture of three *T. ferrooxidans* strains (media 1 through 3, Table 9-2) because it had previously been shown that mixed cultures were more effective than a single pure strain of *T. ferrooxidans* at removing pyritic sulfur in slurries of pulverised coal (Reference 45).

A. cryptum and *A. organovorum* are two species of acidophilic, heterotrophic bacteria that are also found in close association with *T. ferrooxidans*. Acidiphilium species are obligate heterotrophs, obtaining their energy and cell carbon from a variety of organic compounds. They are unable to use any inorganic forms of reduced sulfur or iron as an energy source, and cannot fix carbon dioxide.

Since *T. ferrooxidans* is inhibited by several organic compounds (References 46 and 47), some of which they excrete, it is thought that the association of the heterotrophs might promote the growth of *T. ferrooxidans* by consuming the inhibitory organics (Reference 48). Because coal might contain such inhibitory organic compounds, it was necessary to determine whether the presence of associated heterotrophic microorganisms would be

essential for, or would promote, effective pyrite removal by *T. ferrooxidans*. We found that their presence had no effect on the extent of removal of pyrite by this organism. However, we have not determined whether they affect the rate of removal because we made only one observation 4 months after innoculation. It has previously been demonstrated that the rate of pyritic sulfur removal in slurries of pulverized coal can be enhanced by the addition of associated heterotrophic bacteria to cultures of *T. ferrooxidahs* (Reference 45).

It is important to note that the most effective removal of pyrite occurred when the coal sample was incubated in the presence of *T. ferrooxidans* and its energy source $FeSO_4$. *T. ferrooxidans* catalyzes the reaction:

$$2FeSO_4 + 1/2\ O_2 + H_2SO_4 \xrightarrow{\text{(bacteria)}} Fe_2(SO_4)_3 + H_2O \tag{9-1}$$
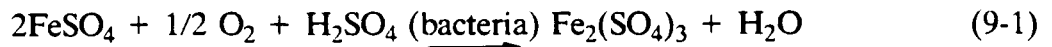
The resulting Fe^{3+} ions of the ferric sulphate can then oxidise the pyrite according to the equation

$$FeS_2 + 2Fe^{3+} \rightarrow 3\ Fe^{2+} + 2\ S^0 \tag{9-2}$$
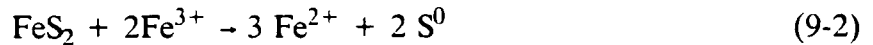
The elemental sulfur can be further oxidized to sulfuric acid primarily by *T. thiooxidans* and some strains of *T. ferrooxidans*, and the ferrous ions are reused as an energy source by *T. ferrooxidans* converting them back to ferric ions.

T. ferrooxidans is also capable of direct oxidation of pyrite:

$$2\ FeS_2 + 7\ 1/2\ O_2 + H_2O \xrightarrow{\text{(bacteria)}} Fe_2(SO_4)_3 + H_2SO_4 \tag{9-3}$$
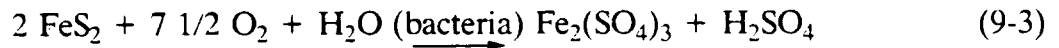
Undoubtedly the reaction given in Equation 9-3 accounts for some of the dissolution of pryite because such dissolution was observed in the absence of added $FeSO_4$. However, since the extent of dissolution is much greater in the presence of added $FeSO_4$, we believe that indirect oxidation by Equations 9-1 and 9-2 is the predominant means of the observed dissolution of the pyrite inclusions.

It is well known that bituminous coals have an extensive micropore structure (Reference 49). These pores measure up to 1.2 nm in width, although bottlenecks in the pores may be only 0.4 to 0.5 nm (Reference 50). Clearly, *T. ferrooxidans* cells, which are

0.5×10^3 nm wide by 1×10^3 nm long could not penetrate the micropores. It is not known whether Fe^{3+} ions with appropriate counter ions could penetrate the micropore system. It s possible that the larger pyrite inclusions observed by the CT are associated with more open spacings, cracks, or cleats, permitting access to solvent carrying Fe^{3+} or, in certain cases, even *T. ferrooxidans* cells. For example, Zwietering and van Krevelen (Reference 52) reported 25% of the pore volume in a British coal had pore radii greater than 103 nm, probably associated with cracks. In an extensive study of pore distribution, Gan et al. (Reference 9) reported pore volumes of between 11.9% and 87.8% greater then 30 nm radius, strongly dependent on coal character. An alternative explanation is that, in the neighborhood of surfaces or planes, either *T. ferrooxidans* cells can directly or indirectly (via production of Fe^{3+}) establish a galvanic effect. This in turn effects the redox chemistry of the more inaccessible pyrite inclusions promoting oxidation of the pyrite.
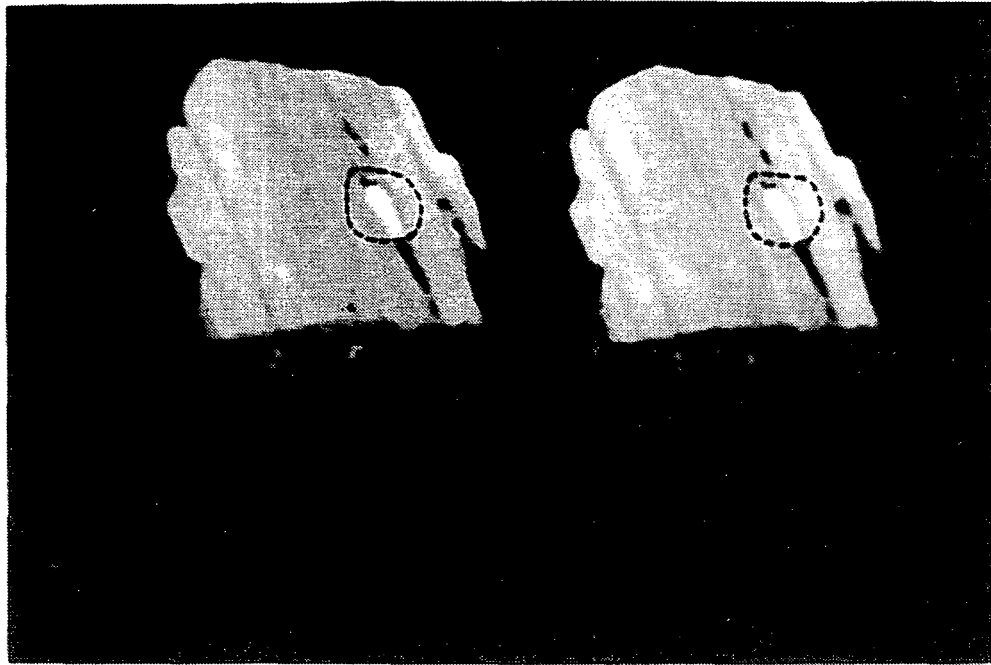
Figure 9-1. X-ray computed tomography images of lump coal incubated in control media #5 (Table 9-2), at time zero (left) and after four months (right). The circled white spot is an iron pyrite inclusion which is apparently unchanged after four months.
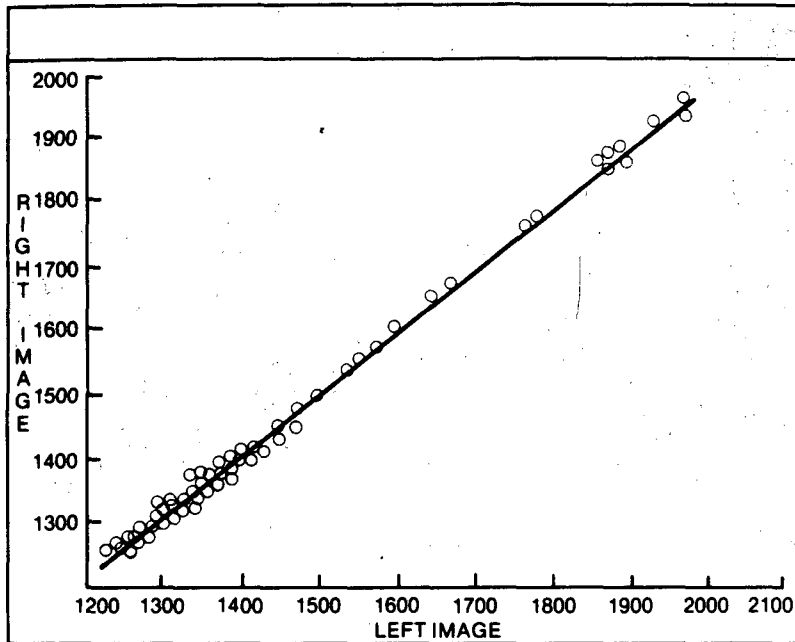
Figure 9-2. A pixel-by-pixel plot of the encircled pyrite inclusion from Figure 9-1, in which CT values for each (x,y) location in the left image are plotted against the corresponding (x′,y′) location in the right image. The slope equals 1.0.
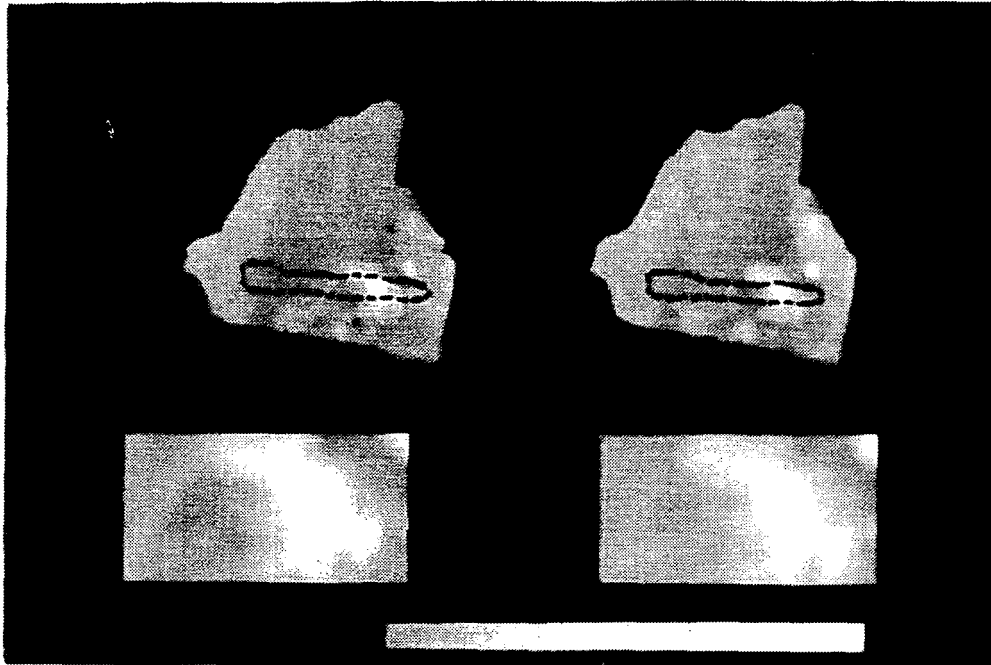
Figure 9-3. CT images of lump coal incubated with media #1 containing *T. ferrooxidans*, at time zero (left) and after four months incubation (right). The rectangular images beneath the lump coal slices are 5X magnifications of the region of interest. The white regions on the left image correspond to pyrite (arrow) and appear grey on the right image (arrow) due to the depletion of pyrite. The bar at the bottom of the figure is the grey scale employed.
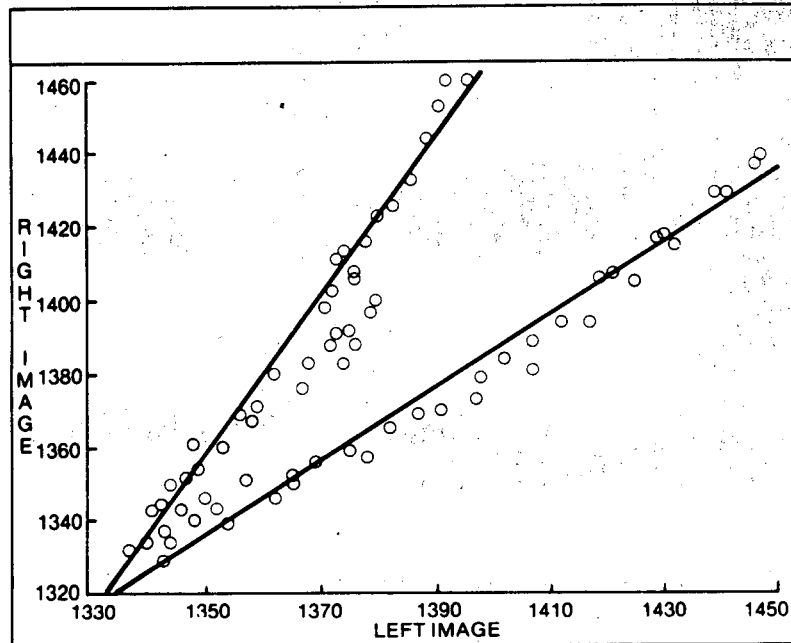
Figure 9-4 for the coal incubated in media #1, containing *T. ferrooxidans.* CT values
for the various (x,y) locations in the left image are plotted vs. the
corresponding (x′,y′) values in the right image. The resulting two lines in
the figure correspond to a region that was unaffected by the medium
(slope = 1) and another that was depleted of pyrite (slope = 2.3).

Table 9-1

ULTIMATE AND PROXIMATE ANALYSIS OF COAL
USED IN MICROBIAL DESULFURIZATION

ULTIMATE ANALYSIS

	As Received	Dry
	%	%
%Moisture	1.32	0
%Carbon	68.21	69.12
%Hydrogen	4.28	4.34
%Nitrogen	1.03	1.04
%Chlorine	0.11	0.11
%Sulfur	1.72	1.74
%Ash	19.30	19.56
%Oxygen (diff.)	4.03	4.09

PROXIMATE ANALYSIS

	As Received	Dry Basis	MAF
	%	%	
Moisture	2.32	0	
Ash	19.30	19.56	
Volatile	26.50	26.85	
Fixed Carbon	52.88	53.59	
	100.00	100.00	
Btu/lb	12153	12316	15311
Sulfur	1.72	1.74	

9-11

Table 9-2

MEDIA USED FOR MICROBIAL DESULFURIZATION

CELLS	MEDIA						
	1 9K/ $FeSO_4$	2 $FeSO_4$	3 9K/ $FeSO_4$	4 9K/ $FeSO_4$	5 9K/ $FeSO_4$	6 9K/	7 NYPE
Thiobacillus ferrooxidans ATCC 19859	+	+	+				
T. ferrooxidans ATCC 33020	+	+	+				
T. ferrooxidans ATCC 13598	+	+	+				
T. acidophilus ATCC 27807		+				+	
Acidiphilum crytum ATCC 33463		+				+	
A. organovorum ATCC 43141		+				+	

Section 10

SLURRY STABILITY

Five coal water slurries were used, each having different surfactant/ stabilizer additives (TSD is a tradename for an ammonium olignosulfonate):

1. 47.62% coal, 30 lb/ton TSD

2. 47.62% coal, 30 lb/ton TSD, 1 lb/ton Flocon

3. 47.62% coal, 30 lb/ton TSD, 5 lb/ton Lomar CW-11

4. 44.9% coal

5. 45.12% coal, 10 lb/ton TSD

The slurries were imaged for 17 h and subtraction images made up to accentuate any changes that might occur by slurry settling. No significant changes were seen in any of these slurries over this period of time.

Section 11

THREE-DIMENSIONAL VISUALIZATION

For four coals — anthracite, Illinois #6, Pittsburgh #8, and lignite — CT pictures were taken every 1.5 mm down the length of the piece of coal. Since 1.5 mm is the effective thickness of the x-ray imaging plane, we then had a CT number for every volume element in the piece of coal. These numbers could then be displayed along any plane or, as in this case, could be used to generate 3-D images of the coal. Using the CT data, surfaces of equal density were created for the coal by extrapolation between neighboring voxels if necessary. Figures 11-1 through 11-3 show different isodensity contours on a piece of Pittsburgh coal. The 1200 contour corresponds closely to the surface density of the coal. Two views of the 3-D shape are shown in Figure 11-1; the bottom one shows that the 1200 density is found primarily on the surface and not inside the lump of coal. The 1250 contour shows bedding plane structures with mineral matter in them, while the 1300 contour pictures (Figure 11-3) show the 3-D structure of heavily mineral-laden planes. Figure 11-4 shows similar 3-D images of a coke from Pittsburgh #8 coal. The CT numbers at which the contours have been drawn are much lower than those used for coal. The images show several contours within the coke that have the same density. This should not be surprising after the discussion of pyrolysis behavior in Section 7.1.3.

11-1

PITTSBURGH COAL, 1200 CONTOUR

PITTSBURGH COAL, 1200 CONTOUR

Figure 11-1. Three-dimensional image of isodensity contours on Pittsburgh #8 coal. Density set at 1200 CT numbers.

Figure 11-2. Three-dimensional image of isodensity contours on Pittsburgh #8 coal. Density set at 1250 CT numbers.
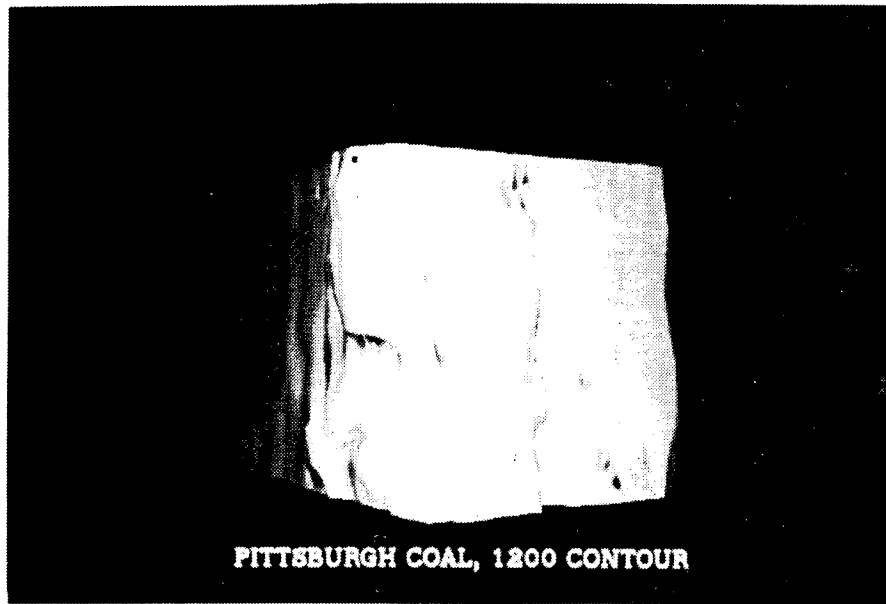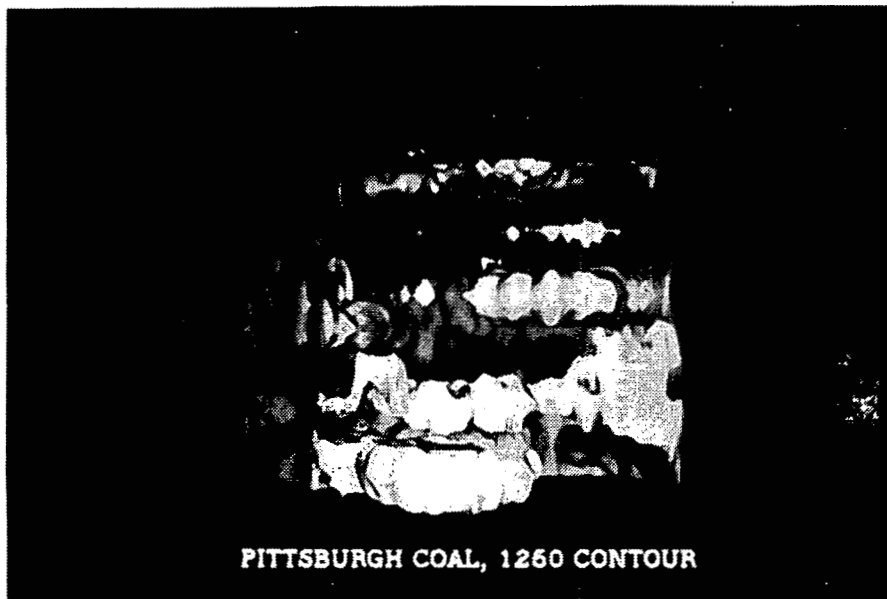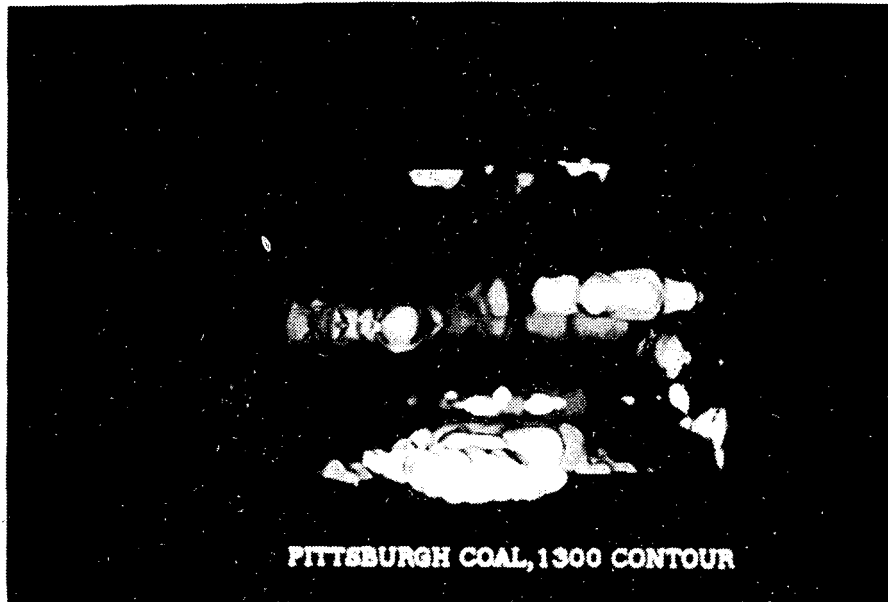
Figure 11-3. Three-dimensional image of isodensity contours on Pittsburgh #8 coal. Density set at 1300 CT numbers.
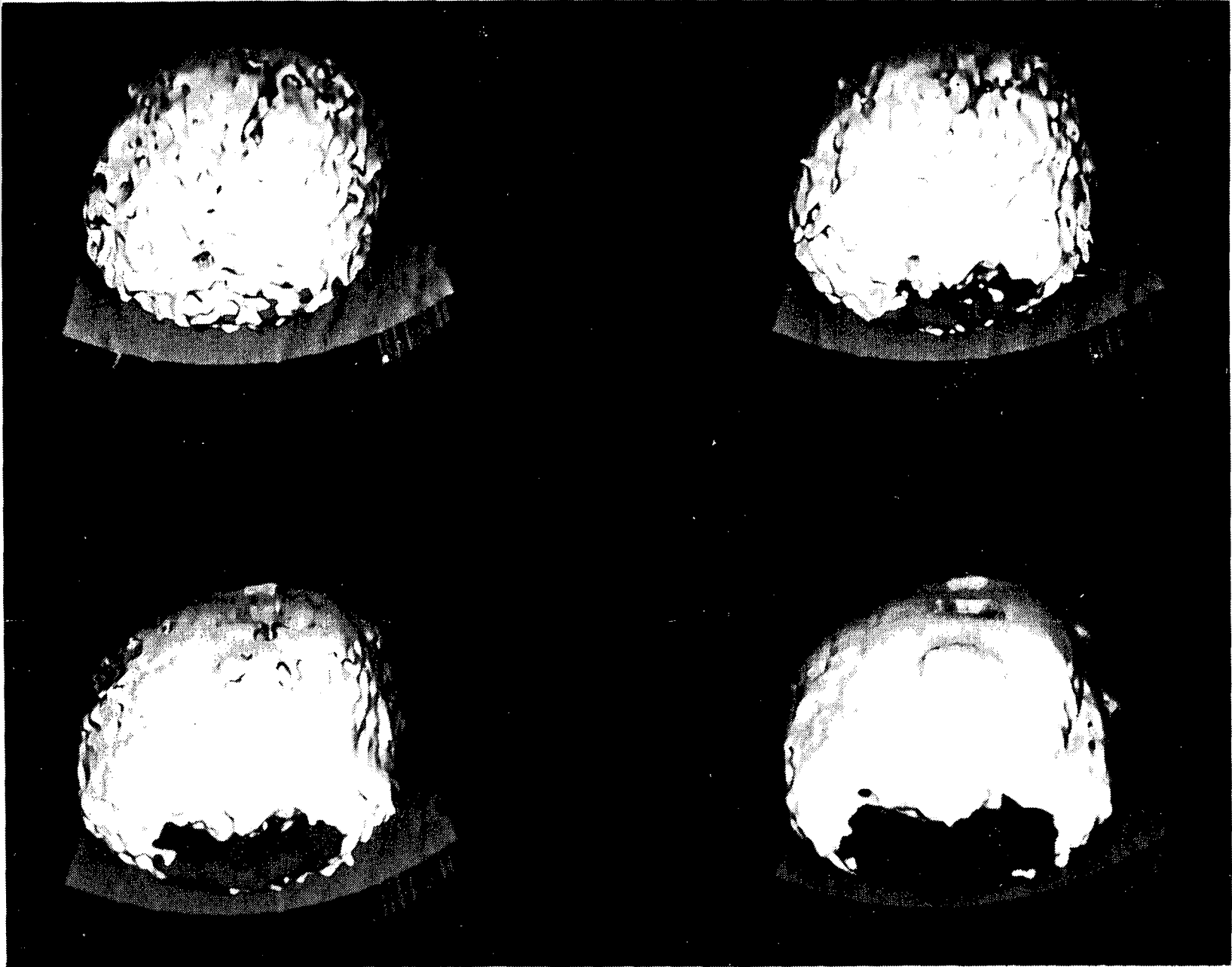
Figure 11-4. Three-dimensional image of Pittsburgh #8 char

Section 12

SUMMARY

This work was primarily intended as a series of scoping experiments to determine the applicability of the CT technique to problems related to coal utilization, particularly gasification. A large number of different types of experiments were carried out with the most promising areas being in —

1. *Gas flow within the coal or char.* With the use of a xenon probe, the complicated patterns of gas flow and penetration could be followed in time and in three dimensions. More sophisticated mathematical tools than those available for this work will be necessary to explain the experimental data. Simplified to a 1-D case, we obtained diffusion coefficients similar to those in the literature for vitrinite.

2. *Pyrolysis and reaction.* The CT experiments provided a new visualization of these phenomena that is particularily useful for modelling studies on fixed bed reactors. The CT shows how quickly the internal regions of the coal heat up, what their internal temperature distribution is, where the pyrolysis zone is within the coal as a function of time and temperature, and, in the case of lignite, where the steam/water front is. The CT also shows the regions of high porosity in the char and where in the char the reactant gases reach and are able to attack. This could be used to give an effective reacting area for the char in a gasifier configuration.

3. *Fluidization phenomena.* Even though the CT has a data acquisition time of 9 s (shorter times down to 2 s are now available on commercial machines, and multiple flash x-ray tubes can bring the time scale down to milliseconds), several different parameters relating to recirculation within the bed can be readily measured, again with a 3-D capability.

Section 13

REFERENCES

1. "Technical Aspects of Computed Tomography" in *Radiology of the Skull and Brain* (T.H. Newton and D.G. Potts, eds.), C.V. Mosby Co., St. Louis, 5 (1981).

2. *Reconstruction Tomography in Diagnostic Radiology and Nuclear Medicine* (M.M. Ter-Pogossian, M.E. Phelps, G.L. Brownell, J.R. Cox, Jr., D.O. Davis, and R.G. Evans, eds.), University Park Press, Baltimore (1977).

3. G.R. Dyrkacz and E.P. Horwitz, *Fuel*, 61, 3 (1982).

4. R.E. Franklin, *Trans. Faraday Soc.*, 45, 274 (1949).

5. D.W. van Krevelen, *Coal*, Elsevier (1961).

6. O.P. Kahajan and P.L. Walker, Jr., in *Analytical Methods for Coal and Coal Properties* (C. Karr, Jr., ed.), Vol 1, Academic Press (1978).

7. E. Stach, M.-Th. Mackowsky, M. Teichmuller, G.H. Taylor, D. Chandra, and R. Teichmuller in *Coal Petrology*, Gebruder Borntraeger, Chap. 2.2 (1975).

8. R.E. Grim in *Clay Mineralogy*, McGraw-Hill (1953).

9. H. Gan, S.P. Nandi, and P.L. Walker, Jr., *Fuel*, 51, 272 (1972).

10. J.O. Hirschfelder, C.F. Curtiss, and R.B. Bird, *Molecular Theory of Gases and Liquids* (John Wiley and Sons, New York, 1st Edition, 1954), p. 1111.

11. E.D. Thimons and F.E. Kissel, *Fuel*, 52, 274 (1973).

12. P.L. Walker, Jr., "Microporosity in Coal: Its Characterization and Implications for Coal Utilization," *Phil. Trans. R. Soc. Lond.*, A300, 65 (1981).

13. R.M. Barrer, *Diffusion in and Through Solids* (Cambridge University Press, 1st Edition, reprinted 1951), Chap II.

14. F.S. Karn, R.A. Friedel, B.M. Thames, and A.G. Sharkey, Jr., *Fuel*, 49, 249 (1970).

15. R.M. Barrer and D.M. Grove, *Trans. Faraday Soc.*, 47, 833 (1951).

16. R.B. Bird, W.E. Stewart, and E.N. Lightfoot, *Transport Phenomena* (John Wiley and Sons, New York, 1963), p. 511.

17. S.P. Nandi and P.L. Walker, Jr., *Adv. in Chem. Series*, 55, 379 (1966).

18. K.A. Kini, *Fuel*, 43, 173 (1964).

19. A.L. McClellan and H.F. Harnsberger, *Coll. and Interface Sci.*, 23, 577 (1967).

20. S. Badzioch, D.R. Gregory, and M.A. Field, *Fuel*, 43, 267 (1964).

21. D. Merrick, *Fuel*, 62, 540 (1983).

22. G.R. Rose, R.F. Zebransky, L.M. Stock, C.B. Huang, V.R. Srinivas, and K. Tse, *Fuel*, 63, 1339 (1984).

23. O. Morel, and F.J. Vastola, *ACS Preprints*, 29, 2, Division of Fuel Chem., St. Louis, April 8-13, 1984.

24. C.L. Spiro, D.W. McKee, P.G. Kosky, E.J. Lamby, and D.H. Maylotte, *Fuel*, 62, 323 (1983).

25. A.E. Almstedt and E. Olsson, *Proceedings of the Seventh International Conference on Fluidized Bed Combustion*, Philadelphia, Pa, 25 Oct. 1982.

26. G.F. Barreto, J.G. Yates, and P.N. Rowe, *Chem. Eng. Sci.* (UK), 38, 3, 345-350 (1983).

27. S.Biyikli, K.Tuzula, and J.C. Chen, DOE Report PC-30214-T7, Oct. 1983.

28. L.T. Fan, T. Ho, and W.P. Walawender, *J. Am. Inst. Chem. Eng.*, 29, 1, 33-39 (1983).

29. G.E. Fasching, D.R. Goff, and D.A. Maxfield, DOE Report MC-16050-1197 (1982).

30. *Proceedings of the Third Annual Advanced Gasification Projects Contractors' Meeting* (M.R. Ghate, ed.), Morgantown, WV (1983).

31. G.M. Homsy, DOE Report PC-30244-T4, Sept. 1981.

32. D.H. Maylotte, E.J. Lamby, P.G. Kosky, and R.L. St. Peters, *Proc. 41st Ironmaking Conference*, 41 (AIME), Pittsburgh, p. 297 (1982).

33. M.T. Nicastro and L.R. Glicksman, *Chem. Eng. Sci.* (UK), 39, 9, 1381-1391, (1984).

34. P.N. Rowe and H.J. MacGillivary, *Int. Conf. on Fluidized Bed Combustion: Systems and Applications*, London, UK, Nov. 1980.

35. P.N. Rowe, L. Santoro, and J.G. Yates, *Chem. Eng. Sci.* (UK), 33, 1, 133-140 (1978).

36. P.N. Rowe and C.X.R. Yacono, *Chem. Eng. Sci.* (UK), 31, 12, 1179-1192, (1976).

37. N.Yutani et al., *Chem. Eng. Sci.*, (UK), 38, 4, 575-582 (1983).

38. M.C. Zhang, P.M. Walsh, and J.M. Beer, *Proceedings of the Seventh International Conference on Fluidized Bed Combustion*, Philadelphia, Oct. 1982.

39. P.R. Dugan and W.A. Appel in *Metallurgical Applications of Bacterial Leaching and Related Microbiological Phenomena* (L.E. Murr, A.E. Torma, and J.A. Brierley, eds.), pp. 223-250, Academic Press, N.Y. (1978).

40. G.F. Andrews and J. Maczuga, *J. Biotech. Bioeng. Symp. No. 12*, 33 (1982).

41. C.M. Detz and G. Barvinchak, *Mining Congress Journal*, 65, 75 (1979).

42. M.R. Hoffman, B.C. Faust, F.A. Panda, H.H. Koo, and H.M. Tsuchiya, *Appl. Environ. Microbiol.*, 42, 259 (1981).

43. J.H. Lobos, T.E. Chisholm, L.H. Bopp, and D.S. Holmes, *Int. J. Syst. Bact.*, 1986, in press.

44. M.P. Silverman and D.G. Lundgren, *J. Bact.*, 77, 642 (1959).

45. P.R. Dugan in *Microbial Chemoautotrophy*, 1980, pp. 3-9.

46. C. Schaitman and D.G. Lundgren, *Canadian J. Microbiol.*, 11, 23 (1962).

47. A. Matin, *Ann. Rev. Microbiol.*, 32, 433 (1978).

48. A.P. Harrison, *Ann. Rev. Microbiol.*, 38, 265 (1984).

49. W.R. Grimes in *Coal Science*, 1, 21 (1982).

50. S-K Wu and L.D. Kispert, *Fuel*, 64, 1681 (1985).

51. T.M. Olsen, P.R. Ashmanm, A.E. Torma, and L.E. Murr in *Biogeochemistry of Ancient and Modern Environments*, Australian Academy of Science, Canberra, p. 693 (1980).

52. P. Zweitering and D.W. van Krevelan, *Fuel*, 33, 331 (1954).

53. W.H. McMaster, N. Kerr Del Grande, J.H. Mallett, and J.H. Hubbell, *Compilation of X-ray Cross Sections*, UCRL-50174, Sec. II, Rev 1.